INVESTIGATIONS ON MEGAWATT CLASS SUB-THz WAVE COAXIAL CAVITY GYROTRON OSCILLATORS

Ph.D THESIS

by

YUVARAJ S

DEPARTMENT OF ELECTRONICS AND COMMUNICATION ENGINEERING
INDIAN INSTITUTE OF TECHNOLOGY ROORKEE
ROORKEE - 247667, INDIA
NOVEMBER, 2018

INVESTIGATIONS ON MEGAWATT CLASS SUB-THz WAVE COAXIAL CAVITY GYROTRON OSCILLATORS

A THESIS

Submitted in partial fulfilment of the requirements for the award of the degree of

DOCTOR OF PHILOSOPHY

in

ELECTRONICS AND COMMUNICATION ENGINEERING

by

YUVARAJ S

DEPARTMENT OF ELECTRONICS AND COMMUNICATION ENGINEERING
INDIAN INSTITUTE OF TECHNOLOGY ROORKEE
ROORKEE – 247 667 (INDIA)
NOVEMBER, 2018

©INDIAN INSTITUTE OF TECHNOLOGY ROORKEE, ROORKEE- 2018
ALL RIGHTS RESERVED

INDIAN INSTITUTE OF TECHNOLOGY ROORKEE

CANDIDATE'S DECLARATION

I hereby certify that the work which is being presented in the thesis entitled **"INVESTIGATIONS ON MEGAWATT CLASS SUB-THz WAVE COAXIAL CAVITY GYROTRON OSCILLATORS"** in partial fulfilment of the requirements for the award of the Degree of Doctor of Philosophy and submitted in the Department of Electronics and Communication Engineering of the Indian Institute of Technology Roorkee, Roorkee is an authentic record of my own work carried out during a period from July, 2014 to November, 2018 under the supervision of Dr. M. V. Kartikeyan, Professor, Department of Electronics and Communication Engineering, Indian Institute of Technology Roorkee, Roorkee.

The matter presented in this thesis has not been submitted by me for the award of any other degree of this or any other Institution.

(YUVARAJ S)

This is to certify that the above statement made by the candidate is correct to the best of my knowledge.

(M. V. Kartikeyan)
Supervisor

The Ph. D. Viva-Voce Examination of **Mr. YUVARAJ S**, Research Scholar, has been held on **May 13, 2019.**

Chairperson, SRC **Signature of External Examiner**

This is to certify that the student has made all the corrections in the thesis.

Signature of Supervisor **Head of the Department**

Dated: 13.05.2019

ABSTRACT

Energy requirement of the world is increasing at an alarming rate due to fast economic growth and increased urbanization. The thermonuclear fusion promises to deliver highly efficient, clean and sustainable energy for future energy demands. For the fusion reaction to take place, the temperature inside the reactor must be increased to 150 million Kelvin. In the controlled fusion experiments, electron cyclotron resonance heating and current drive (ECRH&CD) is considered to be an effective way of heating confined plasmas. The required high power millimeter wave radiations are provided by the gyrotron oscillators. Currently in International Thermonuclear Fusion Reactor (ITER), twenty four 1 MW conventional cavity gyrotrons operating at 170 GHz are planned for installation at the ECRH system.

Next generation fusion reactors like DEMOnstaration (DEMO) tokamak are planned to prove the commercial feasibility of the fusion energy. In ITER, it is experienced that electron cyclotron current drive (ECCD) efficiency is lower than other current drives (CDs) like ion cyclotron CD, neutral beam CD, and lower hybrid CD. In a future commercially attractive tokamaks, for achieving stable operation condition for several hours, the ECRH system should be optimized to provide higher ECCD efficiency. Simulation studies on the ECRH&CD system of a DEMO tokamak demand gyrotrons operating at the frequencies above 200 GHz for an optimum ECCD efficiency. Multifrequency operation of these gyrotrons provides flexibility to the ECRH system for other applications like plasma startup, bulk heating and in the upgraded versions of other existing tokamaks. Furthermore, fast frequency tunability of these gyrotrons in steps of 2-3 GHz would be advantageous for stabilization of the neo-classical tearing modes (NTM) by using non-steerable, fixed launchers. Introduction to thermonuclear fusion and a brief overview of different classes of gyro-devices are discussed in Chapter 1 of the thesis.

The major challenge in the development of megawatt class gyrotrons operating at higher frequencies is to keep control over the ohmic wall loading under allowable cooling limit i.e. $2\,\mathrm{kW/cm^2}$. To reduce the ohmic wall loading at high power operation, oversized cavities are used as an interaction cavity in gyrotrons. However, conventional overmoded cavities lead to the problem of mode competition and voltage depression. Mode competition can be controlled by using a coaxial cavity as the interaction circuit. Insert in the coaxial cavity also reduces the voltage depression of the electron beam and thus increases the limiting current. Consequently, the operational beam current of the coaxial cavity gyrotrons can be increased to a higher value and therefore can be operated at higher power levels compared to conventional cavity gyrotrons. Basic interaction mechanism of gyrotrons and major sub-assemblies of the high power gyrotrons are presented in detail in Chapter 2. Detailed literature review on the development of high power gyrotrons for

plasma heating applications are also presented in this chapter.

Feasibility studies of a 2 MW, dual frequency (220/251.5 GHz) coaxial cavity gyrotron for the probable application in the next generation fusion tokamaks are carried out in Chapter 3. The desired cavity mode pair is chosen by considering the technical constraints for multifrequency operation and geometry of the interaction circuit is optimized for the targeted output power with maximum interaction efficiency. In this design study, a coaxial cavity with triangular corrugations on the insert is used as the interaction circuit. Triangular shaped corrugations on the insert are reported as having the advantage of reducing the localized heating on the insert walls compared to the rectangular or wedge shaped corrugations. RF behavior studies are performed with time dependent multi-mode calculations for both the operating frequencies. Further, startup studies are also performed with beam space charge neutralization using realistic non-uniform magnetic field profile.

Design studies of the electron gun and output system of the proposed dual frequency (220/251.5 GHz) coaxial cavity gyrotron are carried out in Chapter 4. The magnetron injection gun and the magnetic guidance system are designed for required beam parameters determined through RF behavior studies. Output system design studies include physical design of a common nonlinear taper (NLT), a quasi-optical launcher (QOL), and a single disk RF window to support dual regime operation. The NLT is designed with maximum transmission efficiency and minimum mode conversion of the desired mode pair at their respective operating frequencies. The dimpled wall launcher is designed such that it supports, the conversion of the both cavity modes into Gaussian-like mode and the single disk RF window is designed for the effective extraction of high power output RF beam at the desired operating frequencies. Further, design studies are carried out for this proposed dual regime gyrotron to explore the possibility at the third operating frequency of 283 GHz in Chapter 5. The operational cavity mode for this operating frequency (283 GHz) is selected such that the same physical structure of the gyrotron that has already been designed for the dual regime operation would be used for this operation also. RF behavior studies are performed for this 283 GHz operation, and the startup calculations are also carried out. In addition, design studies of the electron gun and the output system are performed to confirm whether these components support the additional operating frequency of 283 GHz.

The design studies of a triple frequency (170/204/236 GHz) coaxial cavity gyrotron are carried out in Chapter 6 that is suitable for plasma heating application in the commercial fusion DEMO tokamak class prototype reactor. To reduce the spatial and maintenance requirements of the heating systems in the DEMO tokamak, the output power of the proposed gyrotron is targeted at $\approx$ 3MW for all the three operating frequencies. In addition to the physical and technical constraints of the multifrequency operation, cavity modes

for this gyrotron are chosen with the mode spread angle of $72^\circ \pm 0.5^\circ$ to support a dual beam output system. RF behavior studies predict the possibility of obtaining 3 MW at the desired operating frequencies in the proposed gyrotron. The geometry of the magnetron injection gun is optimized for generating required electron beam determined through RF behavior studies to support this multifrequency operation. Startup calculations are also carried out with beam space charge neutralization to ensure the 3 MW continuous wave operation at all the three operating frequencies.

In the practical development of coaxial cavity gyrotrons, axes of the outer cavity, coaxial insert, and the electron beam must align together. Any misalignment in the axes of the insert and the outer cavity would change the electromagnetic field structure in the coaxial interaction cavity. Field analysis of the coaxial cavity with misaligned triangular corrugated insert is carried out using surface impedance model (SIM) and full wave analysis (SHM) in Chapter 7. Effect of insert misalignment on the eigenvalue and oscillating frequency of the cavity modes in the interaction cavity of coaxial cavity gyrotron are studied. Finally, Chapter 8 summaries the contribution of this thesis in the development of coaxial cavity gyrotrons for the application in the ECRH system of the experimental tokamaks with the future scope of the present work.

As an outline, in this thesis feasibility studies of the high power, multifrequency coaxial cavity gyrotrons for the probable applications in the next generation fusion tokamaks are carried out. Suitable physical design studies of the major sub-assemblies of gyrotrons supporting the multifrequency operation are performed. In addition, the field analysis of a triangular corrugated coaxial cavity with a misaligned inner rod is also carried out using both SIM and SHM methods.

ACKNOWLEDGEMENTS

The work presented in this thesis is accomplished with the timely help I received from the various people during my doctoral study. I indeed feel grateful and obliged to all of them.

Firstly, I would like to express my sincere gratitude to my supervisor **Prof. M. V. Kartikeyan** for his continuous support and strong belief on me during every stage of this course. His encouragement and suggestions have brought the best out of me and also give confidence towards taking new challenges. In addition to the technical skills, I learned many life lessons from him which I will carry throughout my life.

I would like to thank other members of my research committee **Prof. D. Singh**, **Prof. R. K. Panigrahi** and **Prof. Puneet Jain** for their suggestions and reviews, which immensely helped me to widen my research knowledge in various perspectives. I would also like to extend my thanks to the **Prof. A. Patnaik**, **Prof. K. Rawat** and **Prof. N. P. Pathak** for their lectures and guidance on RF & Microwave Engineering, which helped me to learn a lot in this exciting field. I further extend my gratitude to all office staffs in the Department of Electronics Communication Engineering for their assistantship in handling all the documentation work during this course.

My deepest gratitude to my seniors **Dr. Gaurav Singh Baghel, Dr. Sukwinder Singh** and **Dr. Jagannath Malik** for their immense help and guidance from the beginning of my research study. I am lucky to have their support even after completing their doctoral degree. My big thanks goes to **Dr. Madan Singh Chauhan** for his valuable suggestions and discussions on high power microwave devices. I always cherish those moments we both enjoyed together on the international conference tour. I would also like to thank **Ms. Delphine Alphonsa Jose** for her timely help and proof reading most of my research articles.

I wish to express my thanks to **Mr. Himanshu Maurya**, **Mr. Ajeet Kumar** and **Mr. Sambaiah Pelluri** for their suggestions and emotional support during the critical phase of my life. I would also like to thank my juniors and other members of Millimeter/THz wave laboratory **Ms. Surbhi Adya, Mr. Debasish Mondal, Mr. K. Venkateswara Rao, Ms. Priya Suresh Nair, Ms. Anmol Jain** and **Mr. Aditya Singh Thakur** for being there and helping me during the course of thesis writing.

I wish to express my love and gratitude to my Ph.D. friends **Mr. Rakesh Sharma**, **Mr. Tushar Goel**, **Mr. Raj Kumar**, **Mr. Om Prakash**, **Dr. Arvind Sharma**, **Mr. Karan Gumber**, **Mr. Praveen**, **Mr. Sandeep** and **Mr. Narender** for all fun we had and never-ending dining table discussions. My deepest thanks goes to **Dr. Raj Kumar**, **Dr. Chockalingam**, **Mr. Kasi Viswanathan**, **Mr. D. Karthik**, **Dr. Raja** and **Ms. Pallavi Gupta** for their love and support bestowed on me during my days at

Roorkee which help me to keep away from unwanted pressures.

I wish to express my heartfelt love and gratitude to my parents, **Mr. Sivasubramanian and Mrs. Thangapandiammal**, for their love, care, patience and strong belief on me in all ups and downs during this course and my life in general. I would also like to express thanks to my loving sister, **Ms. Janani**, for never letting me feel lonely in life. Above all, I am grateful to the Lord Almighty for providing me the opportunity to achieve all this.

(Yuvaraj S)

To

my Amma, Appa

and Janu

Contents

List of Figures

List of Tables

Chapter 1

Introduction

1.1 Introduction to Thermonuclear Fusion

According to the UN report in the year 2018, world population is increasing at a rate of 1.09% per annum, and by 2050 the population of the world would reach 9.8 billion [1]. Due to the fast economic growth and increased urbanization, the energy requirement of the world is increasing at an alarming rate. Eighty percent of the present energy demands are fulfilled by the fossil fuels, which emit an unacceptable amount of the greenhouse gases. The renewable energy sources like hydro, solar, wind, tidal provide clean energy, but their capability to fulfill the entire energy demands is still a topic of discussion [2]. On the other hand, the controlled thermonuclear fusion promises to provide long-term, sustainable clean energy for the future requirements [3].

The nuclear fusion reaction is the same one that occurs in the core of the sun and stars, in which two lighter hydrogen nuclei collide, fuse together to form a heavier atom of helium. According to the Einstein's famous mass-energy equivalence [4], $E = \Delta m.c^2$, an enormous amount of the energy (E) released during this reaction can be realized as the difference in masses of the heavier atom and two colliding lighter atoms (Δm), where c is the velocity of the light. The temperature required for the occurrence of this fusion reaction in the sun is around 15 million Kelvin [5]. Fusion community has identified that the most efficient fusion reaction that can be conducted in a laboratory setup is the fusion of two hydrogen isotopes namely deuterium (D) and tritium (T). The DT fusion reaction is given by [6]

$$^{2}_{1}\mathrm{D} + ^{3}_{1}\mathrm{T} \mapsto ^{4}_{2}\mathrm{He}(3.5\ \mathrm{MeV}) + \mathrm{n}(14.1\ \mathrm{MeV}) \tag{1.1}$$

By fusing two lighter hydrogen isotopes, helium atom and a neutron are formed with the release of 17.6 MeV of energy. DT fusion reaction is considered efficient since it

produces high energy gain with very low temperature requirements.

To achieve this fusion reaction in the laboratory, following conditions should be satisfied [5]:

- A very high temperature of around 150 million Kelvin, to overcome the ion-ion electrostatic repulsive force between the nuclei (Coulomb Barrier), so that strong nuclear force can takeover.
- Sufficient density of plasmas, which provides a favorable environment for the elements to collide and generate energy.
- Sufficient confinement time for holding the dense plasma, as the plasma starts to expand over the available volume.

Inside the core of the fusion reactor, due to very high temperature, particles get ionized and the electrons are separated from the nuclei and forms plasma. In plasma state, charge particles (positively charged nuclei and negatively charged electrons) are free to move. DC magnetic field is used to control and confine this hot plasma. Various heating methods are used concurrently in the reactor to achieve the required temperature of plasma for the fusion reaction. Inside the core of the reactor, the magnetic fields are used to control the hot plasma, which induce the current. The induced current energizes the plasma particles (ions and electrons) as it travels. These energized particles start to collide, which creates the resistive effect that results in heating. This type of heating is termed as ohmic heating, and it depends on the induced plasma current and the resistance. As the temperature of the plasma increases, resistance created by the collision of particles decrease; hence the plasma temperature can be increased only up to certain limited level through the ohmic heating.

In order to further heat the plasmas to the required threshold level, external heating methods are used. Two different external heating methods are used in the reactor. One is the neutral beam injection (NBI), and another is the radio frequency (RF) heating. In the NBI, ionized deuterium particles are accelerated to the required energy level. These particles are passed through the ion neutralizer where ions get neutralized. These high energy neutral beams are then shooted into the heart of the reactor, where they collide with the plasma particles to generate heat [7].

In the RF heating, high frequency electromagnetic waves are injected into the reactor for heating the plasmas. Inside the core, charged particles of the plasmas gyrate around the guiding magnetic field. According to the cyclotron interaction, injected electromagnetic waves transfer its RF energy to the charge particles increasing its kinetic energy. Energized charge particles collide with each other and cause the heating effect. Based on the charge of the particle this heating is divided into two categories (a) Electron Cyclotron Resonance Heating (ECRH), (b) Ion Cyclotron Resonance Heating (ICRH). For

ICRH, tetrodes are used for the generation of the electromagnetic waves [8], and in the ECRH system gyrotrons are used as sources for the microwave generation [9]. Compared to other heating methods, ECRH is the most effective heating method that is suitable for both version of fusion reactors (tokamak and stellarator) because of the following advantages [10]:

- In the ECRH, heating is done using a narrow pencil-like RF beam, and hence localized heating can be done to avoid cooling of certain plasma areas.
- In the ECRH system transmitting antennas, launchers and mirrors can be kept away from the core, as the RF beams can be transmitted in vacuum and coupling of the beam is also not sensitive to the parameters of the plasma edges.
- The ECRH method of heating is also identified as an ideal candidate for controlling the magneto hydro dynamics (MHD) instabilities occurring in the fusion reactors.

In the experimental tokamaks, for the ECRH application, high power electromagnetic waves are required in the range of 100-250 GHz [11] and hence, it is required to develop sources which can operate at higher frequencies and greater power levels [12]. Solid state power amplifiers are capable of generating and amplifying signals at millimeter wave ranges and are widely used in communication systems [13], [14]. Solid state devices are also used in the control circuits of particle accelerators and fusion tokamaks [15]. However, they are not capable of generating high power RF signals required for plasma heating applications. For these high power applications, conventional microwave tubes (transit time electron beam devices) like klystron, traveling wave tubes can be preferred. However, the size of the interaction circuit of the microwave tubes is directly related to the wavelength of RF wave; hence at higher frequencies the power handling capability of these devices is limited [16]. To overcome these limitations, the fusion research community made an immense effort towards the development of the new era of the fast wave devices [17]. These fast wave devices are capable of generating/ amplifying electromagnetic waves with very high power levels in millimeter to sub-millimeter wavelength ranges.

1.2 Brief Overview of Gyro-Devices

Gyro-devices are the kind of fast wave devices in which the electromagnetic waves travel with a phase velocity greater than the speed of light [18]. Electron cyclotron maser (ECM) and free electron maser (FEM) are two different categories of the fast wave devices. The gyro-devices belong to the ECM kind of fast wave devices [19]. In the ECMs, coherent electromagnetic waves are generated or amplified through simulated emission of radiation from the relativistic electron beam [20]. In presence of the magnetic field, the weakly

relativistic gyrating electron beam emits electromagnetic radiations whose electric field is transverse to the direction of propagation. Coherent electromagnetic radiation occurs when the contribution from the electron beam enhances the already existing RF wave in the interaction region. This is possible when the synchronism is achieved between the cyclotron frequency of the gyrating electron beam and the frequency of the electromagnetic wave in the interaction cavity [21]. On the contrary to the linear beam devices, the size of the interaction circuit in the gyro-devices is not directly related to the wavelength of EM radiation. Moreover, in the interaction region of the ECM, there is no requirement of dielectric loading or periodically rippled walls, and a simple cylindrical waveguide is used as the interaction circuit. The oversized waveguide allows the use of high power electron beam with larger beam radius. This makes the gyro-devices to generate or amplify high power electromagnetic waves in millimeter to sub-millimeter wavelength ranges [18]. There are some analogies that exist between linear beam devices and gyro-devices. In both types of devices, bunching of the electron beam occurs after initial energy modulation and bunching continues even after the modulating RF field is removed in the drift region [16]. However in the linear beam devices, the electron beam remains in the favorable bunching phase only for the half cycle of RF wave at the interaction cavity. But in the gyro-devices, once the favorable bunching is achieved, the electron beam remains in this favorable phase throughout the interaction region.

Gyrotron

Gyrotrons are one of the earliest developed most popular ECM devices those are widely used for the plasma heating applications in the experimental tokamaks. In the early of 1970's, Russian development on a magnetron injection gun generated the hollow electron beam with high transverse velocity paved the way for the development of high power gyrotrons [22]. In the gyrotrons, weakly relativistic electron beam (electron beam energy $(U_b) < 100\,\text{keV}$) with high transverse momentum is used. The interaction region of the gyrotron is a smooth cylindrical cavity, which is operated close to the resonant frequency of the waveguide mode. As the electromagnetic wave in the cavity is close to the cutoff frequency, the axial wave number of the RF is near to zero, and Doppler shift is negligible for the case of gyrotron interaction. The frequency of oscillation is determined by the relativistic factor of the electron beam and the external applied magnetic field [9], [23]. The resonance condition is also possible between the RF wave and harmonics of the electron cyclotron. In the harmonic operation of the gyrotron, for the given frequency the magnetic field requirement is reduced by the harmonic factor 's' [17]. In addition to the plasma heating application, gyrotrons are also developed for other industrial, medical and scientific applications like sintering of ceramics [24], [25], DNP-NMR spectroscopy [26],

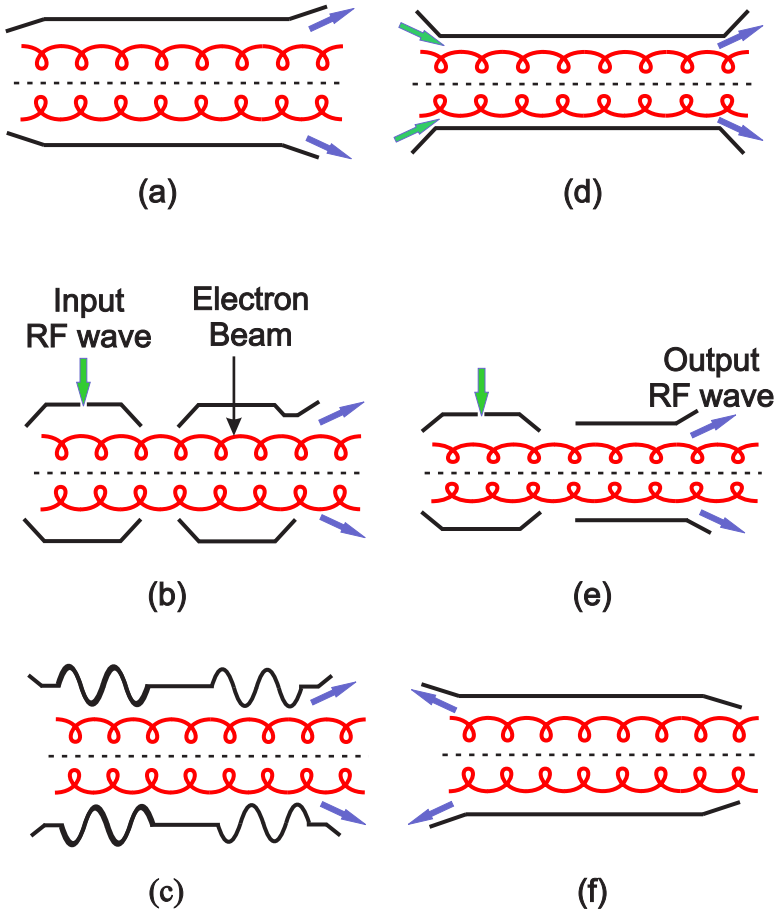

Figure 1.1: Schematic of the interaction region in different gyro-devices: (a) Gyrotron, (b) Gyro-klystron, (c) CARM (d) Gyro-TWT, (e) Gyro-twystron, (f) Gyro-BWO [17].

[27] and generation of soft X rays. Possibility of generating high power orbital angular momentum (OAM) modes in gyrotron by the natural excitation of gyrating electron beam has been reported in [28] and thus millimeter wave gyrotrons can also find application in the long-distance wireless communication [29].

Gyro-klystron

Gyro-klystron is an amplifier class of device whose interaction mechanism is similar to that of the gyrotron. However, in the gyro-klystron initial energy modulation of the electron beam is done by the input low power RF wave which needs to be amplified. The input RF wave is coupled to the input cavity, where the energy modulation of the electron beam occurs and creates orbital bunching. The bunched electron beam travels through the drift section and excites the RF field in the output cavity. The RF field excited in the output cavity has the same frequency and phase of the input waveform. The energy lost by the electron beam is used for amplifying the RF field [30]. Additional cavities are placed between the input and output cavities for increasing the gain of the tube [31].

Cyclotron Auto Resonance Maser

Cyclotron auto resonance maser (CARM) oscillator is operated with the highly relativistic electron beam ($U_b > 1$ MeV) with the interaction mechanism same as that of the gyrotron but operated far away from the cutoff region. Since the phase velocity of the EM wave is close to the speed of light, the increase in electron cyclotron frequency (due to the energy loss in the beam) is compensated by the Doppler term and this phenomenon is called auto-resonance [17]. Due to large Doppler shift, compared to the gyrotron, the magnetic field requirement in the CARM for the given frequency is less. Feedback mechanism by the Bragg resonator is required in the CARM to avoid other low-frequency parasitic interactions [32]. In the CARM, the electron beam with a low to moderate velocity ratio is preferred and the efficiency of the CARM is sensitive to the parallel electron velocity spread [33].

Gyro-Traveling Wave Tube

In a gyro- traveling wave tube amplifier (gyro-TWT), a smooth cylindrical waveguide is used as the interaction circuit, and the moderately relativistic electron beam is used [34]. In the gyro-TWT, the axial wave number (k_z) is small but greater than zero and the transverse bunching of the electron beam dominates over the axial bunching. In the interaction region, the group velocity of the traveling wave matches with the axial velocity of the electron beam. The input RF wave to be amplified is coupled inside the waveguide with the specific mode pattern [35], [36]. To gain benefit from the auto resonance, the cutoff frequency of the waveguide is set less than the electron cyclotron frequency. Compared to the gyro-klystron, the gyro-TWT amplifier offers wider bandwidth and therefore are widely used as an output amplifier in the millimeter wave radar systems [37], [38]. However, conventional helix TWT amplifiers are still dominating the field of space communication due to their robustness and guaranteed lifetime [39], [40].

Gyro-Twystron

Gyro-twystron is a hybrid type of amplifier which uses the input cavity same as that of the gyro-klystron and the output cavity is replaced by a long cylindrical waveguide. The presence of the output waveguide overcomes the problem of microwave breakdown that occurs in the output cavity of the gyro-klystron at high power operations [41]. In the input cavity, the RF wave to be amplified modulates the electron beam energy and creates the orbital bunching. The bunched electron beam travels through the field free drift region and excites the electromagnetic wave in the output waveguide section. As the device is of a hybrid type, it gains the advantage of both gyro-klystron and gyro-TWT. To increase

the gain of the amplifier, intermediate cavities are placed between the input cavity and the output waveguide section [42].

Gyro-Backward Wave Oscillator

Gyro-backward wave oscillator (BWO) is a fast wave counterpart of conventional BWO. In a gyro-backward wave oscillator (BWO), the magnetic field and the electron beam parameters are adjusted for the cyclotron interaction between the electron beam and the RF wave traveling in a direction opposite to the electron beam motion [43]. Conventional BWO operating in THz frequency range are also being developed to understand plasma turbulence in nuclear fusion reactors [44]. In the gyro-BWO, the resonant frequency is highly dependent on the accelerating voltage of the electron beam, and thus by tuning the accelerating voltage, the operating frequency can be varied very fast. Due to the Doppler down shift, for the given frequency the magnetic field requirement in the gyro-BWO is higher than that of the gyrotron. The overall efficiency of the gyro-BWO is less compared to that of the gyrotron, as the amplitude field strength of the EM wave in the gyro-BWO is high at the entrance and low at the exit of the electron beam [45].

1.3 Motivation

The thermonuclear fusion promises to deliver clean and sustainable energy for the future energy demands. For the fusion reaction, to take place temperature inside the reactor must reach 150 million Kelvin. In the plasma fusion experiments, electron cyclotron resonance heating and current drive (ECRH&CD) is considered the most effective way of heating magnetically confined plasmas [10]. Gyrotrons are the promising millimeter and sub-THz wave sources those are widely employed in experimental tokamaks for ECRH&CD application, and are capable of generating power in the range of several hundred kilowatts to few megawatts [46]. Currently in Wendelstein 7-X (W7-X) stellarator, ten gyrotrons each delivering 1 MW continuous wave (CW) (1800 s) power at 140 GHz are successfully installed for the plasma heating [47]. Quasi-optical transmission lines are used for the transmission of RF power to the core of the W7-X stellarator. In International Thermonuclear Experimental Reactor (ITER), 24 gyrotrons are proposed for the ECRH applications, and each gyrotron emits 1 MW-long pulse (3600 s) power, at 170 GHz [48], [49]. ITER is the world's largest fusion tokamak aiming to prove the nuclear fusion as the commercial, large-scale and clean energy production. The major objective of the ITER is to generate the electrical power of 500 MW with the functional power gain of 10 and to stabilize the fusion plasma for the longer time period. European Union 140 GHz gyrotron holds the record of an output power of 0.92 MW for the pulse duration of 30 minutes

with 44% efficiency. A 110 GHz gyrotron developed by JAEA-TOSHIBA achieved the maximum output power of 1.5 MW for the 4 s pulse with 45% efficiency [50]. Russian 170 GHz ITER gyrotron delivers the output power of 0.99/1.2 MW for the pulse length of 1000/100 s with the efficiency of 53% in both the cases [51]. Japanese 170 GHz ITER gyrotron holds the world record energy of 2.88 GJ (0.8 MW, 1 hour) with the efficiency of 57% [52].

One of the main design goals in the development of the high frequency megawatt class gyrotrons is to keep the ohmic wall loading under the prescribed limit (i.e. $2\,\mathrm{kW/cm^2}$) [17]. To obtain the ohmic wall losses under this limit, the gyrotrons are operated in the higher order modes. However, this results in severe mode competition problems as the mode spectrum at these higher order modes are very dense. Therefore, it is difficult to attain an efficient single mode operation in a conventional gyrotron just with beam positioning. In such a scenario, the usage of a coaxial insert reduces the mode competition [53]. The eigenvalues of operating modes in a coaxial cavity depend on the radii ratio of the outer cavity to the insert. As a result, in a coaxial cavity with downtapered insert, the diffractive Q factor of modes depends on the slope of the eigenvalue curve. Thus, by selecting the insert radius, it is possible to alter the diffractive Q factor of the competing modes, thereby reducing the mode competition in the cavity. The coaxial cavity also reduces the voltage depression of the annular electron beam, consequently increases the limiting current, which opens up the possibilities of operating the gyrotron at higher beam currents. Introducing corrugations on the insert not only helps to exercise better control over the mode rarefaction but also reduces the ohmic wall loading on the surface of the insert [54]. Short pulse experiments on a 2 MW, 170 GHz coaxial cavity gyrotron with rectangular corrugated insert have been carried out at KIT, Germany [55].

In addition to the ECRH&CD applications, experimental tokamaks require RF beams at different frequencies for various other applications such as plasma startup, plasma stability control, bulk heating, collective Thomson scattering diagnosis, and so on [56]. Therefore, to cater these multiple requirements, multifrequency gyrotrons are being developed [57]. This is mainly because employing a multifrequency gyrotron can significantly improve the adaptability of an ECRH/ECCD systems to operate at different frequencies and function in diverse experimental setups without any momentous increase in construction costs [58]. Also, fast step-tunable operation (few seconds) of the gyrotron in steps of 2-3 GHz allows the use of fixed non-steerable mirrors inside the torus for stabilization of the neo-classical tearing modes (NTM) [59]. A common single-disk window can be used for the multifrequency operation of the gyrotron, however, for the step-tunable operation broad band Brewster type window is required [60]. Experimental long-pulse (2 s) operation of a 1 MW, multifrequency gyrotron (104/137/170/203 GHz) has been reported

by Japanese researchers in [61]. A dual-frequency gyrotron (105/140 GHz) is installed in the ECRH system of the ASDEX-U (German Tokamak) [62]. The step-tunable operation of a D-band gyrotron in the frequency range of 124-169 GHz has been performed at KIT, Germany [60]. A triple-frequency gyrotron (82/110/138 GHz) is developed for the plasma heating application in JT-60 SA (Japan Tokamak) [63]. Two 1 MW dual frequency gyrotrons (84/126 GHz) are proposed for the upgraded version of ECRH system in the TCV (Swiss Tokamak) [64].

Energy generation in the fusion reactor is directly related to the number of fusion reactions that occur inside the core. Thus, larger the size of the core, greater the number of fusion reactions and hence increased energy generation. Fusion community is aiming to reduce the electricity production cost in the future machines [3]. Thus, gyrotrons for the future tokamaks must be operated at higher frequency and power levels. Besides, to overcome the existing challenges in the steady-state fusion operation, future machines must ensure adequate reliability and increased tritium self-sufficiency [65]. DEMOnstration power plant (DEMO) is expected to be the first commercial prototype of the fusion reactor aimed to promote the generation of the fusion power in a large commercial scale [66], [67], [68]. In the ITER, it is experienced that electron cyclotron current drive (ECCD) efficiency is lower than other CDs (like ion cyclotron CD, neutral beam CD, and lower hybrid CD) [69]. In a commercially attractive tokamak like DEMO, to achieve stable condition for long hours, the ECRH system should be optimized to provide greater ECCD efficiency [12]. Simulation studies on the ECRH system of the DEMO tokamak predicted that by launching beams in the mid-plane, ECCD efficiency could be limited by second harmonic absorption and this can be improved when the RF waves are injected from the top of the tokamak [70], [59]. As per DEMO fusion 2012 base line, for the improved ECCD efficiency, the ECRH system should ensure the millimeter wave power of 50 MW in the frequencies above 200 GHz [12], [58]. Thus in the future commercial reactors, high power sub-millimeter wave gyrotrons will be required for their ECRH systems [71]. For the frequencies above 200 GHz, coaxial cavity gyrotrons are preferred as they can reduce the problem of mode competition, and can also be operated at higher power levels [72]. Feasibility analysis of the coaxial cavity gyrotrons operating at the frequencies above 200 GHz, with multifrequency operationability to support the ECRH systems of the future fusion reactors needs to be done.

A rectangular corrugated coaxial cavity is widely analyzed for using as the interaction cavity in the gyrotrons. Most of the design studies and experimental operations on coaxial cavity gyrotrons were carried out using rectangular corrugated coaxial interaction cavity [73], [55]. In the coaxial cavity gyrotrons, compared to cooling of the outer cavity, the insert cooling is critical and thus, peak ohmic loading of the insert need to

be controlled. A novel coaxial interaction cavity for gyrotrons with triangular corrugated insert was proposed by S. Singh *et al.* [74]. Triangular slots on the insert not only offer better mode rarefaction but also reduce the problem of localized heating. Mathematical formulations for the dispersion relation, wall losses and quality factor of the triangular corrugated coaxial cavity using surface impedance model (SIM) and full wave approach were reported. Considering the advantages of the triangular corrugated coaxial cavity, design studies of the gyrotrons can be carried out using this proposed novel interaction cavity.

1.4 Research Objectives and Problem Statement

The main objective of this thesis is to perform the design studies of the megawatt class coaxial cavity gyrotron oscillators with dual/multifrequency operational capability for the probable applications in the future commercial tokamaks. To reduce the ohmic loading on the coaxial insert and also to keep control over the mode competition, a coaxial cavity with triangular corrugated insert is used as an interaction circuit in the design studies. The number of gyrotrons required in the ECRH system is directly related to the single unit output power of gyrotron. To reduce the spatial and maintenance requirements of the ECRH system in the future tokamaks, the design studies are also carried out for the multifrequency coaxial cavity gyrotron with increased output RF power. In coaxial cavity gyrotrons, outer cylindrical cavity and insert must align in the same axis. However, due to some practical problems like cathode deformations, increase in the ohmic loading of the insert or poor assembling, there may be misalignment between the axes of the insert and the cavity. Hence, to analyze the effect of insert misalignment on the field structure, field analysis is carried out for the triangular corrugated coaxial cavity. To achieve these objectives, the following tasks are considered and are successfully solved.

- RF behavior studies of a dual regime (220/251.5 GHz) coaxial cavity gyrotron.
- Electron gun and output system design studies of a 220/251.5 GHz dual regime coaxial cavity gyrotron.
- Design studies of a dual frequency gyrotron extended to the third operating frequency of 283 GHz.
- Design studies of a 3 MW triple frequency (170/204/236 GHz) coaxial cavity gyrotron.
- Analysis of the RF interaction cavity with misaligned triangular corrugated coaxial insert.

1.5 Organization of Thesis

In this thesis, feasibility analysis of the dual/multifrequency coaxial cavity gyrotrons are performed for the plasma heating applications in the future commercial tokamaks like DEMO reactor. Design studies of the major components of the coaxial cavity gyrotrons are carried out for supporting multifrequency operation. Field analysis is also carried out for the triangular corrugated coaxial cavity with misaligned insert.

The thesis is organized into eight chapters. Chapter 1 discusses the introduction to the thermonuclear fusion with the need of RF sources for heating the plasmas in the experimental fusion tokamaks. The brief overview of different classes of gyro-devices, motivation towards the present research work followed by the problem statements involved in this thesis are also discussed in this Chapter.

In Chapter 2, the basic electron cyclotron interaction principle of the gyrotron is discussed along with the major components of gyrotrons. Literature survey on the megawatt class gyrotrons developed for plasma heating application in the experimental tokamaks is also presented in this chapter.

Feasibility analysis of a 2 MW, dual frequency (220/251.5 GHz) coaxial cavity gyrotron is presented in Chapter 3. A triangular corrugated coaxial cavity is used in this design studies to reduce the problem of the localized heating. Operating frequencies are selected such that the designed gyrotron can be used in the ECRH systems of the future commercial tokamaks. Cavity mode pair is selected based on the mode selection strategy of multifrequency gyrotrons. The geometry of the RF interaction cavity is optimized for the dual frequency operation in the proposed gyrotron. Cold cavity design, mode competition calculations, and self consistent single mode calculation are performed for both operating modes. Time dependent multi-mode calculations predict that RF output power of 2 MW can be obtained in both the modes at their respective frequencies. Further, startup calculations are carried out with beam space charge neutralization for both the operating frequencies.

Design studies of an electron gun and output coupling system supporting the dual regime (220/251.5 GHz) coaxial cavity gyrotron are discussed in Chapter 4. The coaxial magnetron injection gun is designed for the generation of a hollow electron beam with desired beam parameters. Design studies of the output coupling system comprising of a nonlinear taper, a quasi-optical launcher, and a single disk RF window to support dual frequency operation are also carried out in this chapter.

In Chapter 5, design studies are performed to explore the feasibility of operation at third frequency of 283 GHz in an already reported dual regime (220/251.5 GHz) gyrotron. Operating cavity mode at this frequency is chosen such that the physical geometry of the gyrotron used in the current operation is same as those reported in the dual regime design

studies. RF behavior studies are performed for this operating frequency. Further, design studies of the electron gun and output coupling system are also carried out to support this third operating frequency of 283 GHz. These studies confirm that RF output power of 2 MW can be obtained in the proposed coaxial cavity gyrotron at all the three desired frequencies.

Chapter 6 comprises feasibility studies of a triple frequency (170/204/236 GHz) coaxial cavity gyrotron. Frequencies are selected such that the proposed gyrotron can be used in the future commercially attractive DEMOnstration (DEMO) tokamak. Considering the fact that number of gyrotrons required in the ECRH system can be reduced by increasing the output power of a single gyrotron unit, in this design study output power of the gyrotron is targeted to 3 MW. Time dependent multi mode calculations estimate that RF power of 3 MW can be obtained in the chosen cavity modes. Magnetron injection gun design studies are performed for obtaining electron beam with desired beam parameters. The startup behavior calculations are also performed at all the three desirable frequencies with beam space charge neutralization.

In Chapter 7, field analysis of a triangular corrugated coaxial cavity with misaligned insert is carried out. The mathematical formulation for the dispersion relation of a coaxial cavity with a misaligned insert is derived using the surface impedance model and full wave approach. The effect of the insert misalignment on the eigenvalue of the cavity modes in the coaxial cavity gyrotron is studied.

Finally, Chapter 8 summaries the contribution of this thesis towards the development of megawatt class coaxial cavity gyrotrons used for the plasma heating application in the experimental tokamaks along with the future scope of the present work.

Chapter 2

Basics of Gyrotron Oscillator and Literature Survey

2.1 Basic Principle of Gyrotron

Gyrotrons are the fast wave vacuum electron devices that work on the principle of electron cyclotron resonance which are capable of generating kilowatts to megawatts of power in millimeter and sub-THz wave ranges [21]. In the gyrotron, a hollow electron beam generated by an electron gun is transferred to an interaction cavity by the accelerating voltage under the influence of the external applied magnetic field. The gyrating electron beam interacts with the electromagnetic (EM) wave in the open ended interaction cavity and transfers its kinetic energy to the EM wave [22]. The high power EM wave is then separated from the electron beam and radially coupled out of the tube through output coupling system (which includes a quasi-optical launcher, metallic mirrors, and a RF window). The spent electron beam is collected in a collector that may also includes an energy recovery system to improve the overall tube efficiency [17]. The schematic of a gyrotron with a coaxial cavity as the interaction circuit is shown in Figure 2.1

2.1.1 Electron Cyclotron Interaction Mechanism

In the presence of the magnetic field, the electrons gyrate around the magnetic field lines with the angular cyclotron frequency (Ω_o) [16]. By relating Lorentz force and centripetal force, Ω_o can be determined as

$$\Omega_o = \frac{eB_o}{m_e} \tag{2.1}$$

where e and m_e are the charge and mass of the electron. B_o is the magnetic field. For higher values of the accelerating voltage, the electron velocity (v) becomes weakly rela-

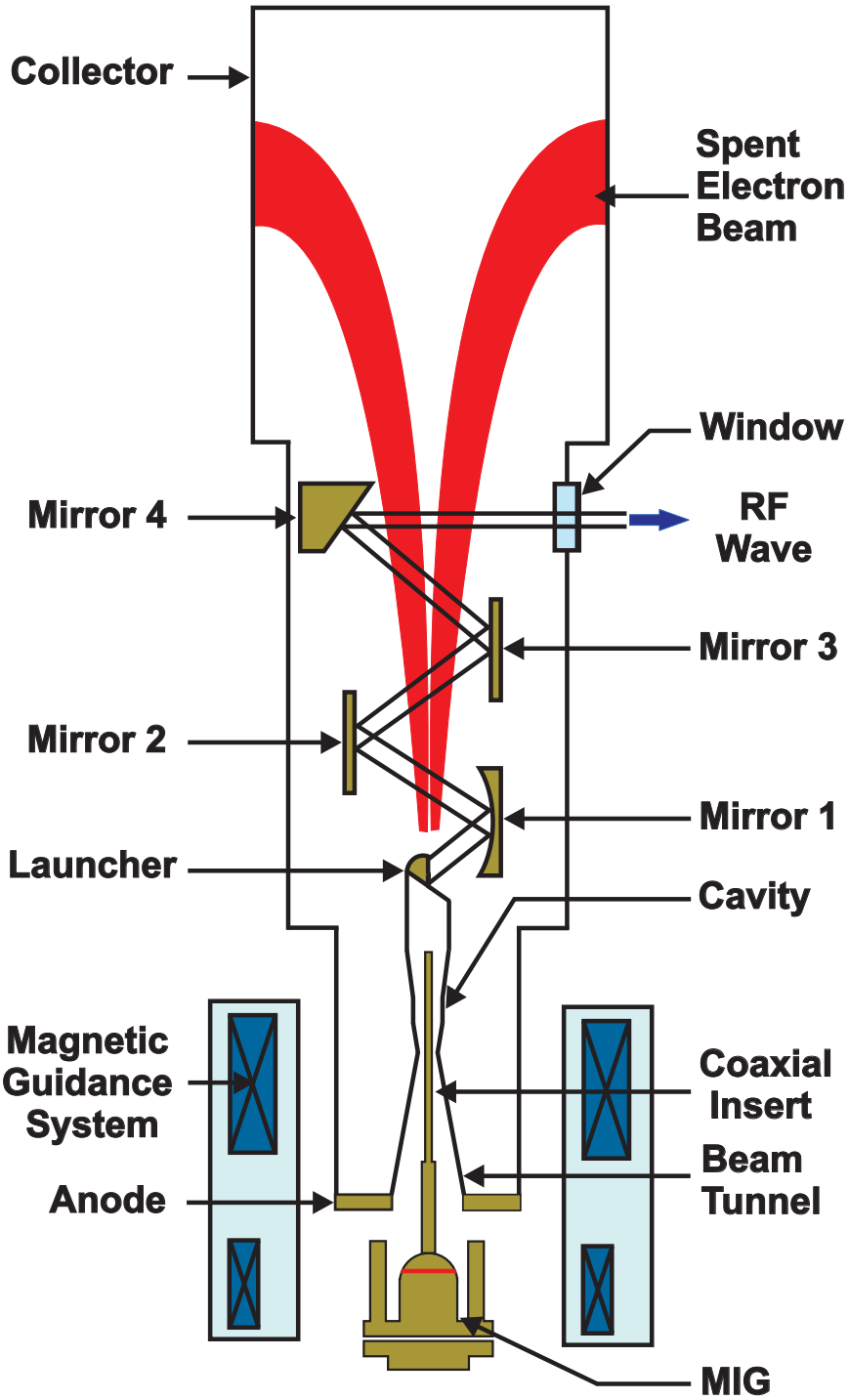

Figure 2.1: Schematic of a coaxial cavity gyrotron with radial beam output [17].

tivistic and the relativistic factor, or Lorentz factor (γ) is given by [17]

$$\gamma = \frac{1}{\sqrt{1-\left(\frac{v}{c}\right)^2}} = 1 + \frac{W_{kin}}{m_e c^2} \tag{2.2}$$

where W_{kin} is the kinetic energy of the electron beam, and c is the velocity of light. The equation (2.1) is then updated to include the relativistic effect of the electron beam and the relativistic electron cyclotron frequency (Ω_c) is given by

$$\Omega_c = \frac{eB_o}{\gamma m_e} \tag{2.3}$$

The Larmor radius of the electron beam (r_L) can be calculated through

$$r_L = \frac{v_\perp}{\Omega_c} = \frac{m_e \gamma v_\perp}{eB_o} \tag{2.4}$$

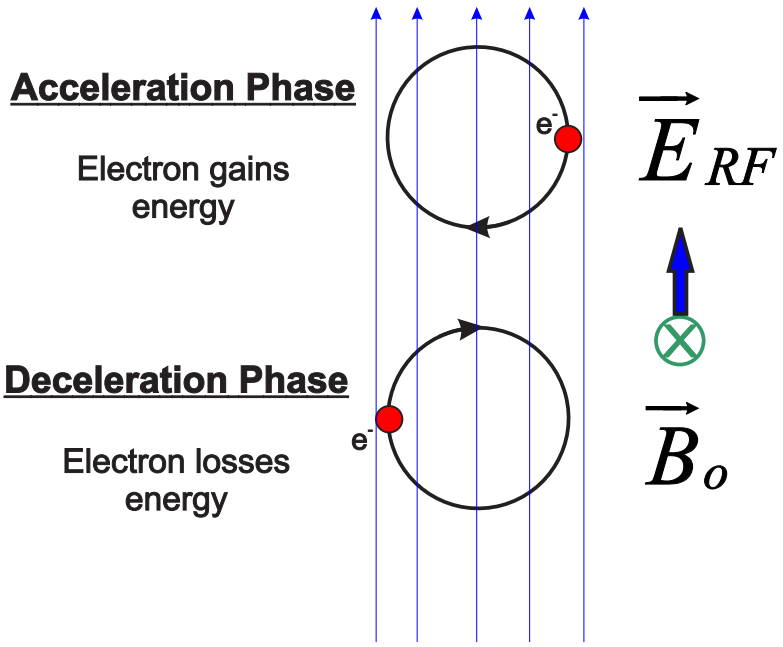

Figure 2.2: Electron cyclotron interaction mechanism [21].

In the presence of the electromagnetic field, whose angular frequency (ω) is synchronous with the relative electron cyclotron frequency (Ω_c), the energy exchange between the electron beam and the EM wave occurs. Based on the relative phase of the electron beam with the RF wave, the particles may be accelerated or decelerated. If the frequency of RF wave is set slightly higher than the cyclotron frequency, then particles in the accelerating phase behave differently from those in the decelerating phase. As shown in Figure 2.2, the particle in the accelerating phase gains energy and thus increases the relativistic factor (γ). Increase in γ decreases the cyclotron frequency (Ω_c) and hence the

frequency difference between the RF wave and the electron cyclotron $|\omega - \Omega_c|$ increases. Thus the particle soon leaves this unfavorable phase.

Whereas, the particle in the decelerating phase loses its kinetic energy and thus the value of γ decreases. This leads to the increase of Ω_c and hence the frequency difference $|\omega - \Omega_c|$ decreases. Thus the particle continues to remain in this favorable phase. Over the period of time, more particles start to accumulate in this favorable decelerating phase and support the energy transfer to the RF wave and this phenomenon is called "bunching". If the electron remains in the favorable phase for a very long time, they lose more energy and leaves this phase and consequently energy transfer from the RF to the electron beam occurs, and this is referred as "over-bunching". So, for the energy transfer from the electron beam to the electromagnetic wave, RF frequency should be slightly greater than the electron cyclotron frequency [75], [76] and is given by

$$\omega \geq \Omega_c \tag{2.5}$$

If the electron particles are non-relativistic, then the net energy transfer over the cycle would be zero. It can be noted from the equation (2.3), for a given accelerating potential of the electron beam, the external applied magnetic field determines the frequency of oscillation.

Considering the axial motion of electrons with the velocity v_z, frequency of the EM wave is shifted by the Doppler term. In the cylindrical waveguide, the free space wave number of the EM wave (k_o) is given by [77]

$$k_o^2 = k_\perp^2 + k_z^2 \tag{2.6}$$

where $k_\perp$ is the cutoff wavenumber of the TE mode in the cylindrical waveguide and k_z are the azimuthal and axial wave numbers of the EM wave.

For the EM wave moving in the positive z direction, the phase component of the wave ($\omega t - k_z z$) should be close to the rotational motion of the electron (Ωt). For the resonance condition, the difference between the phase of the EM wave and the rotational motion of particles should not vary over the time [78], and this is given by

$$\begin{aligned} \frac{d}{dt}(\omega t - k_z z - \Omega_c t) &\geq 0 \\ \frac{d}{dt}(\omega t - k_z v_z t - \Omega_c t) &\geq 0 \\ (\omega - k_z v_z - \Omega_c) &\geq 0 \end{aligned} \tag{2.7}$$

In the above equation (2.7), $k_z v_z$ is the Doppler term. The resonance condition also

occurs for the harmonics of the electron cyclotron frequency [79] and is given by

$$(\omega - k_z v_z - s\Omega_c) \geq 0 \tag{2.8}$$

From equation (2.8) it is understood that, if the particle loses its kinetic energy, Ω_c increases meanwhile, the axial velocity of the particle also decreases and for the RF wave with constant axial wave number, once the resonance condition is achieved it will remain throughout the operation and this is referred as auto-resonance [21]. Generally, gyrotrons are operated near to cutoff frequency for which k_z approach towards zero and hence, Doppler effect will be negligible for the case of gyrotron operation [76].

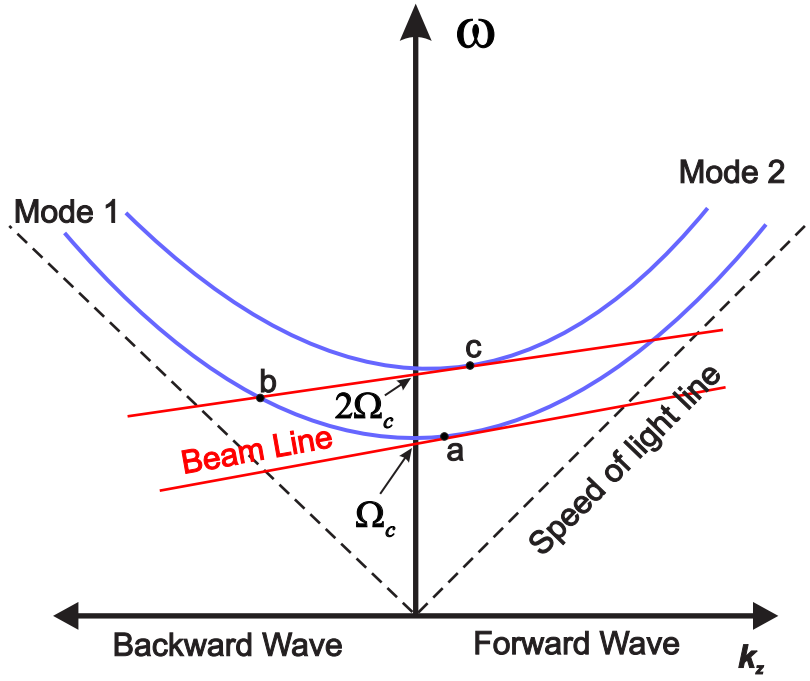

Figure 2.3: Dispersion diagram of the cavity modes in gyrotron with the electron beam line [17].

The beam wave interaction mechanism can be explained through the dispersion diagram or Brillouin diagram [17], [80] and is shown in Figure 2.3. The hyperbolas in the diagram represent the dispersion curves for TE modes as given in equation (2.6) and the beam wave line is given by the following equation.

$$(\omega - k_z v_z) = s\Omega_c \tag{2.9}$$

The interaction between the hyperbola and the straight line represents the resonance condition for the beam wave interaction. Point 'a' represents the resonance condition in the gyrotron. Here, the RF frequency is close to the electron cyclotron frequency and is also near to the cutoff frequency of the waveguide mode. Electron cyclotron interaction

also occurs for the backward traveling wave and is represented by point 'b'. At this point, the operating frequency is far away from the cutoff frequency of the mode. The resonance condition is also possible at the harmonics of the cyclotron frequency and point 'c' represents the interaction between the RF wave and the second harmonic of the electron cyclotron.

2.2 Major Components of the Gyrotron

2.2.1 Electron Gun and Beam Tunnel

In the gyrotron, a magnetron injection gun (MIG) generates a hollow electron beam, which interacts with the RF wave in the interaction cavity and transfers its kinetic energy. The MIGs are operated under the temperature limited region of operation and the electrons emitted from the heated emitter surface travels under the influence of the accelerating voltage and external magnetic field. For megawatt class gyrotrons, dispenser cathodes containing porous tungsten filled with special oxides are used [16]. Unlike the electron gun of linear beam devices, in gyrotrons the cathodes offer electron beam with beam current independent of applied accelerating voltage and geometry of the emitting surface [81], [82]. Cross section of the MIG geometry along with the electron beam trajectory is shown in Figure 2.4. The external magnetic coils are the superconducting coils cryogenically cooled, which generate desired magnetic field profile. The main coil placed around the interaction cavity is responsible for the maximum magnetic field in the cavity center. A compensating coil around the beam tunnel region reduces the magnetic field towards the gun region. The gun coils around the cathode region are required for optimizing the field in the emitter region [78].

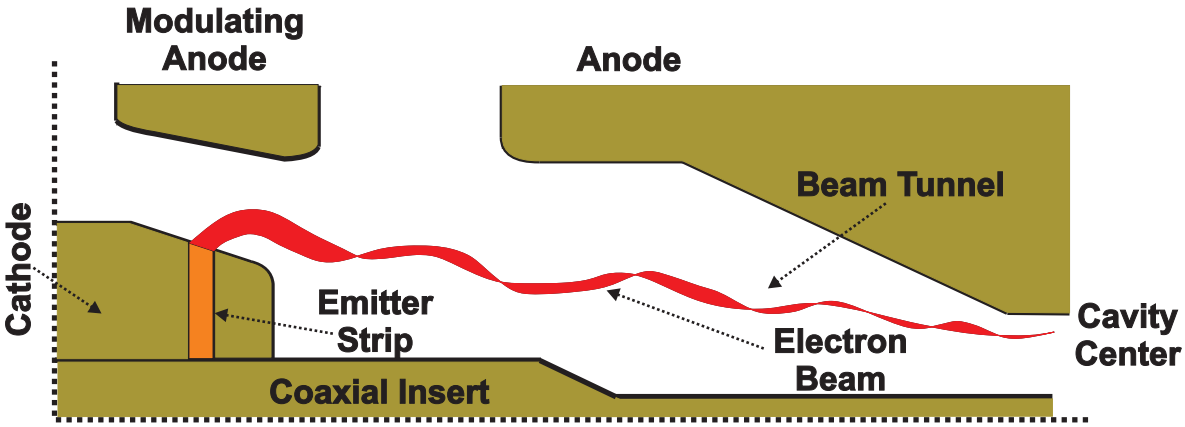

Figure 2.4: Geometry of the MIG with beam tunnel and electron beam trajectory [83], [84].

Based on the geometry of the MIG, they are classified into two types: (a) Diode type, and (b) Triode type. In a triode type MIG, an additional electrode (modulating anode) is available for controlling the beam trajectory [17].

The electrons emitted from the cathode are accelerated towards the anode or modulating anode by the electric field created by the potential difference between the electrodes. Under the influence of the external magnetic field, these emitted electrons travel in a cycloidal path and form the hollow electron beam whose radius is very much greater than the guiding center radius of the electron. The annular electron beam transfers its energy to the waveguide mode in the RF interaction cavity, and the spent electron beam is absorbed in the collector. Since, the electron beam interacts with the circularly polarized TE modes in the cavity, only the transverse component of the electron velocity ($v_\perp$) is responsible for energy transfer to the RF wave. However, the axial velocity component of the beam (v_z) should be sufficient enough for transport of the beam towards the cavity and after interaction towards the collector region [23].

The electron velocity ratio or pitch factor (α) is given by

$$\alpha = \frac{\beta_\perp}{\beta_z} \tag{2.10}$$

where $\beta_\perp$ and β_z are the normalized perpendicular and axial electron velocities. The normalized total electron velocity (β) is given by $\sqrt{\beta_\perp^2 + \beta_z^2}$. Ideally, for the effective electron cyclotron interaction, the electron velocities should not have any spread. However, due to the practical constraints in the design of the MIG, the electron beam would have inevitable spread in their velocity components [85].

The magnetic field in the region between the emitter and the interaction cavity is increased adiabatically whereas, the magnetic moment in this region remains constant [86] which is given by

$$\frac{\gamma m_e \beta_\perp^2}{B(Z)} = constant \tag{2.11}$$

So, for the increasing magnetic field the transverse electron velocity increases and hence, α increases as the beam travels from the emitter to the interaction cavity. Under the adiabatic approximation, the spread in the transverse velocity of the beam ($\delta\beta_\perp$) is constant, and the spread in the velocity ratio can be estimated using [87]

$$\delta\alpha = \left(1 + \alpha_o^2\right) \delta\beta_\perp \tag{2.12}$$

where α_o is the mean value of the pitch factor. The ratio of the magnetic field in the interaction cavity center (B_o) to the magnetic field in the emitter (B_g) is called magnetic

compression (b) and is given by B_o/B_g. The electron beam radius in the cavity center (R_b) is related to the emitter radius (R_c) through magnetic compression and is given by

$$b = \frac{B_o}{B_g} = \left(\frac{R_c}{R_b}\right)^2 \tag{2.13}$$

From the above equation (2.13), the guiding center spread at the center of the interaction cavity can be determined through

$$\Delta r_{gc} = \frac{r_{E_{max}} - r_{E_{min}}}{b^{1/2}} \tag{2.14}$$

where $r_{E_{max}}$ and $r_{E_{min}}$ are the maximum and minimum values of the electron beam radius at the emitter.

The efficiency ($\eta_\perp$) in which power gained by the RF wave (P_{elec}) from the perpendicular electronic power ($P_\perp$) is given by

$$\eta_\perp = \frac{P_{elec}}{P_\perp} \tag{2.15}$$

The theoretical maximum value of $\eta_\perp$ is calculated as $\approx 72\%$ [23]. The efficiency with which energy is transfered from the electron beam is called total electronic efficiency (η_{elec}) and is given by

$$\eta_{elec} \approxeq \frac{\alpha^2}{1+\alpha^2} \cdot \eta_\perp \tag{2.16}$$

A beam tunnel is an isolation region down tapered between the electron gun and the interaction cavity, consists of a series of absorbing materials of specific geometry to avoid any parasitic oscillations reaching the emitter side [88]. In the beam tunnel region, the magnetic field is highly non-homogeneous and increases towards the cavity region, and therefore the electron beam radius decreases to the desired value at the interaction cavity center. The design of the beam tunnel is challenging for the electron beam with high energies.

2.2.2 Interaction Cavity

Conventional Cylindrical Cavity

An interaction cavity in the gyrotron consists of three sections: (1) an input taper, (2) a straight midsection and (3) an output taper and is shown in Figure 2.5. Interaction of the electron beam with the RF wave occurs in the straight midsection [89]. The interaction cavity behaves like a resonant cavity in which the normalized electric field follows a Gaussian profile [90]. The diffractive Q factor (Q_d) of the mode in the cavity predomi-

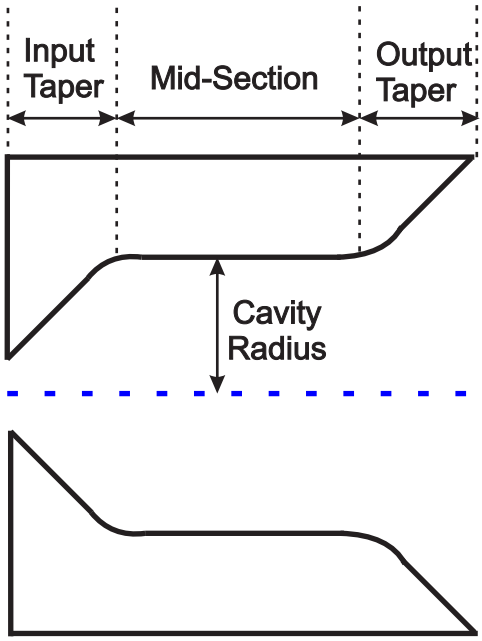

Figure 2.5: Geometry of a interaction circuit in a conventional cylindrical cavity gyrotron [17].

nantly determines the efficiency of the beam wave interaction. By adjusting the midsection length, Q_d of the mode can be varied. The input down taper prevents the EM wave traveling towards the gun region. The output up taper connects the midsection to the output coupling system and supports the output coupling of the RF wave. The taper angles are fixed such that they should not support any mode coupling or mode conversion [91]. In the field calculations, the effect of the mode coupling due to the taper can be avoided if their angles are fixed less than 7° [78]. To avoid sharp transitions, tapers are connected to the straight midsection through parabolic roundings [89].

Coaxial Cavity

In a coaxial cavity, a down tapered insert is included to control the mode competition [92]. Figure 2.6 shows the geometry of the coaxial cavity used as the interaction circuit in the gyrotron. The eigenvalue of the modes in the coaxial cavity depends on the radii ratio of the outer cavity to that of the insert ($C = R_o/R_i$). The dispersion relation for the non-corrugated coaxial cavity can be derived by applying the boundary conditions and is given by [53]

$$J_m'(\chi)Y_m'\left(\frac{\chi}{C}\right) - Y_m'(\chi)J_m'\left(\frac{\chi}{C}\right) = 0 \tag{2.17}$$

Figure 2.7 shows the dependence of the eigenvalue over the radii ratio (C) for the mode $TE_{31,17}$. The minimum value of the eigenvalue curve corresponds to the caustic radius of the mode. The fields in the cavity can be effectively modified for the insert radius close

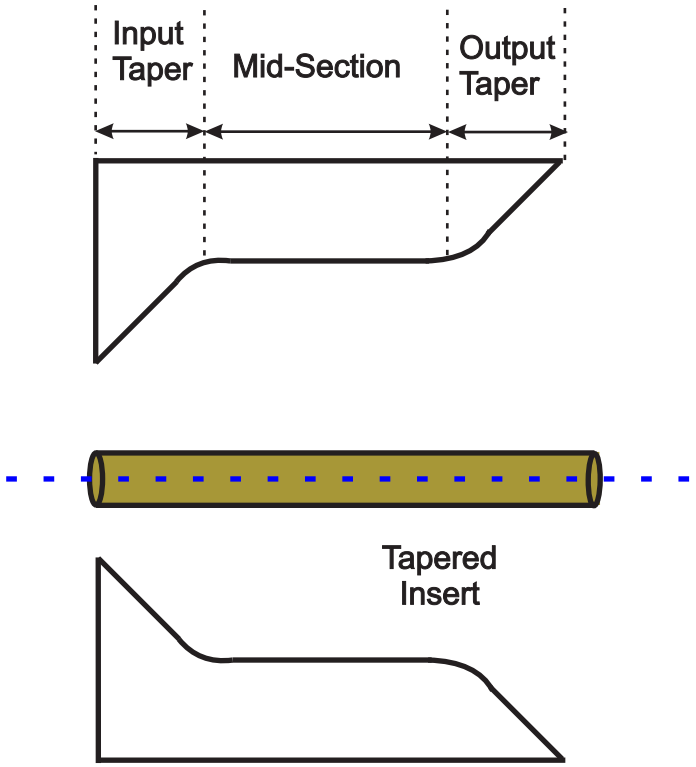

Figure 2.6: Geometry of a interaction circuit in a coaxial cavity gyrotron [17], [53].

to the caustic radius of the mode. The effect of the insert is better for the modes with the relative caustic radius of around 0.3. For the coaxial cavity with down tapered insert, in the operating C range, the negative slope of the eigenvalue curve decreases the cutoff frequency consequently, Q_d of the mode also decreases. The start oscillation current (I_{st}) of the mode is inversely propositional to the Q_d of the mode and therefore, for the decreasing value of Q_d, I_{st} increases. Similarly, the positive slope of the eigenvalue curve increases the Q_d of the mode and consequently I_{st} of the mode decreases.

The coaxial cavity with down tapered insert can be mathematically represented by the tapered cylindrical cavity as given in [53]

$$\Delta R_{eq} = \left(1 - \frac{C}{\chi}\frac{d\chi}{dC}\right) + \left(\frac{C^2}{\chi}\frac{d\chi}{dC}\right)\Delta R_i \tag{2.18}$$

In the operating C range, the modes with $\frac{d\chi}{dC} > 0$, according to the above equation (2.18), the coaxial cavity behaves like a down tapered cylindrical cavity and hence Q_d of the mode increases. In the same way, for the modes with $\frac{d\chi}{dC} < 0$, the coaxial cavity is mathematically equivalent to an up tapered cylindrical cavity and therefore Q_d of the mode increases. Thus, by the selective modification of the diffractive Q factor of the competing modes, the mode competition can be controlled [93]. In addition to the mode rarefaction, the wall losses on the insert should be minimized. The positive slope

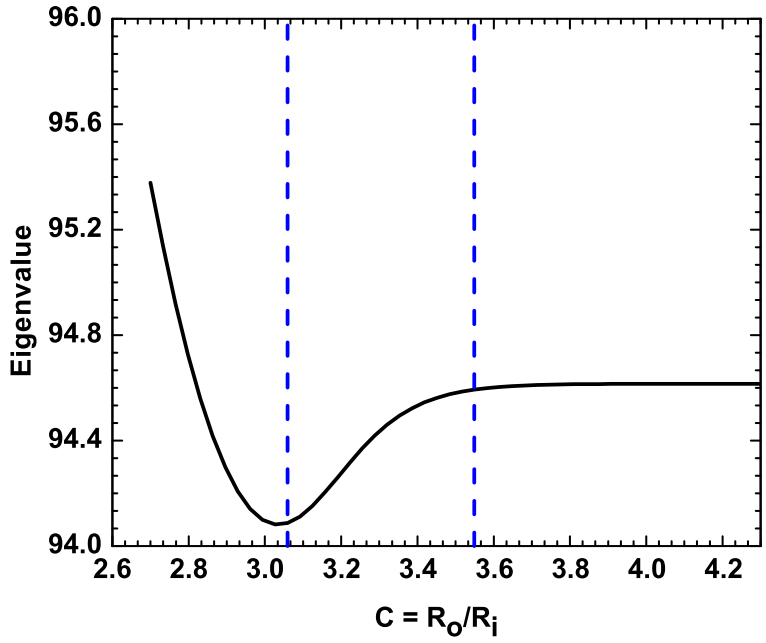

Figure 2.7: Eigenvalue curve of the cavity mode $TE_{31,17}$ in a coaxial cavity with non-corrugated insert [73].

of the eigenvalue curve is avoided in the operating radii ratio as the ohmic wall loading significantly increases for higher values of the diffractive Q factor. The flat region in the eigenvalue curve resembles that the energy is concentrated in the cavity region as in the conventional cylindrical cavity. The slope region of the eigenvalue curve represents that the fields are concentrated in the slot and thus increases the ohmic losses on the insert [54]. Hence, the insert radius is selected such that the eigenvalue curve of the desired mode lies near the flat region and that of the competing modes lie near the negative slope region. Corrugations on the insert walls shift the positive slope region of the eigenvalue curve towards the right, and this enhances the mode selectivity of the insert. The wedge shaped- and rectangular shaped corrugations on the insert of the coaxial cavity were investigated widely for the use in the high power gyrotrons [94] and the cross section of a coaxial cavity with wedge shaped corrugations on the insert is shown in Figure 2.8. In 2015, S.Singh *et al.*, had proposed the triangular shaped corrugations on the insert walls for reducing the problem of localized heating on insert walls compared to rectangular corrugated insert [74]. The research activities are going in the domain of material sciences to develop materials with low DC conductivity so that ohmic wall loading of the cavity can be controlled [95].

In the gyrotrons, due to the effect of space charge fields, the beam voltage gets reduced from the accelerating voltage, and this is referred as the voltage depression. The

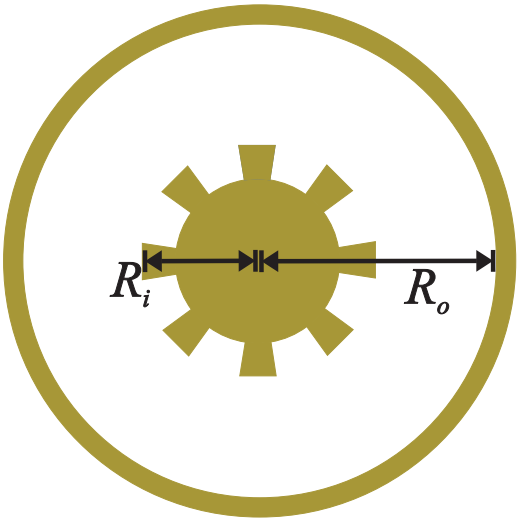

Figure 2.8: Cross section of a coaxial cavity with wedge shaped corrugated insert [96].

limiting current, the maximum beam current beyond which mirroring of the beam occurs, is inversely proportional to the voltage depression. By inserting the inner rod in the cylindrical cavity, the voltage depression can be reduced and thereby increasing the limiting current. In the gyrotrons, the operational beam current is generally fixed less than the half of the limiting current. Thus, in the coaxial cavity gyrotrons, as the limiting current is higher compared to the conventional cavity gyrotrons, they can be operated at the higher values of the operational beam current. In order to reduce mode competition in the overmoded cavity of high power gyrotrons, metallic photonic band-gap structures (PBG) are also used as the interaction circuit [97]. The metallic PBG behaves in a similar way like electromagnetic band gap structures in suppressing the out of band frequencies [98], [99], [100], [101].

2.2.3 Output Coupling System

In the gyrotron, an output coupling system separates the high power RF wave from the electron beam and facilitates the efficient transmission of the RF wave through the transmission line or metallic mirrors. The output system of gyrotrons is classified into two types as (a) simple axial output system, and (b) radial or transverse output system [102]. For low power gyrotrons ($P_{out} < 50\,\text{kW}$), the axial output system is preferred, in which a collector waveguide supports the axial transmission of the output RF wave. In high power gyrotrons used for the plasma heating applications, the radial output system is used, in which an internal mode converter transforms the cavity mode into Gaussian-like mode. Similarly, in other high power microwave (HPM) devices mode converters are used for converting TM modes into circular TE modes so that high power RF signal can be effec-

tively transmitted [103], [104], [105].

Nonlinear Taper (NLT)

A nonlinear taper (NLT) is used to connect the interaction cavity of the gyrotron to a quasi-optical launcher (QOL) or to the collector waveguide [102]. The ratio of the input radius of the QOL or the collector waveguide to the cavity radius is termed as the oversize factor. The designed NLT should have very high transmission efficiency for the operating modes and should avoid any mode conversion. The length of the NLT should be as compact as possible to support the opening of beam trajectory towards the launcher [106]. In high power gyrotron, it is quite challenging to design a compact NLT by avoiding any mode conversion along the transmission. The insert in the coaxial cavity is down tapered and is extended up to the output end of the NLT. The geometry of the NLT is optimized through particle swarm optimization technique [107], [108].

Internal Mode Converter

In the radial output system, the internal mode converter consists of a quasi-optical launcher and metallic reflectors or mirrors for converting the cavity mode into a free space Gaussian like mode. The schematic of the radial output system is shown in Figure 2.9. The launcher is a waveguide antenna that transforms the waveguide mode and radiates into the free space [109]. In the launcher, the wall perturbations are synthesized for converting the cavity mode at the operating frequency into free space mode with high Gaussian content [110]. The launcher wall perturbations convert the input cavity mode into the mode mixture that consists of neighboring higher order modes [111]. At the launcher cut, the mode mixture results in the radiating RF field. The launcher parameters are optimized for delivering a highly focused Gaussian like beam with the reduced stray radiation at the launcher cuts. The designed launcher should be as compact as possible to support the diverging electron beam towards the collector [112]. Nano computer numerical control (CNC) machining technology is used for the fabrication of launcher with desired wall perturbations [113]. For the multifrequency operation of gyrotrons, launcher wall perturbations should support all the desired cavity modes at their respective frequencies [114].

The radiated RF beam from the launcher is further improved through the metallic mirrors. The shape and the surface profiles of the mirrors selectively optimize the beam properties of the RF wave. The size of the mirrors are determined by the incident field distributions. By using the internal mirror system, waist of the RF wave is optimized towards the window plane. After the launcher, the reflector is usually a quasi-elliptical mirror, which converts the radiated beam into paraxial wave beam. Surface profiles of

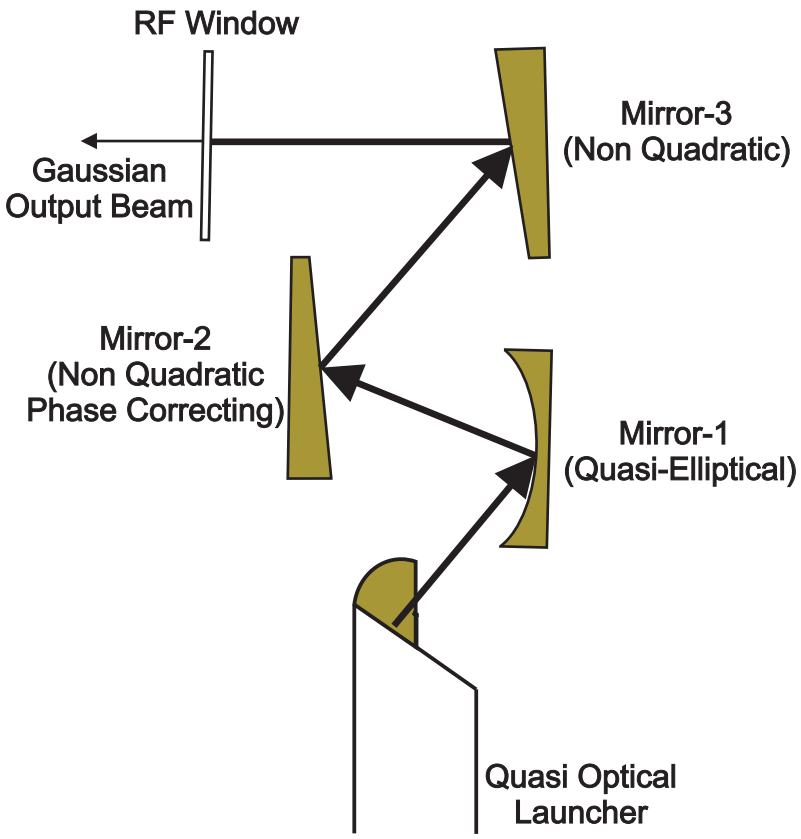

Figure 2.9: Schematic of the radial output system in gyrotron including quasi-optical launcher, metallic mirrors and RF output window [115].

the mirrors that are only used for the focusing of the wave beams are usually of quadratic functions. Surface profiles of the phase correcting mirrors are complex and are synthesized for achieving the desired beam properties of the RF wave [116]. In addition to the internal mirror system, the gyrotron also consists of a set of external mirrors that are called matching optics unit (MOU). The MOU further modifies the RF beam to facilitate the transmission of high power RF beam through the external transmission lines.

RF window

In the gyrotrons, high power output beam is extracted through an RF window that acts as a barrier between the vacuum inside the gyrotron and the outer transmission line. The RF window materials are characterized by very low loss tangent, high mechanical and thermal strengths [117]. The most widely used RF window materials are chemical vapor deposited (CVD) diamond, Silicon Nitride, Boron Nitride, Sapphire and Au doped silicon [118], [119]. Different ceramics are being developed for using as the RF window in high power gyrotrons [120]. Among other window materials, CVD diamond is widely used in megawatt class CW gyrotrons as it offers very low RF losses, better thermo-mechanical strengths and can handle power level up to 2 MW [121]. The CVD diamonds are manufactured by growing diamond on the substrate of a hydrocarbon gas mixture [122]. The RF windows mainly used are of the following types :

- Single disk RF window
- Double disk RF window
- Brewster angle window

The single disk window is used for the transmission of RF power at the frequencies that are the integer multiples of the transparent basic frequency (f_b). The expression for f_b is given by $\frac{c}{2.d.\sqrt{\varepsilon_r}}$, where d is the window thickness and ε_r is the dielectric constant of the material. In the double disk windows, liquid coolant is used in the gap between the two disks to improve the overall thermal conductivity of the window [117]. The Brewster angle window gives the minimum reflection at any frequency if the wave is incident at the window with an angle corresponds to Brewster angle. The Brewster angle windows offer wide bandwidth and are generally used for the step-tunable operation of gyrotrons [60].

Collector

In gyrotrons, after RF interaction the spent electron beam got diverged and absorbed in the collector. The electron beam is diverged towards collector using the magnetic sweeping systems. The collector portion is usually insulated from other major components of the gyrotron. In the depressed collector operation, the spent electron beams are de-accelerated

before they are finally absorbed, and the de-accelerated energy is recovered by the power supply which increases the overall tube efficiency [123]. In the CW operation, the design of the depressed collector is challenging as very high residual energy is available on the spent electron beam [124]. The depressed collector system improves the overall lifetime of the tube and also reduces the cooling requirements. The depressed collector operation in gyrotron are explained in detail in [125], [126] and the proposed multi-stage depressed collector concept was presented in [127], [128].

The efficiency of the gyrotron with the output RF power (P_{out}) is given by [78]

$$\eta = \frac{P_{out}}{P_{beam}} \tag{2.19}$$

where P_{beam} is the DC beam power. P_c is the power recovered by the collector system and the collector efficiency is given by

$$\eta_c = \frac{P_c}{P_{beam} - P_{out}} \tag{2.20}$$

The overall tube efficiency (η_{total}) of the gyrotron under depressed collector operation is given by

$$\eta_{total} = \frac{\eta}{1-(1-\eta)\eta_c} \tag{2.21}$$

The future commercially attractive tokamaks like DEMO require gyrotrons with overall efficiency of 60% and this can only be achieved through the multi-stage depressed collector concept.

2.3 Literature Survey

The megawatt class gyrotrons are widely developed for the plasma heating applications in the fusion reactor. The size of the core and the confining magnetic field determine the frequency of RF wave required for plasma heating. The conventional cavity gyrotrons were developed by various research groups for tokamaks like ASDEX-U, JT-60SA, and ITER and also for W7-X stellarator. The coaxial cavity gyrotrons were also developed for achieving tube with the single unit output power of greater than 1 MW. State of the art of high power gyro-devices and free electron laser are collectively brought together every year by M. Thumm [129]. In this section, some important megawatt class gyrotrons developed for nuclear fusion applications are discussed.

2.3.1 Conventional Cavity Gyrotrons

140 GHz Gyrotrons

A 140 GHz gyrotron was developed at Karlsruhe Institute of Technology (KIT), Germany for plasma heating application. The cavity mode for this operation was chosen as $TE_{22,6}$ and an output power of around 1 MW was obtained. This gyrotron was equipped with a diode type MIG, a quasi-optical launcher and a single stage depressed collector [125]. In 1997, the step-tunable operation of this gyrotron was performed in the frequency range of 114 to 166 GHz. Fourteen modes were excited in this frequency range, and the output power was measured for the short pulse operation. For the first time single disk output window was replaced with the Brewster angle window of quartz glass fused with silica [130]. In 2001, the magnetic system of this 140 GHz gyrotron was replaced with the hybrid magnetic system to support the fast frequency tuning. The hybrid magnetic system consists of a normal conducting copper magnet along with the super conducting magnets. The fast frequency tuning of 15 GHz (132-147 GHz) has been achieved in the time step of 1 s [131]. This tube was modular and supports the easy replacement of all the key components. To support broadband operation, components were designed such that those can be operated in a wide range. In 2002, the cavity mode of this gyrotron was changed from $TE_{22,6}$ to $TE_{22,8}$ at 140 GHz. This was done to support the collaboration between KIT, Germany, and Institute of Applied Physics (IAP), Nizhny Novgorod, Russia [132]. Later, diode type MIG of the tube was replaced with that of developed by IAP, Russia. In 2009, the quasi optical mode converter was designed to support frequency step-tuning of this gyrotron in the frequency range of 105-143 GHz. The mode converter consists of a dimple wall launcher, one quasi-elliptical mirror, two toroidal mirrors. Nine different cavity modes in the frequency range have been converted into the Gaussian mode with the Gaussian content of greater than 90% for all the modes [114].

In 2014, for the first time, this 140 GHz gyrotron was installed with an elliptically brazed Brewster angle CVD diamond window. The frequency step-tuning operation has been carried out for the short pulse of 3 ms. Ten different modes were excited in the frequency range of 111.6-165.7 GHz with a minimum power of 830 kW. The maximum output power of 1.3 MW was obtained at 143.3 GHz for $TE_{23,8}$ mode. For $TE_{22,8}$ mode at 140 GHz, maximum output efficiency of 27.5% was achieved. For six different modes, the output power was reported greater than 0.9 MW. The Gaussian content of the output beams of all modes was sufficiently good and was in good agreement with simulation results. This experimental operation gives confidence for the step-tunable operation of gyrotron in the megawatt scale, and it also confirms the feasibility of using the CVD diamond window as Brewster angle window [60]. In 2015, step-tunable operation was

carried out in this 140 GHz, $TE_{22,8}$ mode gyrotron with a longer interaction cavity. The experimental operation was performed for the short pulse of 0.5 ms. The objective of this experiment was to compare the performance of the gyrotron in this new configuration of the longer cavity (higher diffractive Q factor) with the older configuration. Nine modes were excited in the frequency range of 124.2-169.2 GHz with the minimum power of 1 MW. The output power and efficiency were improved in all the modes. The maximum efficiency of 37% (without depressed collector) was obtained with the output power of 1.21 MW for $TE_{23,8}$ mode at 143.3 GHz. By increasing the beam current at 143.3 GHz, maximum output power of 1.44 MW with the efficiency of 35% was reported [133].

For the ECRH system of the ASDEX-U tokamak, dual frequency gyrotrons were developed by IAP, Russia. The cavity modes were selected as $TE_{17,6}$/$TE_{22,8}$ for the respective operating frequencies as 105.1/140.1 GHz. Under the single stage depressed collector operations, the reported output powers were 0.85/0.95 MW at 105.1/140.1 GHz with the efficiency of 50/52% for the pulse length of 300 s. Further, two more gyrotrons are planned for this ECRH system with frequency step-tuning capability in the frequency range 105-140 GHz. These proposed gyrotrons would enable the ECRH system to control the MHD instabilities without the need of steerable mirrors inside the hot plasma region [62]. The initial experimental results of the frequency step-tunable gyrotron were reported. For this operation, the quasi-optical launcher was designed to efficiently convert the cavity modes into the free space Gaussian like modes at the specified frequency range. The short pulse experiments were carried out using a Brewster window of Boron Nitride (BN) ceramic disc of 120 mm diameter. Eleven different modes were excited in the frequency range of 105-145 GHz for the pulse duration of 0.15 ms [134]. Later, the BN Brewster window was replaced by a Brewster CVD diamond window. For the pulse length of 100 ms, 1 MW output power was reported at 140 GHz and 0.8 MW power was obtained at the frequencies 105, 117, 128 GHz. In 2012, this gyrotron was tested up to the pulse length of 3 s at all the four frequencies [135].

The European research laboratories in collaboration with the tube industry Thales Electron Devices (TED), France developed the series of 140 GHz gyrotrons for the ECRH system of the W7-X stellarator at Max-Planck-Institut für Plasmaphysik (IPP) Greifswald, Germany. Ten gyrotrons were developed, including pre-prototype, prototype, one gyrotron from Communication & Power Institutes (CPI), USA and seven series of gyrotrons (SN1 to SN7), for supporting the 10 MW ECRH system. These gyrotrons consist of a diode type MIG gun, quasi-optical mode converter, single stage depressed collector (SDC) and single disk CVD diamond window. The operating cavity mode at 140 GHz was $TE_{28,8}$ mode. Under long pulse operation (1800 s), the reported output power of SN1 gyrotron was 0.92 MW with single stage depressed collector efficiency of 44% and de-

pressed collector potential of 28.5 kV. The dual frequency operation was also carried out with the prototype gyrotron. The RF output window of this gyrotron had the transparent frequencies at both 104/140 GHz. Two cavity modes were chosen in the 104 GHz range; one is $TE_{21,6}$ mode resonating at 103.8 GHz, and another is $TE_{22,6}$ mode at 103.6 GHz. As the output coupling system of this gyrotron supported well for $TE_{21,6}$ mode, this mode had been chosen as the operating cavity mode. The output power was reported as 0.41 MW with 27% (SDC) efficiency for the pulse length of 10 s [47].

A 140 GHz gyrotron was developed at CPI, USA for W7-X stellarator, and the operating cavity mode was $TE_{28,7}$. Under the short pulse operation (6ms), the reported output power was 916 kW with the efficiency of 35% (SDC). At CPI, USA due to the limitation in facility, long pulse operation was carried out for the lower beam current of 22.9 A, accelerating voltage of 81 kV and the pulse length of 10 min. The reported output power was 480 kW with the depressed potential of 25 kV. A 104 GHz operation was also carried out with this gyrotron for the cavity mode of $TE_{22,5}$. For the short pulse operation, at 104 GHz the reported output power was 520 kW for the accelerating voltage of 60 kV, beam current of 40 A and depressed collector potential of 15 kV. Later, long pulse operation was performed at W7-X for the pulse length of 30 minutes and the output power of 800 kW was reported with 33.6%(SDC) efficiency. For the pulse duration of 20 ms, at W7-X output power was reported greater than 900 kW for this gyrotron [136] [137].

Another 140 GHz gyrotron was developed at CPI, USA for the ECRH&CD applications in EAST tokamak, China. The design of this gyrotron was almost similar to that of developed for the W7-X stellarator, with the optimization of the interaction cavity and MIG geometries. The quasi-optical mode converter was improved for the better Gaussian mode conversion of the output beam, and the collector design was upgraded. The operating cavity mode was the same as $TE_{28,7}$. The objective of this gyrotron was to produce the output power of 900 kW for the pulse length of 1000 s. The factory tests at CPI, USA reported that for the short pulse operation maximum output power of 924 kW was obtained and for the long pulse of 1000 s, with the beam current less than 25 A, the output power of 500 kW was obtained [138].

170 GHz ITER Gyrotrons

A 170 GHz gyrotron is under development at CPI, USA for the ECRH application in ITER tokamak with the CW power of 500 kW; however, this gyrotron is targeted to achieve 1 MW CW power. Initial test results of this gyrotron were reported as 600 kW output power for the short pulse operation and 300 kW power for the long pulse of 15 s. The operating cavity mode was chosen as $TE_{31,8}$. The following factors had been identified for the lower value of the output power, and those were: 1. The severe mode competition

due to the startup scenario of modulating anode voltage, 2. The operation at the lower magnetic field was throttled by the excitation of modulating anode current, 3. With the increase of operating voltage, power absorption in the beam tunnel increases. The device has been re-modeled with further improvement in the key components, especially replacement of triode type MIG with that of diode type and a new beam tunnel. The short pulse tests were carried out in this re-modeled gyrotron and the output power of 1 MW obtained for accelerating voltage of 79.4 kV and beam current of 50 A and 500 kW output power was reported for the lower beam current of 25 A and accelerating voltage of 78 kV. In both the cases, depressed collector potential was 20 kV. Further, efforts are underway to increase the pulse length of this gyrotron [139].

In 2008, European research institutes along with the industrial partner TED, France had started to develop a 170 GHz gyrotron for the plasma heating applications in ITER tokamak. According to the plan, industrial CW prototype would be manufactured by TED, France and short pulse (SP) prototype would be developed by KIT, Germany. The main aim of this SP prototype was to validate the major components of the industrial tube in terms of the output power, efficiency, and the Gaussian content of the output beam. The cavity mode was chosen as $TE_{32,9}$ for this operation. In 2015, SP prototype was tested in two phases at KIT, Germany. In the initial phase, the tube was tested with MIG developed for the 170 GHz coaxial cavity gyrotron and in the later stage of testing, regular MIG developed for this gyrotron was installed. In these test results, 1.2 MW output power was reported with the depressed collector efficiency of 40% and the Gaussian content of the output beam was $\approx$ 98% [48], [49].

After the success of the SP prototype gyrotron, industrial prototype has been developed with full capability for CW operation. The industrial tube was delivered to KIT, Germany in the early of 2016 for testing up to the pulse length of 180 s. The short pulse experiments were carried out in this industrial prototype mainly to align the axis of gyrotron with the external magnetic field axis and also to optimize the parameters for the maximum output power and efficiency. The two operating points were identified namely high voltage operating point (HVOP) and low voltage operating point (LVOP). However, detailed tests were performed for the LVOP and only brief operations were performed for the HVOP. In the short pulse operations of this industrial prototype, the 1 MW output power was reported with the 97% Gaussian content of the output power [142]. The long pulse operation was carried out for the pulse length of 180 s and output power of 0.85 MW was reported for both LVOP and HVOP with the efficiency of 38% and 35%, respectively. The Gaussian content of the output beam was 97%. The long pulse experiments of this gyrotron are planned to be carried out at Swiss Plasma Center (SPC), Lausanne [141].

IAP, Russia is also involved in the development of gyrotrons for ITER tokamak. A

Table 2.1: State of the Art of 170 GHz Conventional Cavity Gyrotrons developed for the ITER tokamak [129]

Group	Mode / Power	Salient Points
JAEA, Japan [52], [140]	$TE_{31,8}$ / 1.0 MW	This gyrotron holds world record of energy of 2.88 GJ. Reported output power were: 1 MW with 55% (SDC) efficiency for 800 s pulse. 0.8 MW with 57% (SDC) efficiency for 1000 s pulse.
GYCOM / IAP, Russia [51]	$TE_{25,10}$ / 1.0 MW	1 MW output power was reported for the pulse duration of 500 s and 1000s with an efficiency of 53% (SDC) in both the cases. Slightly modifying this ITER gyrotron 1.2 MW power was obtained for 1000 s pulse with an efficiency of 53% (SDC).
CPI, USA [139]	$TE_{31,8}$ / 1.0 MW	The short pulse tests reported 1 MW power with an efficiency of 33.67%(SDC). The long pulse tests are in progress.
European research institutes in collaboration with TED, France [141]	$TE_{32,9}$ / 1.0 MW	1 MW output power was reported in the short pulse tests. Gaussian content of the output beam was 97%. Under the long pulse operation (180 s) 0.85 MW power was reported with an efficiency of 38%. Further, experiments are planned for the longer pulses.

170 GHz $TE_{25,10}$ ITER prototype gyrotron was developed and the experimental tests were carried out at 1 MW for the pulse duration of 500 s and 1000 s. The overall efficiency of the tube was 53% under depressed collector operation. The test results showed that the reliability of the ITER prototype gyrotron was 95%. By slightly modifying the ITER gyrotron prototype, the output RF power was increased to 1.2 MW for the pulse length of 1000 s with the efficiency of 53%(SDC) [51]. Another $TE_{28,12}$, 170 GHz gyrotron was developed to achieve the increased output power of 1.5-1.7 MW under CW operation. The output power of 1.5 MW was obtained for the pulse length of 2.5 s with the efficiency of 50% (SDC) [143].

Japan Atomic Energy Agency (JAEA), Japan developed a 170 GHz ITER gyrotron. This gyrotron was equipped with a triode type MIG, a quasi-optical launcher, a depressed collector and a single disk CVD diamond window. The cavity mode chosen was $TE_{31,8}$ and output RF power reported was 1 MW with 55%(SDC) efficiency for 800 s pulse and 0.8 MW with 57%(SDC) efficiency for the pulse length of 1 hour. This gyrotron holds the world record of the energy of 2.88 GJ [52]. This gyrotron had undergone the repetitive operation as a part of the reliability test. The 800 kW/600 s pulse with the efficiency of 52-57% was repeated at the interval of 20-30 minutes. Out of the 88 shots, 72 shots were successful with the full oscillation of 600 s resulting in the 82% success rate of this reliability test [140].

After the success of the ITER gyrotron, in JAEA progress were made to develop the gyrotron capable of generating CW power greater than 1.2 MW. A 170 GHz $TE_{31,9}$ gyrotron was developed with the design similar to that of the ITER gyrotron. The short pulse operation of this gyrotron reported the output power of 1 MW with 33% efficiency. In long pulse operation, 0.61 MW of output power was obtained for the pulse length of 10 s with 51% (SDC) efficiency [144]. Later, the operational cavity mode was changed to $TE_{31,11}$ for supporting multi-frequency operation and the peak ohmic wall loading for this mode is less compared to $TE_{31,8}$ mode so that RF output power of this gyrotron can be reached to 1.5 MW. The cavity modes chosen for the multi-frequency operation (104/137/170/204 GHz) were $TE_{19,7}$/$TE_{25,9}$/$TE_{31,11}$/$TE_{37,13}$. In short pulse operation, the output power was reported to be around 1.3 MW for both the frequencies 137/170 GHz. In long pulse operation at 170 GHz, for the 2 s pulse the output power of 1.23 MW was reported with the efficiency of 47%(SDC) and 1.0 MW was reported with 49%(SDC) efficiency. For the pulse length of 230 s, 1 MW RF power was obtained and for 1000 s pulse 0.51 MW power was obtained at 170 GHz [145]. For the 2 s pulse, 1.03/1.01 MW power was reported at 104/137 GHz with the efficiency of 41/42%(SDC). At 203 GHz, 0.9 MW was obtained for the short pulse operation with 18% efficiency and for the 5 s pulse 0.42 MW RF power was reported with 38%(SDC) efficiency [61].

Table 2.2: State of the Art of Megawatt class Conventional Cavity Gyrotrons [129]

Group	Frequency / Mode / Power	Salient Points
140 GHz Gyrotrons		
KIT, Germany [125]	140 GHz / $TE_{22,6}$ / 1 MW	Developed for ASDEX-U tokamak. Further, step tunable operation was carried out in the range 114-116 GHz.
European research institutes in collaboration with TED, France [47]	140 GHz / $TE_{22,8}$ / 1 MW	Developed for the W7-X stellarator. 0.92 MW output power reported for the pulse length of 1800 s with an efficiency of 44% (SDC). Dual frequency operation was carried out at 104/140 GHz.
CPI, USA [136] [138]	140 GHz / $TE_{28,7}$ / 1 MW	Developed for W7-X stellarator. Under the long pulse operation (30 min.), the output power was 0.8 MW with 33.6% (SDC) efficiency.
	140 GHz / $TE_{28,7}$ / 1 MW	Developed for EAST tokamak. 924 kW was reported under the short pulse operation. 500 kW was reported under the long pulse operation (1000 s) with the beam current of 25 A.
Low Frequency Gyrotrons		
MIT, USA [146]	110 GHz / $TE_{22,6}$ / 1.5 MW	Developed for DIII-D tokamak. Under the short pulse (3 ms) test 1.5 MW output power was reported with an efficiency of 50% (SDC).
CPI, USA [137]	117.5 GHz / $TE_{20,9}$ / 1.8 MW	Developed for DIII-D tokamak. In the short pulse test (6 ms) maximum output of 1.67 MW obtained. The long pulse operation was performed for the lower beam current of 25 A.

Table 2.3: State of the Art of Multifrequeny Gyrotrons (Conventional Cavity Gyrotrons) [129]

Group	**Frequency/ Mode/ Power**	**Salient Points**
European research institutes in collaboration with TED, France [47]	103.8/140 GHz $TE_{21,6}/TE_{28,8}$ 1.0 MW	Developed for W7-X stellarator. Output power of 0.41/0.92 MW at 103.8/140 GHz for 10s/1800 s pulse with 27/44% (SDC) efficiency.
GYCOM / IAP, Russia [62]	105.1/140.1 GHz $TE_{17,6}/TE_{22,8}$ 1.0 MW	Developed for ASDEX-U tokamak. Output power of 0.85/0.95 MW at 105.1/140.1 GHz for 300s pulse with 50/52% (SDC) efficiency.
MIT, USA [147]	110/124.5 GHz $TE_{22,6}/TE_{24,7}$ 1.5 MW	Developed for DIII-D tokamak. In the short pulse operation (3 s) at 110 GHz, 1.25 MW output power reported with an efficiency of 30%. At 124.5 GHz, 1.0 MW power reported with 24% efficiency.
JAEA, Japan [63] [61]	82/110/137.6 GHz $TE_{17,6}/TE_{22,8}/TE_{27,10}$ 1.0 MW	Developed for JT60-SA Tokamak. Output power of 0.4/1.0/1.0 MW reported at 82/110/137.6 GHz for 2/100/100 s pulse with 35/45/43% (SDC) efficiency.
	104/136.8/ 170/203 GHz $TE_{19,7}/TE_{25,9}/$ $TE_{31,11}/TE_{27,13}$ 1.0 MW	Developed for ITER Tokamak. **104 GHz:** 1.03 MW output power for 2 s pulse with an efficiency of 41% (SDC). **137 GHz:** 1.01 MW output power for 2 s pulse with an efficiency of 42% (SDC). **170 GHz:** 1.0/0.51 MW output power for 230/1000s pulse with an efficiency of 46/46% (SDC). **203 GHz:** 0.42 MW output power for 5 s pulse with an efficiency of 38%(SDC).

Low Frequency Gyrotrons ($<$ 140 GHz)

A 117.5 GHz gyrotron was developed for DIII-D tokamak at CPI, USA and initial tests were performed in 2013. The short pulse tests reported the output power of 1.8 MW for the beam current of 60 A, accelerating voltage of 98 kV and depressed collector potential of 25 kV. For the beam current of 50 A, output power was reported as 1.5 MW. However, due to high voltage stand-off and discharge problems, long pulse operation of this gyrotron was not able to carry out. Later, some changes were done on the electron gun geometry of this gyrotron to reduce the trapping of electrons in the regions of the electron gun and beam tunnel. In 2017, test results were reported. The operating cavity mode was $TE_{20,9}$. In short pulse tests ($<$6 ms), maximum output power reported was 1.67 MW. The long pulse operation was performed for the beam current of 25 A, accelerating voltage of 95 kV and the reported output power was 530 kW for the pulse length of 10 s with the depressed potential of 17 kV. By increasing the accelerating potential to 99 kV, the output power was reported to be 700 kW for the pulse length of 1 s with the depressed potential of 20 kV [137].

JAEA also developed gyrotrons for plasma heating application in JT-60SA tokamak. A dual frequency gyrotron (110/138 GHz) was developed, and in 2015 the specified output power of 1.0 MW for the pulse length of 100 s was achieved at both the operating frequencies. This gyrotron consists of a triode type MIG, single stage depressed collector, quasi-optical launcher and CVD diamond window of thickness 2.29 mm [50]. Later, in this gyrotron 82 GHz operation was carried out with $TE_{17,6}$ mode and obtained the output power of 0.4 MW with the efficiency of 35%(SDC) for the 2 s pulse [63].

Massachusetts Institute of Technology (MIT), USA developed gyrotrons for plasma heating application in DIII-D tokamak. A 110 GHz gyrotron developed for this purpose with the reported output power of 1.4 MW in the $TE_{22,6}$ mode for 2.6 μs pulse. Under full voltage operation (96 kV) of the electron gun with the beam current of 40 A, this tube reported 37% efficiency without any depression of the collector potential. This experiment was performed without the installation of internal mode converter and depressed collector. The results of this experiment were promising in achieving 50% efficiency under the depressed collector operation [148]. In 2005, the cavity (V-2003) of this 110 GHz gyrotron was replaced with the new cavity (V-2005). The feature of this V-2005 cavity was the lower value of diffractive Q factor of the cavity mode and hence ohmic wall loading can be reduced. In short pulse experiment, the reported output power was 1.67 MW at 42% efficiency under normal operation. The mode competition was also reduced in the tube with V-2005 cavity compared to the tube with the V-2003 cavity. The calculated ohmic wall loading of this V-2005 cavity was 0.8 kW/cm^2 [149]. In 2007, single stage depressed collector operation of this 110 GHz was carried out. For the pulse of 3 ms, the 1.5 MW

output power was reported with the efficiency of 50% (SDC). The internal mode converter used in this gyrotron consists of a launcher, and four mirrors for phase correction. The experimental results were compared with the simulation results and were in good agreement as the simulations included after cavity interaction effects also [146], [150].

In 2014, modifications were carried out on the existing 1.5 MW, 110 GHz gyrotron to support dual frequency operations (110/124.5 GHz). The cavity modes were chosen as $TE_{22,6}$/$TE_{24,7}$ for the frequencies 110/124.5 GHz. The electron gun and magnetic guidance system of the 110 GHz gyrotron were retained for this dual frequency operation and the key components like interaction cavity, internal mode converter, and RF window were remodeled. The mode converter consists of a dimpled wall launcher along with four mirrors. The single disk window of fused quartz was used for this short pulse operation, and this will be replaced by the CVD diamond window for the long pulse operation. The experimental operation was carried out for the pulse of 3 μs with the accelerating voltage of 98 kV, the beam current of 42 A and obtained the output RF power of 1.25 MW with 30% efficiency at 110 GHz and 1.0 MW with 24% efficiency at 124.5 GHz. The maximum output power of 1.4 MW was reported at 110 GHz with the efficiency of 32% [147].

2.3.2 Coaxial Cavity Gyrotrons

Earlier Developments on the Coaxial Cavity Gyrotrons

Earlier developments on the coaxial cavity gyrotrons were started in the early 1970's in Russia with the motivation towards the reduction of mode competition in the overmoded gyrotron cavities. In the first experimental operation on coaxial cavity gyrotron, the presence of the insert eliminated the competing mode $TE_{5,2}$ and the output power of 400 kW was obtained in the desired mode $TE_{9,1}$ at 15 GHz with an efficiency of 45% [151]. The second experiment on coaxial cavity gyrotron was carried out at 45 GHz with the desired cavity mode of $TE_{15,1}$ in 1973. For the pulse of 100 μs, the RF output power of 1.25 MW was obtained with an efficiency of 35%. This was the first ever experiment in which the output power was reported to be greater than 1 MW. In the 1980's, a 100 GHz coaxial cavity gyrotron experiment was carried out for the pulse duration of 100 μs. The reported output power was 2.1 MW in the mode $TE_{26,10}$ with an efficiency of 30%. The ohmic wall loading of the cavity was calculated to be around 1.5 kW/cm^2. Even though the experiments on coaxial cavity gyrotrons were successful, researchers did not show much interest and this may be due to two prime reasons. The first reason was that in the early 1980's, the requirements of gyrotrons in the fusion reactor were like to generate RF power at the frequencies below 100 GHz for the pulse of around 0.1 s and the conventional cavity gyrotrons were enough to satisfy these requirements. The second reason was the unavail-

ability of the output RF window to handle very high power in the long pulse operation. Later in the 1990's, developments in the research of CVD diamond window paved the way for the development of megawatt class CW coaxial cavity gyrotrons [46].

In 1991, Barroso *et al.* studied the use of a coaxial cavity as the interaction structure in gyrotron. These studies demonstrated that the use of coaxial cavity resonator reduces the mode competition problem. It was also shown that with the use of the tapered insert, the quality factor of the competing modes can be modified. A coaxial cavity interaction circuit was designed for 280 GHz gyrotron with the desired cavity mode of $TE_{26,10}$. Even though the frequency separation between the $TE_{26,10}$ and its competing neighbor was 0.6%, but their Q factor ratio was 6.5 and thus, the mode competition problem was reduced with tapered insert [152]. Later, the desired mode was changed to $TE_{42,7}$ and the interaction cavity was designed. In addition to the geometrical variations of the insert, calculations were performed for the insert with lower electrical conductivity. For the case of the coaxial cavity with insert of lower conductivity, there was a significant reduction in the Ohmic Q factor of the competing modes. Thus, these studies suggested that combination of both geometrical and electrical conductivity variation of the insert could be used for the effective mode rarefaction [72].

In 1994, Nusinovich developed the general theory of the coaxial cavity gyrotron. The mode selective properties of the coaxial resonators with tapered insert were explained with the help of modified Vlasov's equation for such structure. The mathematical formulas for the eigenvalue and ohmic losses were derived. The startup scenario and mode competition in the 1 MW, 280 GHz coaxial cavity gyrotron were discussed with numerical simulation. It was observed that due to the high ohmic losses occurring on the inner rod, this structure face main restrictions for use in the continuous wave operation [53].

In 1996, the design of a 3 MW, 140 GHz coaxial cavity gyrotron was reported by MIT, USA and the cavity mode was chosen as $TE_{21,13}$ [153]. The theoretical simulations were carried out for the three different configurations of the interaction cavity, the first was the conventional cavity (without coaxial insert), the second was the coaxial cavity with smooth straight insert without any tapering and the third was the coaxial cavity with the tapered insert. The highest theoretical efficiency was reported as 45% for the case of the coaxial cavity with straight insert and it was observed that the mode competition in the coaxial cavity was found to be less compared to the conventional cylindrical cavity. Thus, this configuration of the coaxial cavity with straight insert was finalized for the experimental operations. The gyrotron based on this design was manufactured and the assembly constituted of an inverse MIG (IMIG), an internal mode converter, and a single parabolic mirror. The IMIG was tested for 3 μs with the maximum cathode voltage of 103 kV, the beam current of 93 A and it was capable of delivering DC power up to 10 MW.

Table 2.4: State of the Art of Coaxial Cavity Gyrotrons (Non-Corrugated Insert) [94]

Group	Frequency/ Mode / Power	Salient Points
USSR/ Russia [151] [46]	15 GHz / $TE_{9,1}$ / 0.5 MW	First experimental operation on gyrotron with coaxial insert. 400 kW output power was reported with an efficiency of 45%.
	45 GHz / $TE_{15,1}$ / 1.25 MW	For the pulse of 100 μs, 1.25 MW output power was reported with 35% efficiency.
	100 GHz / $TE_{26,10}$ /2.1 MW	For the pulse of 100 μs, 2.1 MW output power was reported with 30% efficiency.
MIT, USA [154]	140 GHz / $TE_{21,13}$ / 3.0 MW	Gyrotron includes coaxial cavity with smooth wall insert, inverse MIG, internal mode converter with single mirror. For the pulse of 3 μs, 0.5 MW output power obtained and maximum power of 1 MW obtained in the $TE_{27,11}$ mode with 15% efficiency.

The initial tests of this tube reported severe mode competition with only 0.5 MW power obtained in the desired mode and the maximum of 1 MW obtained in the $TE_{27,11}$ mode at 142 GHz with an efficiency of 16%. The obtained efficiency was only half of that predicted through the theoretical calculations and the reasons for this poor efficiency were found as the asymmetric emission of the cathode and relative misalignment in the axes of the electron beam, coaxial insert and cavity. Later, tests were carried out with the gyrotron in which mode converter was removed and cathode was replaced with the new one. With the new cathode, 1.1 MW output power was reported in the desired mode. The tests were also performed for the conventional cavity as the interaction circuit to understand the mode competition in the tube. In this case 0.9 MW of power was reported in the desired mode, however theoretically 1.4 MW was predicted. From these experimental results, it was observed that reduced power in the desired mode was mainly due to the asymmetric emission of the cathode caused by non-uniform heating of emitter and non-uniform emitter coating [154].

Developments on the Coaxial Cavity Gyrotrons with Corrugated Insert

In 1996, C.T. Iatrou *et al.* studied the coaxial cavity with corrugated insert for high power gyrotron. The field expressions for the rectangular corrugated coaxial cavity were derived using surface impedance method (SIM) and mathematical formulation for the eigenvalue, ohmic wall loading was also obtained. By using the developed mathematical model coaxial cavity has been designed and the mode competition in the cavity was studied using the eigenvalue curves. The theoretical approximations were validated through MAFIA code simulations [54]. Furthermore, C.T. Iatrou has also investigated mode selective properties of two different coaxial resonator structures. The first was the cavity with resistive insert up tapered towards the output end and the second configuration was the coaxial cavity with longitudinally corrugated down tapered insert. Among these two configurations, the second design provided the better mode rarefaction. The variation in the ohmic wall loading on both inner and outer conductor with the depth of corrugation for different modes was studied. An approximate mathematical formula for diffractive Q factor of the cavity modes in the corrugated coaxial cavity was derived. It was found that there would not be any severe mode competition caused by the surface modes. Additionally, it was observed that there may be severe mode competition problem due to the second harmonic modes and this can be avoided by properly choosing the corrugation depth [155].

The coaxial cavity gyrotrons were developed at KIT, Germany in collaboration with IAP, Russia for the frequencies 140 GHz and 165 GHz and these gyrotrons used coaxial cavities with longitudinally corrugated insert. The motivation behind this was to develop the tubes with the single output power of greater than 1 MW. In the initial stage of development of a 140 GHz coaxial cavity gyrotron axial RF output was considered. The experimental results reported the maximum power of 1.17 MW in the mode $TE_{28,16}$ at 27.2% efficiency for the pulse length of < 0.5 ms. Over the wide range of operating parameters, the single mode of operation was experienced. The reasons behind the lower efficiency were reported as high voltage shoot at the starting of pulse and window reflections leading to the severe mode competition. Frequency step-tuning operation was also carried out with this gyrotron and twenty modes were excited in the frequency range 115.6 GHz-164.2 GHz. The reported output powers were 0.9 MW in the $TE_{25,4}$ mode at 123.0 GHz, 1.16 MW in the $TE_{32,18}$ mode at 158.9 GHz and the power obtained in the other modes were limited due to the window reflections [156]. Later, this tube was remodeled with an internal mode converter and a single stage depressed collector. The dual beam RF output system was designed for the first time in which conversion was done in two steps. In the first step, the cavity mode $TE_{28,16,-}$ was transformed to the evanescent whispering gallery mode $TE_{76,2,+}$ and later this mode was converted into two Gaussian beams using rippled wall dual cut launcher. The maximum output RF power was reported

Table 2.5: State of the Art of Coaxial Cavity Gyrotrons (Longitudinally Corrugated Insert) [94], [129]

Group	Frequency/ Mode / Power	Salient Points
KIT, Germany Collaboration with IAP, Russia [156] [157] [158] [73]	140 GHz / $TE_{28,16}$ / 1.5 MW	Tube includes an inverse MIG and a dual beam output system. Output RF power - 0.95 MW for the pulse length of 0.5 ms with an efficiency - 20% /29% (SDC).
	165 GHz / $TE_{31,17}$ / 1.5 MW	Tube includes a coaxial MIG and a single beam output system. Vlasov Launcher with two mirrors. Output power - 1.5 MW for the pulse length of 1 ms with an efficiency - 30%/48% (SDC).
IAP, Russia [159]	140 GHz / $TE_{28,16}$ / 1.5 MW	Similar design to that of German tube. Short pulse tests were carried out for the time period of 50 μs. By biasing the insert, frequency step-tuning operation was performed.
EGYC * Collaboration among CRPP (now SPC), Switzerland; KIT, Germany; HELLAS, Greece; CNR, Italy; ENEA, Italy. [55]	170 GHz / $TE_{34,19}$ / 2.0 MW	Tube includes Coaxial MIG, Advanced quasi optical launcher system. Gaussian content in the output RF beam was 96%. **Under normal operation:** Output power- 2.3 MW, Efficiency - 30%, Pulse length 1 ms. **Under depressed collector operation:** Output power - 2.1 MW/1.9 MW with efficiency - 46%/48%, Pulse length of 3.5 ms. Progress are being made for the long pulse operation.

Table 2.6: Important Theoretical Developments in the Design of High Power Coaxial Cavity Gyrotrons [94], [129]

Paper	Salient Points	Year
Nusinovich *et al.* [53]	General theory of a coaxial cavity gyrotron with smooth insert. Expressions derived for the eigenvalue and ohmic losses. Mode competition and startup scenario were discussed for 280 GHz gyrotron.	1994
Iatrou *et al.* [54]	Field analysis of a coaxial cavity with longitudinally corrugated insert using SIM. Mathematical formulations were obtained for the eigenvalue and ohmic wall losses. Validation done with numerical code MAFIA.	1996
B. Piosczyk [83]	Novel 4.5 MW (90 kV, 50 A) coaxial MIG developed for 165 GHz coaxial cavity gyrotron. Electrons are extracted towards anode and not towards insert as in inverse MIG.	2001
O. Dumbrajs [160]	Field expressions were derived for a coaxial gyrotron cavity with longitudinally corrugated insert using SIE. Ohmic losses were calculated using the SIE method and compared with SIM model.	2004
Ioannidis *et al.* [161]	Field expressions were derived using SHM. Compared to SIE, calculations were converging very fast in SHM. Results obtained were very close with other published results.	2006
J. Jin *et al.* [162]	Novel numerical method has been proposed for the analysis of fields in the launcher walls. Algorithm was developed to synthesize the waveguide wall. For 170 GHz coaxial cavity gyrotron with $TE_{34,19}$ mode, advanced launcher of length 309.6 mm has been designed. Fundamental Gaussian mode content obtained was 96.3%.	2009
S. Singh *et al.* [74] [163]	Field analysis of coaxial cavity with triangular corrugated insert has been carried out using SIM. Expressions for ohmic losses, peak wall losses, and quality factor were derived.	2016
	Full wave approach (SHM) has been applied for the field analysis of coaxial cavity with triangular corrugations on the insert. Mathematical expressions for eigenvalue and ohmic losses have been derived.	2017

as 0.95 MW with an efficiency of 20% and under depressed collector operation efficiency was increased to 29%. The reasons behind the poor performance of this tube were found to be due to the poor design of the internal mode converter and instabilities in the electron beam caused by the poor performance of the emitter. The single mode operation range observed in this experiment was found to be wide and the results were in good agreement with the theoretical calculations [157].

In addition to the collaborative work between KIT, Germany, and IAP, Russia, there were also independent developments on the coaxial cavity gyrotrons happened at IAP, Russia. A 140 GHz tube was developed similar to that of the German coaxial cavity gyrotron. The desired RF output power was 1.5 MW, and the cavity mode was chosen as $TE_{28,16}$. This tube was equipped with an inverse MIG for the electron beam generation, and short pulse tests were carried out for the pulse of 50 μs. To verify the mode selection capability of the corrugated coaxial cavity two different tests were performed, one with a smooth outer cavity and another with a corrugated outer conductor. It was reported that mode selectivity was better in the coaxial cavity with corrugated outer conductor. The experiments were also performed by biasing the insert, and in the certain magnetic field range, variations of the output RF power was reported for varying potentials of the cathode and insert, and the maximum efficiency of 50% was obtained. By varying the insert biasing voltage and the beam current, frequency tuning operation was also performed in this gyrotron for the fixed values of the magnetic field and the cathode potential [159].

Barroso *et al.* studied the resonant properties of the coaxial cavity with longitudinally corrugated insert for the use as interaction circuit in megawatt class gyrotrons. The mathematical expressions for the eigenvalue, ohmic wall loading and fields in the cavity were derived using SIM. The effect of corrugation parameters on the eigenvalue and slope of the eigenvalue curve were studied in detail. The theoretical results were validated with the experimental measurements of total Q factor and resonant frequencies of the modes in the frequency range 8-16 GHz. The experimental results were in agreement with the theoretical prediction with an error of 0.5%. These studies strongly recommended the use of the coaxial cavity with corrugated insert for megawatt class gyrotrons operating at very high frequencies [164].

In 1999, a 165 GHz coaxial cavity gyrotron was developed, and the initial tests were performed at KIT, Germany. In these years, there were considerable developments in the CVD diamond windows capable of handling CW RF power of around 2 MW, so this gyrotron was built with an internal mode converter that can support single beam radial output. The mode converter used in this tube consists of a quasi-optical launcher, one quasi-elliptic mirror and another non-quadratic phase correcting mirror. For the nominal beam parameters, the output power reported was 1.3 MW with 27.3% efficiency and the

efficiency was increased to 41% for the operation with the depressed collector. For the beam current of 70 A, maximum output power of 1.7 MW was reported. Overbuching was observed in the tests due to the high diffractive Q factor of the interaction cavity. In this experiment an inverse MIG (IMIG) was used which was not originally developed for this 165 GHz operation and in the later stages of the experiment on this tube, the IMIG was replaced with the newly developed coaxial MIG (CMIG) [158]. In 2000, the step-tunable operation of this tube was performed, and the output window was replaced with silicon nitride Brewster window. Nineteen modes were excited in the frequency range of 134-169.5 GHz, and the frequency separation between the mode was about 2.2 GHz. As the ohmic loading on the insert walls depends on the frequency, the frequency step-tuning was limited in case of the coaxial cavity gyrotron [165].

In 2001, KIT, Germany developed a novel 4.5 MW electron gun for the coaxial cavity gyrotrons to overcome the drawbacks of the IMIG. In this coaxial MIG (CMIG), electrons were extracted towards the anode and not towards the insert (as in that of IMIG). The advantage of this novel gun arrangement was the reduced radial size of the gun and hence, the overall bore hole radius of the magnetic guidance system can be reduced. The other advantages of this gun were coaxial insert can be fully cooled and adjusted during operation, a triode type of operation was also possible in this MIG within the certain range by biasing the insert. The mechanical vibration of the insert was also reported to be less in this novel design [83].

In 2004, experimental results of a 165 GHz gyrotron were reported for the short pulse of 1 ms. In this experiment, the newly developed CMIG was installed, and an output RF power of 1.5 MW was obtained with 30% efficiency and 48% (SDC) efficiency for the depressed collector voltage of 34 kV. The maximum power of 2.2 MW was obtained for the beam current of 84 A. The effect of insert misalignment on the gyrotron operation was also investigated, and leakage current on the insert was also measured as a function of collector voltage in this experiment. These results confirmed the feasibility of manufacturing 2 MW, 170 GHz CW coaxial cavity gyrotron for ITER tokamak [73].

In 2002, O. Dumbrajs proposed a novel coaxial cavity with corrugated insert to improve mode competition scenario in a high power gyrotron, in which corrugation depth on the insert is axially varying. The novel structure was analyzed using the SIM method. From these analytical results, it was observed that ohmic losses on the insert walls got re-distributed and reduced [166]. O. Dumbrajs derived the mathematical expressions for the ohmic wall losses in a coaxial cavity with corrugated insert using Singular Integral Equation (SIE) method which included all the spatial harmonics. Since the most widely used SIM model does not include spatial harmonics in the calculations, which may give an erroneous result when the number of the corrugations are less than the twice of the

azimuthal mode index. The ohmic losses calculated using SIE method was found to be lower than that calculated using SIM [160]. Z.C. Ioannidis *et al.* mathematically calculated the dispersion relation, the field distributions, and the ohmic losses for a coaxial cavity with longitudinally corrugated insert based on Space Harmonics Method (SHM). Since the SHM includes only very few harmonics in the calculation compared to Singular Integral Equation(SIE) method, SHM gets converged very fast. The eigenvalue and ohmic losses calculated using this method gave very close results with other published results [161].

The design of a compact launcher for the coaxial cavity gyrotron is quite complex, as the relative caustic radius of the desired cavity mode in the coaxial cavity gyrotron is usually around 0.3. In 2009, Jin *et al.* proposed a new method for the analysis of fields on the walls of the oversized waveguide. The proposed method can be used for simulation of fields on the waveguide walls with arbitrary perturbations, considering the wall perturbations to be shallow and smooth. Along with this analytical method, an iterative algorithm was also developed for the synthesis of wall deformations for the required field distribution. By using this new algorithm, a quasi-optical launcher of length 309.6 mm was designed and fabricated for the 170 GHz coaxial cavity gyrotron and Gaussian content of the output wave beam from this launcher was around 96.3%. This conversion was much better compared to the conventional dimpled wall launcher of 600 mm long with a transformation efficiency of 86% [162].

The development of a 170 GHz, 2 MW modular pre-prototype coaxial cavity gyrotron for ITER tokamak and in upgraded systems of other existing tokamaks is in progress at KIT, Germany. This gyrotron consists of a triode type coaxial MIG, an internal mode converter, and a single stage depressed collector system. In the short pulse operation of this gyrotron, the reported output power was greater than 2 MW with an electronic efficiency of 30%. In the depressed collector operation, the output power was reported as 2.2 MW with an overall efficiency of 48%. Currently, this tube is upgraded to achieve the long pulse operation with the pulse length up to 1 s [55].

Some design studies were carried out to understand the feasibility of a coaxial cavity gyrotron with an output RF power of greater than 2 MW. Kartikeyan *et al.* have reported the feasibility of a 5.0 MW, 170 GHz coaxial cavity gyrotron using very high volume mode in 2003 [167] and in 2004, feasibility studies of a 140 GHz, 3.0-3.5 MW coaxial cavity gyrotron with a dual beam output have been reported by the same group [168]. In 2013, Beringer *et al.*, have reported the feasibility of a 4 MW, 170 GHz coaxial cavity gyrotron with the detailed physical designs of the major components. The cavity mode was chosen as $TE_{52,31}$, and an internal mode converter was designed with a launcher of dual cuts that would generate two 2 MW Gaussian beams [169].

In 2015, S. Singh *et al.* had done field analysis of a triangular corrugated coaxial cavity for megawatt class gyrotron. The advantage of this structure was that the problem of localized heating on the insert walls could be reduced compared to that of the rectangular corrugated insert. The SIM model was used for the mathematical formulation of the dispersion relation, wall losses, and quality factor of this new structure [74]. Later in 2017, full wave approach (SHM) was used for the field analysis of a coaxial gyrotron cavity with triangular corrugated insert. The mathematical formulas were derived for the eigenvalue and ohmic wall losses. The convergence of SHM to SIM in this cavity was also discussed under specific conditions. By including harmonics, variation in the eigenvalue was observed to be less; however, there was a significant variation in the ohmic wall losses [163].

Chapter 3

RF Behavior of a Dual Frequency Triangular Corrugated Coaxial Cavity Gyrotron

3.1 Introduction

The next generation fusion reactors, like European DEMO, Japanese DEMO, require gyrotrons operating at frequencies above 200 GHz with the long pulse power of greater than 1 MW [12], [58]. One of the major design goals in the development of megawatt class gyrotrons is to keep the ohmic wall losses of the cavity within its limit. Higher order modes are chosen for megawatt class gyrotrons, so that for the given frequency the radius of the cavity would be large, which can limit the peak wall loading of the cavity. Higher order operating mode poses severe mode competition problems and this can be overcome by introducing an insert in the conventional weakly tapered cavity resonator. The insert in the coaxial cavity also reduces the voltage depression of the electron beam and consequently increases the limiting current. Corrugations on the insert offer a better trade off between the mode selection and the ohmic wall loading of the insert [155]. Thus, coaxial gyrotrons would be a better choice for the future fusion reactors requiring megawatt of power at frequencies above 200 GHz.

Short pulse operation of a 170 GHz coaxial cavity gyrotron for ITER tokamak has been reported by KIT, Germany with the output power of 2.2 MW and an interaction efficiency of 33% [170], [55]. Recently, research activities are going on for the development of multi-frequency gyrotrons since these offer a wide flexibility in experimental conditions of fusion reactors without significant increase in the construction costs [171]. A dual frequency gyrotron operating at the frequencies of 140 GHz and 105 GHz was installed in the ASDEX-U (German Tokamak) [172]. Step tunable operation of the D-band

Table 3.1: Design goals and physical constraints.

Frequency	220 GHz	251.5 GHz
Output Power	2.0 MW, CW	2.0 MW, CW
Diffractive Q	1000-2000	1500-2500
Beam Voltage	84-87 kV	82-85 kV
Beam Current	70 A	68 A
Magnetic Field at Cavity Center	8.85-8.90 T	10.09-10.11 T
Velocity Ratio	≈ 1.30	≈ 1.30
Total Output Efficiency	$> 35\%$	$> 35\%$
Estimated Wall Loading	< 2 kW/cm^2	< 2 kW/cm^2
Total Internal Losses	$< 8\%$	$< 8\%$

gyrotron operating in the frequency range 124-169 GHz was performed at KIT [171]. The JT 60SA (Japan Tokamak) uses a 110/138 GHz dual frequency gyrotron, which also has an additional operational frequency of 82 GHz [63].

This chapter focuses on the possibility of the dual regime operation of a megawatt class coaxial cavity gyrotron. This proposed gyrotron can be used for plasma heating, current drive and plasma stabilization in the future fusion reactors. As the fusion community is in quest to fix the power-frequency-efficiency of the gyrotrons used in the future tokamaks, one can explore the operation of the gyrotron at 220 GHz. Another exciting area is the space power grid, where enormous solar power will be collected in the space (low earth orbits) and distributed to the earth stations using solar power satellites [173]. 220 GHz is selected for the downward transmission as the atmospheric absorption has a relative minimum at this frequency. Currently, a solid state modular framework is considered for the up conversion task, however, a gyrotron based module may also be considered for this application. 220 GHz can be considered as a possible frequency for the future fusion experiments. The design of a MW-class triple frequency regime(220/247.5/275 GHz) conventional cavity gyrotron has been reported in [174]. In the current design, 220 GHz is the principal frequency and the additional frequency (251.5 GHz) is selected with the aim that the designed gyrotron can support multiple requirements of RF power in the next generation tokamaks.

In the present chapter, the RF behavior of a dual regime 220/251.5 GHz, 2.0 MW, continuous wave coaxial cavity gyrotron is presented. Based on the mode selection strategy of multi-frequency gyrotrons [175], operating modes are selected. Triangular slots on the insert offer a good mode selection and also reduce the problem of localized heating. Eigenvalue and ohmic loss calculations of a triangular corrugated coaxial cavity gyrotron using the Surface Impedance Model (SIM) and the full wave approach were reported by Singh *et al.* [74], [163]. Mode selection, cold cavity design, mode competition calculations and single mode self-consistent calculations are performed with our in-house

code Gyrotron Design Suite 2018 (GDS 2018) [176]. In single mode computations, beam parameters are optimized for maximum RF power and ohmic wall losses are also calculated. As a next step, time dependent multi-mode calculations are done using the SELF-T code [93] with the mode eigenvalues obtained from GDS 2018 [176]. Start-up scenarios are carried out for both operating frequencies with a non-uniform realistic magnetic field before and after space charge neutralization using the optimal electron beam parameters obtained from the triode type coaxial Magnetron Injection Gun (MIG) design studies using ESRAY [177]. For the present dual frequency coaxial cavity gyrotron, design goals and physical constraints are presented in Table 3.1.

3.2 Frequency and Mode pair Selection

220 GHz is selected as the principal frequency for the dual regime coaxial cavity gyrotron and the second frequency (251.5 GHz) is chosen such that the proposed gyrotron can be used for multiple requirements. According to the transparency condition of the RF window which is given by

$$f_t = \frac{c}{2d\sqrt{\varepsilon_r}}N \tag{3.1}$$

where f_t is the transparent frequency, c is the velocity of the light, N is an integer, d is the thickness and ε_r is the dielectric constant of the window. Typically for megawatt class operation, the thickness of the CVD diamond window is chosen between 1.5 mm and 2.5 mm. For the present design, the thickness of the single disk CVD diamond window ($\varepsilon_r = 5.67$) is considered as 2.00 mm. Transmission and reflection coefficients of this window along the frequency are shown in Figure 3.1. The designed window has the -20 dB transmission bandwidths of 2 GHz around the frequencies 220.1 GHz ($7\lambda/2$), 251.5 GHz ($8\lambda/2$) and 282.9 GHz ($9\lambda/2$).

For megawatt class, sub-THz wave gyrotrons, usually higher order modes with eigenvalue greater than 100 are chosen, so that ohmic wall loading can be maintained under the permissible limit. Mode competition in the coaxial cavity can be better controlled for the modes with the relative caustic radius (m/χ_{mp}) of ≈ 0.3 (χ_{mp} is the eigenvalue of the $TE_{m,p}$ mode, m and p are the azimuthal and the radial index of mode, respectively). In addition to these considerations, the mode pair for the dual regime gyrotron should satisfy the following conditions

1. As the cavity radius should be same for all the operating frequencies, the modes are chosen such that their corresponding resonant frequencies lie in the transmission bandwidth of the RF window.
2. The relative caustic radius (m/χ_{mp}) of the modes should be approximately same so

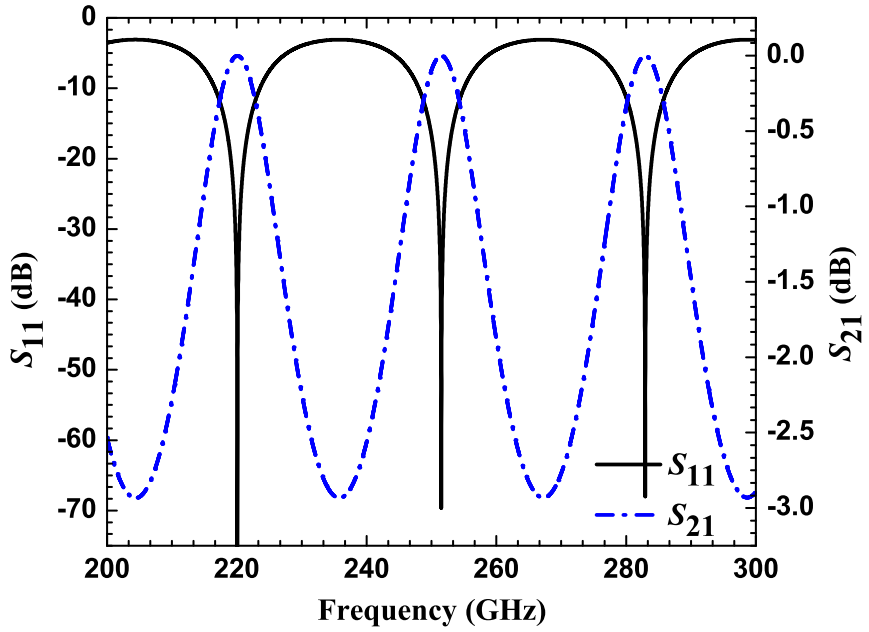

Figure 3.1: Transmission and reflection coefficients of a synthetic diamond RF window along the frequency [176].

that the common output system (Quasi Optical Launcher, internal mirror system, window and Matching Optics Unit) can be used.

3. The electron beam radius of the chosen modes should be approximately same in order that the common magnetron injection gun system can be used for the electron beam generation.

Mode pairs that satisfy these conditions are listed in Table 3.2 and the voltage depression (V_d) for these mode pairs are calculated through the formulation given in [17]. From the Table 3.2, the modes $TE_{48,30,-}$ and $TE_{55,34,-}$ (negative sign indicates co-rotating mode) are selected for operation at 220 GHz and 251.5 GHz, respectively.

Table 3.2: Mode selection for dual regime operation [176]

f_r (GHz)	m	p	χ_{mp}	R_o (mm)	R_b (mm)	V_d* (kV)	m/χ_{mp}
220.000	46	29	150.7898	32.726	10.395	1.70	0.305
250.841	52	33	171.9283	32.726	10.282	1.58	0.302
220.000	47	29	152.1125	33.013	10.616	1.91	0.309
252.487	54	33	174.575	33.013	10.600	1.90	0.309
220.000	**48**	**30**	**156.7365**	**34.016**	**10.838**	**2.12**	**0.306**
251.530	**55**	**34**	**179.1992**	**34.016**	**10.834**	**2.12**	**0.307**
220.000	50	30	159.3778	34.590	11.281	2.49	0.314
251.006	57	34	181.8403	34.590	11.244	2.46	0.314
220.000	51	29	157.3780	34.156	11.502	2.65	0.324
251.403	58	33	179.8422	34.156	11.420	2.59	0.323

(* For the calculation of V_d, electron beam voltage, beam current and velocity ratio are 85 kV, 68 A and 1.27, respectively)

3.3 Interaction Structure Design

The main parts of the interaction circuit are input down taper, straight mid section, linear up taper and the corrugated insert. Tapers are connected to the midsection through parabolic rounding so as to avoid mode conversion due to sharp transitions. As the gyrotron operates close to the cutoff frequency of the $TE_{m,p}$ mode, the radius of the cavity (R_o) is given by $R_o = \chi_{mp}.c/(2\pi f_r)$ (f_r is the resonant frequency of the cavity). In the present design R_o is selected as 34.00 mm (instead of 34.016 mm) so as to compensate the frequency down shift due to the cavity thermal expansion. The corresponding resonant frequencies of the mode pair are 220.117/251.630 GHz. The insert radius (R_i) is chosen so as to control both mode competition and the ohmic wall loading on the insert. The insert is down tapered with an angle of -1^o and has triangular corrugations on its wall as presented in Figure 3.2. R_d is the depth, l is the width and $S = 2\pi R_i/N$ is the periodic

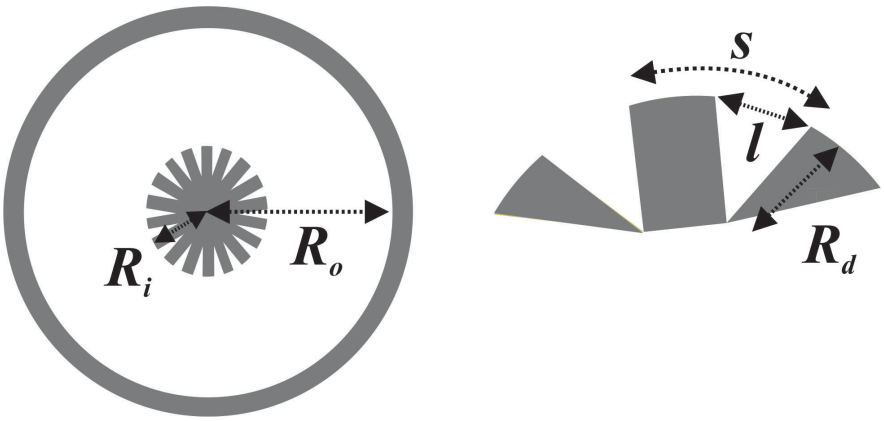

Figure 3.2: Cross section of a triangular corrugated coaxial cavity [74].

spacing of the triangular slot on the insert. Ohmic losses on the insert can be reduced by increasing the number of slots (N). In a rectangular corrugated insert, the base of the slots becomes closer for the large number of slots. Since, the wall loading is maximum at the bottom of the slot it creates the problem of localized heating. Whereas in a triangular corrugated insert, side walls are farther for the large number of slots and this reduces the localized heating problem [163]. As the number of slots is sufficiently large, the fields inside the slots are homogeneous and therefore the Surface Impedance Model (SIM) is used for these design studies.

The eigenvalue curves for the desired mode pair along with their competing modes are shown in Figure 3.3. For the coaxial cavity with down tapered insert, the diffractive quality factor of the mode decreases for the negative slope of the eigenvalue curve and increases for the positive slope. Thus by selective modification of the diffractive quality factor of the competing modes, mode competition can be controlled. In addition to the mode rarefaction, wall losses on the insert should be minimized. Positive slope of the eigenvalue curve is avoided in the operating radii ratio as the ohmic wall loading significantly increases for higher values of the diffractive quality factor. The flat region in the eigenvalue curve resembles that the energy is concentrated in the cavity region as in the conventional cylindrical cavity. The slope region of the eigenvalue curve represents that the fields are concentrated in the slot and thus increase the ohmic losses on the insert [155]. Hence the R_i is selected such that the eigenvalue curve of the desired mode lies near the flat region and that of the competing modes lie near the negative slope region. For the present design R_i is selected as 8.95 mm at the middle of the interaction structure, R_d is optimized as 0.5 mm and the l/S ratio is 0.7.

From the Figure 3.3, it is observed that in the operating range of C (3.78-3.85), eigenvalue of the desired mode pair ($TE_{48,30}$, $TE_{55,34}$) lies in the flat region and the coaxial insert does not influence the diffractive quality factor of these modes. Whereas the diffractive quality factor of the competing modes ($TE_{m-3,p+1}$, $TE_{m-2,p+1}$) are reduced as the eigenvalue curves of the corresponding modes lie in the negative slope region. Thus the mode competition is effectively controlled by the corrugated insert for the both frequencies of operation. In the coaxial cavity, main competing modes are azimuthal neighbors ($TE_{m\pm1,p}$), which are least influenced by the coaxial insert.

After considering the trade-off between the output efficiency and ohmic wall loading, L_2 is selected as 12.5 mm. The normalized field amplitude profile for both operating frequencies along with the cavity geometry are presented in Figure 3.4. Once the initial dimensions of the cavity are fixed, mode competition calculations are performed for the desired mode pair. The electron beam radius calculated for the maximum coupling with the operating mode pair $TE_{48,30}$/$TE_{55,34}$ is 10.838/10.834 mm. The mode spectrum of

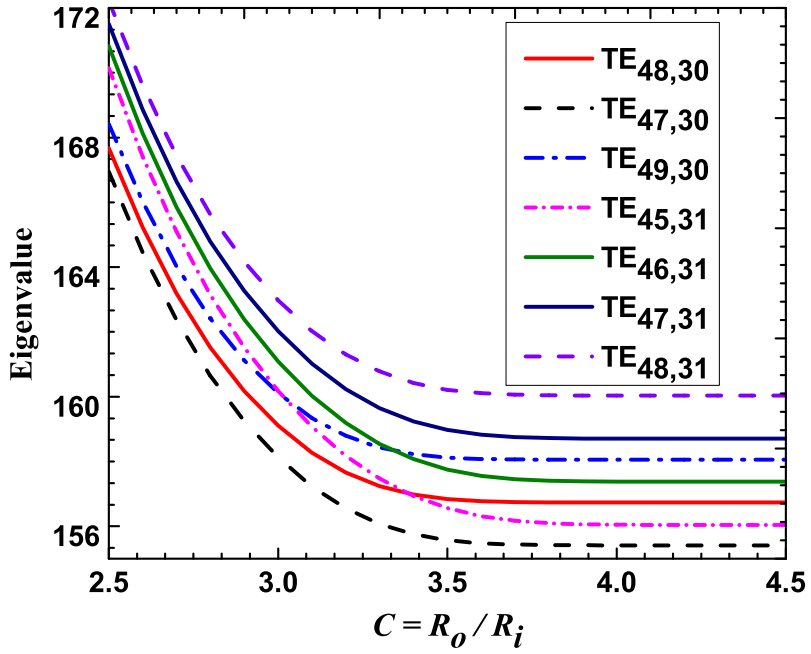

(a)

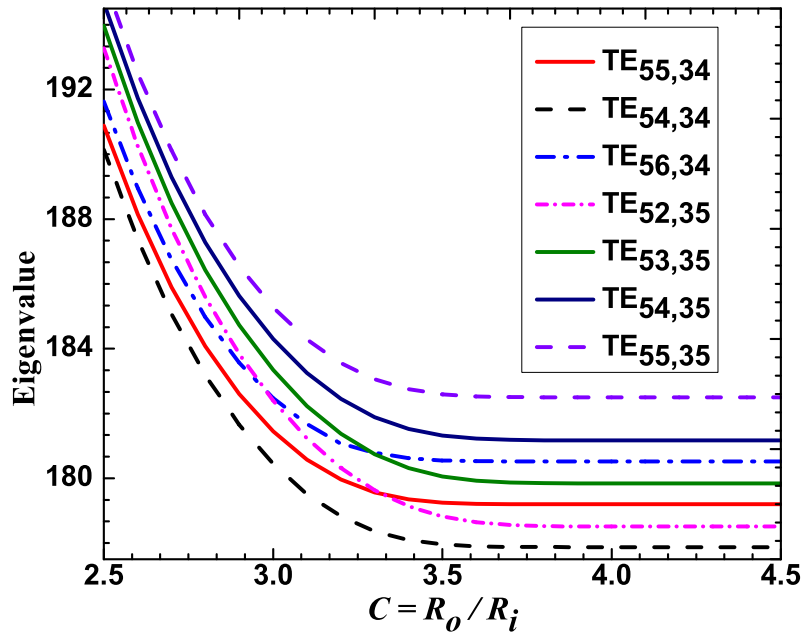

(b)

Figure 3.3: Eigenvalue curves for the desired mode (a) $TE_{48,30}$ at 220 GHz (b) $TE_{55,34}$ at 251.5 GHz, along with the competing modes (R_o=34.00 mm, R_d=0.5 mm, l/S=0.7, N=130) [176].

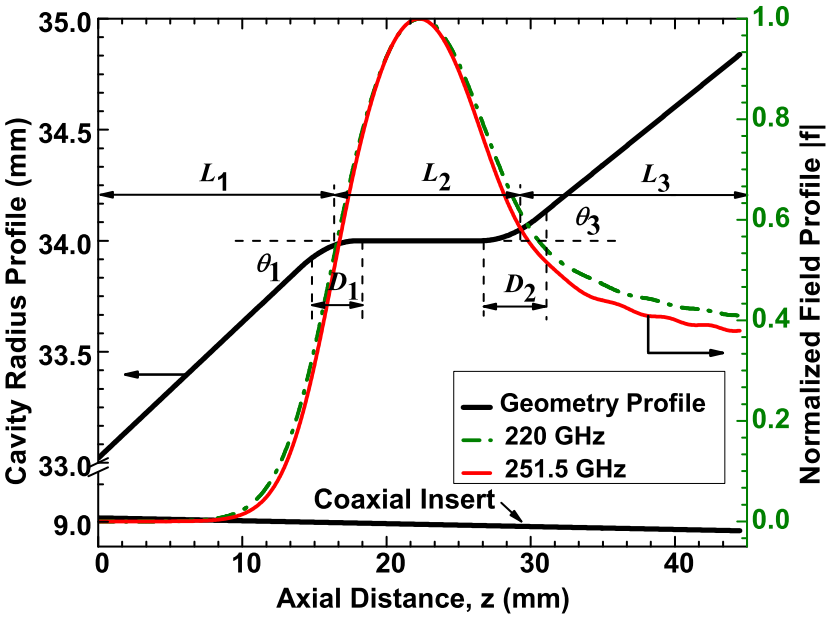

Figure 3.4: Normalized field amplitude along the cavity geometry [176].

the product of diffractive quality factor and the coupling coefficient ($Q_d * C.C$) for the frequency range of $\pm$5GHz around the operating frequencies are shown in Figures 3.5. In these calculations, modes with ($Q_d * C.C$) value greater than 50% of that of the main modes are only considered. The mode spectra are also plotted for the conventional hollow cavity in order to understand the effect of insert on the diffractive quality factor of the competing modes and are shown in the Figure 3.6. In the hollow cylindrical interaction cavity, the main competing modes are $TE_{m-3,p+1}$ and $TE_{m-2,p+1}$ (whose resonant frequencies lie close to that of the desired modes), whereas in the coaxial cavity due to the presence of the down tapered insert, competition from these modes are negligible as the diffractive quality factor of these modes get reduced. However, in the coaxial cavity as observed from the Figure 3.5 the main competing modes are the azimuthal neighbors ($TE_{m\pm1,p}$), $TE_{m,p+1}$ and $TE_{m-(3,2,1),p+1}$ and these modes are well separated from the desired modes.

After the mode competition calculations, single mode self-consistent computations are performed for the desired mode pair to calculate the output RF power and wall losses. The beam parameters and the peak magnetic field at the interaction are optimized for the maximum efficiency. For the calculation of wall losses, conductivity of the copper is taken as $\sigma = 1.4 \times 10^7$ S/m (instead of $\sigma_{Cu} = 5.7 \times 10^7$ S/m at room temperature) in order to include the effects of surface roughness and high operating temperature. In the

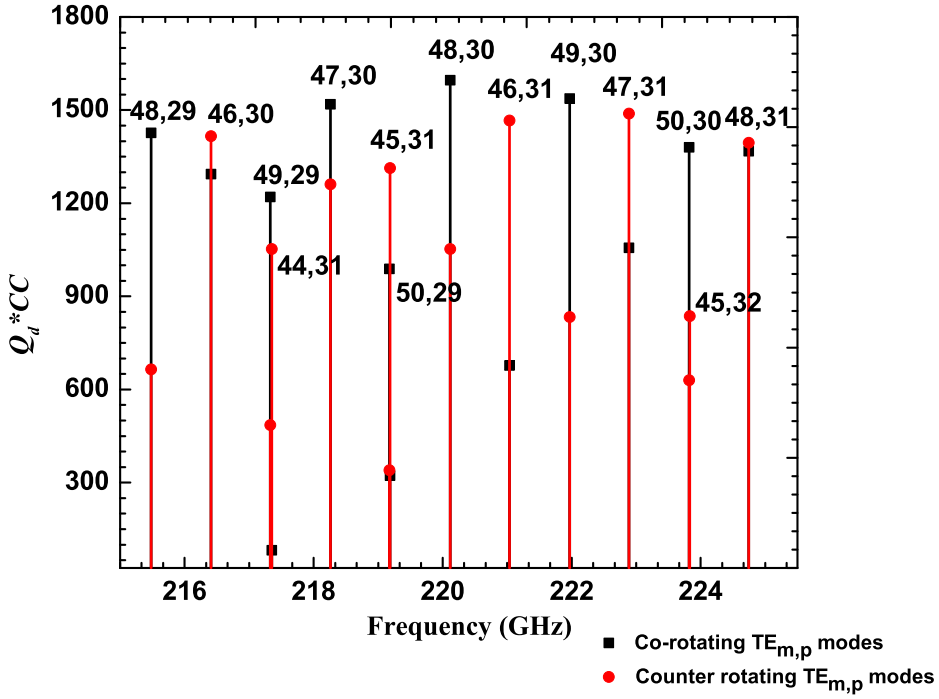

(a) 220 GHz operation

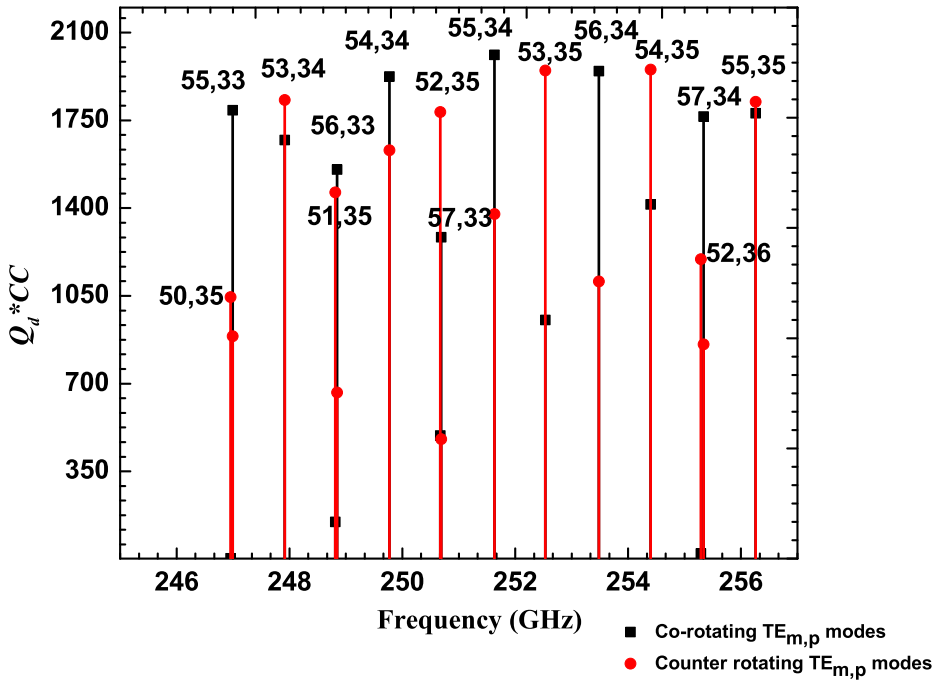

(b) 251.5 GHz operation

Figure 3.5: Mode spectrum of Q_d times coupling coefficient in the coaxial cavity for the desired mode of (a) $TE_{48,30}$ with R_b = 10.838 mm (b) $TE_{55,34}$ with $R_b = 10.834$ mm [176].

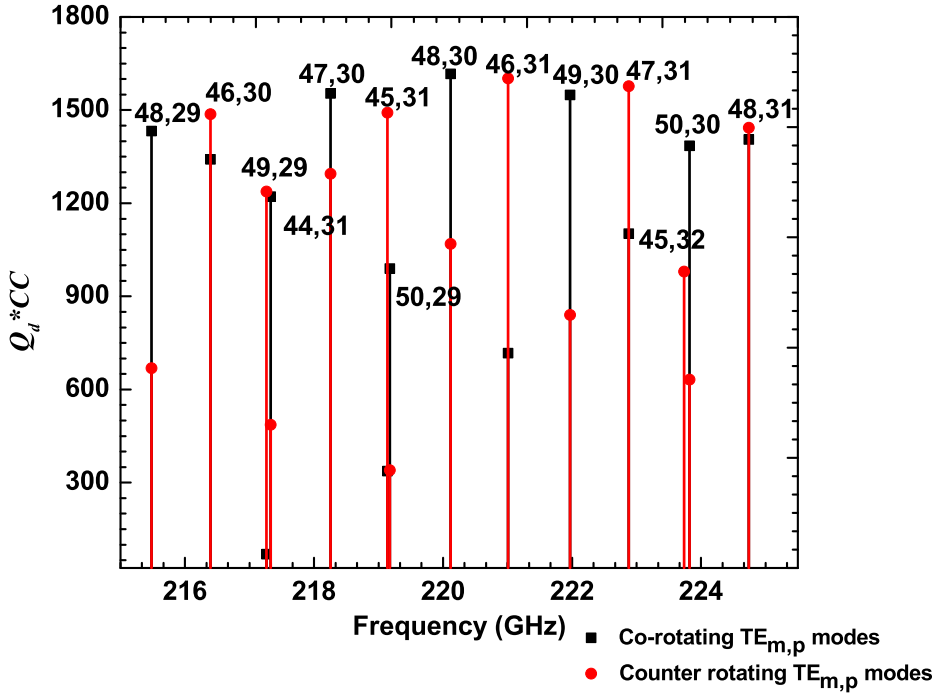

(a) 220 GHz operation

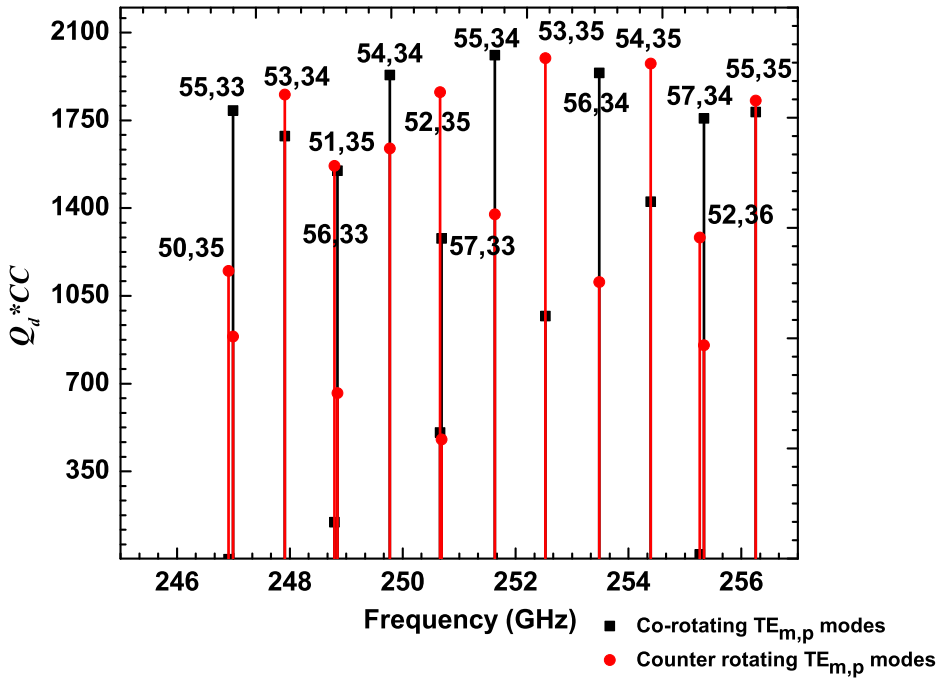

(b) 251.5 GHz operation

Figure 3.6: Mode spectrum of Q_d times coupling coefficient in the conventional hollow cavity for the desired mode of (a) $TE_{48,30}$ with R_b = 10.838 mm (b) $TE_{55,34}$ with R_b = 10.834 mm [176].

Table 3.3: Cavity dimensions and Single mode results [176].

Parameters	**220 GHz**	**251.5 GHz**
$L_1/L_2/L_3$ (mm)	16 / 12.5 / 16	16 / 12.5 / 16
$\theta_1/\theta_2/\theta_3(^\circ)$	3.5 / 0 / 3.0	3.5 / 0 / 3.0
D_1/D_2 (mm)	4.0 / 4.0	4.0 / 4.0
$R_o/R_i/R_b$ (mm)	34.00 / 8.95 / 10.838	34.00 / 8.95 / 10.834
f_r (GHz)	220.1175	251.6298
Q_d	1596.80	2011.89
V_b (kV)	87	85
I_b (A)	70	68
α	1.27	1.27
B_o (T)	8.872	10.100
η_{elec} incl. ohmic losses (%)	35.51	34.78
P_{out} (MW)	2.163	2.01
ρ_o (kW/cm^2)	1.75	1.91
ρ_i (kW/cm^2)	0.13	0.04
Total Power Loss (kW)	43.9	45.4
Q_{ohmic}	107208	116076
V_d (kV)	2.26	2.21
I_L (A)	430.80	418.09

triangular corrugated insert, the slot impedance becomes zero for second harmonic modes at the depth of 0.304 λ_o and maximum at the depth of 0.38 λ_o [163]. To minimize the wall losses on the insert for both operating frequencies, the depth of the slot is optimized to 0.5 mm. Single mode computation results along with the cavity geometry dimensions are presented in Table 3.3.

3.4 Time Dependent Multi-mode Simulations

Mode eigenvalues for the triangular corrugated coaxial cavity are obtained from GDS 2018 [176] and are used in the multi-mode calculations [93]. Time dependent simulations are performed for both frequencies for the time period of 3000 ns with the time step of 0.01 ns [93]. The beam voltage (V_b) increases linearly from (55-87 kV / 55-85 kV), whereas beam current (I_b), velocity ratio (α) and peak magnetic field at interaction (B_o) are kept constant (70 A, 1.27, 8.867 T)/(68 A, 1.27, 10.105 T) for the operation at 220/251.5 GHz. Simulations are performed for a number of 35 electrons with the longitudinal step size of 50 μm. Simulation results confirm that the RF power in the chosen modes reaches the desired power level of ≈2.0 MW and are shown in Figure 3.7 for both the desired frequencies.

Start-up behaviors of this dual regime coaxial gyrotron are carried out with the beam

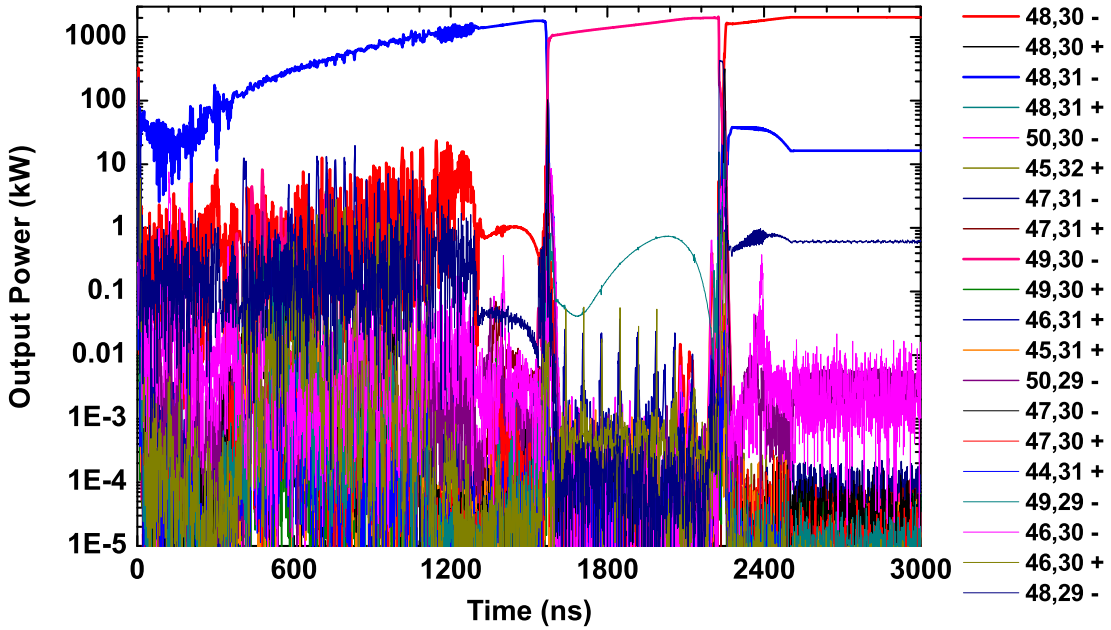

(a) 220 GHz Operation.

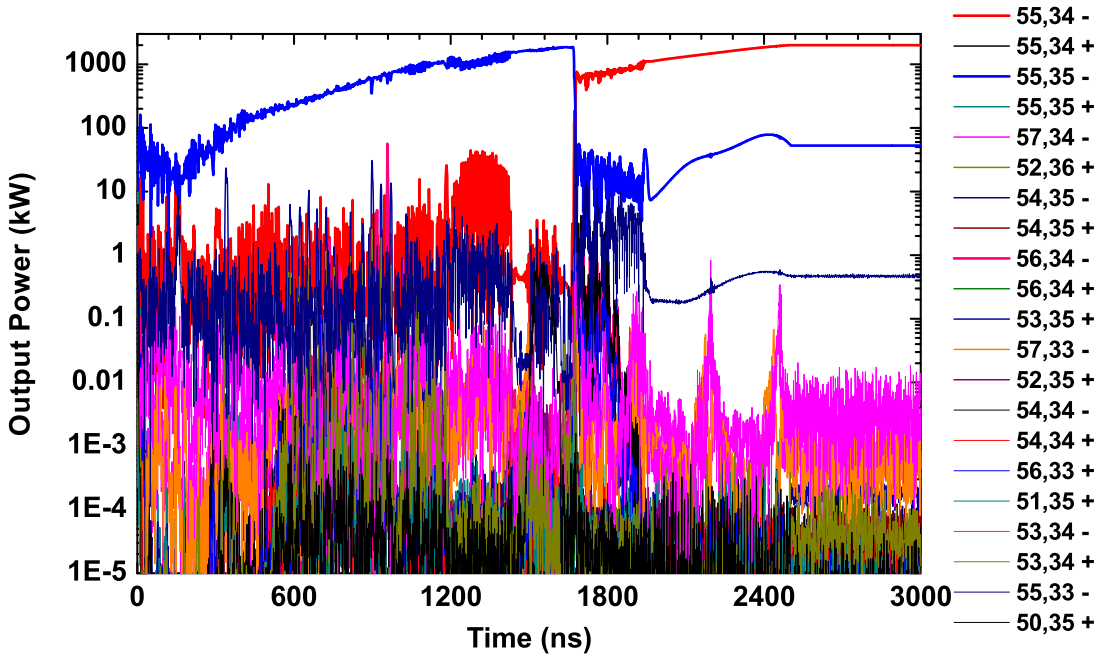

(b) 251 GHz Operation.

Figure 3.7: Time dependent calculations for the (a) $TE_{48,30,-}$ mode along with the competing modes with $V_b = 50\text{-}87$ kV, $B_o = 8.867$ T, $\alpha = 1.27$ and $I_b = 70$ A, (b) $TE_{55,34,-}$ mode along with the competing modes with $V_b = 50\text{-}85$ kV, $B_o = 10.105$ T, $\alpha = 1.27$ and $I_b = 68$ A. Logarithmic scale is used for the illustration of the output power, P_{out} (kW) [176], [93].

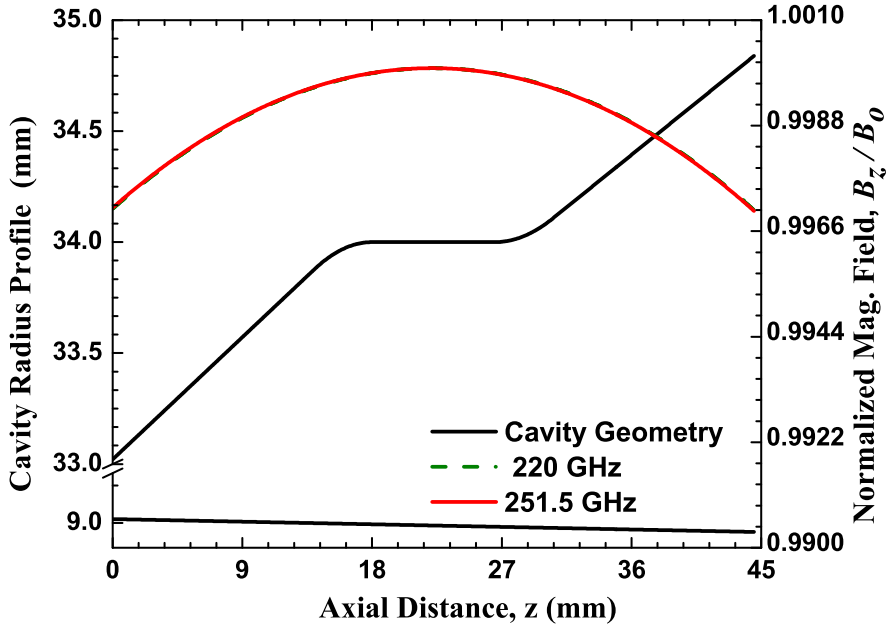

Figure 3.8: Normalized magnetic field along the interaction cavity [176].

space charge neutralization. For a more realistic assessments the simulations are carried out with the non-uniform magnetic field obtained from the magnetic guidance system design and is depicted in Figure 3.8. Start-up scenarios in the high power gyrotrons are explained in detail by Nusinovich [178], [179]. Start-up scenarios are mainly of two types: diode and triode type [180], [181]. Start-up scenario in the current study is of diode type, where the modulation anode voltage varies proportionally with the accelerating voltage.

During the start-up operation, due to the DC space charge fields, the beam voltage (V_b) is reduced by the voltage depression (V_d) [182], [183]. In the experimental operation of gyrotrons, the typical time required for the start-up analysis is around 50 μs. The coaxial insert reduces the voltage depression to $\approx$ 2 kV for megawatt class operation in the coaxial cavity gyrotron. In the long pulse operation, the electron beam interacts with the molecules of the residual gases in the interaction space and create ions. These ions partially neutralize (about 60-70%) the DC space charge and there by increasing the beam voltage (V_b) close to the applied accelerating voltage (V_{acc}) [184], [185]. During the neutralization process, the transverse momentum ($\gamma\beta_\perp$) of the beam remains adiabatically invariant and henceforth α decreases accordingly. Depending on the initial beam parameters and the background pressure, the typical time required for this neutralization process ranges between hundred milli seconds and few seconds [186].

The electron beam parameters used for the start-up behavior are obtained from ES-

RAY calculations [177] of the designed triode type coaxial MIG and are shown in Tables 3.4-3.7. Start-up calculations are carried out for both frequencies and the results for the complete space charge neutralization case are illustrated in Figures 3.9-3.10. In the present design studies ideal electron beam is considered, ignoring the effect of electron beam thickness and beam velocity spread. Effect of the misalignment of the coaxial insert on the RF behavior is also not considered in the present studies.

In the start-up analysis of the 220 GHz operation, V_b rises from 48.3 kV to 85.055 kV in the time period of 3000 ns and B_o is optimized to 8.867 T. Initially, the parasitic mode $TE_{48,31,-}$ oscillates until V_b reaches 68.75 kV, after that the main mode $TE_{48,30,-}$ starts to dominate and reaches the stable power level of 1770 kW. For the complete space charge neutralization case, V_b increases from 85.03 kV to 87 kV over the time interval of 3000 ns and the output power of the main mode increases to 1984 kW. However, in the partial space charge neutralization case (60%), V_b increases up to 86 kV and the main mode power is around 1937 kW. Although in the present start-up studies, the voltage rise time of 3000 ns is very fast compared to the typical experimental voltage rise time of 50 μs, the rise time of 3000 ns is enough to predict any possible excitation of the competing modes. Similarly, in the start-up behavior of 251.5 GHz operation B_o is optimized to 10.105 T. The high frequency competing mode $TE_{55,35,-}$ dominates until V_b reaches 69 kV, then the main mode $TE_{55,34,-}$ gets excited and grows to the stable power of 1794 kW. For the complete space charge neutralization case, the power in the main mode increases to 1986 kW, however for the partial space charge neutralization case (60%), it reaches only up to 1933 kW.

From the Figures 3.9-3.10, it is observed that in both the operating frequencies (220 GHz and 251.5 GHz), competing modes ($TE_{48,31-}$ and $TE_{55,35-}$) are radiating power of around 20 kW along with the desired operating modes ($TE_{48,30-}$ and $TE_{55,34-}$). These competing modes are resonating at 220.73 GHz and 252.21 GHz, respectively and they have relatively high coupling to the electron beam. These spurious modes can be identified as the backward waves in the downtaper section of the cavity. Parasitic backward waves can be suppressed by designing closed downtaper section, but this results in reducing the interaction efficiency of the operating mode. The occurrence of spurious backward waves can be understood as the first indication of maximum radiated power for the operating mode. Similar observations are also reported in [57], [169]. Design of downtaper in the high power coaxial cavity gyrotron is therefore a trade-off between maximum interaction efficiency of the desired operating mode and the sufficient suppression of the corresponding spurious oscillations [169]. The parasitic modes slightly reduce the interaction efficiency of the operating mode pair, but still the interaction efficiency of around 33% is obtained with both the operating frequencies. Mode competition studies with

Table 3.4: Electron beam parameters for the start-up behaviour of 220 GHz operation-before space charge neutralization [177].

V_{acc} (kV)	V_m (kV)	I_b (A)	V_b (kV)	α	$\beta_\perp$
87	40.0	70.0	85.055	1.2827	0.4059
80	36.5	69.0	78.162	1.1183	0.3709
73	32.5	68.5	71.191	1.0225	0.3424
66	28.5	67.5	64.187	0.9615	0.3178
58	26.0	65.5	56.245	0.8585	0.2817
50	24.5	64.5	48.300	0.6936	0.2315

Table 3.5: Electron beam parameters for 220 GHz operation - after complete space charge neutralization [177].

Scenario	V_b (kV)	I_b (A)	α	$\beta_\perp$
Before space charge neutralization	85.055	70	1.2827	0.4059
After space charge neutralization	87	70	1.2419	0.4045

fast rise time give different results on the excitation of the parasitic modes [187]. In the present start-up calculations by reducing the voltage rise time, RF power of the competing modes decrease. For the rise time of 50 ns, power in the competing modes reduce to less than 15 kW, however by further reducing the rise time cause the high frequency competing modes to dominate over the chosen mode pair. Effect of fast voltage rise time on the excitation of parasitic modes in megawatt class gyrotron were discussed in [183], [187].

Time dependent multi-mode calculations are also done for the hollow cavity interaction circuit with the same nominal beam parameters and the magnetic field to understand the effect of insert on the mode competition. The multi-mode calculations are performed for both frequencies with the V_b increases linearly from (50-85 kV/50-87 kV). From these calculations, it is observed that even for the hollow cylindrical cavity desired RF power is obtained in the chosen mode pair. This confirms that mode competition in the gyrotrons can even be controlled only by positioning the electron beam. However, due to the absence of the coaxial insert, voltage depression V_d of the electron beam in the hollow cavity increases to 14 kV and the limiting current is 104 A for the accelerating voltage of around 85 kV. Henceforth in the start-up calculations V_b is increased only up to 73 kV, and so the high frequency parasitic modes dominate over the growth of the desired mode pair. Thus in the megawatt class operations, main role of coaxial insert is to reduce the voltage depression along by reducing the mode competition.

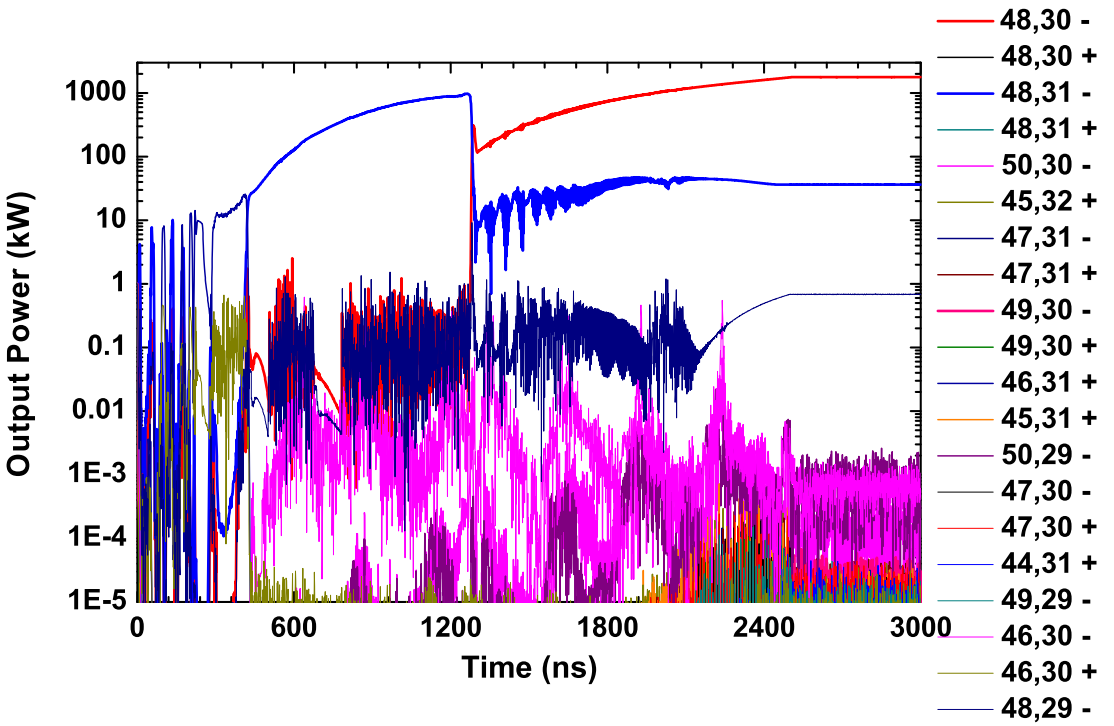

(a) before space charge neutralization.

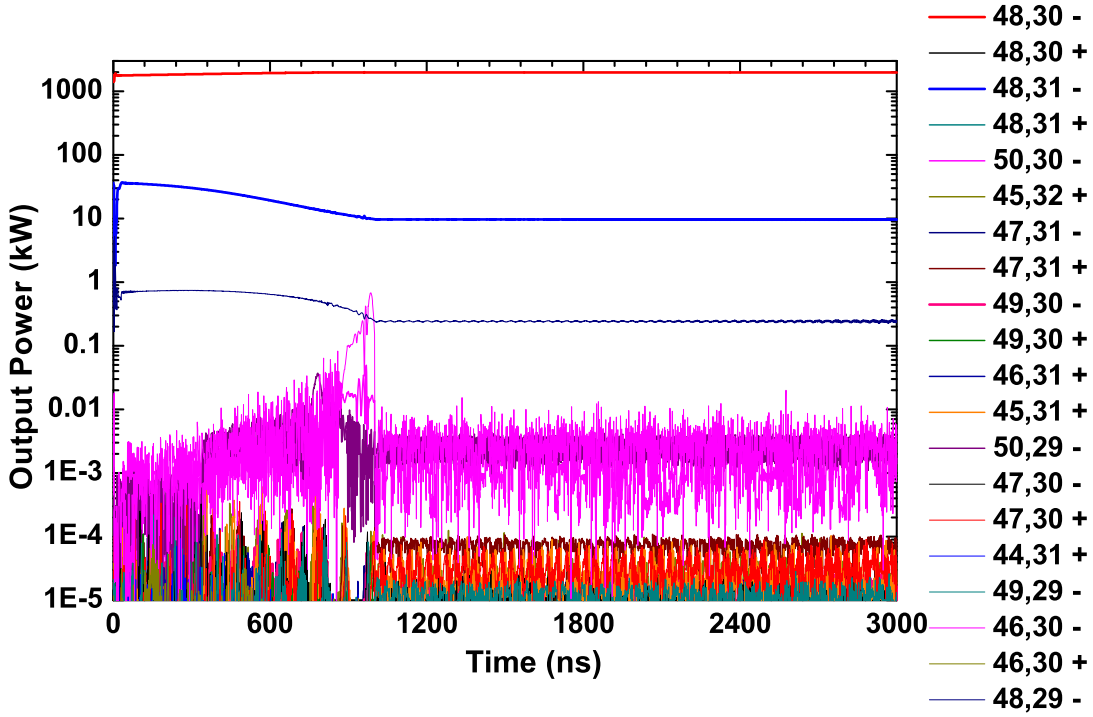

(b) after complete space charge neutralization.

Figure 3.9: Time dependent calculations for the $TE_{48,30,-}$ mode along with the competing modes with (a) $V_b = 48.300$-85.055 kV (b) 85.055-87 kV, $B_o = 8.867$ T, α and I_b vary accordingly. Logarithmic scale is used for the illustration of the output power, P_{out} (kW) [176], [93].

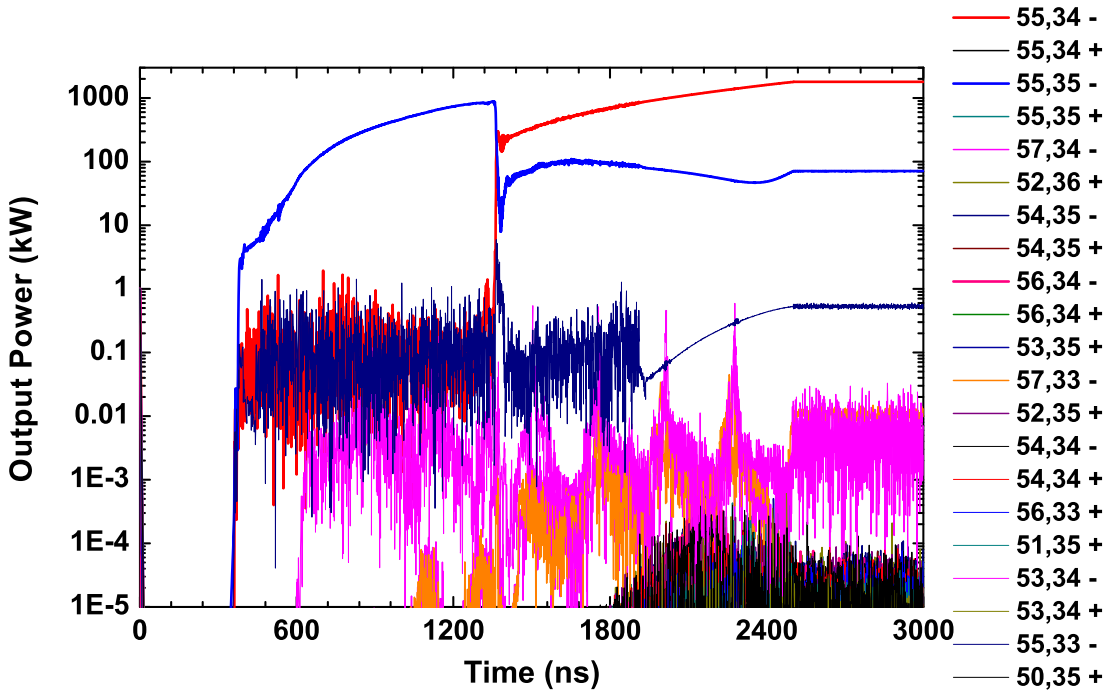

(a) before space charge neutralization.

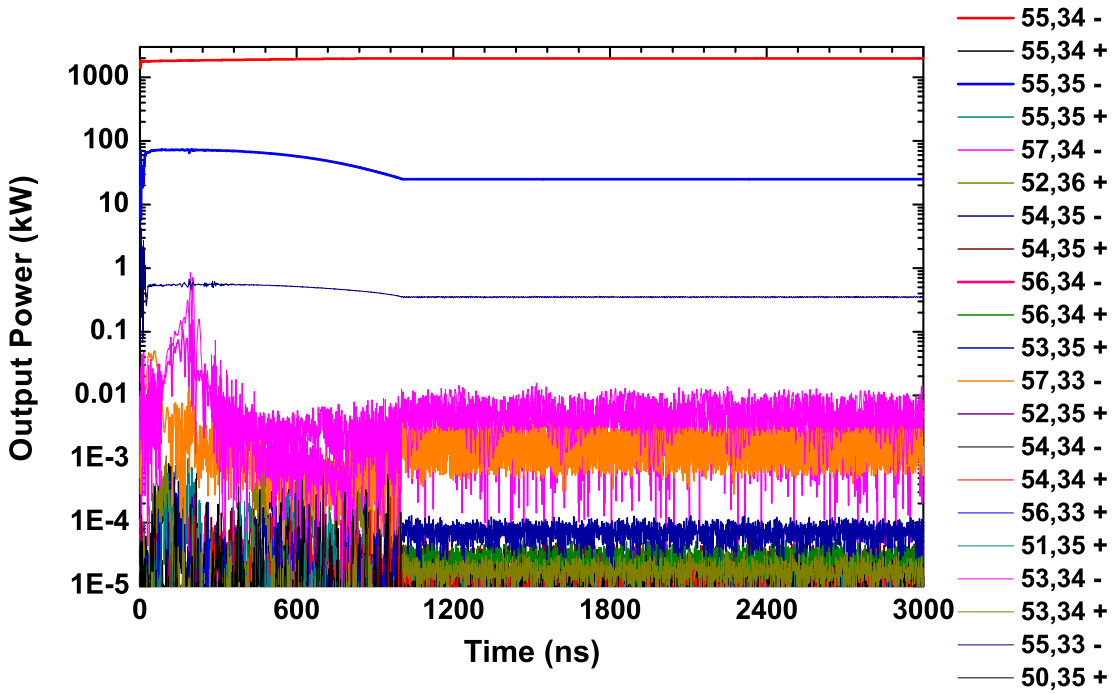

(b) after complete space charge neutralization.

Figure 3.10: Time dependent calculations for the $TE_{55,34,-}$ mode along with the competing modes with (a) $V_b = 48.466$-83.092 kV, (b) 83.092-85 kV, $B_o = 10.105$ T, α and I_b vary accordingly. Logarithmic scale is used for the illustration of the output power, P_{out} (kW) [176], [93].

Table 3.6: Electron beam parameters for the start-up behaviour of 251.5 GHz operation-before space charge neutralization [177].

V_{acc} (kV)	V_m (kV)	I_b (A)	V_b (kV)	α	$\beta_\perp$
85	31.00	68.00	83.092	1.2693	0.4005
78	28.50	66.00	76.200	1.1491	0.3709
71	27.80	65.00	69.307	1.0052	0.3348
64	27.60	63.80	62.404	0.8480	0.2930
57	25.10	63.00	55.427	0.7323	0.2578
50	24.10	62.00	48.466	0.5599	0.1988

Table 3.7: Electron beam parameters for 251.5 GHz operation - after complete space charge neutralization [177].

Scenario	V_b (kV)	I_b (A)	α	$\beta_\perp$
Before space charge neutralization	83.092	68	1.2693	0.4005
After space charge neutralization	85	68	1.2291	0.3992

3.5 Conclusions

In this chapter, the RF behavior of a 220/251.5 GHz, 2.0 MW, dual regime coaxial cavity gyrotron has been presented. The triangular corrugated insert helps in the mode rarefaction and also reduces the problem of localized heating. Based on the mode selection strategy of multi-frequency gyrotrons, the mode pair has been chosen as $TE_{48,30}$/$TE_{55,34}$. Mode competition calculations revealed that the operating mode pair is well separated from their parasitic modes. Cold cavity design, mode competition and self-consistent single mode computations have been performed with our in-house code GDS 2018. Single mode and the time dependent multi-mode calculations have predicted the RF power growth in the chosen modes. Start-up analyses have been carried out for both frequencies with realistic magnetic field profile before and after space charge neutralization using nominal electron beam parameters obtained from the MIG design calculations. These studies confirm that continuous wave power of ≈ 2 MW can be obtained at both frequencies with an interaction efficiency of 33%.

Chapter 4

Electron Gun and Output Coupling System for a Dual Frequency Coaxial Cavity Gyrotron

4.1 Introduction

The dual regime operation of gyrotron requires a common electron gun, RF interaction cavity and output coupling system to support both the operating frequencies. ECRH systems developed for the future commercially attractive reactors like DEMO are aimed to have improved current drive efficiency and therefore these systems require megawatt class of gyrotrons (1-2 MW) operating at higher frequencies ($\geq$ 200 GHz) [57]. Coaxial cavities can overcome the mode competition problem by introducing a corrugated insert. The presence of the insert in the coaxial cavity also reduces the voltage depression of the electron beam and hence the coaxial cavity gyrotron can operate at a higher beam current than that of the conventional cavity gyrotron [163]. Thus, coaxial cavity gyrotrons are preferred for the ECRH systems in future tokamaks. Short pulse operations of the coaxial cavity gyrotrons operating at 140 GHz, 165 GHz and 170 GHz have been carried out in KIT, Germany [156], [73], [55]. In addition to ECRH&CD applications, experimental tokamaks need RF beams at different frequencies for various other applications like plasma startup, plasma stability control, bulk heating, Collective Thomson Scattering (CTS) diagnosis etc. Therefore in order to cater for these multiple requirements, multi-frequency gyrotrons are being developed. A dual frequency gyrotron (105/140 GHz) is installed in the ECRH system of ASDEX-U (German Tokamax) [172]. The European 140 GHz gyrotron developed for W7-X strellerator can also be operated at additional frequency of 104 GHz [47]. The design of input and output system for a 77/154 GHz dual regime gyrotron has been reported in [188].

RF behavior of a dual regime 220/251.5 GHz, 2 MW, CW coaxial cavity gyrotron has been discussed in Chapter 3. This proposed dual regime gyrotron can be used for the ECRH applications in the future commercial fusion reactors. This chapter focuses on the design studies of a common electron gun, nonlinear taper (NLT), quasi-optical launcher (QOL) and RF window supporting the dual regime operation (220/251.5 GHz) of this proposed coaxial cavity gyrotron. A coaxial magnetron injection gun (MIG) is designed for the generation of hollow electron beam with the desired parameters. Initial geometry of the electron gun is determined through our in-house code Gyrotron Design Suite 2018 (GDS 2018). The MIG is further optimized and simulated through the beam trajectory code ESRAY. A NLT is designed with maximum transmission efficiency at both the operating frequencies. An advanced dimpled wall launcher is designed and numerically optimized through the commercial software, Launcher Optimization Tool (LOT) [189]. The designed launcher efficiently converts both the operating modes into Gaussian like mode. A single disk RF window is designed for the extraction of high power output beam from the gyrotron at their respective operating frequencies. Design of the NLT and the RF window are carried out through GDS 2018 [176].

4.2 Coaxial Magnetron Injection Gun

Magnetron injection guns are used to generate annular electron beams in gyrotrons. The electron beam emitted from the cathode is guided through the external magnetic flux lines. The designed MIG should guarantee the high quality electron beam required for efficient RF interaction [17]. In the dual regime operation of the proposed coaxial cavity gyrotron, the nominal beam parameters required for the generation of the desired output RF power are calculated through RF behavior analysis and are given in Table 4.1.

4.2.1 Initial Design Calculations

For dual frequency operation, the design of the MIG is crucial as the same electron gun is used to generate the desired beam parameters for both the operating frequencies. The

Table 4.1: Nominal Beam Parameters [190]

Frequency	220 GHz	251.5 GHz
Accelerating Voltage (V_{acc})	87 kV	85 kV
Beam Current (I_b)	70 A	68 A
Electron Velocity Ratio (α)	1.28	1.27
Magnetic Field at Cavity Center (B_o)	8.867 T	10.105 T
Electron Beam Radius (R_b)	10.838 mm	10.834 mm

desired mode pair ($TE_{48,30}$ /$TE_{55,34}$) is selected such that the electron beam radius should approximately be the same for both the frequencies (220/251.5 GHz). For the maximum coupling of the electron beam with the RF wave, the electron beam radius is determined as 10.838/10.834 mm for 220/251.5 GHz operations.

A triode type MIG is designed for generating the hollow electron beam with desired parameters. The triode type electron gun is preferred over the diode type as the beam parameters can be effectively tuned for the dual frequency operation in a triode gun. Time dependent multi-mode calculations estimate the maximum magnetic field at the interaction and nominal beam parameters like accelerating voltage, beam current and velocity ratio, required for the desired output power. By using these nominal parameters, Baird calculations are carried out and the initial dimensions of the electron gun like emitter radius, anode radius, cathode modulating anode spacing and emitter slant length are determined [191]. Baird calculations are performed through GDS 2018 [176].

4.2.2 Electron Beam Requirements and Technical Constraints

The quality of the electron beam generated by the MIG is determined by the spread in the electron velocity ratio ($\Delta\alpha$) and the spread in the electron beam radius (ΔR_b). $\Delta\alpha$ should be less than 5%, otherwise this results in increased mode competition and affects the RF power growth in the desired mode. For the efficient transfer of energy from the electron beam to the electromagnetic wave, ΔR_b should not exceed $\lambda/8$ [84]. For the reliable operation of the MIG, empirical relation on the maximum allowable electric field (E_{max}) inside the MIG is given by $E_{max}.V_d \leq 800\,\mathrm{kV^2/mm}$, where, V_d is the potential drop across the electrodes [84].

In the high power operation, E_{max} is limited to a lower value. As a consequence, distance between the electrodes should be increased and overall diameter of the MIG is increased. In a triode type MIG, the voltage drop between the cathode and the modulating anode is less than half of the accelerating voltage. As a result, technical limit on E_{max} is increased and a reduced diameter for the MIG is possible. Hence, a triode type MIG is preferred over a diode type MIG as it gives the scope for a more compact design. Performance of the MIG is determined by the maximum current density at the emitter surface (J_e). A higher value of J_e results in the degradation of the life time of the MIG, while a lower value leads to the increase of the transverse electron velocity spread. In the case of modern emitters, emitter current density of $5\,\mathrm{A/cm^2}$ ensures much better life time of operation [17], [192]. J_e can be reduced either by increasing the axial length of the emitter, resulting in the increase of $\Delta\alpha$ or by increasing the emitter radius leading to the increase of the overall MIG diameter. An important design goal of the MIG is to keep the electron gun as compact as possible in order to reduce the construction costs. Hence

in the design process, a trade off should be maintained between the compactness of the electron gun and the electron beam quality. In addition to these design constraints, the MIG should be designed such that the electron trapping mechanisms like the potential wells and the magnetic mirror effects are avoided.

4.2.3 Magnetic Guidance System

Generally in gyrotrons, solenoids (normal conducting and super conducting coils) are used for providing the necessary magnetic field [193]. In the dual frequency operation, the magnetic field at the cavity center and the nominal beam parameters are obtained by tuning the currents in the magnetic coils. According to the paraxial approximation, the electron beam radius (R_b) is related to the cathode radius ($R_{cathode}$) by

$$R_{cathode} = \sqrt{b}\, R_b \tag{4.1}$$

where, b is the compression ratio ($= B_o/B_{gun}$), B_o is the magnetic field at the center of the interaction cavity and B_{gun} is the magnetic field at the emitter position. The magnetic field increases adiabatically from the emitter region and reaches the maximum at the interaction cavity. As per the adiabatic theory of motion of electrons, magnetic momentum is conserved and transverse momentum of the electrons increases with the magnetic field. Thus, the electron beam properties like velocity ratio, electron beam radius are strongly determined by the magnetic field profile.

After considering the length of the beam tunnel and the complete interaction cavity, the distance between the cathode and the cavity center is fixed as 430 mm. In the present design, five solenoid coils are used to produce the required magnetic field profile. Two main coils are located around the interaction cavity (coils center at 480 mm) for the generation of a constant magnetic field. One compensation coil (coil centers at 165 mm) is aligned between the emitter and the cavity region to reduce the magnetic field along the cathode region. Two gun coils are located around the emitter region (coils center at 50 mm and 2.5 mm) for the effective optimization of the field at the emitter point. Information about the magnetic coils are given in Table 4.2 and the generated magnetic field profiles along the axial length are shown in Figure 4.1. Position of the magnetic coils along the MIG geometry is shown in Figure 4.2. For the present dual regime operation, required magnetic field at the interaction cavity are 8.867 T and 10.105 T for 220 GHz and 251.5 GHz, respectively.

Table 4.2: Optimized Coil Data [176], [177]

Coils	Length ΔZ (mm)	Breadth ΔR (mm)	Coil radius (mm)	No. of turns N_C	Current 220 GHz (A)	Current 251.5 GHz (A)
Main Coil –1	440.00	30.00	120.00	24990	119.87	136.59
Main Coil –2	440.00	15.00	142.50	4930	119.87	136.59
Compensating Coil	70.00	45.0	147.50	2880	-63.5	-71.0
Gun Coil – 1	65.00	25.0	137.50	645	7.5	5.45
Gun Coil –2	20.00	25.00	137.50	610	3.0	3.5

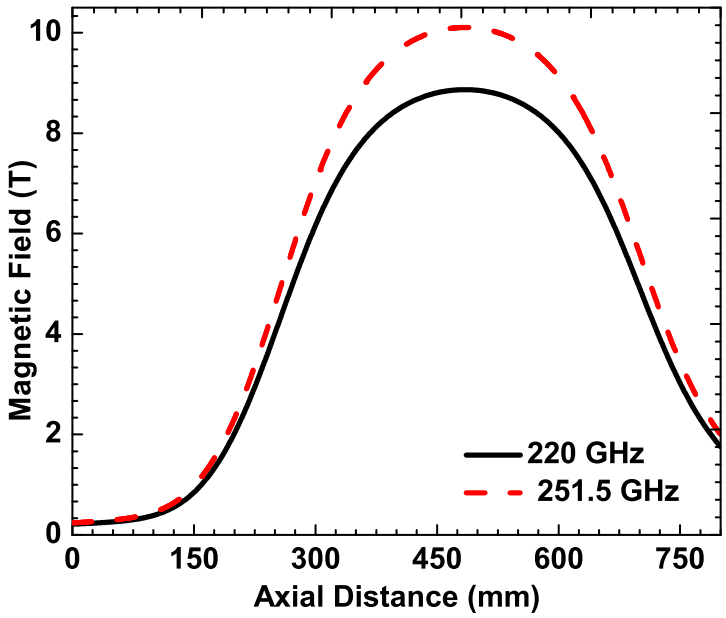

Figure 4.1: Magnetic field profile along the axial length of the gyrotron. Here, emitter position is at z = 50 mm and center of the interaction cavity is at z = 480 mm [176], [177].

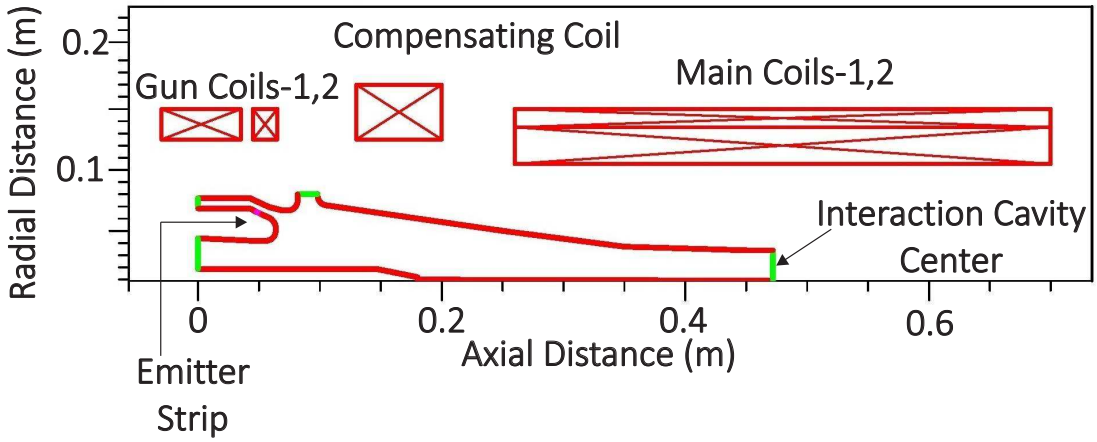

Figure 4.2: Position of the magnetic coils along the MIG geometry [176], [177].

4.2.4 Optimized Gun Design

The triode type coaxial MIG geometry is optimized and simulated using the particle trajectory code ESRAY [177]. The geometry of the electron gun is optimized such that the electron velocity ratio spread ($\Delta\alpha$) and the beam radius spread (ΔR_b) are minimized for both the operating frequencies. Cathode radius is fixed as 64.60 mm. Figure 4.3 shows the variation of $\Delta\alpha$ and ΔR_b as a function of the axial length of the emitter (l_e) and the emitter slant angle (Φ_e). In these calculations, velocity ratio (α) is kept constant by varying the modulating anode voltage, thereby maintaining a constant electric field around the emitter region. Considering the trade-off between the velocity spread and the life time of the emitter, l_e is fixed as 4.40 mm. Φ_e is optimized as 25 $^\circ$ so as to support the quasi laminar flow of the electron beam.

Another important parameter is the cathode to modulating anode gap (d_m). The electric field around the emitter region (E_c) is determined by d_m. α and the spread in α are strongly dependent on E_c. Figure 4.4 shows α and $\Delta\alpha$ for varying d_m. As the modulating anode voltage is less than the half of the accelerating voltage, maximum allowable electric field in the gun region is high in the case of a triode type MIG. d_m is optimized as 8.45 mm and the maximum electric field around the emitter region is 6.0 kV/mm. The optimized design parameters and the simulation results of the triode type coaxial MIG are given in Table 4.3. Electron beam trajectories are calculated for both the operating frequencies in the designed MIG and are shown in Figure 4.5.

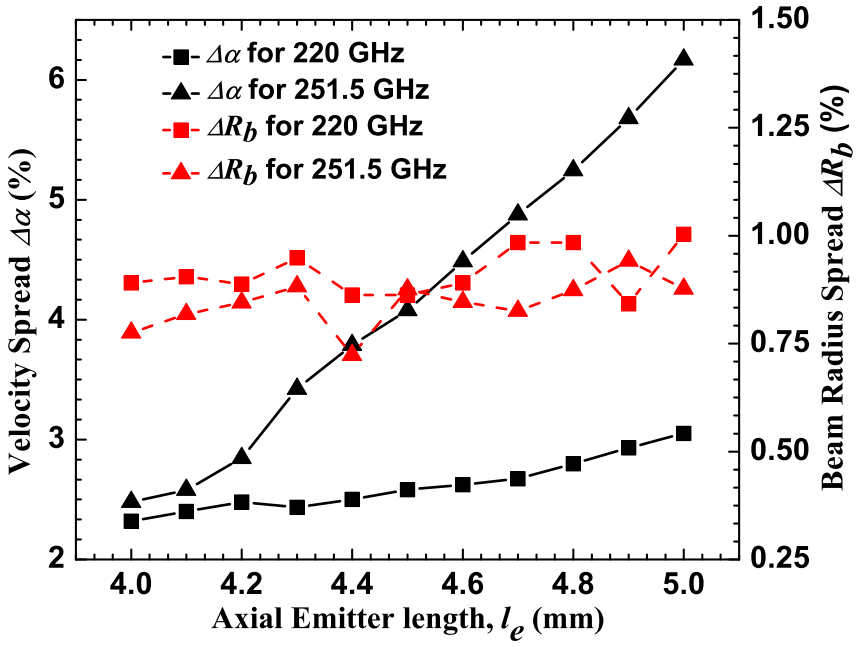

(a)

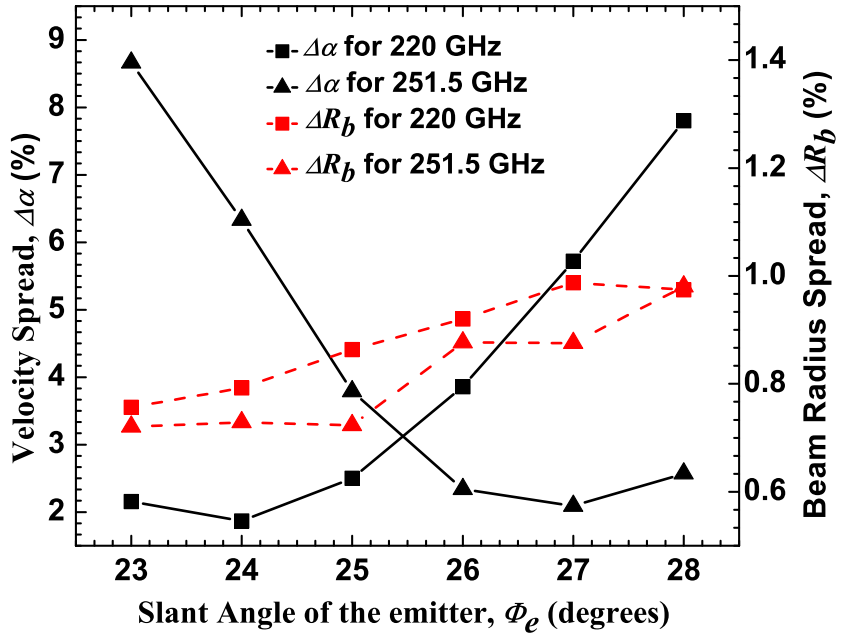

(b)

Figure 4.3: $\Delta\alpha$ and ΔR_b as a function of (a) axial emitter length (mm), (b) emitter slant angle (°), α is kept constant at 1.28/1.27 for 220/251.5 GHz. Other parameters are same as given in Table 4.3 [177].

Table 4.3: Design Parameters and Simulation Results of the Triode Type Coaxial MIG [177]

Parameters		
Frequency	220 GHz	251.5 GHz
Beam current	70 A	68 A
Accelerating voltage	87 kV	85 kV
Mod. anode voltage	40 kV	31.0 kV
Emitter current density	3.8 A/cm^2	3.8 A/cm^2
Cathode radius	64.60 mm	64.60 mm
Cathode angle	25°	25°
Mod. anode angle	25°	25°
Axial width of the emitter	4.4 mm	4.4 mm
Cathode-mod. anode spacing	8.45 mm	8.45 mm
Anode radius	71 mm	71 mm
Results		
Magnetic field at the emitter	0.21433 T	0.2405 T
Compression ratio	41.3708	42.0166
Electric field at cathode	5.9 kV/mm	6.29 kV/mm
Velocity ratio	1.28	1.27
Velocity spread (%)	2.5	3.8
Beam radius (interaction)	10.838 mm	10.834 mm

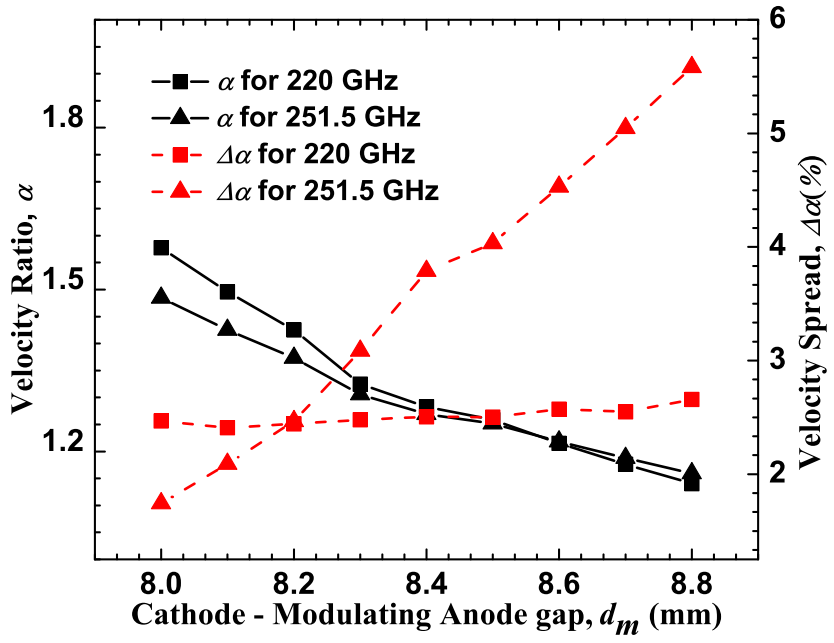

Figure 4.4: α and $\Delta\alpha$ as a function of cathode - modulation anode gap (mm), with other parameters are same as given in Table 4.3 [177].

4.2.5 Parametric Studies on the Designed MIG

Parametric studies are performed on the designed electron gun by varying the accelerating voltage (V_{acc}) and the beam current (I_b). Figure 4.6 shows α and $\Delta\alpha$ for varying V_{acc} and I_b. From Figure 4.6(a), it is understood that there is a linear rise in α with V_{acc} thereby satisfying the adiabatic theory. In order to study the effect of space charges on the electron beam properties, I_b is reduced from its nominal value. When I_b tends to zero, the electric field around the emitter is determined only by the shape of the electrodes and the effect of the local electric field (due to the beam charges) becomes negligible [84]. From Figure 4.6(b), it is observed that α increases slightly for the lower values of I_b and this can be adjusted to the nominal value by varying the modulating anode voltage. Thus the effect of the space charges on the beam properties of the designed triode type MIG is negligible.

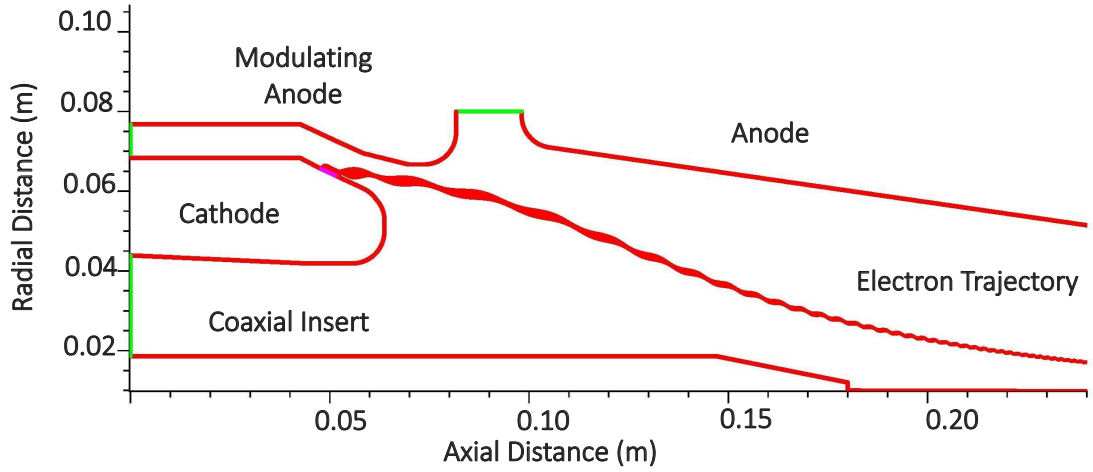

(a)

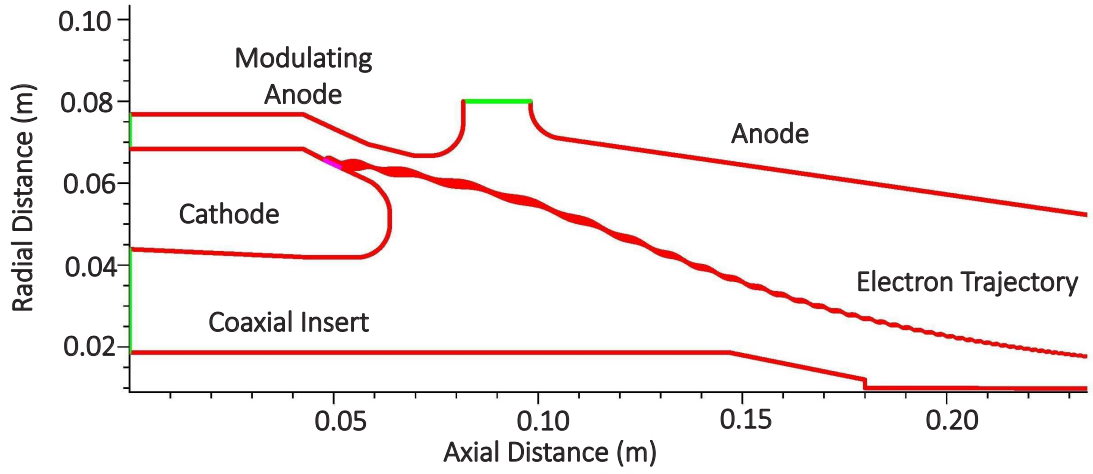

(b)

Figure 4.5: Electron beam trajectory for the operation at (a) 220 GHz, (b) 251.5 GHz [177].

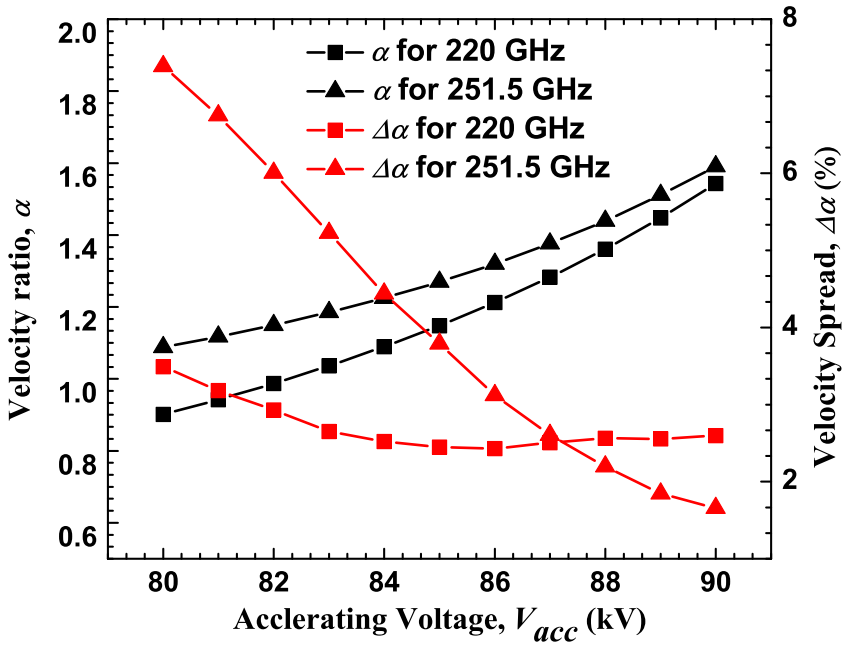

(a)

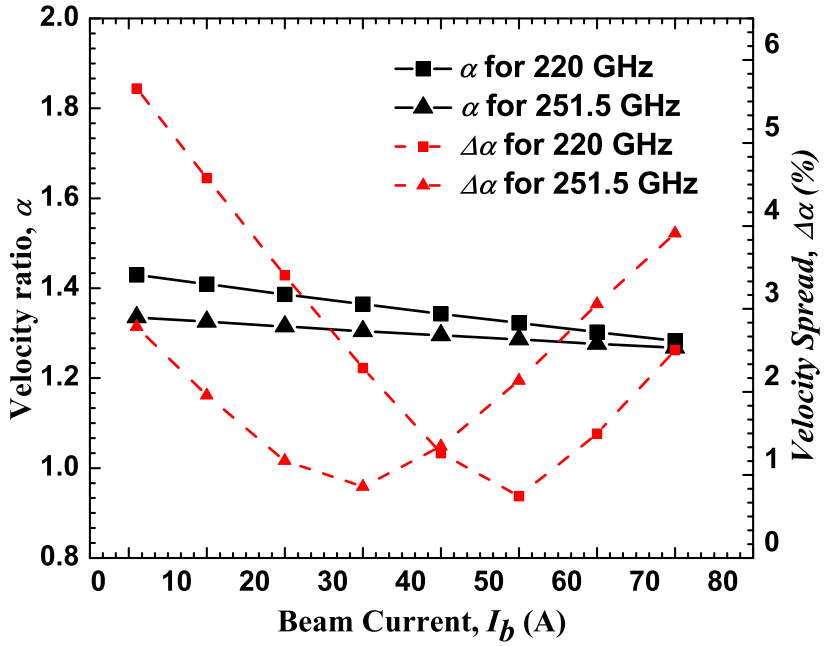

(b)

Figure 4.6: Variation of α and $\Delta\alpha$ with (a) accelerating voltage (kV), (b) beam current (A), with other parameters are same as given in Table 4.3 [177].

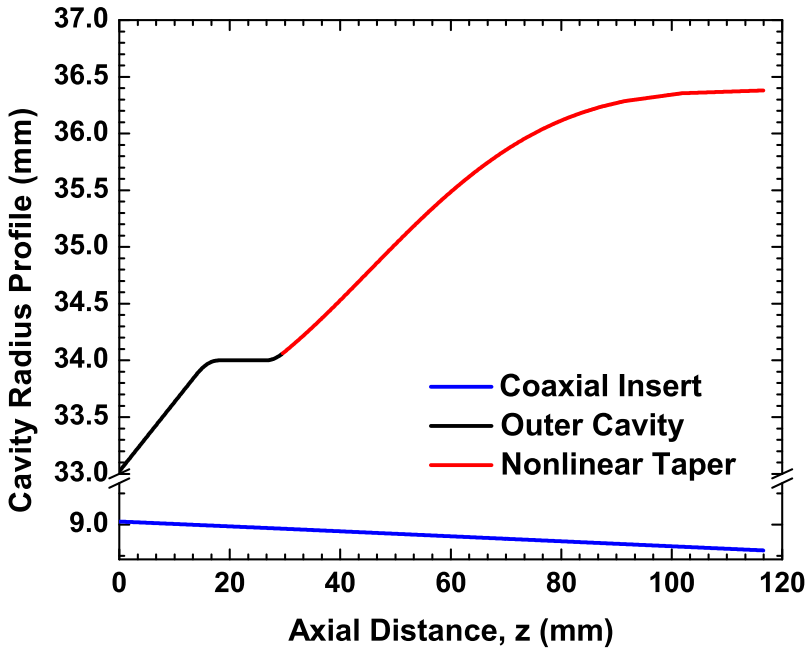

Figure 4.7: The interaction circuit geometry with the optimized NLT. Here, the mid-section radius, R_o is 34 mm and the output radius of the NLT is 36.38 mm (1.07 times R_o) [176].

4.3 Nonlinear Taper

The output system of a gyrotron consists of a NLT, a quasi-optical launcher (QOL), an internal mirror system and a RF output window. The NLT is required to support the transmission of the RF wave from the interaction cavity towards the QOL. The insert in the coaxial cavity is down tapered and is extended up to the output end of the NLT. The designed NLT should have very high transmission efficiency for the operating modes and should avoid any mode conversion. A raised cosine NLT is designed with the output radius of 36.38 mm (1.07 times mid-section radius), which is same as the input radius of the QOL. Length of the NLT is optimized using a particle swarm optimization technique and the overall length of the NLT is 88.10 mm. The interaction cavity consists of a input down taper, a straight mid-section and the NLT. Length of the input taper and the mid-section are 16 mm and 12.5 mm, respectively. Tapers are connected to the straight mid-section through the parabolic rounding in order to avoid unwanted mode conversion. The transmission efficiency of the designed NLT is greater than 99.20% for both the operating modes at their respective frequencies. Design of the NLT is carried out using GDS 2018. The geometry of the interaction cavity along with the optimized NLT is presented in Figure 4.7.

Table 4.4: Launcher design and LOT simulation results [189]

Launcher length (mm)	325.0
Helical cut length (mm)	45.0
Waveguide radius (mm)	36.38
Taper angle (Rad.)	0.002
Gaussian content factor (GCF)	95.86% (for 220 GHz) 96.31 % (for 251.5 GHz)

4.4 Quasi-Optical Launcher

A quasi-optical launcher is used to convert the higher order cavity mode into the linearly polarized Gaussian like mode TEM_{00}. For the dual regime operation, the desired mode pair is selected such that the relative caustic radius ($m/\chi_{m,p}$) of the modes are approximately the same (0.306/0.307 for $TE_{48,30}$/$TE_{55,34}$) so that a common QOL can be used [194]. The QOL is designed such that Gaussian content of the output beam should be high and the stray radiation losses should be minimum. In the present design $m/\chi_{m,p}$ value of the operating mode pair is around 0.3 and hence these modes cannot form a closed polygon in the ray representation. Synthesis of the launcher supporting these modes is quite challenging as it is difficult to obtain the output beam with high Gaussian content and minimum stray radiation losses. In such a case, a QOL with higher order perturbations included in the wall surface deformation can provide the outgoing wave beam with high Gaussian content [116]. The fields inside the launcher are greatly influenced by the oversize factor. In the present design, radius of the launcher is optimized to 36.38 mm with the oversize factor of 1.07 and higher order perturbations are included in the wall surface deformations. The designed launcher is tapered with 0.002 radians and has cut length of 45.00 mm. Launcher length is increased to 325.00 mm, so as to achieve the output beam with high Gaussian content in both the frequencies of operation. In general, while designing the QOL for the higher order modes operating at very high frequencies, a trade-off should be maintained between the Gaussian content of the outgoing wave beam and the compactness of the launcher. The launcher is designed and numerically optimized through the commercial software, Launcher Optimization Tool (LOT).

Figure 4.8 shows the field intensities on the launcher wall for 220 GHz and 251.5 GHz operation. From the field intensity plots, it is observed that the output beams coming out of the launcher cut are down converted to the Gaussian like TEM mode and the field intensities near the cut edges (represented by the white color dotted line) are less than -30 dB for both the operating frequencies thereby minimizing the diffraction losses. Figure 4.9 shows the aperture field intensities for the chosen cavity mode pair at their respective frequencies. The aperture is considered as a rectangular area bounded by the launcher axis,

launcher radius and the axial cut length. From the Figure 4.9, it can be observed that field intensities are symmetric about the wave beam centroid and the side lobes are negligible. Figure 4.10 shows the far field intensities calculated for both cavity modes using the far field approximation ($> 2D^2/\lambda$) and are essentially the same field on the sphere of infinite radius.

Figure 4.11 shows the field intensities in a plane of the launcher cut (i.e. at a distance of 36.38 mm from the gyrotron axis) and in the plane of the possible location of the first mirror (i.e. at a distance of 80 mm from the gyrotron axis). From Figure 4.11, it is understood that the wave beam positions are nearly same for both the operating frequencies and hence a common internal mirror system can be used for further phase corrections. The Gaussian content of the wave beam coming out of the launcher cut are 95.86% and 96.31% for 220 GHz and 251.5 GHz, respectively and this can further be improved by using the phase correcting mirror system. Tolerance limit on the wall perturbations of the designed launcher is $\pm$ 0.01 mm for maintaining the conversion coefficient of greater 90% in both the operating frequencies.

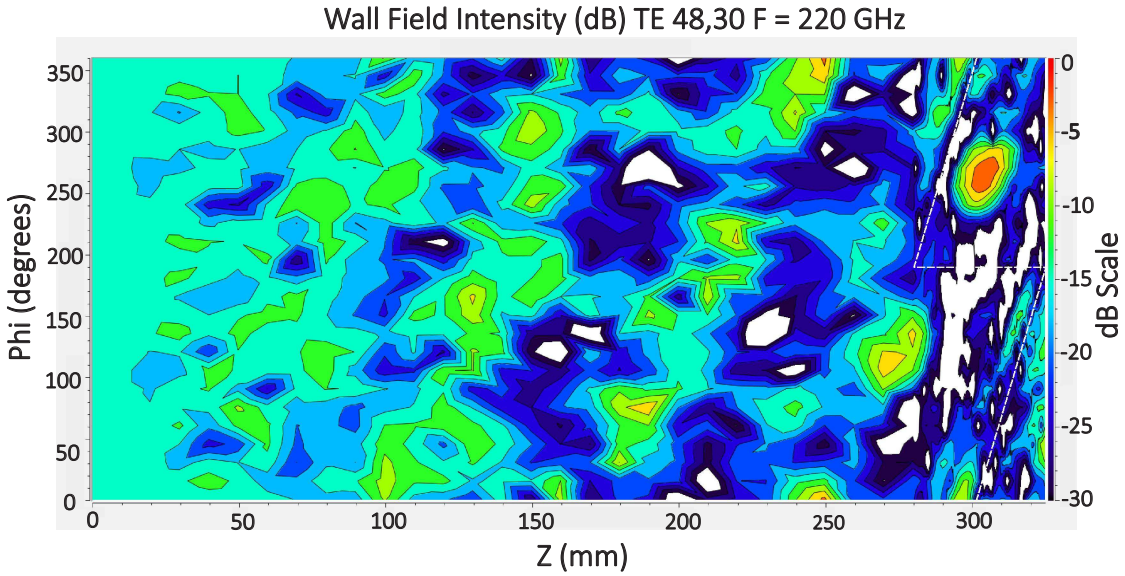

(a) $TE_{48,30}$ mode at 220 GHz

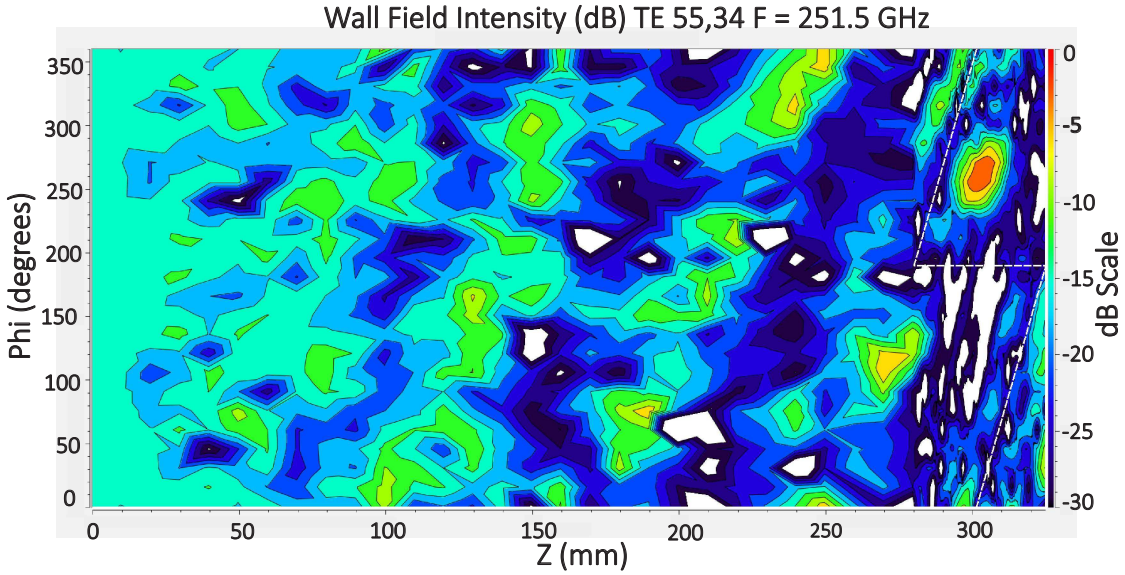

(b) $TE_{55,34}$ mode at 251.5 GHz

Figure 4.8: Field intensity on the unrolled launcher wall [189].

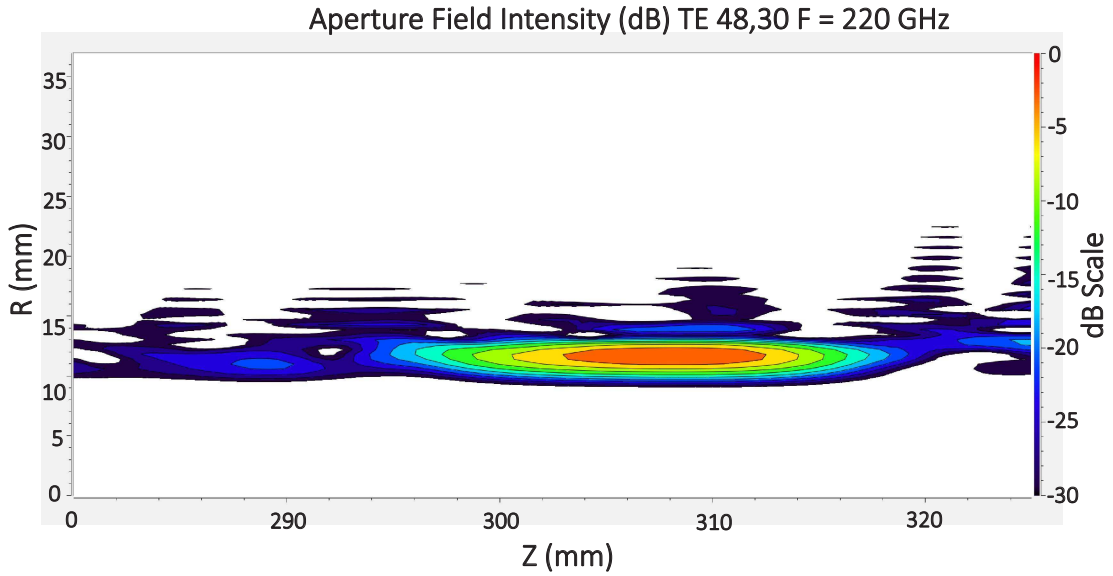

(a)

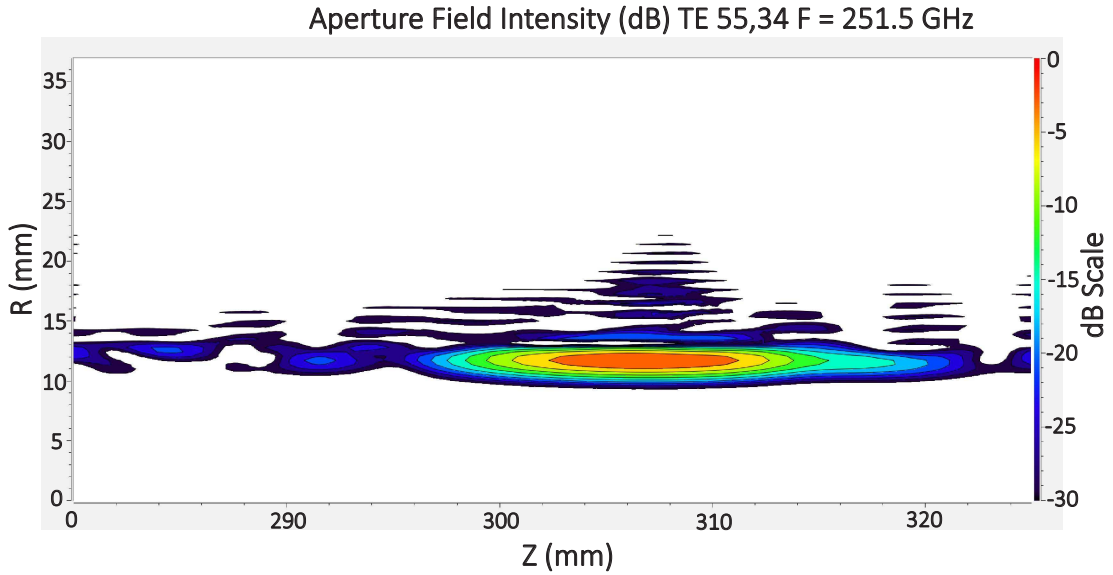

(b)

Figure 4.9: Aperture field intensity for (a) $TE_{48,30}$ mode at 220 GHz, (b) $TE_{55,34}$ mode at 251.5 GHz [189].

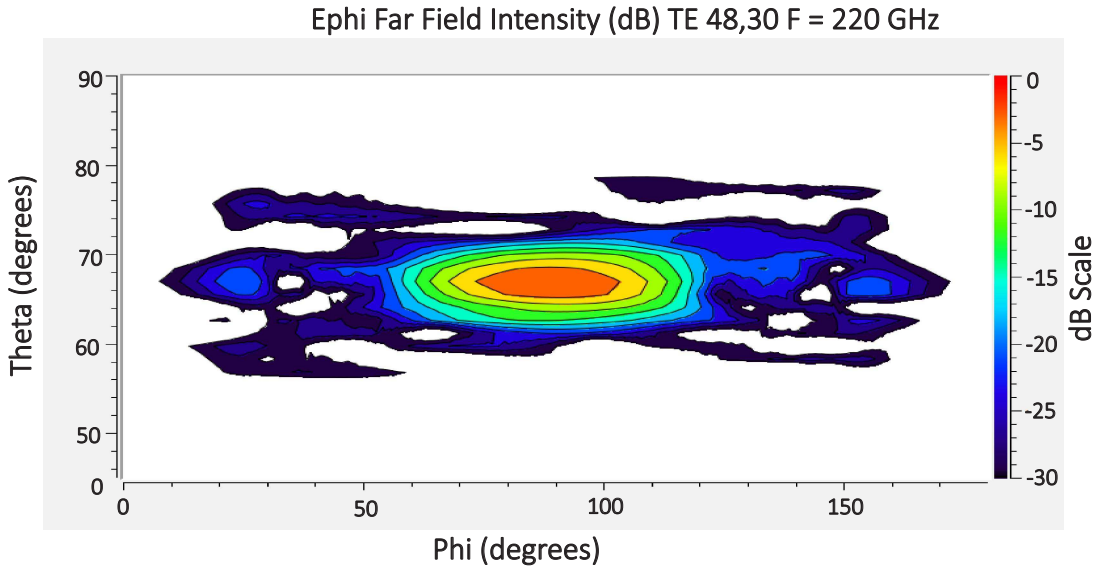

(a)

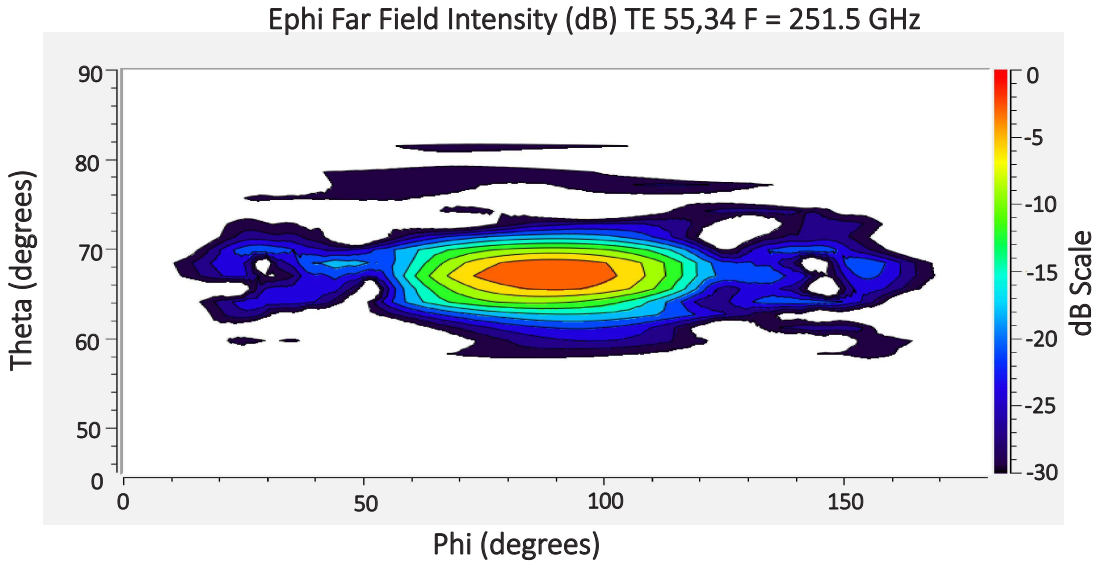

(b)

Figure 4.10: Far field intensity for (a) $TE_{48,30}$ mode at 220 GHz, (b) $TE_{55,34}$ mode at 251.5 GHz [189].

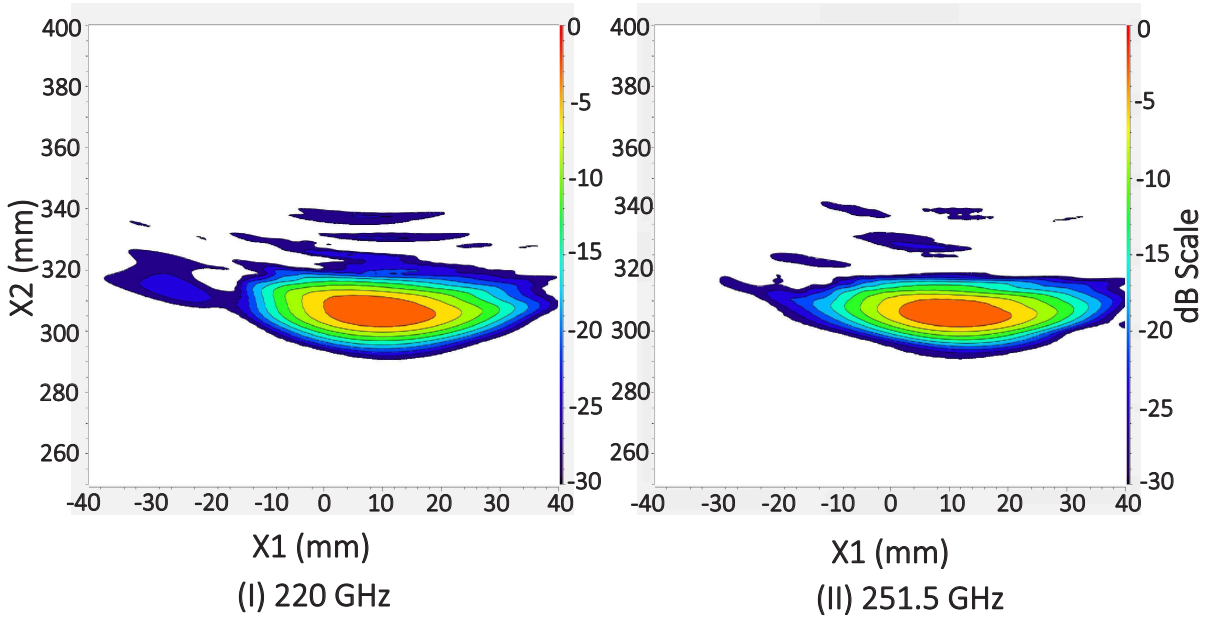

(a)

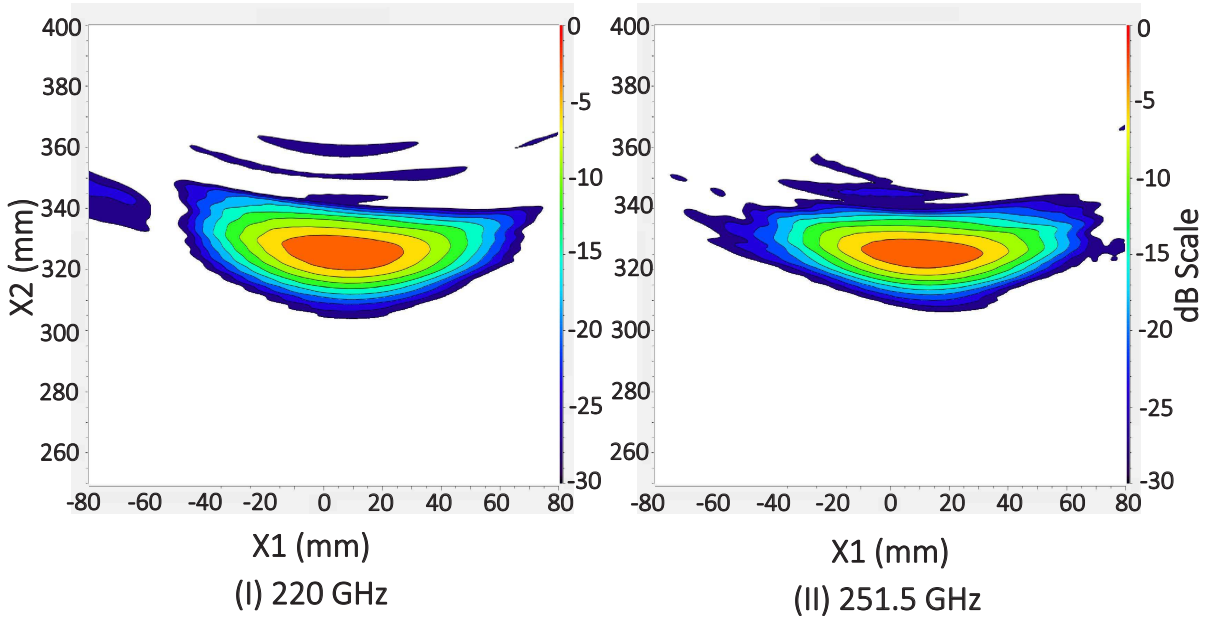

(b)

Figure 4.11: Field intensity in the plane of the (a) launcher cut, (b) possible location of the first mirror [189].

4.5 RF Window

In gyrotrons, the high power output beam is extracted through a RF window that act as a barrier between the vacuum inside the gyrotron and the outer transmission line. RF window materials are characterized by very low loss tangent and high mechanical and thermal strengths. Chemically Vapour Deposited (CVD) diamond window is widely used in megawatt class gyrotrons as it can handle power up to 2 MW [17]. In the present design, single disk CVD diamond window of thickness (d) 2.0 mm and aperture radius of 50 mm is considered. Transparent frequencies of this window are 220.1 GHz, 251.5 GHz and 282.9 GHz. The designed window has the transmission bandwidth of 2 GHz around these frequencies. The transmission coefficient of the output beam passing through the designed window in both the operating frequencies is around 99.97%. The transmission and reflection coefficients of the window at different frequencies are presented in Figure 4.12. Tolerance limit on the thickness of the designed RF window is $\pm$ 0.07 mm for maintaining the maximum reflection coefficient of -20 dB in both the operating frequencies.

Table 4.5: Single disk RF window design and results [176]

Window material	CVD Diamond
Window aperture radius (mm)	45
Window thickness, d (mm)	2.00 $7\lambda/2$ (for 220.1 GHz) $8\lambda/2$ (for 251.5 GHz)
Disk dielectric constant (ε_r)	5.67
Transmission Coefficient (%)	99.98 (for 220.1 GHz) 99.97 (for 251.5 GHz)

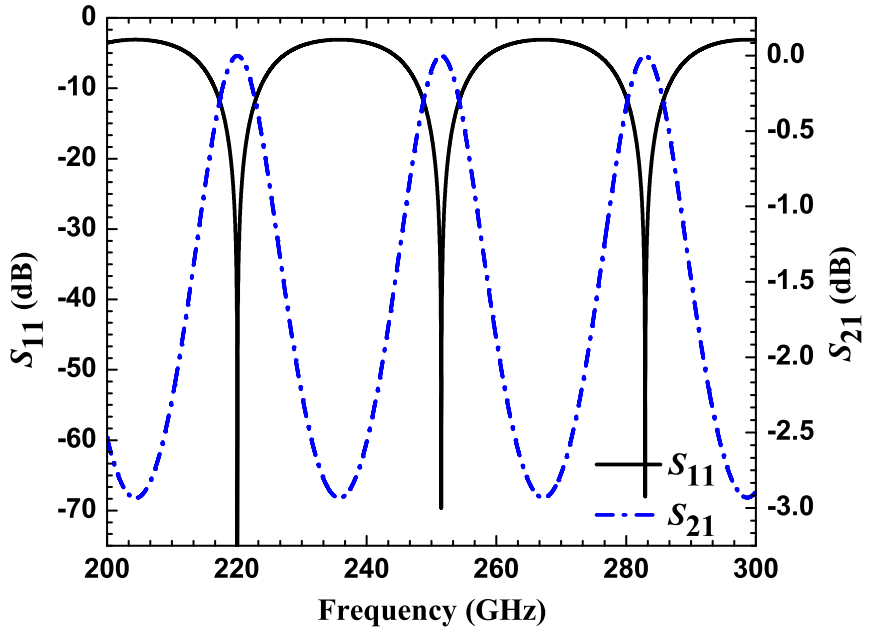

Figure 4.12: Transmission and reflection coefficients of a CVD diamond window along the frequency [176].

4.6 Conclusions

In this chapter, design studies of a common electron gun and output coupling system (includes NLT, QOL and RF window) supporting the dual frequency operation of the coaxial cavity gyrotron have been presented. A triode type coaxial MIG has been designed that generates hollow electron beam with the electron beam radius of 10.838/10.834 mm, velocity ratio of 1.28/1.27, velocity spread of 2.5/3.8%, at the frequencies 220/251.5 GHz, respectively. A nonlinear taper with the raised cosine profile has been designed and has a transmission coefficient of greater than 99% for both the operating modes. An advanced dimpled wall launcher has been designed for supporting the cavity modes with a relative caustic radius of around 0.3. The Gaussian content of the output beam coming out of the launcher cut is greater than 95% for both the operating modes. A single disk CVD diamond window has been designed and is capable of extracting the high power output beam from the gyrotron at both the operating frequencies with reflections less than -50 dB.

Chapter 5

Design studies of a Dual Frequency Coaxial Cavity Gyrotron extended to the third operating frequency - 283 GHz

5.1 Introduction

Current research activities around the world are oriented towards the development of sub-THz wave gyrotrons at megawatt class power levels with multi-frequency operational capabilities. Installing the multi-frequency gyrotrons in the ECRH system would increase the capability of the heating system and thus allowing the tokamak to operate at different experimental scenarios without any major increase in the construction costs [129]. Research groups in Japan have reported an experimental operation of a 1 MW long pulse multi-frequency gyrotron (104/137/170/203 GHz) [61]. KIT, Germany has performed the step tunable operation of a D-band gyrotron in the frequency ranges of 124-169 GHz [129]. The super conducting JT 60SA tokamak under Japan Atomic Energy Agency (JAEA) has prepared for dual frequency gyrotron (110/138 GHz) and with an extended third frequency operation at 82 GHz [63]. This chapter explores the multi-frequency operational capability of an already reported 2 MW dual regime (220/251.5 GHz) triangular corrugated coaxial cavity gyrotron [190] extended to the third operating frequency of 283 GHz. RF behavior studies of this dual regime gyrotron presented in Chapter 3 confirmed that continuous wave power of 2 MW can be obtained at both frequencies with an interaction efficiency of $\approx 33\%$. Design studies of a common electron gun and output coupling system supporting this dual frequency operation of the coaxial cavity gyrotron have been presented in Chapter 4. RF behavior studies are carried out for this gyrotron extended to the third operating frequency of 283 GHz. Mode selection, cold cavity and self-consistent single mode computations are carried out for this operating

Table 5.1: Mode selection for multi-frequency gyrotron [176].

f_r (GHz)	m	p	χ_{mp}	R_o (mm)	R_b (mm)	V_d* (kV)	m/χ_{mp}
220.000	46	29	150.7898	32.726	10.395	2.07	0.305
250.841	52	33	171.9283	32.726	10.282	1.97	0.302
281.817	58	37	193.0657	32.726	10.192	1.89	0.300
220.000	47	29	152.1125	33.013	10.616	2.18	0.309
252.487	54	33	174.5750	33.013	10.600	2.17	0.309
285.114	61	37	197.0375	33.013	10.580	2.16	0.310
220.000	**48**	**30**	**156.7365**	**34.016**	**10.838**	**2.10**	**0.306**
251.530	**55**	**34**	**179.1992**	**34.016**	**10.834**	**2.10**	**0.307**
283.208	**62**	**38**	**201.6619**	**34.016**	**10.829**	**2.09**	**0.307**
220.000	50	30	159.3778	34.590	11.281	2.31	0.314
251.006	57	34	181.8403	34.590	11.244	2.28	0.314
282.149	64	38	204.3028	34.590	11.214	2.25	0.313
220.000	51	29	157.3780	34.156	11.502	2.58	0.324
251.403	58	33	179.8422	34.156	11.420	2.52	0.323
282.942	65	37	202.3059	34.156	11.354	2.47	0.321

(* For the calculation of V_d, electron beam voltage, beam current, radii ratio and velocity ratio are 85 kV, 68 A, 3.8 and 1.27, respectively)

frequency using our in-house code GDS 2018 [176]. The time dependent multi-mode simulations are performed through the SELF-T code [93] with the mode eigenvalues obtained from GDS 2018. Start-up calculations are performed for this operational frequency with beam-space charge neutralization. Subsequently, design studies of the electron gun and output coupling system (includes NLT, QOL and RF window) supporting this third operating frequency 283 GHz in an already proposed dual regime coaxial cavity gyrotron are carried out. Electron gun simulations are carried out using the particle trajectory code ESRAY [177]. QOL design studies are performed through the commercial software Launcher Optimization Tool (LOT).

5.2 Frequency and Mode Selection

220 GHz is selected as a principle frequency so that the designed gyrotron can be used for plasma heating applications in the future tokamaks. Additional frequencies (220/251.5 GHz) are selected such that the designed multi-regime gyrotron can cater the multiple requirements in future fusion plants. The design study of the dual regime operation (220/251.5 GHz) of the present coaxial cavity gyrotron is already presented in [190]. Therefore, 283 GHz is selected as the third frequency for the extended operation of this dual frequency coaxial cavity gyrotron. The operating mode for this 283 GHz operation

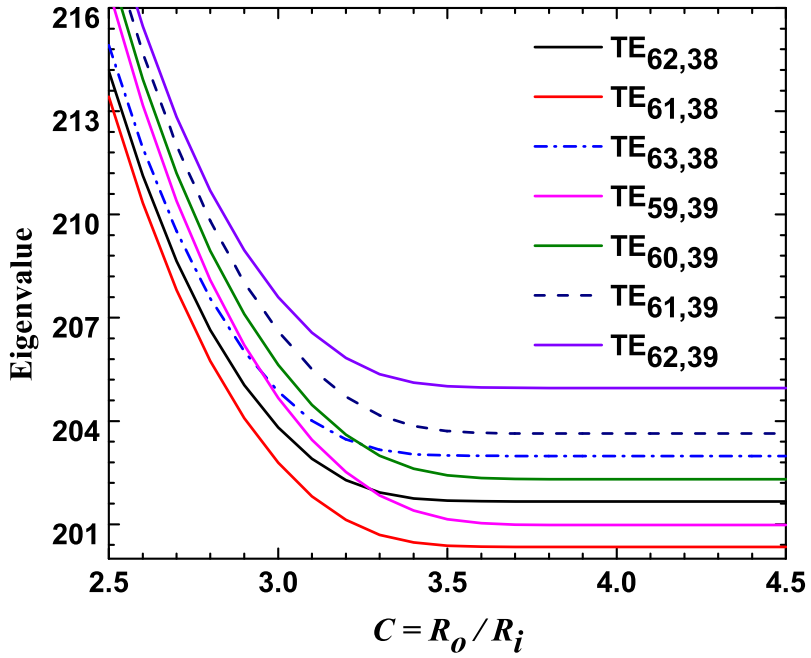

Figure 5.1: Eigenvalue curves for the desired mode $TE_{62,38}$ at 283 GHz along with the competing modes (R_o=34.00 mm, R_d=0.5 mm, l/s=0.7, N=130) [176].

is selected such that the interaction cavity, electron gun and output coupling system designed for the previous dual regime operational studies can also be used for this extended operation. A mode triplet that satisfy all the design goals and the technical constraints of such a multi-frequency gyrotron are given in Table 5.1. The $TE_{62,38}$ mode is chosen as cavity mode for 283 GHz operation.

5.3 Cold Cavity and Self-Consistent Single Mode Calculations

The dimensions of the RF interaction circuit used in the present design study are the same as those reported in the previous dual regime gyrotron studies [190]. Eigenvalue curve for the desired cavity mode along with the competing modes is shown in Figure 5.1. Cold cavity field profiles of all the three operating frequencies along the designed interaction circuit geometry are shown in the Figure 5.2(a). For maximum coupling of the electron beam with the RF wave, the electron beam radius is calculated as 10.824 mm for the chosen mode $TE_{62,38}$. The product of diffractive Q factor and coupling coefficient is calculated for the modes in the frequency range $\pm$ 5 GHz around the operating frequency

Table 5.2: Interaction cavity dimensions and self-consistent single mode calculation results [176].

Parameters	**220 GHz**	**251.5 GHz**	**283 GHz**
$L_1/L_2/L_3$ (mm)	16 / 12.5 / 16	16 / 12.5 / 16	16 / 12.5 / 16
$\theta_1/\theta_2/\theta_3(^\circ)$	3.5 / 0 / 3.0	3.5 / 0 / 3.0	3.5 / 0 / 3.0
D_1/D_2 (mm)	4.0 / 4.0	4.0 / 4.0	4.0 / 4.0
R_o/R_i (mm)	34.00 / 8.95	34.00 / 8.95	34.00 / 8.95
R_b (mm)	10.838	10.834	10.824
f_r (GHz)	220.1175	251.6298	283.142
Q_d	1596.80	2011.89	2518.63
V_b (kV)	87	85	89
I_b (A)	70	68	68
α	1.27	1.27	1.23
B_o (T)	8.872	10.100	11.466
$\eta_{elec.}(\%)$ incl. ohmic losses	35.51	34.78	34.35
P_{out} (MW)	2.163	2.01	2.09
ρ_o (kW/cm^2)	1.75	1.91	2.30
ρ_i (kW/cm^2)	0.13	0.04	0.02
Total Power Loss (kW)	43.9	45.4	52.36
Q_{ohmic}	107208	116076	123411
V_d (kV)	2.26	2.21	2.12
I_L (A)	430.80	418.09	469.43

and the mode spectrum is plotted in Figure 5.2(b).

After the cold cavity calculations, a self-consistent single mode calculation has been performed to optimize the power in the main mode. Electron beam parameters and magnetic field at the interaction cavity (B_o) were optimized for the maximum efficiency in the main mode and the ohmic wall loadings of the outer cavity and the insert walls are also calculated. In this calculation, the conductivity of copper was taken as $\sigma = 1.4\times10^7$ S/m, in order to include the effects of the surface roughness and the high operating temperature. Interaction circuit dimensions and the self-consistent single mode calculation results at all the three operating frequencies are given in Table 5.2.

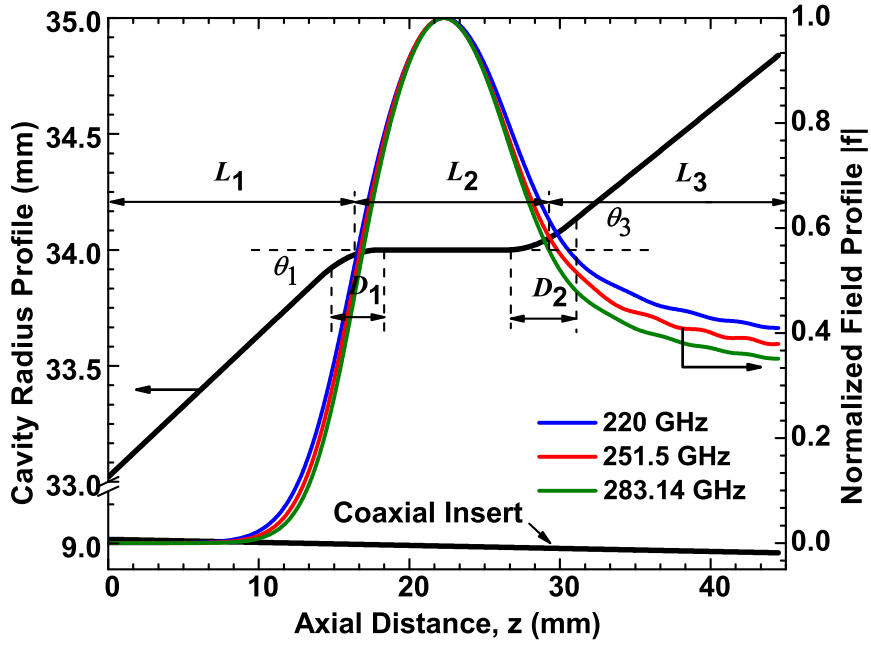

(a)

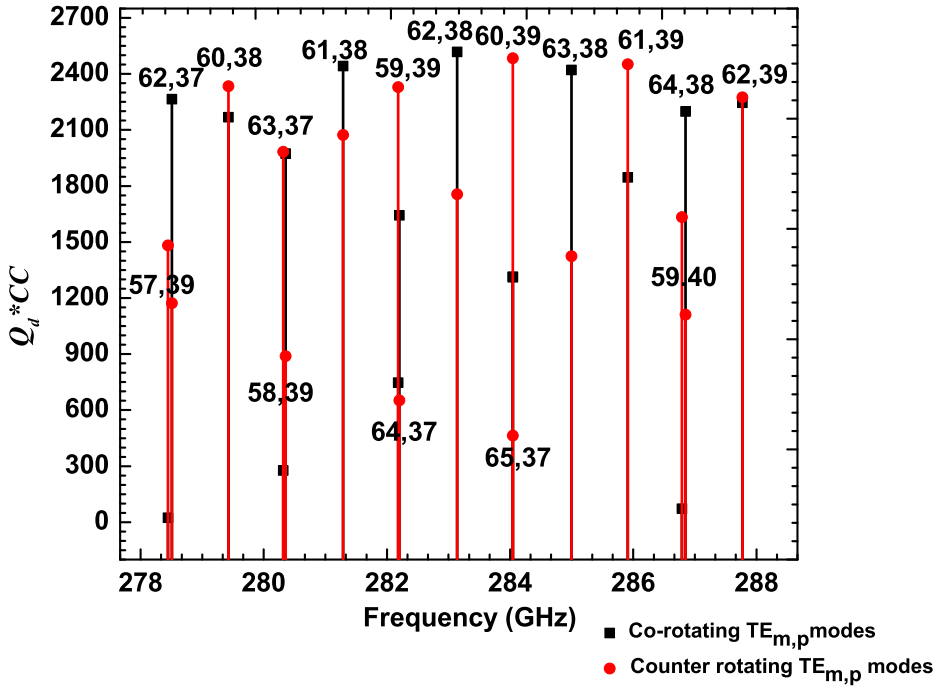

(b)

Figure 5.2: Cold cavity calculation: (a) Cold cavity field profile of the three operating modes along the cavity geometry and (b) Mode spectrum of Q_d times coupling coefficient [176].

5.4 Time Dependent Multi-mode Calculations

For the present 283 GHz operation, time dependent multi-mode calculations are carried out for a duration of 3000 ns with 0.01 ns time step. In the simulation, the beam current (I_b), the velocity ratio (α) and the magnetic field (B_o) are kept constant at the values 68 A, 1.23, and 11.430 T, respectively. While, the beam voltage (V_b) is varied linearly from 50 kV to 89 kV over the time period. The result of this multi-mode simulation is shown in Figure 5.3 and this indicates that there is a power growth in the desired output mode to the required value of 2 MW.

Start-up Behavior with Beam-Space Charge Neutralization

For the present 283 GHz operation, the start-up behavior is studied with beam-space charge neutralization. The electron beam parameters required for the start-up studies are obtained from the design studies of the electron gun using ESRAY code [177] and are given in Tables 5.3-5.5. Start-up calculations are performed for both partial space charge neutralization case (60%) and complete neutralization case (100%) and the results are shown in the Figures 5.4 - 5.5, respectively. For more realistic analysis in these calculations, a nonuniform magnetic field profile obtained from the MIG design studies is used. To obtain stable power in the desired mode the magnetic field is slightly increased from 11.425 T to 11.445 T for the case of complete space charge neutralization. These calculations confirm that in the new 283 GHz operation, 2 MW CW power can be obtained in the desired mode with an efficiency of $\approx 33\%$.

Table 5.3: Electron beam parameters for the start-up behavior - before space charge neutralization (B_o = 11.425 T) [177].

V_{acc} (kV)	V_m (kV)	I_b (A)	V_b (kV)	α	$\beta_\perp$
89	26.63	68.00	87.190	1.2312	0.4035
81	24.50	67.00	79.251	1.1232	0.3733
73	23.00	66.00	71.289	1.0368	0.3441
65	22.00	65.00	63.352	0.9039	0.3059
57	21.00	64.00	55.417	0.7197	0.2519
50	20.00	62.00	48.459	0.5849	0.2055

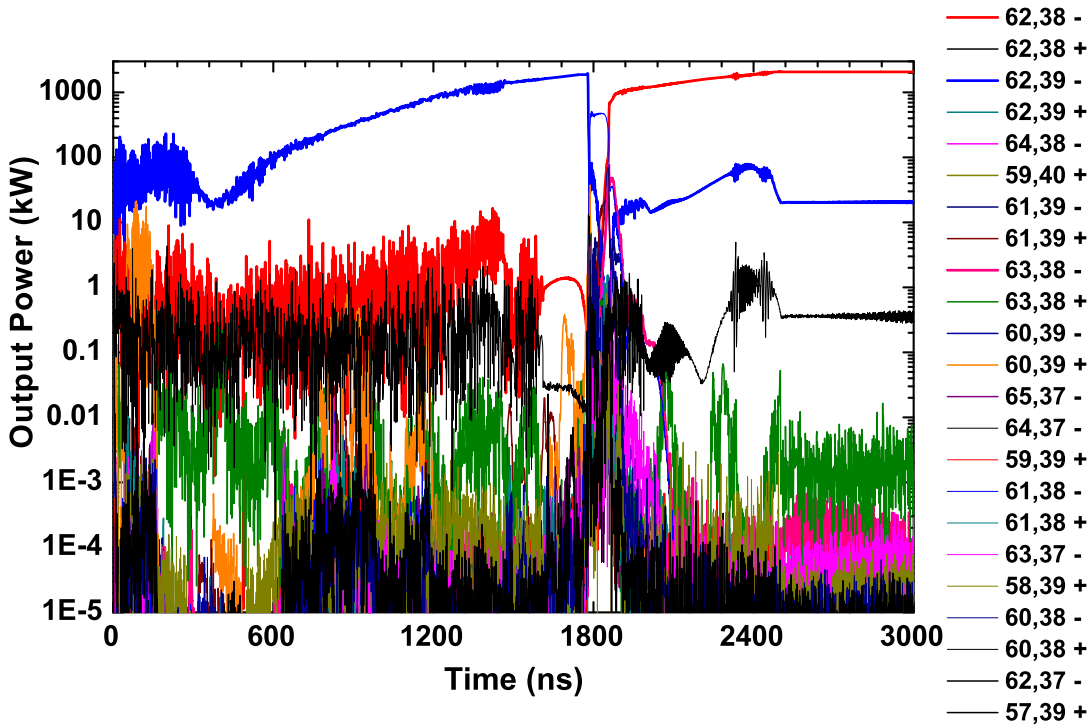

Figure 5.3: Time dependent multi-mode calculations for the $TE_{62,38-}$ mode along with the competing modes with $V_b = 50$-89 kV, $B_o = 11.430$ T, $\alpha = 1.23$ and $I_b = 68$ A. Logarithmic scale is used for the illustration of the output power, P_{out} (kW) [176], [93].

Table 5.4: Electron beam parameters - after 60% space charge neutralization ($B_o = 11.425$ T) [177].

Scenario	V_b **(kV)**	I_b **(A)**	α	$\beta_\perp$
Before space charge neutralization	87.190	68	1.2312	0.4035
After space charge neutralization	88.276	68	1.2106	0.4028

Table 5.5: Electron beam parameters - after 100% space charge neutralization ($B_o = 11.445$ T) [177].

Scenario	V_b **(kV)**	I_b **(A)**	α	$\beta_\perp$
Before space charge neutralization	87.192	68	1.2252	0.4027
After space charge neutralization	89.000	68	1.1918	0.4015

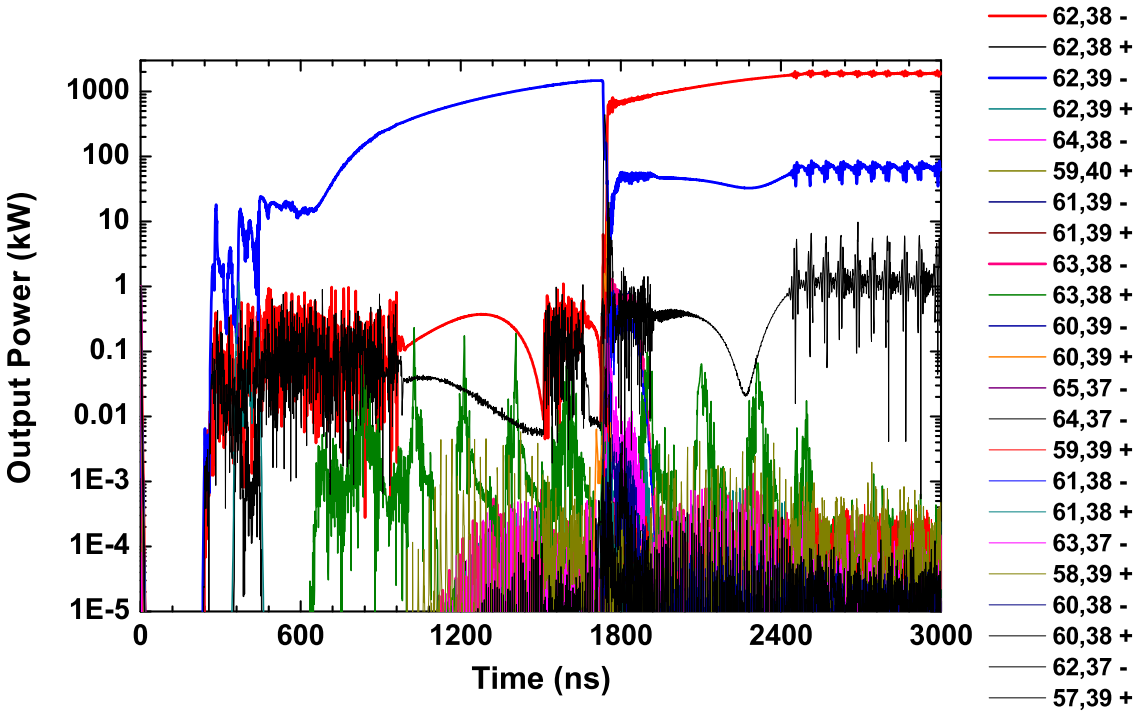

(a) before space charge neutralization.

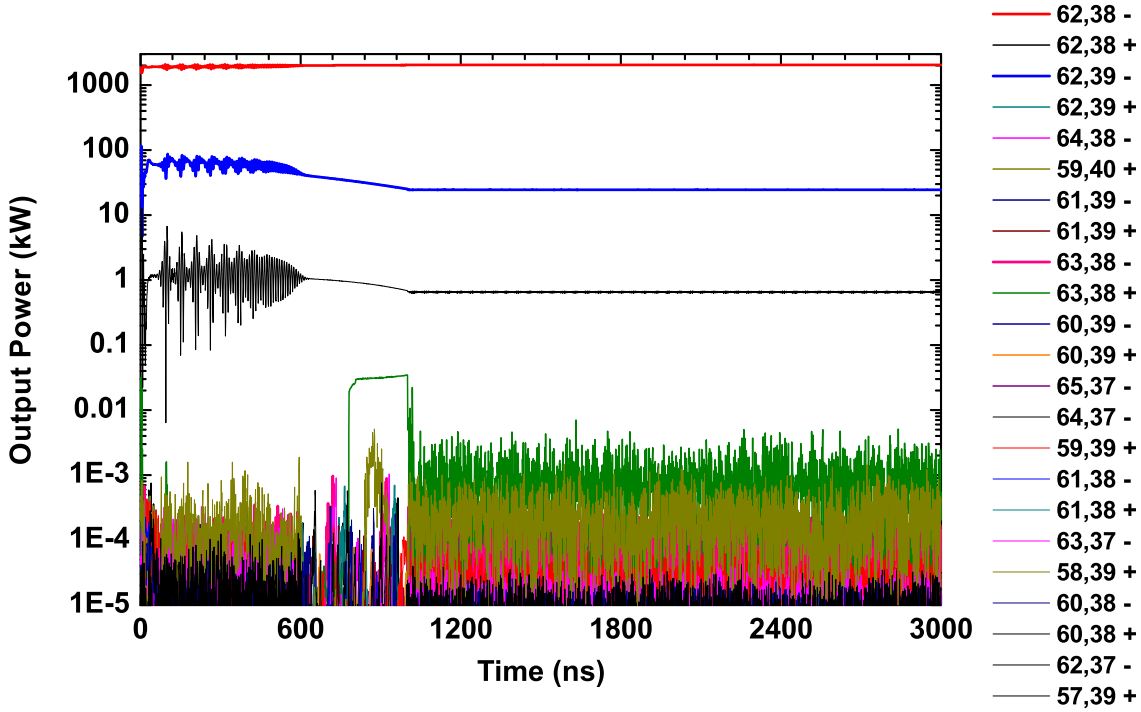

(b) after 60% space charge neutralization.

Figure 5.4: Start-up calculations for the $TE_{62,38-}$ mode along with the competing modes with (a) $V_b = 48.459$-87.190 kV, (b) 87.190-88.276 kV, $B_o = 11.425$ T, α and I_b vary accordingly. Logarithmic scale is used for the illustration of the output power, P_{out} (kW) [176], [93].

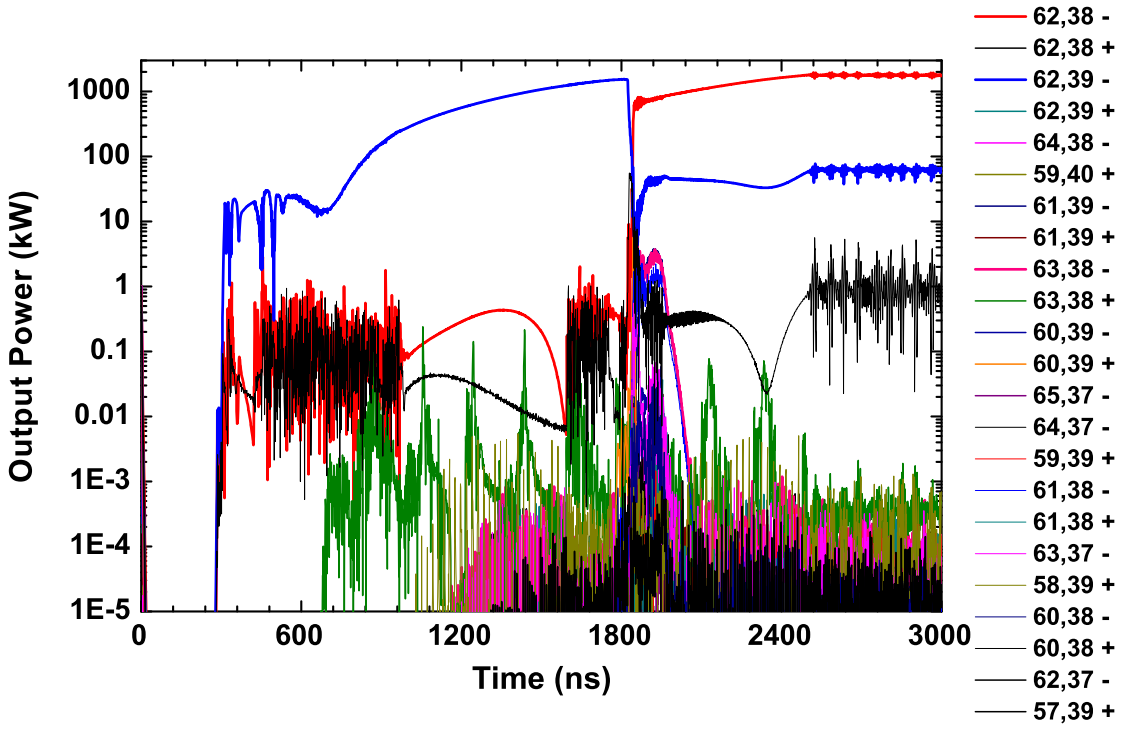

(a) before space charge neutralization.

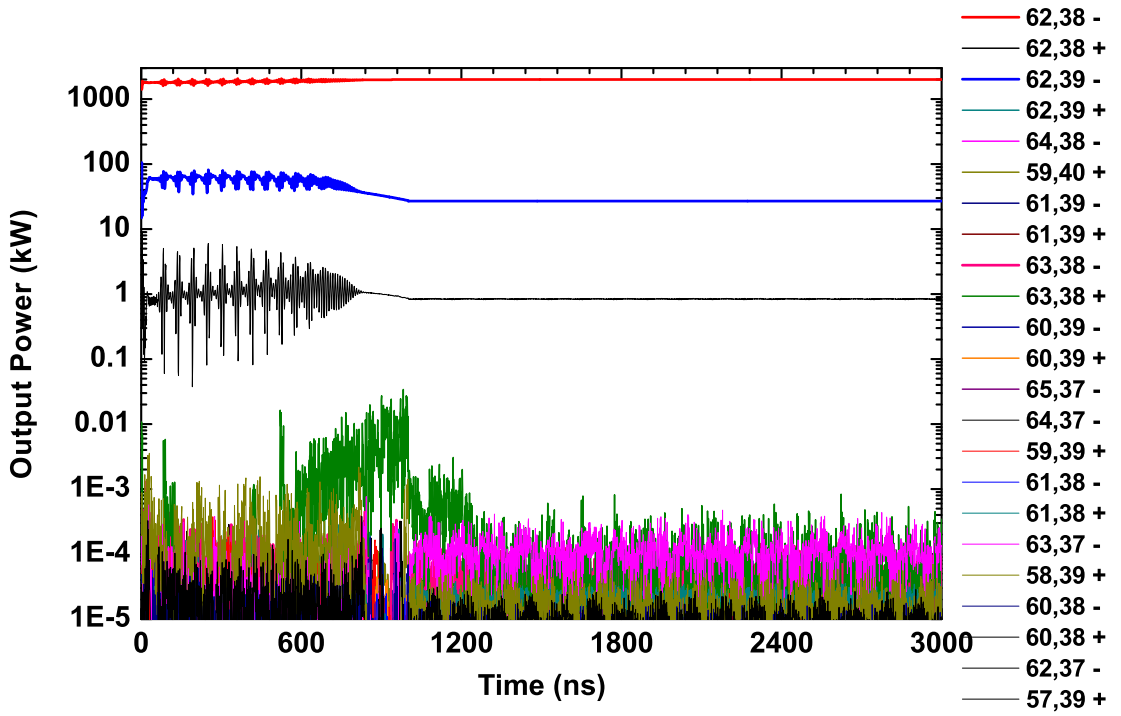

(b) after complete space charge neutralization.

Figure 5.5: Start-up calculations for the $TE_{62,38-}$ mode along with the competing modes with (a) $V_b = 48.459$-87.192 kV, (b) 87.192-89 kV, $B_o = 11.445$ T, α and I_b vary accordingly. Logarithmic scale is used for the illustration of the output power, P_{out} (kW) [176], [93].

5.5 Magnetron Injection Gun

Time dependent multi-mode analysis of the third operating frequency 283 GHz determines the nominal beam parameters like accelerating voltage, beam current, electron velocity ratio and the magnetic field at the interaction cavity required for the generation of the desired RF output power and are given in Table 5.6. In the present design studies, desired beam parameters and the magnetic field required for the third operating frequency are obtained by tuning the coil currents and electrode potentials of already designed electron gun for the dual regime operation. For the maximum coupling of electron beam with the RF wave, electron beam radius is calculated as 10.824 mm. The geometry of the electron gun and the magnetic guidance system used in the current design studies are same as those reported in the previous dual regime design studies. The electron beam generated by the MIG should satisfy the following requirements:

1. Electron velocity ratio spread ($\Delta\alpha$) should be less than 5%, otherwise mode competition increases and affects the RF power growth in the desired mode.
2. Thickness of the electron beam radius (ΔR_b) should be less than $\lambda/8$, so that there will be the efficient energy transfer between the electron beam and the RF wave.

Table 5.6: Nominal Beam Parameters

Frequency	220 GHz	251.5 GHz	283 GHz
Accelerating Voltage (V_{acc})	87 kV	85 kV	89 kV
Beam Current (I_b)	70 A	68 A	68 A
Electron Velocity Ratio (α)	1.28	1.27	1.23
Output RF Power	2.0 MW	2.0 MW	2.0 MW
Magnetic Field at Cavity Center (B_o)	8.867 T	10.105 T	11.425 T
Electron Beam Radius (R_b)	10.838 mm	10.834 mm	10.824 mm

In gyrotrons, solenoids are used for generating the required DC magnetic field. Information about the magnetic coils and the current in the coils for all the three operating fre-

Table 5.7: Optimized Coil Data [177]

Coils	Length ΔZ (mm)	Breadth ΔR (mm)	Coil radius (mm)	No. of turns N_C	Current 220 GHz (A)	Current 251.5 GHz (A)	Current 283 GHz (A)
Main Coil –1	440.00	30.00	120.00	24990	119.87	136.59	154.45
Main Coil –2	440.00	15.00	142.50	4930	119.87	136.59	154.45
Compensating Coil	70.00	45.0	147.50	2880	-63.5	-71.0	-82.5
Gun Coil – 1	65.00	25.0	137.50	645	7.5	5.45	8.43
Gun Coil –2	20.00	25.00	137.50	610	3.0	3.5	6.16

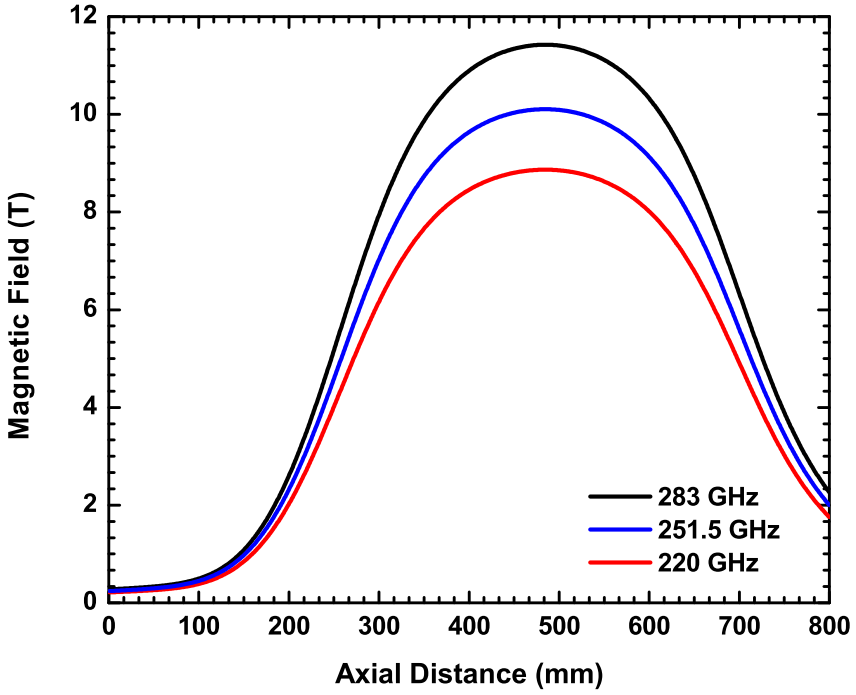

Figure 5.6: Magnetic field profile along the axial length of the gyrotron. Here, emitter position is at z=50 mm and center of the interaction cavity is at z=480 mm [176], [177].

quencies are given in Table 5.7. By optimizing the current in the magnetic coils, required magnetic field at the interaction cavity of 10.864 T is obtained for the current 283 GHz operation and the generated magnetic field profiles for all the frequencies are shown in Figure 5.6. For the current 283 GHz operation, triode type MIG is simulated using the particle trajectory code ESRAY. Modulating anode potential and the magnetic field at the emitter region are optimized for obtaining the desired beam parameters. Simulation results of the triode type coaxial electron gun for 283 GHz operation is given in Table 5.8. The electron beam trajectory is calculated for this operation and is shown in Figure 5.7.

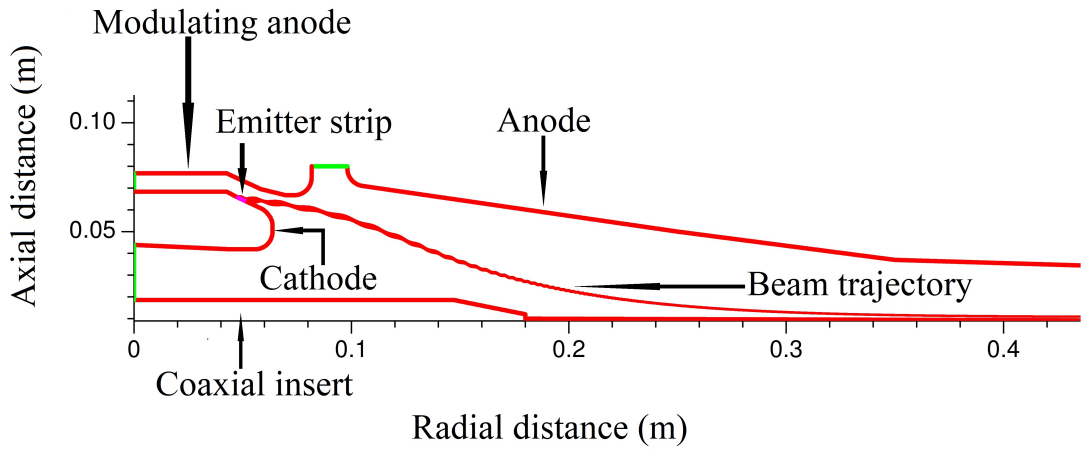

Figure 5.7: Electron beam trajectory of 283 GHz operation in the designed MIG [177].

Table 5.8: Design Parameters and Simulation Results of the Triode Type Coaxial MIG [177]

Parameters			
Frequency	220 GHz	251.5 GHz	283 GHz
Beam current	70 A	68 A	68 A
Accelerating voltage	87 kV	85 kV	89 kV
Mod. anode voltage	40 kV	31.0 kV	26.6 kV
Emitter current density	3.8 A/cm^2	3.8 A/cm^2	3.8 A/cm^2
Cathode radius	64.60 mm	64.60 mm	64.60 mm
Cathode angle	25°	25°	25°
Mod. anode angle	25°	25°	25°
Axial width of the emitter	4.4 mm	4.4 mm	4.4 mm
Cathode-mod. anode spacing	8.45 mm	8.45 mm	8.45 mm
Anode radius	71 mm	71 mm	71 mm
Results			
Magnetic field at the emitter	0.21433 T	0.2405 T	0.333 T
Compression ratio	41.3708	42.0166	34.31
Electric field at cathode	5.9 kV/mm	6.29 kV/mm	6.8 kV/mm
Velocity ratio	1.28	1.27	1.23
Velocity spread (%)	2.5	3.8	1.7
Beam radius (interaction)	10.838 mm	10.834 mm	10.824 mm

5.6 Output Coupling System

Output coupling system of gyrotron includes a NLT, quasi optical laucher, followed by phase correcting mirrors and output RF window. Design studies of the output coupling system supporting this extended operation of 283 GHz are carried out. For the current 283 GHz operation, the same output system components designed for the dual regime operation as discussed in Chapter 4 are used. Output radius of the raised cosine NLT is 36.38 mm, the length of NLT is 88.10 mm. The optimized NLT is shown in Figure 5.8. Transmission efficiency of the chosen mode $TE_{62,38}$ at the desired frequency of 283 GHz in the designed NLT is also greater than 99.20%.

A quasi-optical launcher is used to convert high order cavity mode into free space linearly polarized Gaussian like mode. For this 283 GHz operation, as the relative caustic radius of the cavity mode ($m/\chi_{m,p}$) $TE_{62,38}$ (0.307) is approximately same as that of $TE_{48,30}$/$TE_{55,34}$ (0.306/0.307), the common launcher designed for the dual regime operation can be used. Synthesis of launcher supporting these cavity modes is quite challenging as the $m/\chi_{m,p}$ of these modes are around 0.3. Hence, QOL is designed with higher order perturbations included in the wall surface deformations. QOL is designed and numerically optimized through the commercial software Launcher Optimization Tool (LOT). The common launcher design supporting all the three cavity modes and the simulation results are given in Table 5.9.

Figure 5.9 shows the field intensities on the launcher wall for 283 GHz operation. From the field intensity plot, it is observed that the output beam coming out of the launcher cut is down converted to the Gaussian like TEM mode and the field intensities near the cut edges (represented by the white color dotted line) are less than -30 dB thereby minimizing the diffraction losses. Figure 5.10 shows aperture field intensity of the cavity mode at the frequency of 283 GHz. From this plot it can be noted that for 283 GHz operation field intensities are symmetrical about the centroid of the beam and the side lobe levels are negligible. Figure 5.11 shows the far field intensities calculated using far field approximation ($> 2D^2/\lambda$). Figure 5.12 shows the field intensities in a plane of the launcher cut (i.e. at a

Table 5.9: Launcher design and LOT simulation results [189]

Launcher length (mm)	325.0
Helical cut length (mm)	45.0
Waveguide radius (mm)	36.38
Taper angle (Rad.)	0.002
Gaussian content factor (GCF)	95.86% (for 220 GHz) 96.31 % (for 251.5 GHz) 95.33% (for 283 GHz)

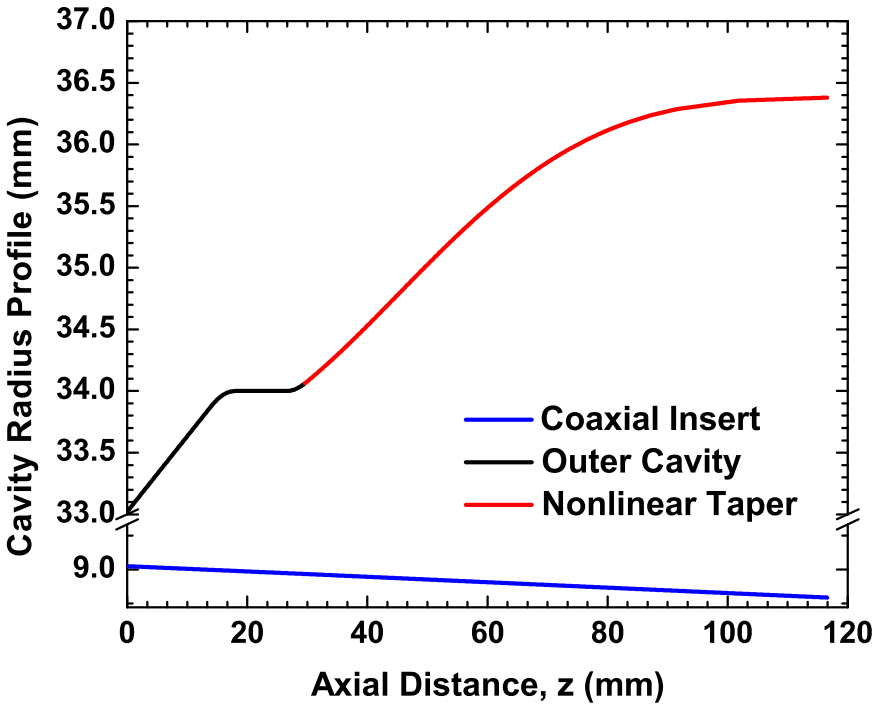

Figure 5.8: The interaction circuit geometry with the optimized NLT. Here, the mid-section radius, R_o is 34 mm and the output radius of the NLT is 36.38 mm (1.07 times R_o) [176].

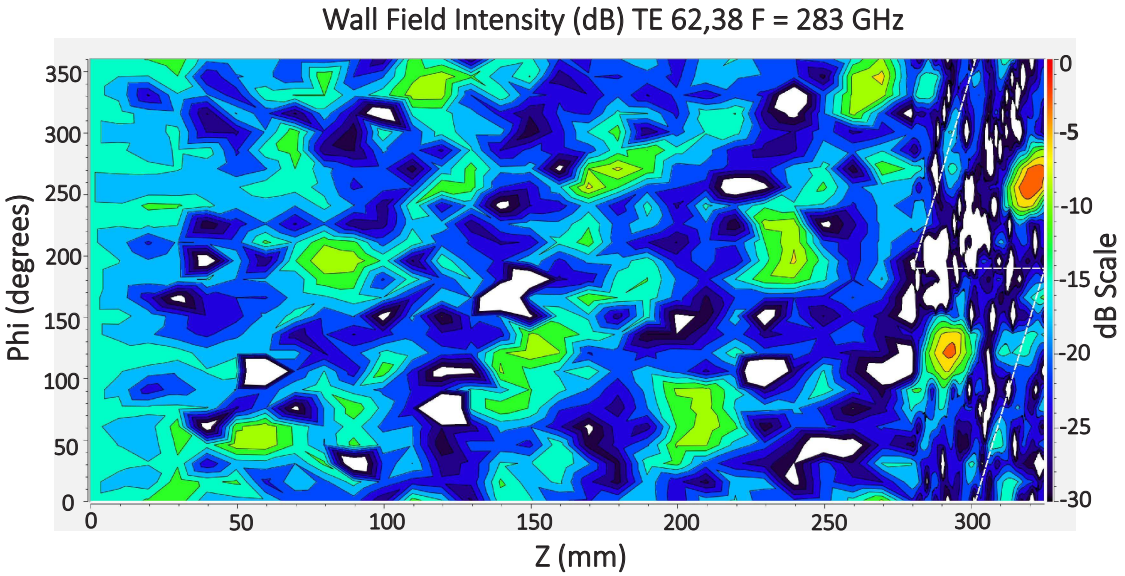

Figure 5.9: Field intensity for the cavity mode $TE_{62,38}$ at 283 GHz on the unrolled launcher wall [189].

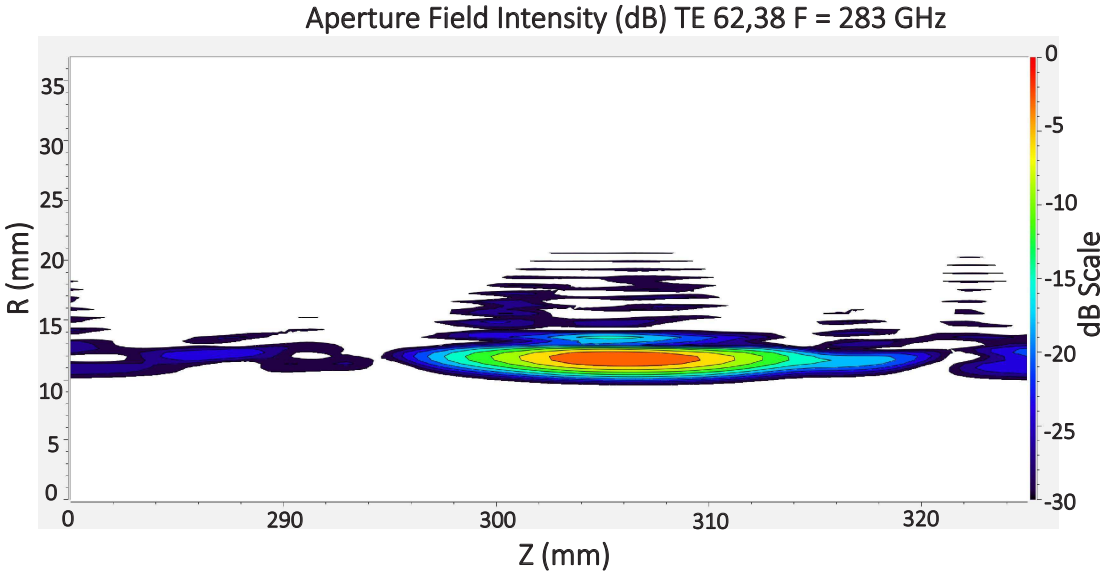

Figure 5.10: Aperture field intensity for the cavity mode $TE_{62,38}$ at 283 GHz [189].

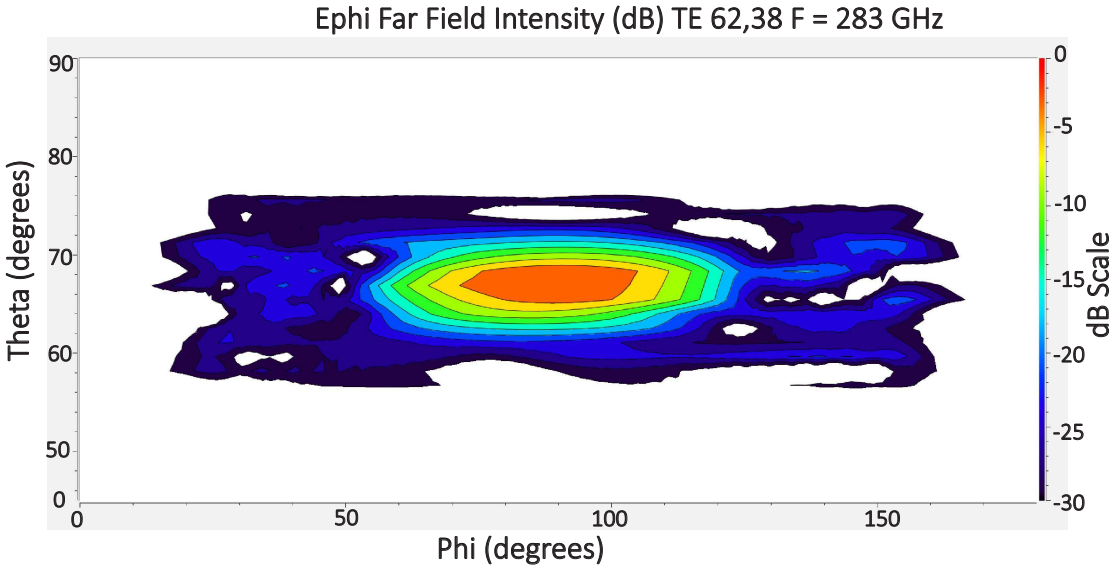

Figure 5.11: Far field intensity for the cavity mode $TE_{62,38}$ at 283 GHz [189].

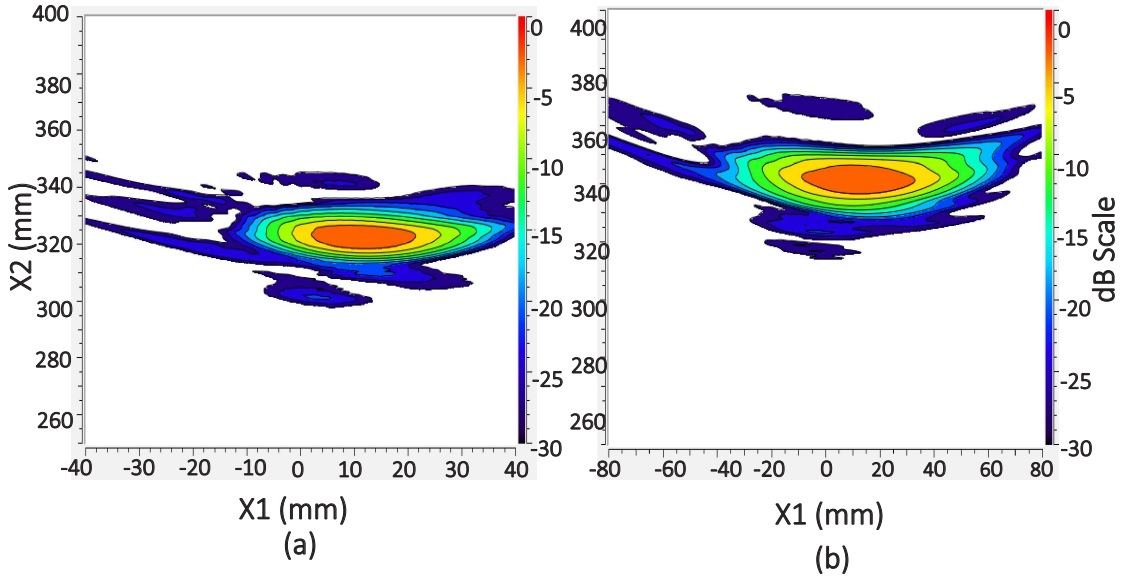

Figure 5.12: Field intensity in the plane of the (a) launcher cut, (b) possible location of the first mirror [189].

distance of 36.38mm from the gyrotron axis) and in the plane of the possible location of the first mirror (i.e. at a distance of 80mm from the gyrotron axis). From Figure 5.12, it is understood that for the current 283ĠHz the wave beam position is nearly same as that for the dual regime operation and hence a common internal mirror system can be used for further phase corrections. The Gaussian content of the wave beam coming out of the launcher cut are 95.86%, 96.31% and 95.33 % for 220 GHz, 251.5 GHz and 283 GHz, respectively and this can further be improved by using the phase correcting mirror system.

The thickness of the already designed single disk CVD diamond window for the dual regime operation is 2.00 mm and this window is transparent around the frequencies 220.1 GHz, 251.5 GHz, 282.9 GHz. The designed window has the transparent bandwidth of 2 GHz around these frequencies and hence the same RF window can be used for this 283 GHz operation. Design parameters and the results of the single disk CVD diamond window are given in Table 5.10. The Transmission coefficient of the outgoing beam through the designed window at all the three operating frequencies is around 99.98%.

Table 5.10: Single disk RF window design and results [176]

Window material	CVD Diamond
Window aperture radius (mm)	45
Window thickness, d (mm)	2.00 $7\lambda/2$ (for 220.1 GHz) $8\lambda/2$ (for 251.5 GHz) $9\lambda/2$ (for 282.9 GHz)
Disk dielectric constant (ε_r)	5.67
Transmission Coefficient (%)	99.98 (for 220.1 GHz) 99.97 (for 251.5 GHz) 99.97 (for 282.9 GHz)

5.7 Conclusions

In this chapter, design studies have been carried out to explore the multi-frequency operational capability of an already reported 2 MW dual regime (220/251.5 GHz) triangular corrugated coaxial cavity gyrotron. The RF behavior of a 2 MW dual regime triangular corrugated coaxial cavity gyrotron has been extended for the third operating frequency of 283 GHz. For this frequency, the operational mode has been chosen as $TE_{62,38}$ by considering the technical constraints of the multi-frequency gyrotron. The geometry of the interaction cavity used in this design study are the same as those reported in the dual regime design studies. Cold cavity design, mode competition and self-consistent single mode calculations have been performed for this operating frequency through GDS 2018. Time dependent multi-mode calculations have predicted the desired output power of 2 MW obtained in the chosen mode. The start-up behavior has been investigated using electron beam parameters and realistic magnetic field profile obtained from MIG design studies, for both partial and complete beam-space charge neutralization cases. These RF behavior calculations predict that 2 MW CW multi-frequency operation (220/251.5/283 GHz) is possible in the designed coaxial cavity gyrotron. Subsequently, design studies have been carried out for the electron gun and output coupling system to support the operating frequency of 283 GHz. These studies confirm that for this extended operation at 283 GHz, the same gyrotron assembly designed for the dual regime operation can be used. Thus the multi-frequency operation (220/251.5/283 GHz) is possible in this proposed triangular corrugated coaxial cavity gyrotron.

Chapter 6

Design Studies of a 3 MW, Multi-frequency DEMO Class Triangular Corrugated Coaxial Cavity Gyrotron

6.1 Introduction

In the fusion tokamaks, ECRH&CD is considered to be effective way of heating the plasmas over the other heating methods. In the ITER tokamak, which is being constructed in France, it is experienced that electron cyclotron current drive (ECCD) efficiency is lower than other CDs (like ion cyclotron CD, neutral beam CD, and lower hybrid CD) and hence under steady state operational scenarios of the ITER, ECCD alone is not sufficient [69]. However, in the future commercially prototype of fusion reactors like DEMO tokamak, which are aimed for achieving stable operation condition for several hours with a high overall machine gain, the ECRH system should be optimized to provide higher ECCD efficiency. Design studies on the ECRH&CD system of the European DEMO tokamak demand gyrotrons operating at the frequencies above 200 GHz for an optimum ECCD efficiency [12]. Multi-frequency operation of these gyrotrons provides flexibility to the ECRH system for other applications like plasma start-up, bulk heating, and also in the upgraded versions of other existing tokamaks like ITER. Compared to the conventional cavity gyrotrons, the coaxial cavity gyrotrons offer flexibility in controlling mode competition and also in the reduction of voltage depression. A 170 GHz pre-prototype coaxial cavity gyrotron developed at KIT, Germany, achieved 2.2 MW output power with 46% efficiency in short pulse experiments [55]. Ohmic loading on the insert is determined by the corrugations on the insert. A triangular corrugated insert reduces the problem of localized

heating compared to a longitudinal corrugated insert. Field analysis for the calculation of diffractive quality factor and ohmic wall loading in the triangular corrugated coaxial cavity using Surface Impedance Model (SIM) and full wave approaches is carried out by S.Singh in [74], [163].

This chapter focuses on design studies of a triple frequency triangular corrugated coaxial cavity gyrotron. 236 GHz is selected as the principle design frequency so that the proposed gyrotron can be used in the ECRH system of a DEMO tokamak. Other frequencies (170/204 GHz) are selected such that the same gyrotron can be used for other applications like plasma start-up and bulk heating. Considering the EUROfusion 2012 guidelines for a DEMO tokamak, gyrotrons with the single unit power of greater than 1 MW will be required to reduce the spatial and maintenance requirements of the ECRH systems [57]. Thus in the current design studies output RF power is targeted to achieve 3 MW at all the three operating frequencies. Earlier design studies on the coaxial cavity gyrotron for increased output RF power of greater than 2 MW were reported in [169], [167], [168]. Mode selection, cold cavity calculations, mode competition studies and self-consistent single mode calculations are performed using our in-house code Gyrotron Design Suite 2018 (GDS 2018) [176]. A triode type coaxial MIG with magnetic guidance system is designed for obtaining the desired beam parameters through the ESRAY code [177]. Start-up calculations are carried out using the SELF-T code [93] with the mode eigenvalues calculated through GDS 2018 [176]. The design goals and constraints of this multi-frequency coaxial cavity gyrotron are given in Table 6.1.

Table 6.1: Design goals and constraints for multi-frequency operation.

Frequencies	170/204/236 GHz
Output RF Power, Pulse Length	3.0 MW, CW
Diffractive Quality Factor	1500-2400
Beam Voltage	100-110 kV
Beam Current	85-90 A
Magnetic Field at Interaction Cavity	$\approx$ 6.8-7.1 T for 170 GHz $\approx$ 8.8-9.0 T for 204 GHz $\approx$ 9.7-9.9 T for 236 GHz
Electron Velocity Ratio	$\approx$ 1.30 - 1.34
Total Output Efficiency	$> 30\%$
Estimated Wall Loading	< 2 kW/cm^2
Total Internal Losses	$< 8\%$

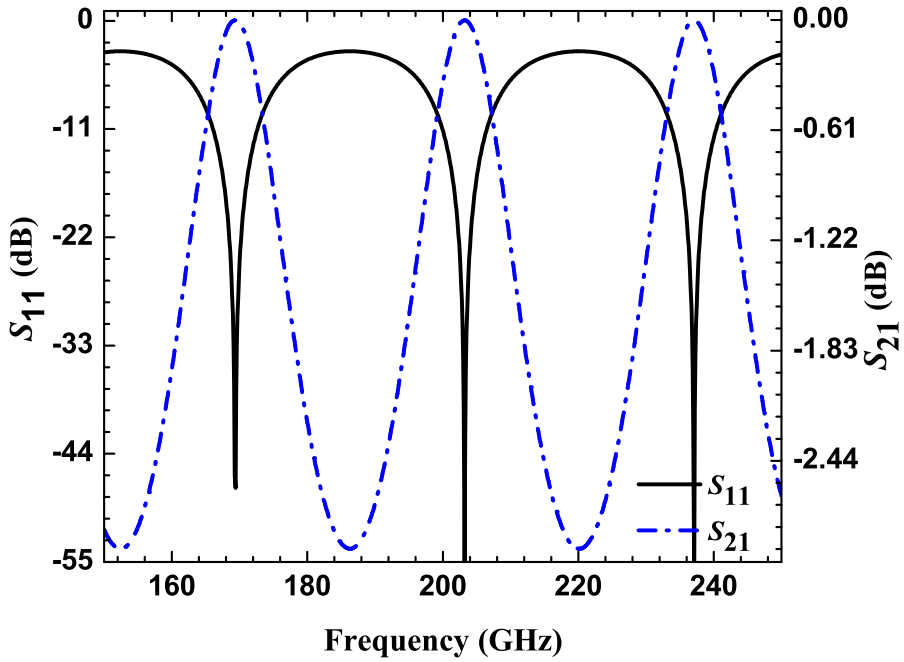

Figure 6.1: Transmission and reflection coefficients of a CVD diamond window of 1.860 mm thickness [176].

6.2 Mode Selection and RF behavior Calculation

For multi-frequency operation of the gyrotron, the transparent frequencies of a single disk RF window must be close to the operating frequencies. In the present study, a single disk CVD diamond window ($\varepsilon_r = 5.67$) of 1.860 mm thickness and 45 mm aperture radius is considered. Transmission and reflection plots of the designed RF window are shown in Figure 6.1. The designed RF window has -20 dB transmission gap of 2 GHz around the transparent frequencies of 169.4/203.2/237.1 GHz.

The cavity mode for the 3 MW DEMO gyrotron operating at the frequency of 236 GHz is selected by considering ohmic wall loading and multi-frequency operationability. Mode selection strategy for multi-frequency operation is explained in detail in [175]. As cavity wall loading increases with frequency and output RF power, for this 236 GHz operation the modes with eigenvalue higher than 200 are considered. Additionally, as output power is targeted to 3 MW, the modes with spread angle of $72^\circ \pm 0.5^\circ$ are considered for supporting a dual beam launcher [169]. After the cavity mode for the primary frequency (236 GHz) is fixed, the modes for the lower operating frequencies (170/204 GHz) are chosen by considering the criteria for multi-frequency operation. The modes chosen for the present multi-frequency operation are $TE_{46,27}$/ $TE_{55,32}$/ $TE_{64,37}$ at their respective

frequencies 170/204/236 GHz.

An interaction cavity of the gyrotron includes a straight midsection, an input taper, an output taper and a coaxial insert. Since the gyrotron operates close to cutoff, the midsection radius (R_o) is calculated according to the desired operating frequency of the chosen cavity mode, and for the current design studies, R_o is determined as 40.55 mm. In cold cavity calculations, the geometry of the interaction cavity is optimized for the required value of diffractive Q factor (Q_d) of the desired modes at their respective resonant frequencies. The diffractive Q factor of the cavity is predominantly determined by the midsection length. The interaction efficiency increases with the increase of the diffractive Q factor. However, for a fixed value of RF output power increase in the diffractive Q factor increases the ohmic Q factor and therefore increases the ohmic wall loading. Hence, for the better trade-off between interaction efficiency and thermal loading of the cavity at all the operating frequencies in the present multi-frequency operation studies, the midsection length (L_2) is optimized as 13 mm. The radius of input down taper is fixed smaller than the midsection radius so that cut-off frequency of the desired modes are higher than their operating frequencies. As a consequence, the RF fields are reflected back and there is minimum transmission towards electron gun. Similarly, the parameters of the output up taper are determined for maximum transmission of the desired modes towards output coupling system. To reduce the excitation of unwanted modes, the tapers are connected to the midsection through parabolic roundings of 4.0 mm.

In the interaction cavity, the field amplitude is maximum around the caustic radius and it decreases drastically for radii smaller than the caustic radius. For better beam mode interaction, the electron beam radius is chosen close to the caustic radius of the desired mode. The insert radius is considered to be smaller than the caustic radius of the desired mode, so that the field profile of the operating mode remains undisturbed. However, the insert radius is optimized such that the fields of the undesirable competing modes are disturbed, thereby reducing their diffractive Q factor. The insert is down tapered so that Q_d of the competing modes can be reduced towards the output end of cavity [74]. In this study, a triangular corrugated insert is used with the insert radius (R_i) of 10.81 mm at the midsection, and the number of slots (N) is fixed as 150. The dimensions of the triangular corrugations influence the slot impedance and consequently the ohmic wall loading on the insert. Considering the thermal loading on the insert at all the three operating frequencies, the depth (R_d) and the spacing of the slot (l) are fixed as 0.5 mm and 0.32 mm. As the number of corrugations is larger than twice the azimuthal index of the chosen cavity modes, the fields in the slots would be uniform, and therefore the SIM is used for the calculation of eigenvalues and ohmic wall loading.

Longitudinal field profiles of the desired modes at the respective resonant frequen-

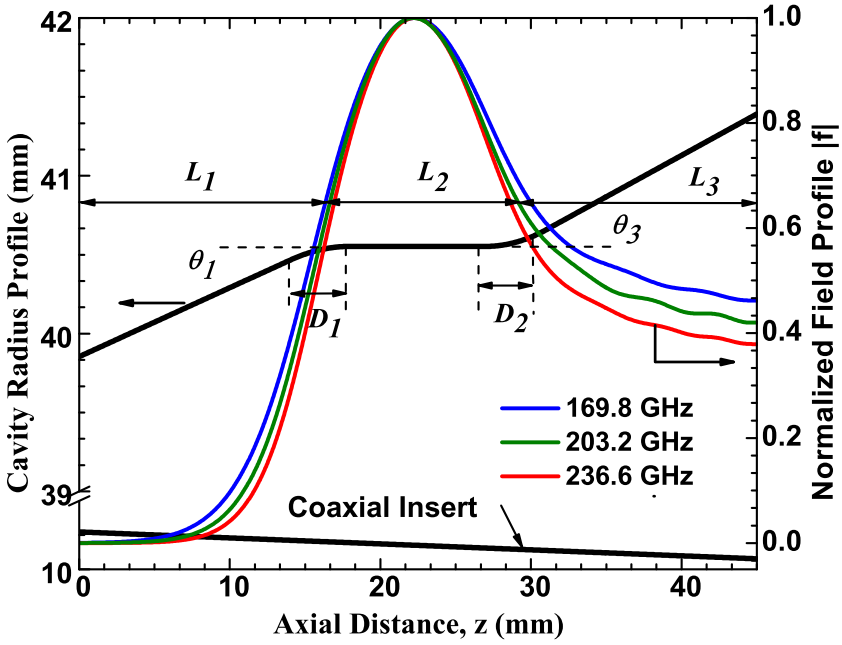

Figure 6.2: Longitudinal field profile of the cavity modes along the interaction cavity [176].

cies are shown along the interaction geometry in Figure 6.2. After cold cavity computations, mode competition studies are carried out. For maximum coupling of the RF with the electron beam, the electron beam radius (R_b) is determined for the chosen modes as 13.472/13.411/13.311 mm at their respective frequencies of 170/204/236 GHz. The product of diffractive quality factor and coupling coefficient ($Q_d * CC$) is calculated with the determined R_b for the most probable competing modes in the frequency range of ± 5 GHz around the operating frequencies and are shown in Figures 6.3-6.5. This product is important since this is inversely propositional to the starting current of the mode. Next step is the initial optimization of electron beam parameters (like beam voltage, beam current and velocity ratio) and magnetic field in the interaction cavity using single mode self-consistent calculations. The beam parameters and the magnetic field are optimized for the required value of output RF power with maximum efficiency. In this calculation, to include the effects of the surface roughness and the high operating temperature, the conductivity of copper is considered as ($\sigma = 1.4 \times 10^7$ S/m) instead of 5.67×10^7 S/m. The optimized dimensions of the interaction geometry and the single mode calculation results are given in Table 6.2.

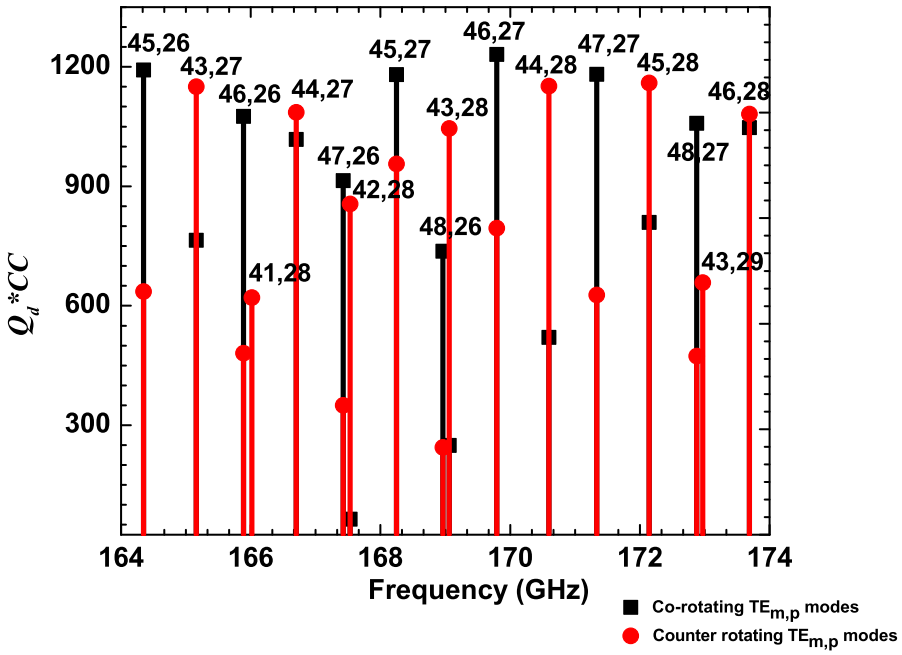

Figure 6.3: Product of diffractive quality factor (Q_d) and coupling coefficient calculated for the most probable competing modes with the beam radius of $R_b = 13.472$ mm for 170 GHz operation [176].

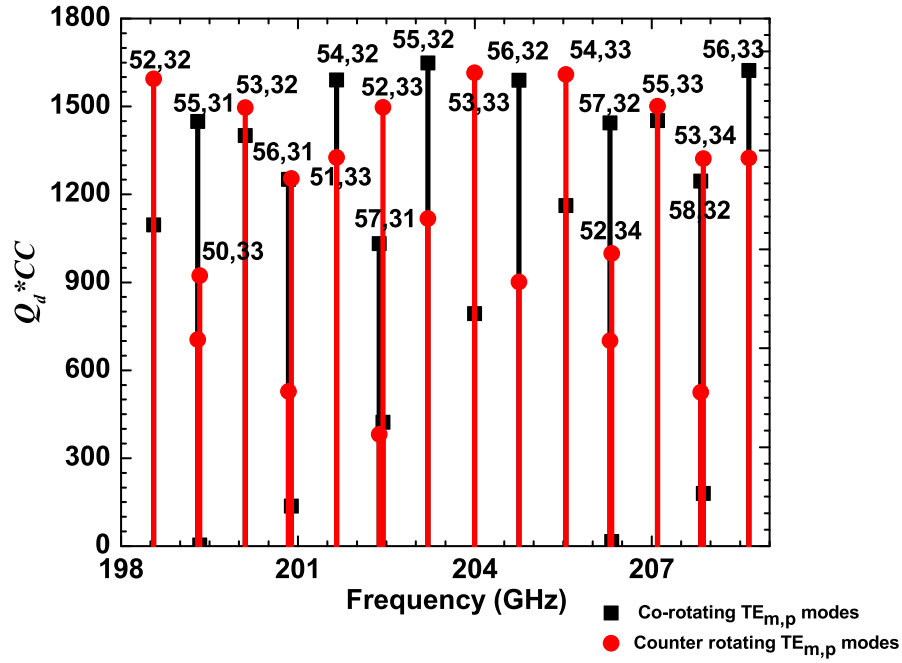

Figure 6.4: Product of diffractive quality factor (Q_d) and coupling coefficient calculated for the most probable competing modes with the beam radius of $R_b = 13.411$ mm for 204 GHz operation [176].

Table 6.2: Dimensions of interaction cavity and Single mode results [176].

Geometrical Parameters of Interaction Cavity			
$L_1/L_2/L_3(mm)$		16 / 13 / 16	
$\theta_1/\theta_2/\theta_3(^\circ)$		2.5 / 0 / 3.0	
$D_1/D_2(mm)$		4.0 / 4.0	
$R_o/R_i(mm)$		40.55 / 10.81	
N		150	
$R_d/l(mm)$		0.5 / 0.32	
Single mode Results			
f_r (GHz)	169.8	203.2	236.6
Q_d	1231.0	1648.83	2212
$V_{acc}(kV)$	103	108	110
$I_b(A)$	90	93	85
$R_b(mm)$	13.472	13.411	13.311
α	1.34	1.30	1.30
$B_o(T)$	6.980	8.430	9.885
η_{elec} incl. ohmic loading(%)	35.25	34.63	32.19
$P_{out}(MW)$	3.27	3.48	3.01
$\rho_o(kW/cm^2)$	1.56	1.91	2.06
$\rho_i(kW/cm^2)$	0.14	0.02	0.02
Total Power Loss (kW)	52.25	63.20	64.80
$V_d(kV)$	3.10	3.04	2.68
$I_L(A)$	454.58	516.53	535.88

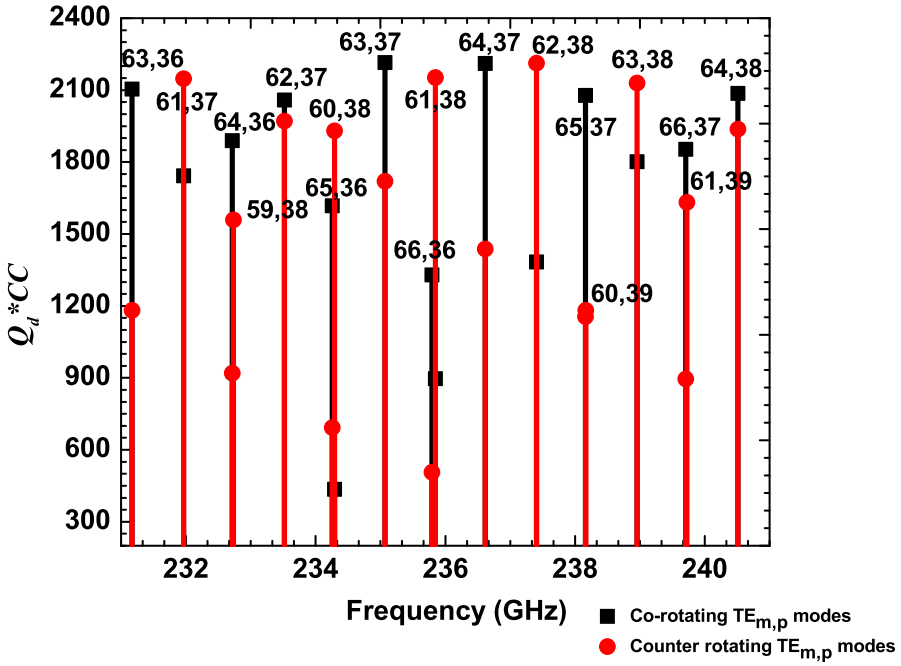

Figure 6.5: Product of diffractive quality factor (Q_d) and coupling coefficient calculated for the most probable competing modes with the beam radius of $R_b = 13.311$ mm for 236 GHz operation [176].

6.3 Design studies of Magnetron Injection Gun

RF behavior studies calculate the nominal beam parameters required for the generation of desired output RF power. MIG design studies are carried out for design and optimization of an electron gun geometry with a magnetic guidance system for generation of a hollow electron beam with the required beam parameters. Initial geometrical parameters like cathode radius, anode radius, emitter slant length, spacing between the electrodes are determined through Baird calculations in adiabatic approximation [191]. Magnetic compression ($b = B_o/B_g$, where B_o is the magnetic field in the cavity, B_g is the magnetic field at the emitter) relates the emitter radius (R_c) to the beam radius (R_e) through Busch theorem in paraxial approximation by $R_c = \sqrt{b}.R_e$. Baird calculations are carried out through GDS 2018 [176].

Next step is the optimization of the electron gun geometry and the magnetic guidance system through the particle trajectory code ESRAY [177]. The main objective of optimization is to design a MIG that can generate a high quality electron beam with the required beam parameters at all the three operating frequencies. The high quality electron beam is the one with low values of velocity ratio spread ($\Delta\alpha$) and beam thickness (ΔR_b). For the efficient interaction of the beam with the RF wave, the thickness of the

Table 6.3: Magnetic Coil Data for multi-frequency operation [176], [177]

Coils	**Length ΔZ (mm)**	**Breadth ΔR (mm)**	**Coil radius (mm)**	**No. of turns N_C**	**Current 170 GHz (A)**	**Current 204 GHz (A)**	**Current 236 GHz (A)**
Main Coil –1	300.00	39.00	197.50	17260	110.00	133.00	154.78
Main Coil –2	300.00	28.00	231.00	9350	110.00	133.00	154.78
Compensating Coil	89.00	56.00	206.00	6010	-57.80	-70.50	-82.75
Gun Coil – 1	56.30	17.00	186.50	1140	8.60	12.00	14.30
Gun Coil –2	25.00	12.00	184.00	900	7.30	8.55	11.00

electron beam should be less than $\lambda/8$. Lower value of $\Delta\alpha$, ensures the growth of RF power in the desirable mode [193]. The magnetic coils used for generation of the required field along the electron gun geometry are shown in Figure 6.6. Two main coils are placed around the interaction cavity for generation of the constant magnetic field around the cavity region. A compensating coil is placed between the cavity region and the emitter region for reducing the magnetic field towards the emitter and optimization of the magnetic field growth towards the cavity region. Two gun coils are located around the emitter region, for optimization of the magnetic field in this region. At the interaction region, the maximum magnetic field required for obtaining desired RF power at the respective frequencies 170/204/236 GHz are 6.985/8.445/9.825 T and the generated magnetic field profiles are shown in Figure 6.7. The dimensions of the magnetic coils along with the number of turns and the coil currents at the respective operating frequencies are given in Table 6.3. Electron beam trajectories are calculated for the desired operating frequencies in the designed coaxial MIG and are shown in Figures 6.8-6.10. The dimensions of the optimized electron gun geometry and the simulation results at all the three operating frequencies are given in Table 6.4.

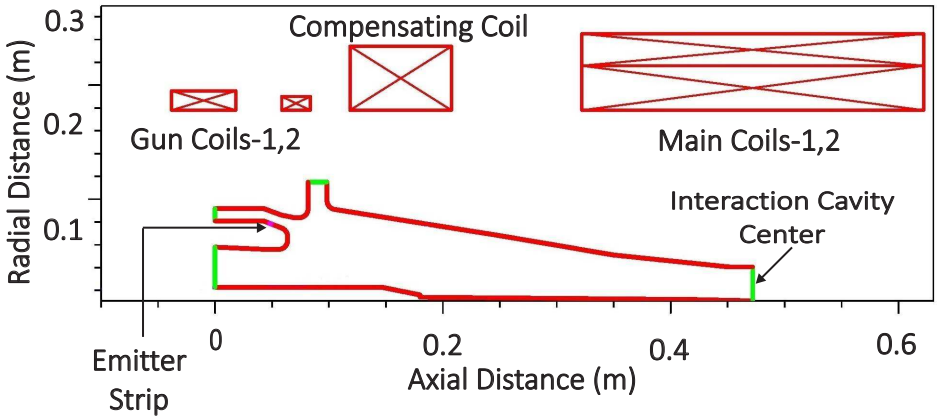

Figure 6.6: Location of the magnetic coils along the electron gun geometry [176], [177].

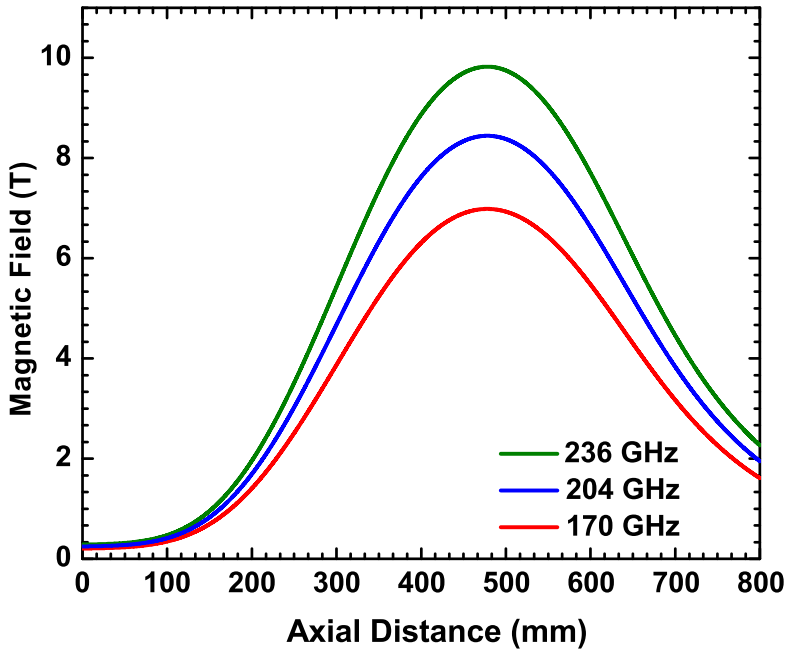

Figure 6.7: Magnetic field profiles obtained for the different operating frequencies [176].

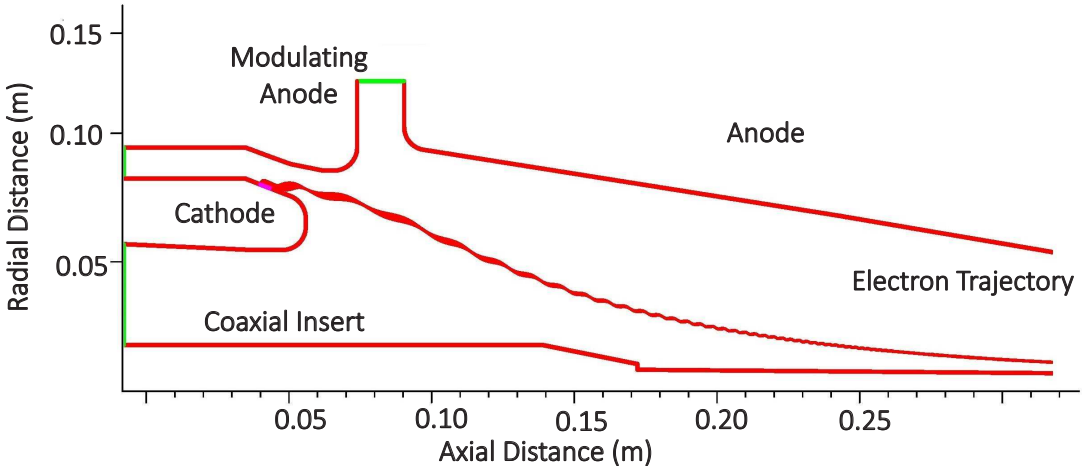

Figure 6.8: Electron beam trajectory in the designed coaxial MIG to support 170 GHz operation [177].

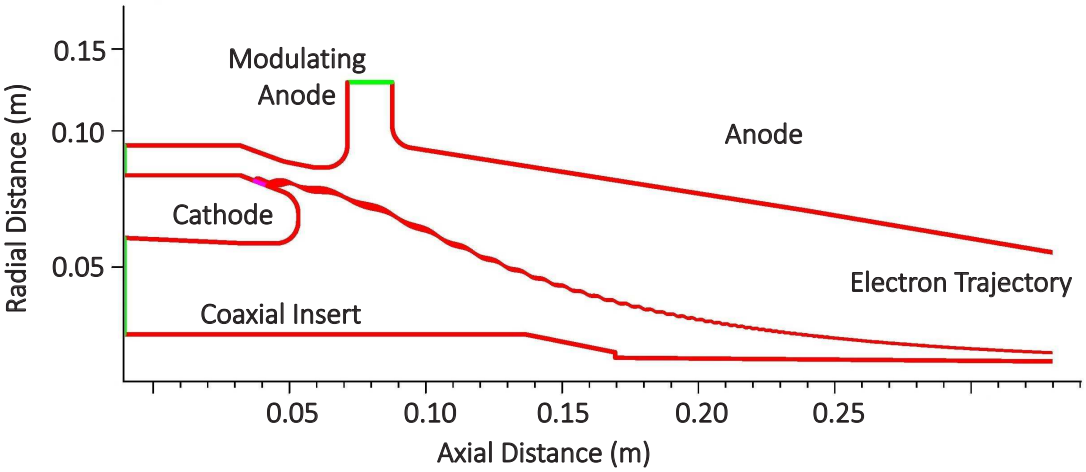

Figure 6.9: Electron beam trajectory in the designed coaxial MIG to support 204 GHz operation [177].

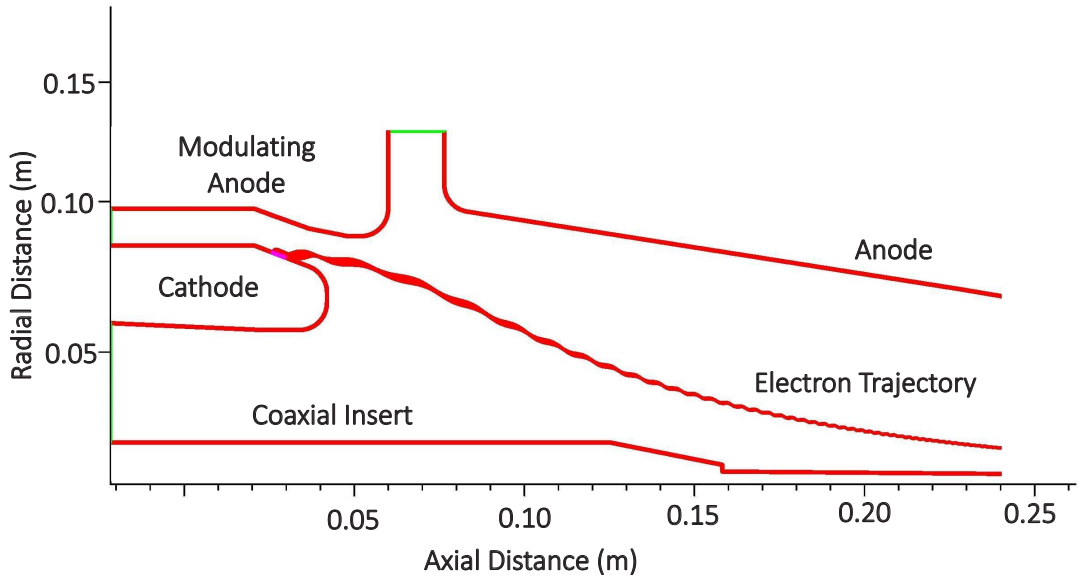

Figure 6.10: Electron beam trajectory in the designed coaxial MIG to support 236 GHz operation [177].

Table 6.4: Geometrical parameters and simulation results of the optimized coaxial MIG [177].

Geometrical Parameters of Coaxial MIG			
Cathode radius		78.00 mm	
Cathode angle		21.00°	
Mod. anode angle		20.50°	
Axial width of emitter		4.5 mm	
Cathode-mod. anode spacing		10.90 mm	
Anode radius		100.60 mm	
Input Parameters			
Frequency	**170 GHz**	**204 GHz**	**236 GHz**
Beam current	90 A	93 A	85 A
Accelerating voltage	103 kV	108 kV	110 kV
Mod. anode voltage	50.50 kV	44.90 kV	37.50 kV
Emitter current density	3.5 A/cm^2	3.5 A/cm^2	3.5 A/cm^2
Results			
Magnetic field at emitter	0.2318 T	0.2772 T	0.3180 T
Compression ratio	30.1337	30.4654	30.8962
Electric field at cathode	4.50 kV/mm	5.75 kV/mm	6.10 kV/mm
Velocity ratio	1.34	1.30	1.30
Velocity spread (%)	3.10	3.50	3.45
Beam radius in cavity	13.472 mm	13.411 mm	13.311 mm

6.4 Time Dependent Multi-mode Simulations

Time dependent multi-mode simulations are carried out to understand, RF power growth in the desired modes under the influence of the competing modes. The multi-mode calculations for the triangular corrugated coaxial cavity gyrotron are carried out through the SELF-T code with the mode eigenvalues obtained from GDS 2018. Multi-mode simulations are performed for all the desired cavity modes at their respective operating frequencies for the time period of 3000 ns with the time step of 0.01 ns. The electron beam voltage (V_b) is varying linearly up to 2500 ns and maintained at the constant value for the last 500 ns. Other beam parameters (like the beam current (I_b), the electron velocity ratio (α) and maximum magnetic field at the interaction cavity (B_o) are maintained constant through out the simulation. In these calculation magnetic field profile is maintained constant throughout the interaction region. The nominal beam parameters used in the time-dependent calculations for the three different operations are given in Table 6.5. Simulation results obtained for the three different frequencies are shown in Figures 6.11-6.13 and these results confirm that for the chosen nominal parameters RF output power in the desired cavity modes reach the power level of ≈ 3 MW at their respective operating frequencies.

Table 6.5: Nominal parameters used in the time dependent multi-mode calculations [176], [93]

Desired Cavity Mode	**Variation in V_b (kV)**	**I_b (A)**	**B_o (T)**	**α**
$TE_{46,27,-}$	60-103	90	6.985	1.34
$TE_{55,32,-}$	60-108	93	8.445	1.30
$TE_{64,37,-}$	60-110	85	9.825	1.30

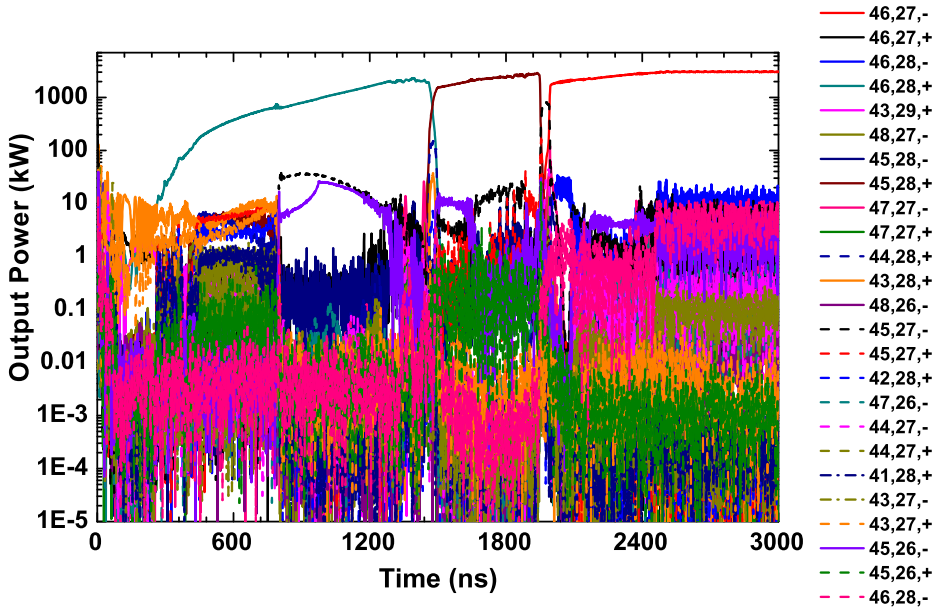

Figure 6.11: Time dependent multi-mode calculations for $TE_{46,27,-}$ mode at 170 GHz along with other competing modes with nominal beam parameters shown in Table 6.5. In this output RF power, P_{out} (kW) is illustrated in logarithmic scale [176], [93].

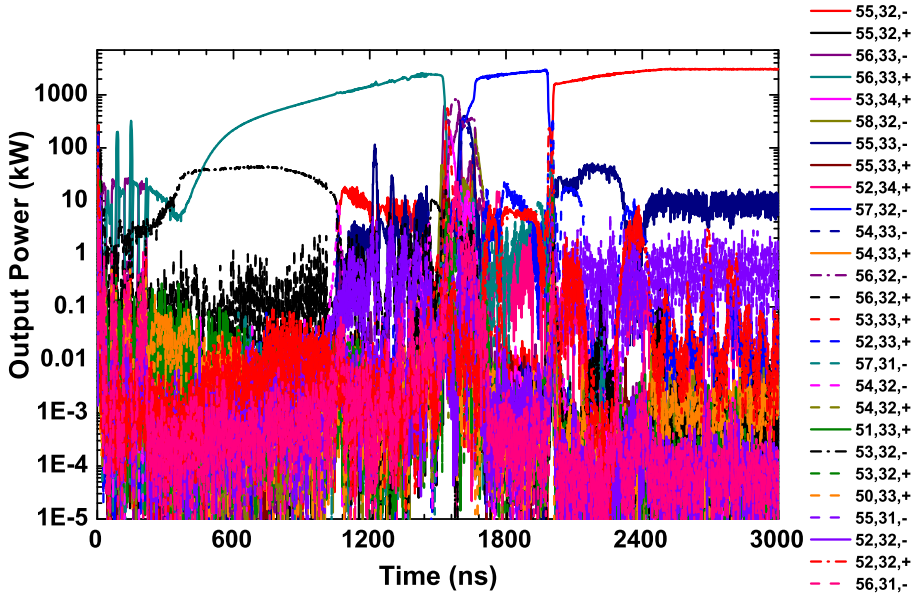

Figure 6.12: Time dependent multi-mode calculations for $TE_{55,32,-}$ mode at 204 GHz along with other competing modes with nominal beam parameters shown in Table 6.5. In this output RF power, P_{out} (kW) is illustrated in logarithmic scale [176], [93].

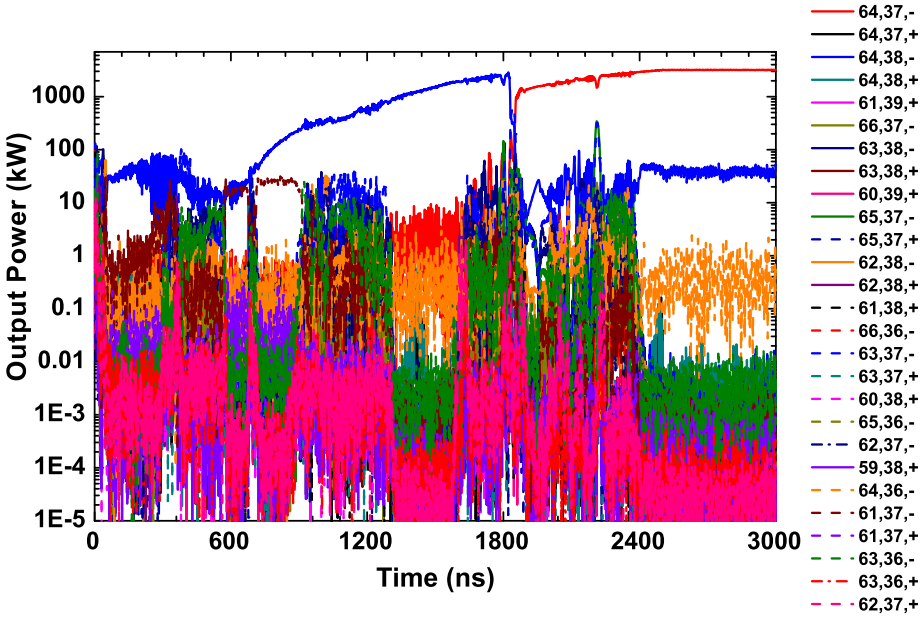

Figure 6.13: Time dependent multi-mode calculations for $TE_{64,37,-}$ mode at 236 GHz along with other competing modes with nominal beam parameters shown in Table 6.5. In this output RF power, P_{out} (kW) is illustrated in logarithmic scale [176], [93].

6.5 Start-up Calculations

In the start-up scenario of 236 GHz operation as shown in Figures 6.14-6.16, the beam voltage (V_b) reduces from the accelerating voltage (V_{acc}) of 110 kV to 107.873 kV, due to the effect of space charge fields [178]. For these calculations, the beam parameters are obtained from the MIG design studies with V_b raises from 58.012 kV to 107.873 kV over the time period of 3000 ns, I_b, and α are varying accordingly. A diode type of start-up scenario is considered in which the modulation anode voltage varies along with the cathode voltage [180]. The maximum magnetic field in the interaction cavity center (B_o) is optimized to 9.840 T. Excitation of the parasitic oscillations in the gyrotron interaction cavity is mainly due to the after cavity interaction occurring in the up-taper section of the cavity. The varying magnetic field profile in the interaction region is responsible for the after cavity interactions [195]. To understand the effect of parasitic oscillations on the startup scenario a nonuniform realistic magnetic field profile obtained from the MIG design studies is used in this calculation. During the initial time of startup, the modes with high relative coupling (larger than 80% of main operating mode) dominate and after V_b raises to 90 kV the desired mode $TE_{64,37,-}$ dominates and remain stabilized.

In the long pulse operation, due to the neutralization of space charge, the beam voltage increases close towards the accelerating voltage (V_{acc}) [184]. Start-up calculations are carried out for both partial (60%-practical case) and complete space charge neutral-

ization (100%-ideal case). Electron beam parameters used for the start-up calculations are given in Tables 6.6- 6.11. In the 236 GHz operation, after space charge neutralization, V_b raises from 107.873 kV to 109.149 kV for 60% neutralization (from 107.873 kV to 110.00 kV for 100% neutralization), α reduces as the transverse momentum ($\gamma\beta_\perp$) of the beam remains constant during the neutralization process [184]. From Figures 6.15 and 6.16, it can be noted that RF power in the desired cavity mode remains stable throughout the neutralization process for both partial and complete space charge neutralization cases. Similarly, for the other two operating frequencies (170/204 GHz), start-up calculations are performed for before and after space charge neutralization and are shown in Figures 6.17-6.22. From the figures, it can be observed that at both operating frequencies, the parasitic modes dominate initially and once V_b reaches to the favorable detuning condition, the desired cavity mode starts to oscillate and dominate over the other competing modes.

For realizing the 3 MW operation in the present design studies higher order modes are chosen, to control the ohmic wall loading. In [196], it is stated that in the multi mega watt gyrotrons non-stationary oscillations occur for the operating cavity modes with the azimuthal index higher than 46. However, this conclusion was drawn from the simulation results which were calculated for the fixed value of beam parameters with the variation in cyclotron resonance mismatch and normalized beam current.

In [197], a more detailed analysis of non-stationary oscillations occurring in the high power gyrotrons was carried out. In this paper effects of azimuthal non-uniformity of the electron emission and non-uniformity of RF wave envelope on the non-stationary process of gyrotron operation were analyzed. Simulation studies were performed for understanding these effects by varying different beam parameters and also initial assumptions. From the simulation results, it was concluded that non-uniformity in the electron emission is one of the prime reason for the azimuthal instabilities occurring in high power gyrotrons. Furthermore, it was also concluded that the stable single-mode operation could be realized in high power gyrotrons operating at higher order modes by properly choosing the beam parameters and the external magnetic field. In 2013, design studies of a 4 MW coaxial cavity gyrotron were performed in which stable single mode of operation was reported for the chosen cavity mode of $TE_{52,31}$ at 170 GHz [169]. Results of the startup studies of the present design confirm that stable operations are possible in all the three chosen modes at the desired frequencies.

Table 6.6: Electron beam parameters for the start-up behavior - before space charge neutralization (170 GHz) [177].

V_{acc} (kV)	V_m (kV)	I_b (A)	V_b (kV)	α	$\beta_\perp$
103	50.5	90.00	100.371	1.3416	0.4400
95	47.50	88.00	92.648	1.1039	0.3938
88	46.50	86.00	85.876	0.8987	0.3440
80	44.60	85.00	77.955	0.7468	0.2961
70	42.75	84.00	68.005	0.5851	0.2368
60	39.50	83.00	58.012	0.4062	0.1654

Table 6.7: Electron beam parameters - after space charge neutralization (170 GHz) [177].

Scenario	V_b (kV)	I_b (A)	α	$\beta_\perp$
Before space charge neutralization	100.371	90	1.3417	0.4400
After 60% space charge neutralization	101.948	90	1.3087	0.4388
After 100% space charge neutralization	103.00	90	1.2893	0.4381

Table 6.8: Electron beam parameters for the start-up behavior - before space charge neutralization (204 GHz) [177].

V_{acc} (kV)	V_m (kV)	I_b (A)	V_b (kV)	α	$\beta_\perp$
108	44.90	93.00	105.478	1.3078	0.4442
100	43.50	91.00	97.762	1.0640	0.3955
90	42.00	88.00	87.915	0.8523	0.3375
80	41.00	86.00	78.020	0.7087	0.2868
70	40.00	84.00	68.121	0.5388	0.2230
60	39.00	83.00	58.097	0.3542	0.1468

Table 6.9: Electron beam parameters - after space charge neutralization (204 GHz) [177].

Scenario	V_b (kV)	I_b (A)	α	$\beta_\perp$
Before space charge neutralization	105.478	93	1.3078	0.4442
After 60% space charge neutralization	106.991	93	1.2791	0.4431
After 100% space charge neutralization	108.00	93	1.2629	0.4424

Table 6.10: Electron beam parameters for the start-up behavior - before space charge neutralization (236 GHz) [177].

V_{acc} (kV)	V_m (kV)	I_b (A)	V_b (kV)	α	$\beta_\perp$
110	37.50	85.00	107.873	1.30	0.4468
100	37.00	83.00	98.131	1.0159	0.3874
90	36.50	80.00	88.235	0.8571	0.3390
80	36.00	78.00	78.293	0.7392	0.2956
70	35.50	76.00	68.387	0.5511	0.2275
60	35.00	75.00	58.348	0.3938	0.1615

Table 6.11: Electron beam parameters - after space charge neutralization (236 GHz) [177].

Scenario	V_b (kV)	I_b (A)	α	$\beta_\perp$
Before space charge neutralization	107.873	85	1.30	0.4468
After 60% space charge neutralization	109.149	85	1.2754	0.4459
After 100% space charge neutralization	110.00	85	1.2605	0.4452

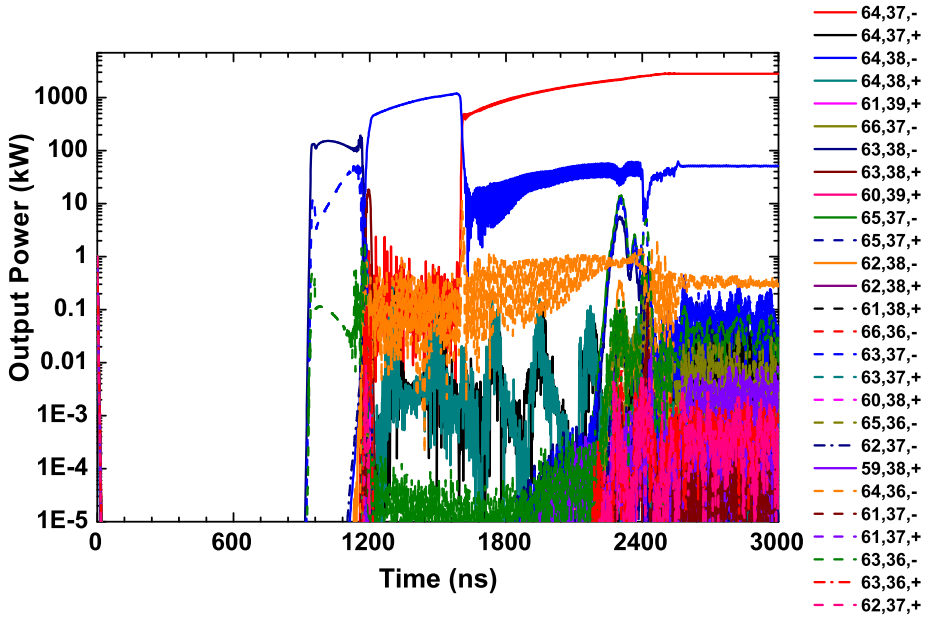

Figure 6.14: Multi-mode calculations - Start-up behavior of the desired mode $TE_{64,37,-}$ mode at 236 GHz before space charge neutralization with $V_b = 58.348$-107.873 kV, $B_o = 9.840$ T, α and I_b vary accordingly. In this output RF power, P_{out} (kW) is illustrated in logarithmic scale [176], [93].

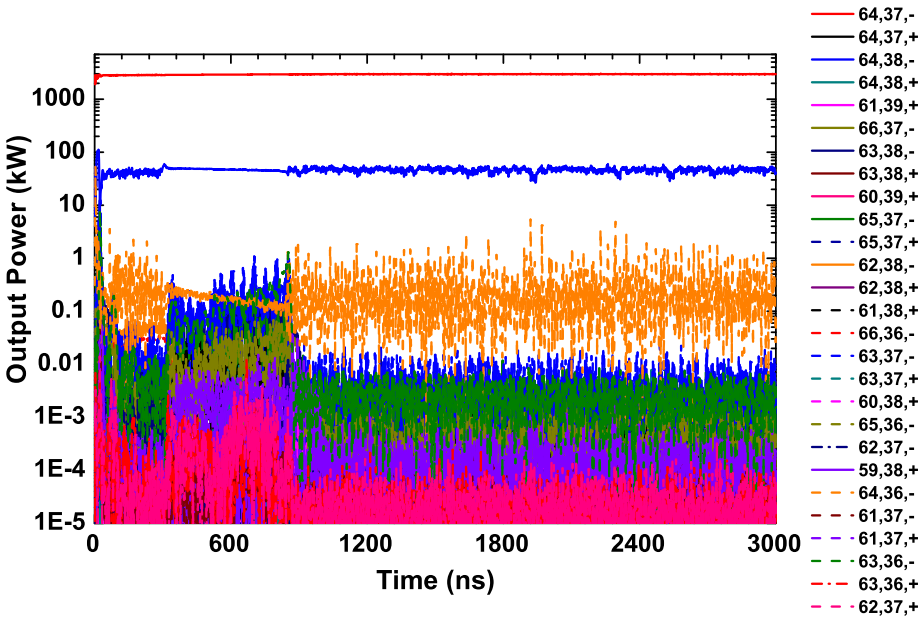

Figure 6.15: Multi-mode calculations - Start-up behavior of the desired mode $TE_{64,37,-}$ mode at 236 GHz after 60% space charge neutralization with $V_b = 107.873$-109.149 kV, $B_o = 9.840$ T, α and I_b vary accordingly. In this output RF power, P_{out} (kW) is illustrated in logarithmic scale [176], [93].

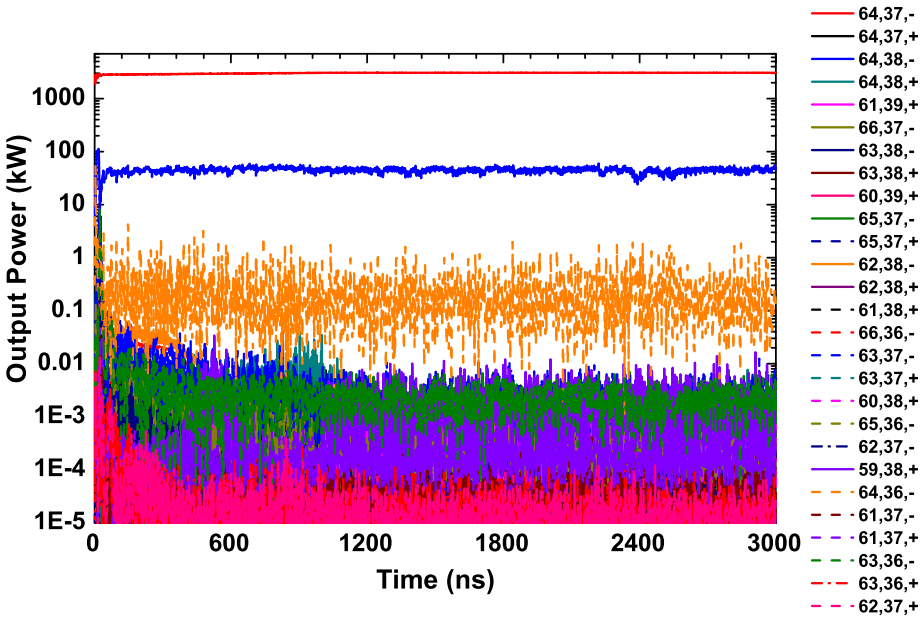

Figure 6.16: Multi-mode calculations - Start-up behavior of the desired mode $TE_{64,37,-}$ mode at 236 GHz after 100% space charge neutralization with $V_b = 107.873$-110.00 kV, $B_o = 9.840$ T, α and I_b vary accordingly. In this output RF power, P_{out} (kW) is illustrated in logarithmic scale [176], [93].

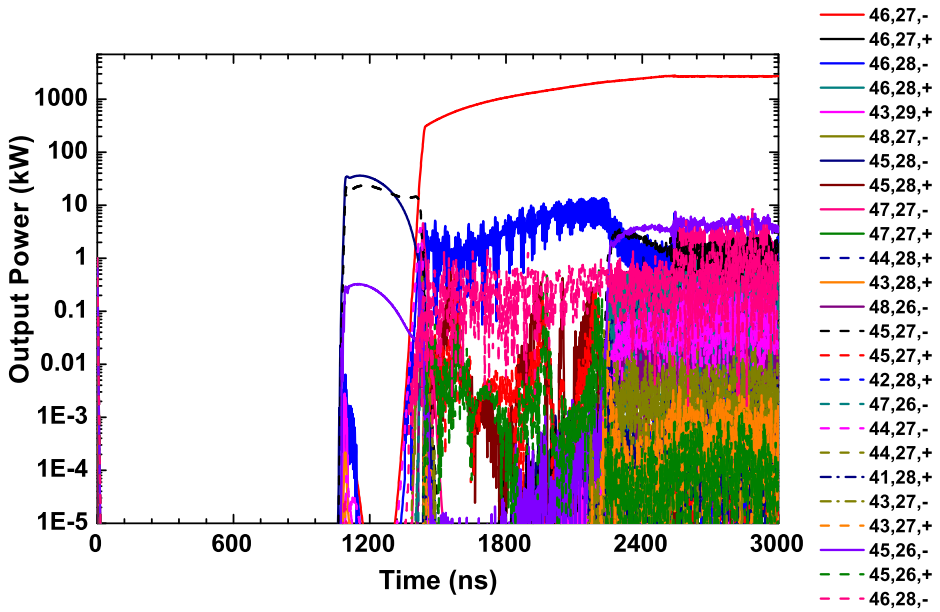

Figure 6.17: Multi-mode calculations - Start-up behavior of the desired mode $TE_{46,27,-}$ mode at 170 GHz before space charge neutralization with $V_b = 58.012$-100.371 kV, $B_o = 6.985$ T, α and I_b vary accordingly. In this output RF power, P_{out} (kW) is illustrated in logarithmic scale [176], [93].

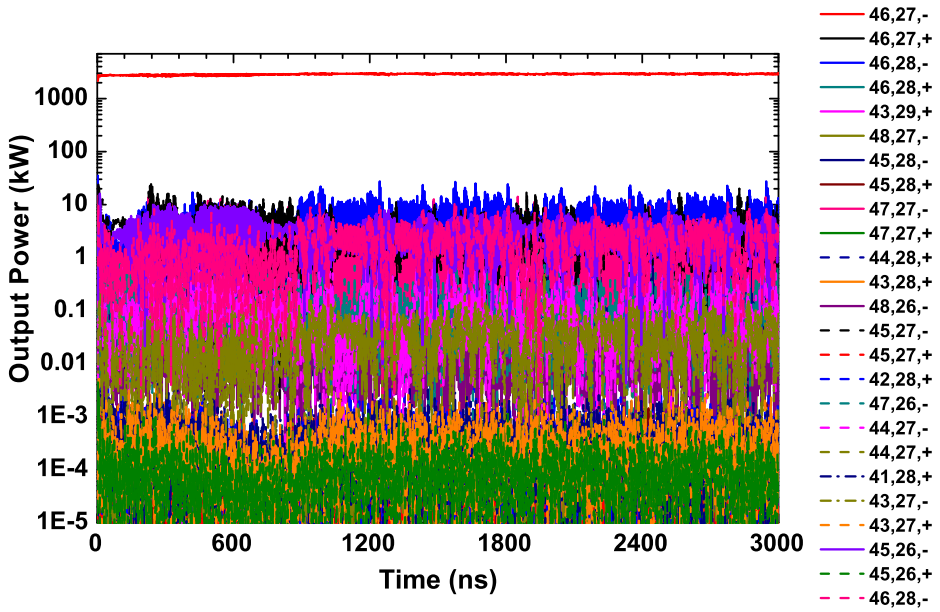

Figure 6.18: Multi-mode calculations - Start-up behavior of the desired mode $TE_{46,27,-}$ mode at 170 GHz after 60% space charge neutralization with $V_b = 100.371$-101.948 kV, $B_o = 6.985$ T, α and I_b vary accordingly. In this output RF power, P_{out} (kW) is illustrated in logarithmic scale [176], [93].

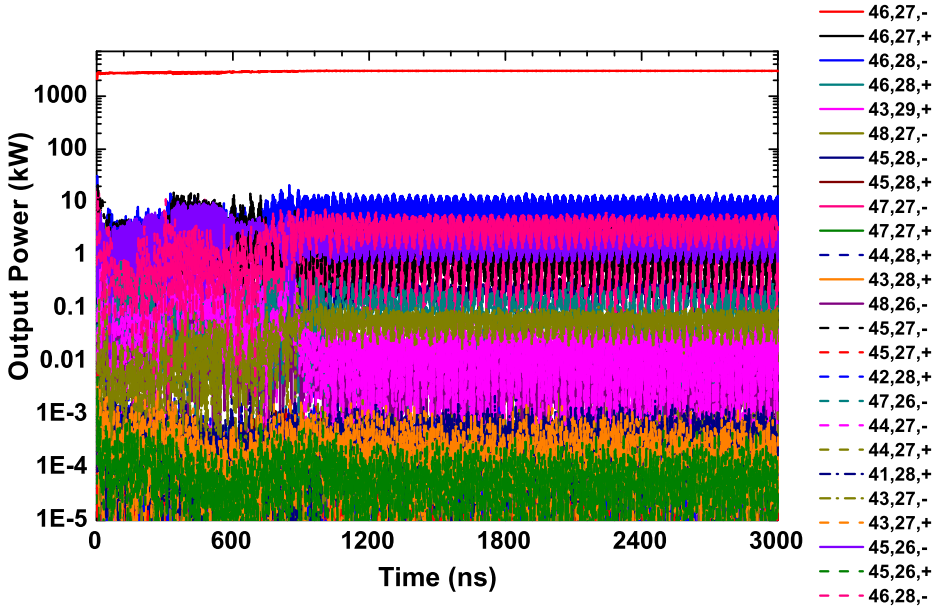

Figure 6.19: Multi-mode calculations - Start-up behavior of the desired mode $TE_{46,27,-}$ mode at 170 GHz after 100% space charge neutralization with $V_b = 100.371$-103.00 kV, $B_o = 6.985$ T, α and I_b vary accordingly. In this output RF power, P_{out} (kW) is illustrated in logarithmic scale [176], [93].

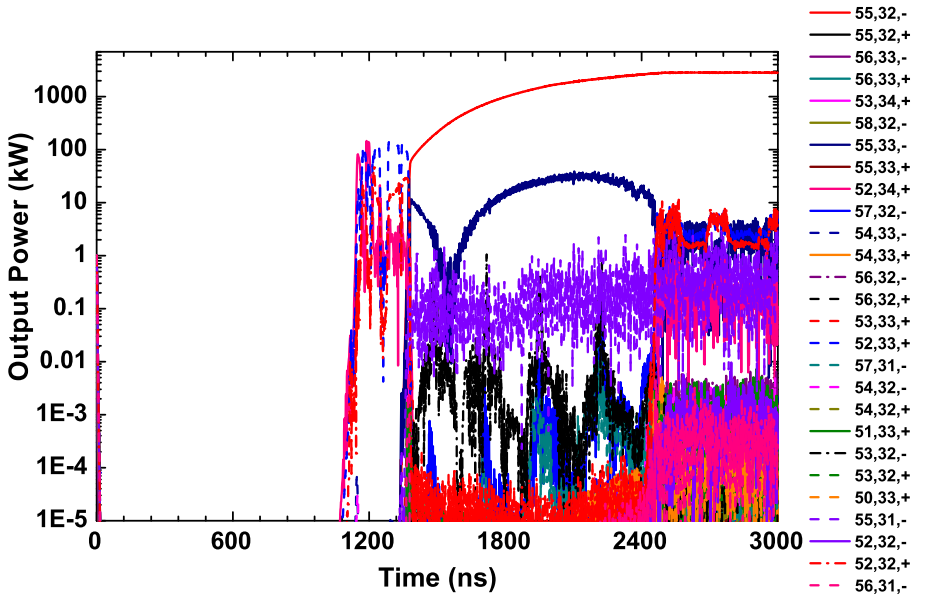

Figure 6.20: Multi-mode calculations - Start-up behavior of the desired mode $TE_{55,32,-}$ mode at 204 GHz before space charge neutralization with $V_b = 58.097$-105.478 kV, $B_o = 8.435$ T, α and I_b vary accordingly. In this output RF power, P_{out} (kW) is illustrated in logarithmic scale [176], [93].

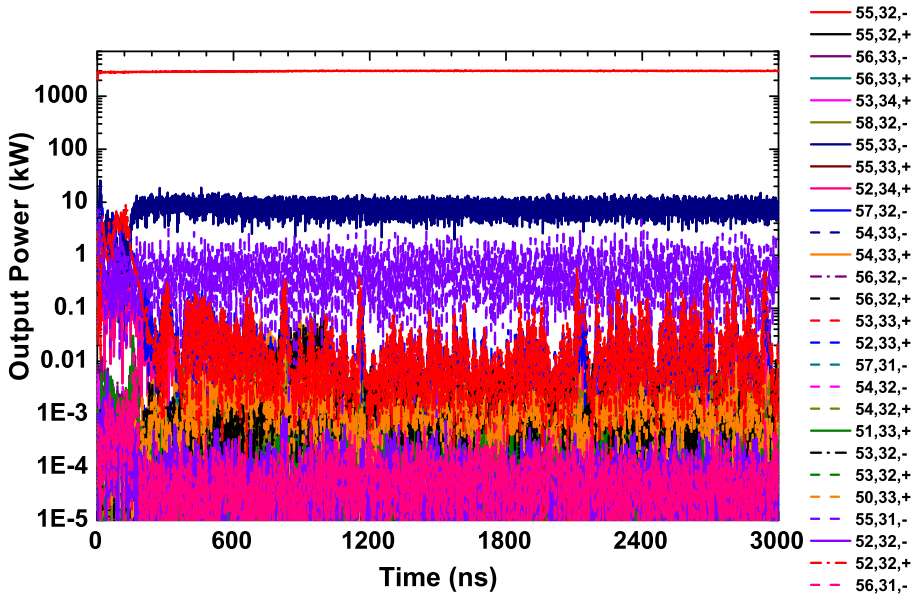

Figure 6.21: Multi-mode calculations - Start-up behavior of the desired mode $TE_{55,32,-}$ mode at 204 GHz after 60% space charge neutralization with $V_b = 105.478$-106.991 kV, $B_o = 8.435$ T, α and I_b vary accordingly. In this output RF power, P_{out} (kW) is illustrated in logarithmic scale [176], [93].

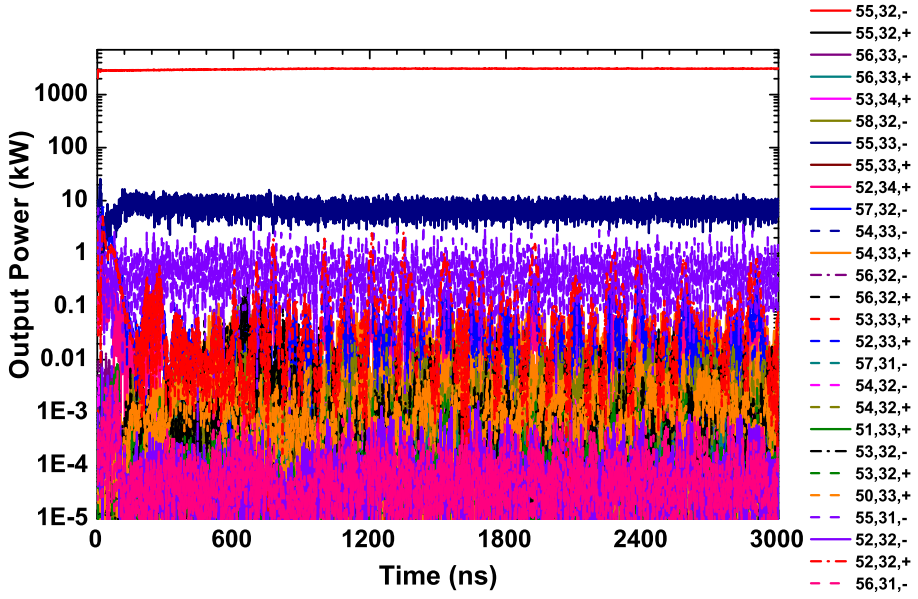

Figure 6.22: Multi-mode calculations - Start-up behavior of the desired mode $TE_{55,32,-}$ mode at 204 GHz after 100% space charge neutralization with $V_b = 105.478$-108.00 kV, $B_o = 8.435$ T, α and I_b vary accordingly. In this output RF power, P_{out} (kW) is illustrated in logarithmic scale [176], [93].

6.6 Conclusions

The design studies of an advanced DEMO class coaxial cavity gyrotron with triangular corrugated insert have been presented in this chapter. Output RF power of the proposed gyrotron has been targeted to 3 MW for reducing the number of RF sources in the ECRH system of a DEMO tokamak. To support this high power operation at the desired operating frequency of 236 GHz the modes with the eigenvalue higher than 200 were considered. By considering all design constraints and multi-frequency operation capability, the cavity modes have been selected as $TE_{46,27}$/ $TE_{55,32}$/$TE_{64,37}$ at the respective frequencies 170/204/236 GHz. The interaction cavity geometry has been optimized through cold cavity calculation, and mode competition studies were performed. The initial beam parameters and the magnetic field were optimized through single mode calculations. A coaxial MIG has been designed for generating the required beam parameters to support this multi-frequency operation. The start-up behavior calculations have been carried out at all the three desirable frequencies with beam-space charge neutralization. These calculations reveal that RF output power of 3 MW can be achieved at all the three desirable frequencies of the proposed DEMO gyrotron.

Chapter 7

Analysis of the RF Interaction Cavity with Misaligned Triangular Corrugated Coaxial Insert

7.1 Introduction

Compared to conventional cavity gyrotrons, coaxial cavity gyrotrons offer several advantages like reducing mode competition, operation at higher power levels because of reduced voltage depression. However, practical development of coaxial cavity gyrotron faces serious issues like proper cooling of the insert, mechanical support of insert as the insert is extended from the cathode of the electron gun to the non-linear taper section. Ideally in coaxial cavity gyrotrons, coaxial insert, annular electron beam and outer resonant cavity all should lie in the same axis and should form concentric circles. However, achieving perfect alignment practically is not possible, and there is always some misalignment between either the axes of the insert and outer resonator or the axes of the electron beam and the outer resonator or all the three axes. Additionally, in gyrotrons, magnetic axis does not form a straight line due to the misalignment in the manufacture of different superconducting coils. This leads to the radial displacement of the gyrating hollow beam. However, in the assembling of gyrotrons, the electron beam can be aligned with the insert axis or outer resonator axis. Proper alignment of the electron beam can also be achieved by using dipole coils. All these misalignments will have serious effect on the operation of gyrotron.

Misalignment in the electron beam creates an unequal voltage depression. This leads to spread in the electron beam energy and consequently reduces the interaction efficiency. Structural misalignment of the inner rod with the resonant cavity changes the field pattern of the TE mode, and axisymmetry of the fields got affected. This changes the field maxi-

mum of the TE mode to the different radial position. Due to misalignment in the electron beam, the electron beam cannot be positioned at the field maximum position of the TE mode. Thus all these misalignments together, reduce the interaction efficiency, output RF power, and stability of the gyrotron. In this chapter, misalignment of the triangular corrugated insert in a coaxial cavity gyrotron is discussed. First, the surface impedance model (SIM) is used for the analysis of the fields in the misaligned system. In this case, fields in the slots are assumed to be homogeneous with a condition that the number of slots should be greater than twice the azimuthal index of the cavity mode. Later, the analysis of the misaligned system is extended for the general case using full wave approach, spatial harmonics method (SHM). The mathematical formulation is derived for the dispersion relation of TE modes in the coaxial cavity with misaligned triangular corrugated insert through both of the approach. Effect of insert misalignment on the eigenvalue and the oscillating frequency of modes in the triangular corrugated coaxial cavity are studied.

7.2 Field Analysis using SIM

Earlier studies on the effect of insert misalignment on the fields of the TE modes in the coaxial cavity were performed through point matching, finite differences, and truncation of series [198], [199], [200], [201]. Later conformal transformation was used in [202], [203] and the Helmholtz equation in the misaligned system was transformed to a weighted Helmholtz equation in a perfect coaxial system. In 1997, Dumbrajs *et al.* studied the effect of insert misalignment in a coaxial cavity gyrotron with rectangular corrugated insert [204]. In this paper, the fields of the modes were represented through azimuthal harmonics then Graff's addition theorem was used in transforming the field expressions of the mode in the misaligned system. In 2000, Zhang *et al.* performed the insert misalignment studies in a coaxial cavity gyrotron with smooth wall insert [205]. In this paper mathematical formulation for the dispersion relation of cavity modes in the misaligned system was derived by using coordinate transformation through Graff's addition theorem and superposition of cylindrical wave functions. In this section, field analysis of the coaxial cavity with misaligned triangular corrugated insert is carried out using SIM approach.

7.2.1 Cavity with Perfectly Aligned Corrugated Coaxial Insert

Figure 7.1 shows cross section of a coaxial cavity with misaligned insert and a perfect coaxial cavity. For better understanding, coaxial cavity with misaligned insert is referred as system A and perfect structure is referred as system B. Field quantities in system B

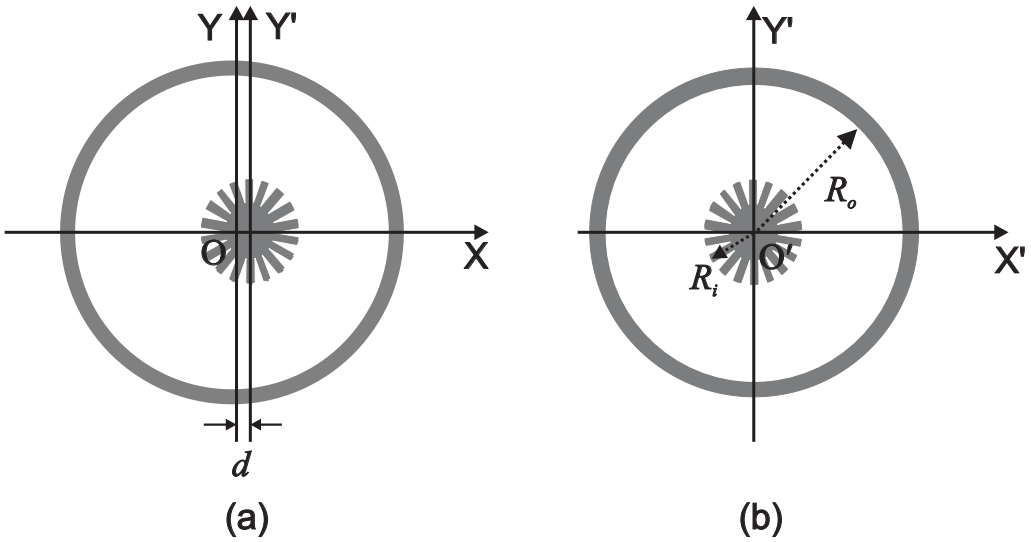

Figure 7.1: Cross section of a triangular corrugated coaxial cavity, (a) misaligned structure (system A), (b) perfect cavity (system B) [74].

are represented by a prime. Field equations of the perfect structure are explained in this section and that for the misaligned coaxial cavity are derived in the following section. R_o and R_i are the radius of the outer cavity and of the inner rod, respectively. N is the number of the triangular slots on the insert, R_d is the depth of the slot and S is the width of the slot. As the number of corrugations are greater than the twice of the azimuthal index of the operating mode, fields inside the slots are homogeneous. Therefore, SIM approach can be used for the field analysis of the coaxial cavity.

The fields inside the triangular slots are given by [74]

$$E_{r'_{slot}}(r',z) = 0$$

$$E_{\phi'_{slot}}(r',z) = k'_{\perp} A_{01} J'_0(k'_{\perp} r') V_{mn} \hat{f}_z$$

$$H_{z_{slot}}(r',z) = -j \frac{k'^2_{\perp}}{k'_o Z_o} A_{01} J_0(k'_{\perp} r') V_{mn} \hat{f}_z \tag{7.1}$$

Axial magnetic field in the coaxial region of the cavity is given by

$$H_{z_{coax}}(R',\phi',z) = \sum_m -j \frac{k'^2_{\perp}}{k'_o Z_o} A_{mn} Z_m(k'_{\perp} R') V_{mn} exp(-jm\phi') \hat{f}_z \tag{7.2}$$

where

$$Z_m(k'_{\perp} R') = J_m(k'_{\perp} R') + B_{mn} Y_m(k'_{\perp} R')$$

V_{mn} is the maximum of axial field structure and $\hat{f}_z$ is the normalized field structure.

Applying the boundary condition at the outer cavity, B_{mn} is given by

$$B_{mn} = -\frac{J_m^{'}(\chi)}{Y_m^{'}(\chi)}$$

where $\chi = k_{\perp}^{'} R_o$ is the eigenvalue of the mode.

By equating the impedance at the interface of the coaxial region and the slot region, dispersion relation for the coaxial cavity with triangular corrugated insert is obtained and is given by

$$J_m^{'}(\chi)\left(Y_m^{'}(\chi/C) + WY_m(\chi/C)\right) - Y_m^{'}(\chi)\left(J_m^{'}(\chi/C) + WJ_m(\chi/C)\right) = 0 \tag{7.3}$$

where W is the normalized impedance at the insert surface and is given by

$$W = \frac{l}{S}\frac{J_1(\chi/C_d)}{J_0(\chi/C_d)} \tag{7.4}$$

and $C_d = R_o/R_d$.

Equation (7.3) is clearly emphasizing the well known fact that single mode can exist in the perfect coaxial cavity with triangular corrugated insert and for different values of azimuthal index m, eigenvalues are different.

7.2.2 Cavity with Misaligned Corrugated Coaxial Insert

In the coaxial cavity with misaligned insert, axis of the insert is misaligned with that of the outer cavity by a distance of d and is shown in Figure 7.1(a). By using the coordinate transformation, radial component of the fields in system A is related to that of system B by [205]

$$\overrightarrow{R} = \overrightarrow{R^{'}} + \overrightarrow{d} \tag{7.5}$$

Graff addition theorem is used for the transformation of the fields in system B to system A. For the triangle $\Delta OPO^{'}$ shown in Figure 7.2, Graff addition formulas are given by [206]

$$J_m(k_{\perp}R^{'}).exp(-jm(\phi^{'} - \phi)) = \sum_{p=-\infty}^{\infty} J_p(k_{\perp}d)J_{m+p}(k_{\perp}R).exp(-jp\phi)$$

$$Y_m(k_{\perp}R^{'}).exp(-jm(\phi^{'} - \phi)) = \sum_{p=-\infty}^{\infty} J_p(k_{\perp}d)Y_{m+p}(k_{\perp}R).exp(-jp\phi) \tag{7.6}$$

For the transverse electric modes, axial magnetic field in the coaxial region of system B

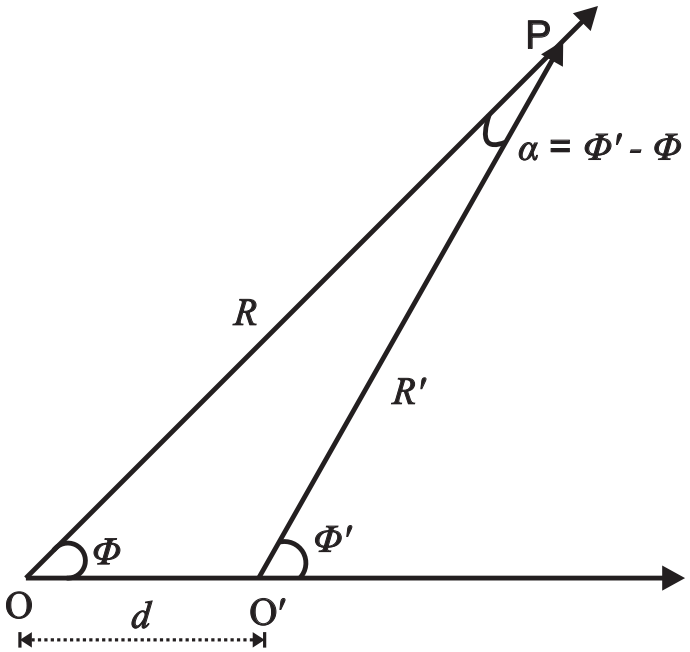

Figure 7.2: Coordinate system used for the analysis of the coaxial cavity with misaligned inner rod.

is given as follows

$$H_{z_{coax}}(R,\phi,z) = \sum_{m}\sum_{p=-\infty}^{\infty} -j\frac{k_{\perp}^2}{k_o Z_o} A_{mn} J_p(k_{\perp}d) Z_{m+p}(k_{\perp}R) V_{mn}.exp(-j(m+p)\phi)\hat{f}_z \quad (7.7)$$

By applying inner and outer boundary condition for system A, dispersion relation is given by

$$\sum_{m}\sum_{p=-\infty}^{\infty} J_p(\chi d/R_o)\left[J'_{m+p}(\chi)\left(Y'_m(\chi/C)+WY_m(\chi/C)\right) - Y'_{m+p}(\chi)\left(J'_m(\chi/C)+WJ_m(\chi/C)\right)\right] = 0 \quad (7.8)$$

By letting $m+p=i$, eigenvalue equations for the transverse electric modes in the triangular corrugated coaxial cavity with misaligned insert can be written as

$$\sum_m J_{i-m}(\chi d/R_o)\left[J_i'(\chi)\left(Y_m'(\chi/C)+WY_m(\chi/C)\right)\right.$$
$$\left.-Y_i'(\chi)\left(J_m'(\chi/C)+WJ_m(\chi/C)\right)\right]=0$$
$$i=0,\pm1,\pm2,\pm3... \quad (7.9)$$

When $d=0$ in equation (7.9), the dispersion relation of the coaxial cavity with misaligned insert is restored to equation (7.3), the dispersion relation of the perfect coaxial cavity, by using the Bessel function properties and are given by [206]

$$\begin{aligned} J_{i-m}(\chi d/R_o) &= 1, \quad for \quad m=i \\ &= 0, \quad for \quad m\neq i \end{aligned} \quad (7.10)$$

From equation (7.9), it is understood that in the misaligned coaxial cavity, single mode eigenvalue solution cannot satisfy the boundary conditions.

7.2.3 Eigenvalue Calculations

A 170 GHz, 2 MW triangular corrugated coaxial cavity gyrotron is considered for the present analysis. Operating mode is chosen as $TE_{34,20}$, the radius of the cavity is 29.54 mm and the mid-section length of the cavity is 16 mm. Figure 7.3 shows the eigenvalue curves for $TE_{34,20}$ mode in the perfect coaxial cavity by solving equation (7.3) for varying depth of slot. In a coaxial cavity with down tapered insert, operating C (=R_o/R_i) range is selected such that, eigenvalue curve of the main mode lies in the constant region and that of the competing modes lie in the negative slope region. Positive slope in the eigenvalue curve is avoided since this increases the ohmic wall loading on the insert. In the present design, insert radius at the midsection of the cavity is chosen as 7.81 mm, width and the depth of the slots are 0.40 mm and 0.45 mm, respectively.

For C = 3.78, the effect of insert misalignment on the eigenvalue of the operating mode $TE_{34,20}$ is calculated using equation (7.9). In this calculation i varies from -6 to +6. As shown in Figure 7.4, in a triangular corrugated coaxial cavity eigenvalue increases with the insert misalignment, however in case of a non-corrugated insert ($R_d = 0.0$ mm), as shown in Figure 7.5, eigenvalue decreases with the misalignment. It is to be observed that for C = 3.78, in case of triangular corrugated insert ($R_d = 0.45$ mm), eigenvalue lies in the negative slope region, but in case of non-corrugated insert ($R_d = 0.0$ mm), eigenvalue lies in the positive slope region.

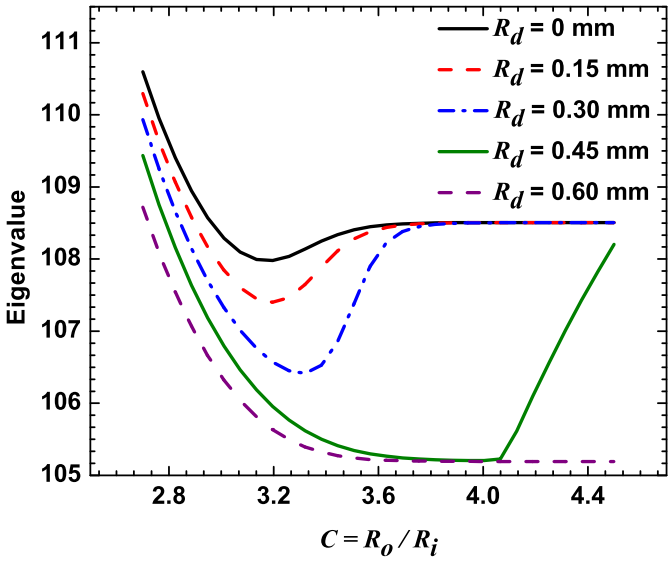

Figure 7.3: Eigenvalue of $TE_{34,20}$ mode in a perfect coaxial cavity for varying slot depth.

The oscillating frequency of the $TE_{m,n}$ mode is given by

$$f = \frac{c}{2\pi}\sqrt{k_\perp^2 + k_z^2} \tag{7.11}$$

where, $k_\perp$ and k_z are the cutoff and axial wavenumber, respectively. k_z is given by $q\pi/L$, where, $q = 1, 2, 3, \ldots$ and L is the midsection length of the cavity.

Figure 7.6 shows shift in eigenfrequency of the $TE_{34,20}$ mode with insert misalignment. From Figure 7.6, it is understood that eigenfrequency of the mode increases with the insert misalignment in the coaxial cavity.

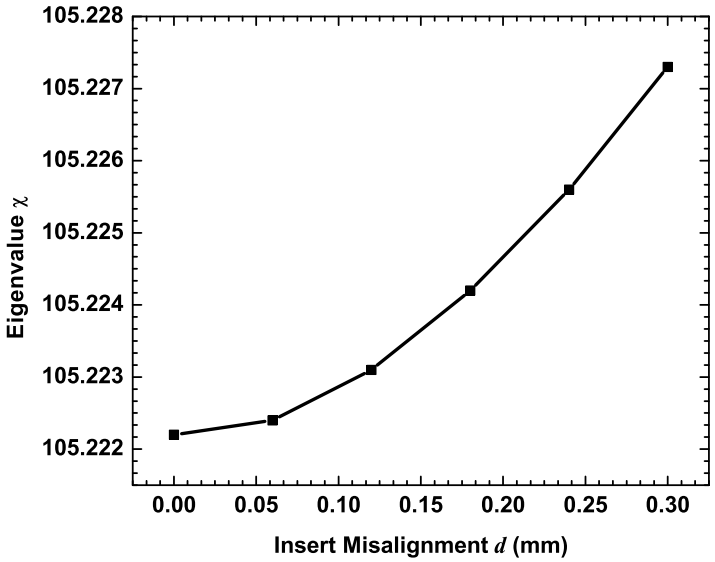

Figure 7.4: Variation in eigenvalue of $TE_{34,20}$ mode with insert misalignment in the coaxial cavity with triangular corrugated insert ($R_d = 0.45$ mm), where radii ratio $C = 3.78$.

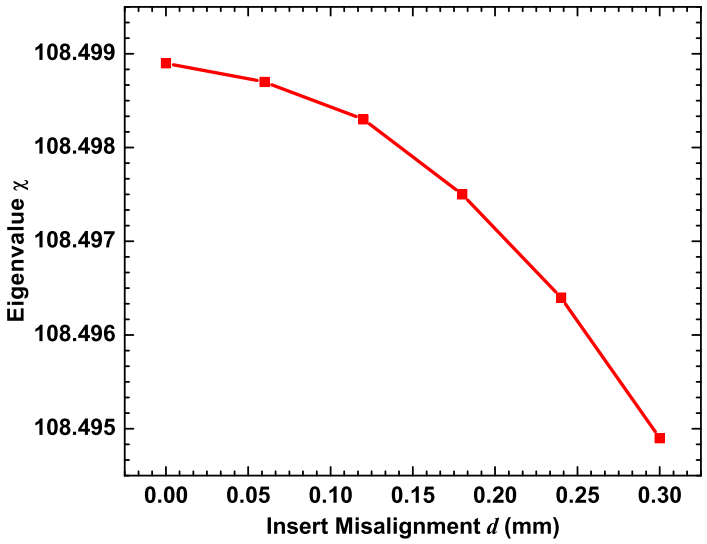

Figure 7.5: Variation in eigenvalue of $TE_{34,20}$ mode with insert misalignment in the coaxial cavity with non-corrugated corrugated insert ($R_d = 0.0$ mm), where radii ratio $C = 3.78$.

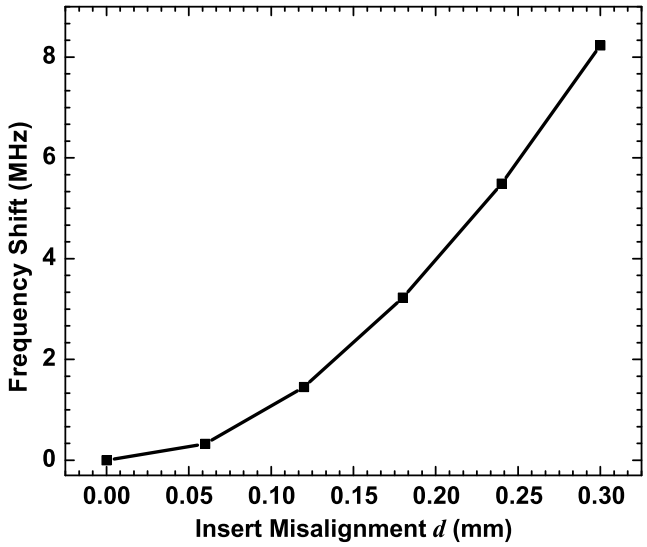

Figure 7.6: Shift in eigenfrequency of $TE_{34,20}$ mode due to insert misalignment in the triangular corrugated coaxial cavity ($R_d = 0.45$ mm), where radii ratio $C = 3.78$.

7.3 Field Analysis using Full Wave Approach

Analysis of the coaxial cavity with misaligned insert carried out using SIM is simple and effective. However, the assumptions of the homogeneous field in the slots is possible only when the number of slots on the insert wall is greater than twice the azimuthal index of the cavity mode. This condition cannot be achieved in all situations particularly when the higher order mode is chosen as the operating cavity mode. Full wave analysis of the corrugated coaxial cavity was carried out using the surface integral equation (SIE) in which the assumption of homogeneity of the fields in the slots is not required [160]. Using this SIE method, two different types of coaxial cavities one with wedge shape corrugations on the insert wall and another with corrugations on the outer resonator wall were analyzed in [96]. Another full wave technique that is popularly used is the space harmonics method (SHM) in which fields are expressed in terms of spatial eigenfunctions [207]. Different waveguide systems are analyzed using this SHM technique [207], [208]. Mathematical formulation of the calculation of eigenvalue and ohmic losses in a coaxial cavity with triangular corrugated insert using SHM was carried out in [163]. In this section, fields in the triangular corrugated coaxial cavity with the misaligned insert are expanded through space harmonics, and the dispersion relation for the cavity modes are derived by applying proper boundary conditions.

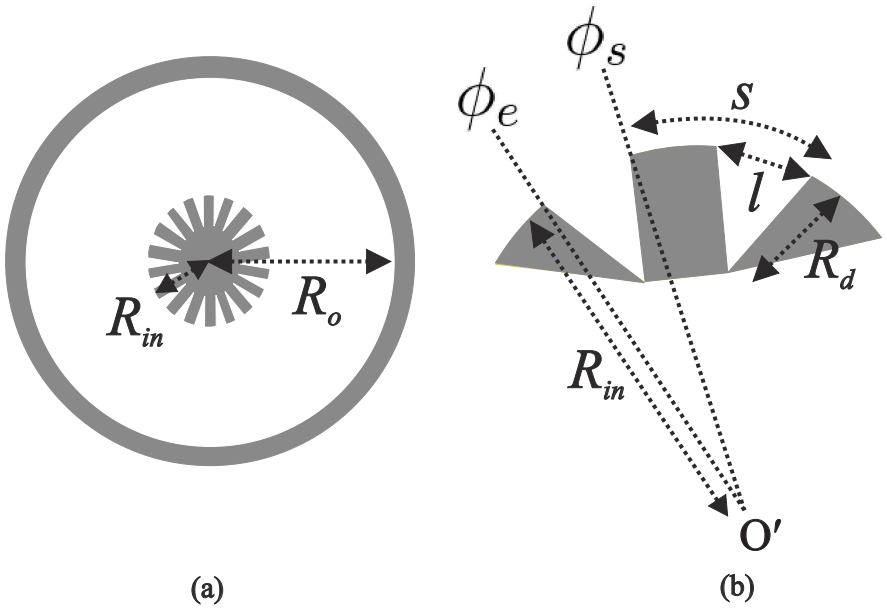

Figure 7.7: Schematic of coaxial cavity with triangular corrugations on the insert slot section [74].

7.3.1 Mathematical Formulation

Cross section of a triangular corrugated coaxial cavity with misaligned insert (system A) and perfect coaxial cavity (system B) are shown in Figure 7.1 of the previous section. Variables representing the electromagnetic fields in the system B are indicated with prime. For the better understanding schematic of the triangular corrugated coaxial cavity is redrawn in Figure 7.7. R_o is the outer cavity radius, R_{in} is the coaxial insert radius, N is the number of triangular corrugations on the coaxial insert, R_d is the depth of a single corrugation l is the slot opening and s be the period of a corrugation. ϕ_e and ϕ_s are the azimuthal variations of the slot, and the angular width of the slot is given by ϕ_L=ϕ_e-ϕ_s. By the general solution of Helmholtz equation for TE modes the axial magnetic field of system B is given by [205],

$$H_{z_{coax}}(R^{'},\phi^{'},z)=\sum_{m}-j\frac{k_{\perp}^{'2}}{k_o^{'}Z_o}A_mZ_m(k_{\perp}^{'}R^{'})V_{mn}exp(jm\phi^{'})\hat{f}_z \tag{7.12}$$

where

$$Z_m(k_{\perp}^{'}R^{'})=J_m(k_{\perp}^{'}R^{'})+B_{mn}Y_m(k_{\perp}^{'}R^{'})$$

V_{mn} is the maximum of axial field structure, $\hat{f}_z$ is the normalized field structure and B_{mn} is given by,

$$B_{mn}=-\frac{J_m^{'}(\chi)}{Y_m^{'}(\chi)}$$

In system A, the axis of the insert is shifted from the axis of the outer cavity by a displacement of d as shown in Figure 7.1(a). For further calculations, the radial components in system A and in system B should be related. This is done by using a coordinate transformation [205] given as,

$$\overrightarrow{R} = \overrightarrow{R^{'}} + \overrightarrow{d} \tag{7.13}$$

In order to transform the field equations from coordinate system of system B to that of system A, Graff addition theorem is used. For the triangle $\Delta OPO^{'}$ shown in Figure 7.2, Graff addition formulas are given by [206],

$$J_m(k_\perp R^{'}).exp(jm\phi^{'}) = \sum_{p=-\infty}^{\infty} J_p(k_\perp d)J_{m+p}(k_\perp R).exp(j(m+p)\phi)$$

$$Y_m(k_\perp R^{'}).exp(jm\phi^{'}) = \sum_{p=-\infty}^{\infty} J_p(k_\perp d)Y_{m+p}(k_\perp R).exp(j(m+p)\phi)$$

Applying these transformations to equation (7.12), axial component of magnetic field in the system A is given by,

$$H_{z_{coax}}(R,\phi,z) = \sum_m \sum_{p=-\infty}^{\infty} -j\frac{k_\perp^2}{k_o Z_o} A_m J_p(k_\perp d) Z_{m+p}(k_\perp R) V_{mn}.exp(j(m+p)\phi)\hat{f}_z \tag{7.14}$$

In the entire calculation, the fields in the slots are considered as the same as the case of perfect system B. However, the fields in the coaxial region are modified and the boundary conditions are also changed. The fields in the coaxial region of the misaligned system A are given by,

$$E_{r_{coax}} = \sum_m jA_m Z_{m+p}(k_\perp R)J_p(k_\perp d)V_{mn}\hat{f}_z exp(j(m+p)\phi).\left(\frac{m+p}{R}\right)$$

$$E_{\phi_{coax}} = k_\perp \sum_m A_m Z^{'}_{m+p}(k_\perp R)J_p(k_\perp d)V_{mn}\hat{f}_z.exp(j(m+p)\phi)$$

$$H_{z_{coax}} = -\frac{jk_\perp^2}{k_o Z_o}\sum_m A_m Z_{m+p}(k_\perp R)J_p(k_\perp d)V_{mn}\hat{f}_z.exp(j(m+p)\phi) \tag{7.15}$$

Here, p varies from $-\infty$ to ∞. In this analysis, slot on the insert is considered as a sectoral cylindrical waveguide of radius R_d and the coordinate system for the slot region $(r^{'}, \psi, z)$ is different from the coaxial region (R,ϕ,z). The new R_i due to the misalignment of the

insert d, is given by,

$$R_i = d.cos\phi + \sqrt{R_{in}^2 - d^2.sin^2\phi} \tag{7.16}$$

The fields inside the triangular slots are given by [163],

$$E_{r'_{slot}} = \sum_{l=0}^{\infty} B_l^i J_{k_l}(k_\perp r') \frac{k_l}{r'} sin\left[k_l\left(\psi + \frac{\psi_L}{2}\right)\right] V_{mn}\hat{f}_z$$

$$E_{\psi_{slot}} = k_\perp \sum_{l=0}^{\infty} B_l^i J'_{k_l}(k_\perp r') cos\left[k_l\left(\psi + \frac{\psi_L}{2}\right)\right] V_{mn}\hat{f}_z$$

$$H_{z_{slot}} = -\frac{jk_\perp^2}{k_o Z_o} \sum_{l=0}^{\infty} B_l^i J_{k_l}(k_\perp r') cos\left[k_l\left(\psi + \frac{\psi_L}{2}\right)\right] V_{mn}\hat{f}_z \tag{7.17}$$

where

$$k_l = \frac{2\pi l}{\psi_L}$$

and

$$\psi_L = 2sin^{-1}\left[\frac{R_i}{R_d} sin\frac{\phi_L}{2}\right]$$

The slot angle ψ is given by [163],

$$\psi = tan^{-1}\left(\frac{R_i sin(\phi - \phi_c)}{R_i cos(\phi - \phi_c) - S_0}\right)$$

$$\phi_c = \frac{\phi_s + \phi_e}{2}$$

$$S_0 = R_i cos(\phi_c - \phi_s) - \sqrt{R_d^2 - (R_i sin(\phi_c - \phi_s))^2}$$

B_l is the field magnitude, V_{mn} is the maximum of axial field structure and $\hat{f}_z$ is the normalized field structure. The boundary conditions governing the interface between the slot region and the coaxial region, is given by [163],

$$H_{z_{coax}}(R_i, \phi, z) = H_{z_{slot}}(R_{slot}, \psi, z); [for: \phi_s \leq \phi \leq \phi_e] \tag{7.18}$$

$$E_{\phi_{coax}}(R_i, \phi, z) = E_{\psi_{slot}}(R_{slot}, \psi, z); [for: \phi_s \leq \phi \leq \phi_e] \tag{7.19}$$

where,

$$R_{slot}(\psi) = R_d - \sqrt{(R_i sin(\phi - \phi_c) - R_d sin(\psi))^2 + (R_i cos(\phi - \phi_c) - R_d cos(\psi) - S_0)^2}$$

Substituting the corresponding field equations in the boundary condition (7.18) and applying the mode orthogonality property by multiplying with $cos\left[k_l\left(\psi + \frac{\psi_L}{2}\right)\right]$,

For every i^{th} slot,

$$\sum_{t=-\infty}^{\infty} A_t . J_t(k_\perp d) . R^i_{k_t} = B^i_l . R_{k_l} \tag{7.20}$$

$$R^i_{k_t} = \int_{-\frac{\psi_L}{2}}^{\frac{\psi_L}{2}} Z_{k_t}(k_\perp R_\phi) . exp(jk_t\phi^i) . cos\left[k_l\left(\psi + \frac{\psi_L}{2}\right)\right] d\psi$$

$$R_{k_l} = \int_{-\frac{\psi_L}{2}}^{\frac{\psi_L}{2}} J_{k_l}(k_\perp R_{slot}) . cos^2\left[k_l\left(\psi + \frac{\psi_L}{2}\right)\right] d\psi$$

where $k_t = m + t$.

Similarly, substituting the corresponding field equations in the boundary condition (7.19) and applying the mode orthogonality property by multiplying with $exp(-jk_u\phi)$ where $k_u = m + u$,

$$A_u . J_u(k_\perp d) . R_{k_u} = \sum_{i=1}^{N} \sum_{l=0}^{\infty} B^i_l R^i_{k_u} \tag{7.21}$$

$$R_{k_u} = \int_0^{2\pi} Z^{'}_{k_u}(k_\perp R_\phi) d\phi$$

$$R^i_{k_u} = \int_{\phi^i_s}^{\phi^i_e} J^{'}_{k_l}(k_\perp R_{slot}) . cos\left[k_l\left(\psi + \frac{\psi_L}{2}\right)\right] . exp(-jk_u\phi) d\phi$$

Substituting for B^i_l from equation (7.20) in equation (7.21) the final dispersion relation is obtained as:

$$\sum_{t=-\infty}^{\infty} A_t \, D_{ut} = 0 \qquad u = 0, \pm 1, \pm 2, ..., \pm\infty \tag{7.22}$$

$$D_{ut} = J_t(k_\perp d) \sum_{i=1}^{N} \sum_{l=0}^{\infty} \left(\frac{R^i_{k_t} . R^i_{k_u}}{R_{k_l}} - \delta_{ut} . R_{k_u} \right)$$

where

$$\delta_{ut} = 1, \quad for \quad u = t$$
$$= 0, \quad for \quad u \neq t$$

For a non-trivial solution, the determinant of D_{ut} must be zero. Solving this, the eigenvalue of a triangular corrugated coaxial cavity with misaligned insert can be obtained.

7.3.2 Eigenvalue Calculations

For the present studies, a 2 MW, 170 GHz coaxial cavity gyrotron operating with the cavity mode of $TE_{34,20}$ is considered. The coaxial cavity with triangular slots on the insert wall is considered as the interaction cavity. The radius of the outer cavity (R_o) is 29.54 mm, the depth of the triangular slots is 0.45 mm, and the midsection length of the interaction region is 16 mm. Using the SHM approach, variation in the eigenvalue of $TE_{34,20}$ mode with the insert misalignment for the radii ratio C = 3.78 is calculated and is shown in Figure 7.8. Shift in eigenfrequency of $TE_{34,20}$ mode with insert misalignment is shown in Figure 7.9. Variation in the eigenvalue of $TE_{34,20}$ mode with insert misalignment for the different number of slots on the insert is calculated using both approaches SIM and SHM and are shown in Figures 7.10-7.12. From the figures, it can be observed that as the number of slots increases eigenvalue calculated using SIM approaches the eigenvalue calculated through SHM approach.

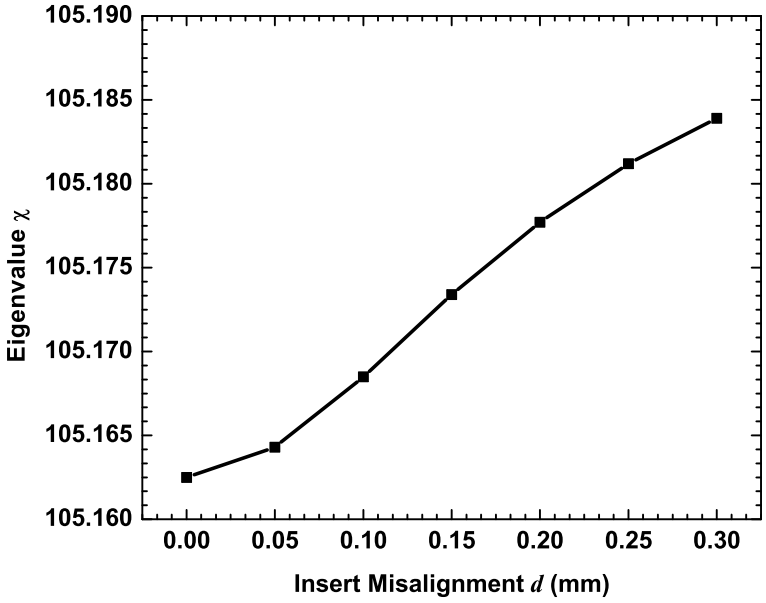

Figure 7.8: Variation in eigenvalue (calculated by SHM approach) of $TE_{34,20}$ mode with insert misalignment in the triangular corrugated coaxial cavity (N =75) where radii ratio C =3.78.

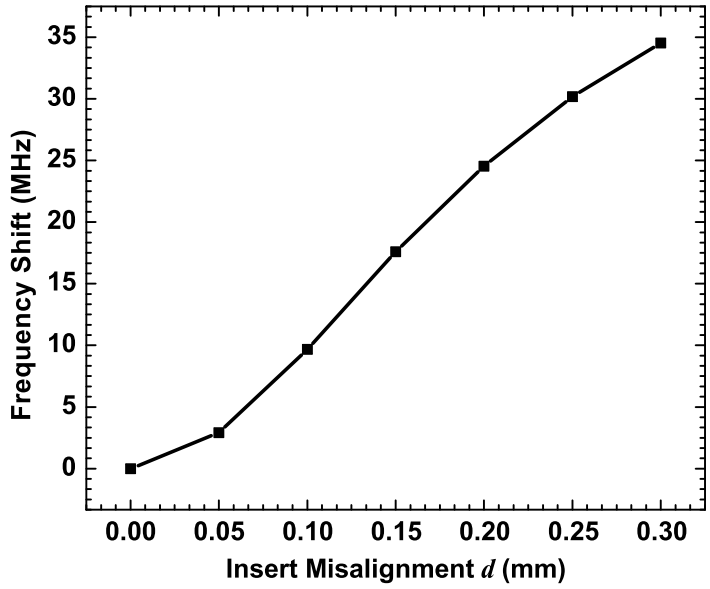

Figure 7.9: Shift in eigenfrequency (calculated by SHM approach) of $TE_{34,20}$ mode with insert misalignment in the triangular corrugated coaxial cavity (N =75) where radii ratio C =3.78.

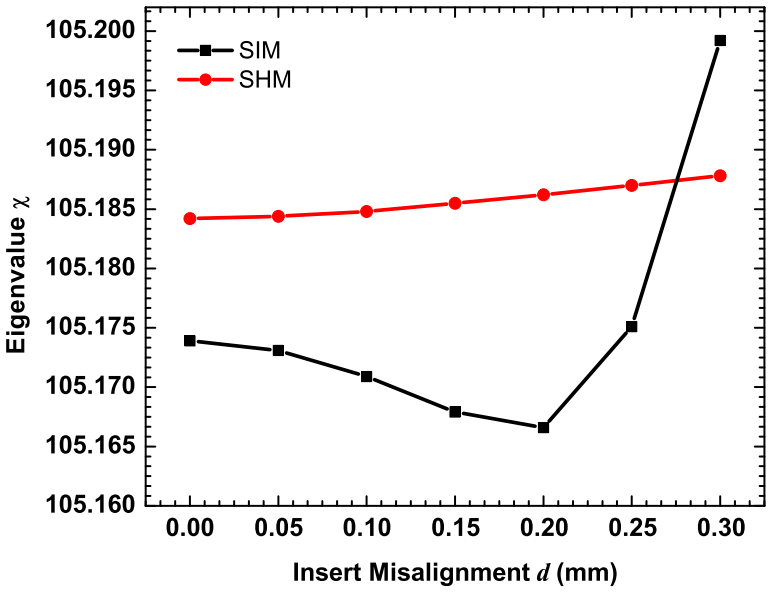

Figure 7.10: Variation in eigenvalue of $TE_{34,20}$ mode in a triangular corrugated coaxial cavity with insert misalignment for radii ratio C =3.78, N=50.

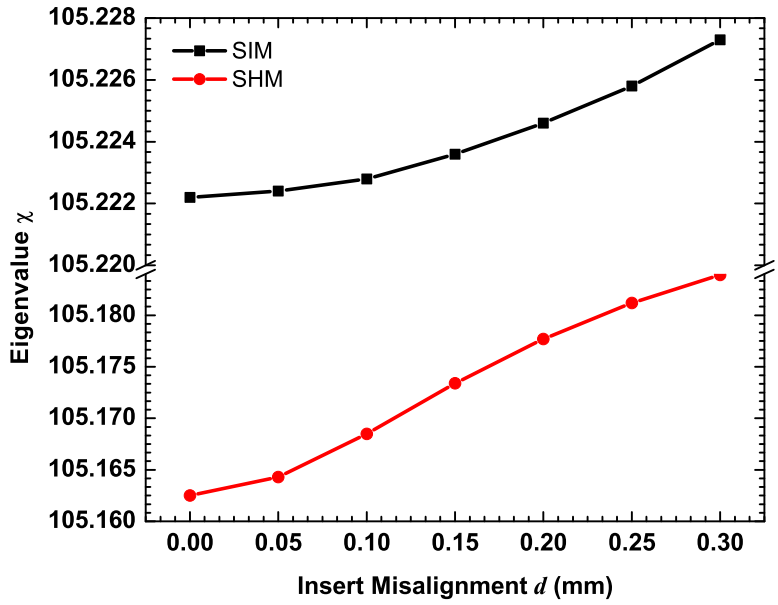

Figure 7.11: Variation in eigenvalue of $TE_{34,20}$ mode in a triangular corrugated coaxial cavity with insert misalignment for radii ratio C =3.78, N=75.

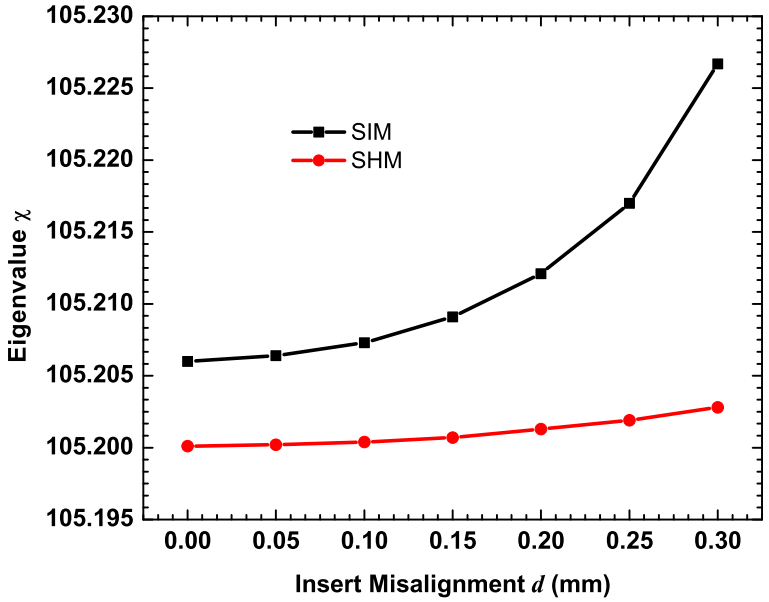

Figure 7.12: Variation in eigenvalue of $TE_{34,20}$ mode in a triangular corrugated coaxial cavity with insert misalignment for radii ratio C =3.78, N=125.

7.4 Conclusions

In the practical development of coaxial cavity gyrotron, there is always some misalignment exist between the axes of the outer resonant cavity and the coaxial insert. Misalignment in the insert changes the field structure of the operating cavity mode in the interaction region, and these effects should be properly considered. In this chapter effect of insert misalignment in the triangular corrugated coaxial cavity for megawatt class gyrotron has been carried out. Field analysis of the coaxial cavity with misaligned insert has been carried out using SIM approach, and later the analysis has been extended for the general case using full wave approach (SHM). The mathematical formulation for the dispersion relation of the cavity modes in the misaligned system has been derived using both the approaches. Effect of insert misalignment on the eigenvalue of the $TE_{34,20}$ mode in 170 GHz, 2 MW triangular corrugated coaxial cavity gyrotron has been studied. These studies quantitatively describe the effect of insert misalignment in the cavity modes of the triangular corrugated coaxial cavity gyrotron.

Chapter 8

Conclusion and Future Scope

8.1 Major contributions of this thesis

The prototypes of next-generation commercial fusion tokamaks like DEMO power plant are aimed for achieving stable operation over several hours and thereby increasing overall machine gain. It is foreseen that ECRH&CD systems would be applied in the various experimental stages of the fusion tokamaks. Initial design studies of the ECRH systems for these future machines suggest that for the effective heating of plasma, RF power will be required at the frequencies above 200 GHz. In the present work, feasibility analysis of the coaxial cavity gyrotrons have been carried out with the aim that these gyrotrons can find applications in the ECRH systems of the future fusion machines. Physical design studies of the major sub-assemblies of these coaxial cavity gyrotrons have been performed with the multifrequency operational capability to support multi-purpose applications. In the coaxial cavity gyrotrons cooling of the insert is critical and hence, in all these design studies coaxial cavity with triangular corrugated insert has been used as an interaction cavity. Triangular corrugations on the insert reduce the problem of localized heating on the insert walls. In addition, field analysis of the triangular corrugated coaxial cavity has been carried out to qualitatively understand the effect of the insert misalignment.

General introduction to thermonuclear fusion, requirement of high power RF waves in the fusion reactors for the ECRH application have been discussed in Chapter 1. Evolution of fast wave devices for the plasma heating application in the fusion tokamaks and different types of fast wave devices especially gyro-devices have also been in this chapter. Basic interaction principle, major sub-assemblies of gyrotron and literature survey on mega-watt class gyrotrons developed for plasma heating applications have been discussed in Chapter 2.

Feasibility studies of a 2 MW, dual frequency coaxial cavity gyrotron have been carried out in Chapter 3 and physical dimensions of the interaction cavity were determined

through the RF behavior studies. Desired operating frequencies (220/251.5 GHz) were chosen such that the designed gyrotron can be used for the multiple applications in the future fusion tokamaks. In the proposed space-power grid, 220 GHz is selected as the down link frequency and the designed gyrotron can also be considered as the millimeter wave source for the conversion of DC solar power into millimeter wave signal. By considering dual frequency operational criteria of coaxial cavity gyrotron and other technical constraints of megawatt class operation, cavity modes for the chosen frequencies (220/251.5 GHz) were selected as $TE_{48,30}/TE_{55,34}$. Physical parameters of the interaction cavity were optimized through cold cavity calculations and the calculated Q_d at the desired frequencies were 1597/2012. To understand the mode competition, product of Q_d and coupling coefficient were calculated for the desired mode pair and competing modes in the frequency range of $\pm$ 5 GHz around the desired frequencies. In the self-consistent single mode calculations, beam parameters and the magnetic field were optimized for maximum efficiency of $\approx$ 35% with the desired output power of 2 MW at both the operating frequencies. Time dependent multi mode calculations were performed in which all competing modes were considered along with the operating mode and beam parameters were varied over time. Simulation results predicted that there was a stable growth of RF power in the chosen cavity modes at the desired frequencies. Startup calculations were carried out for both before and after space charge neutralization cases with realistic beam parameters obtained from MIG studies. Startup calculation results confirmed that the 2 MW, CW dual regime operation is feasible in the proposed coaxial cavity gyrotron.

Physical design studies of the electron gun and output coupling system have been carried out in Chapter 4 to support dual regime operation of the proposed coaxial cavity gyrotron. RF behavior studies determined the beam parameters required for the stable operation at the desired frequencies. A triode type coaxial MIG was designed along with the magnetic guidance system for the generation of the required beam parameters and the magnetic field profile. Initial geometrical parameters of the electron gun were determined through Baird calculations and these were finally optimized along with the magnetic coils through the beam trajectory simulations. The designed electron gun generates a hollow electron beam with the beam radius of 10.838/10.834 mm, velocity ratio of 1.28/1.27, velocity ratio spread of 2.5/3.8% at the frequencies 220/251.5 GHz, respectively. Output coupling system of the gyrotron includes a nonlinear taper, a quasi-optical launcher and a RF window. The NLT was designed with raised cosine profile and the geometrical parameters of the NLT were optimized through particle swarm optimization technique. The designed NLT was analyzed through scattering matrix code. The transmission coefficient of the designed NLT is greater than 99% for both the chosen modes at their respective frequencies. The design studies of QOL were carried out through commercial tool LOT.

The advanced dimple wall launcher was designed to convert the chosen cavity modes into free space Gaussian like mode at their desired frequencies. The overall length of the designed launcher is 325.00 mm and Gaussian content of the output beam coming out of the launcher cut is greater than 95% for both the operating modes. A single disk CVD diamond window was designed with the thickness of 2.00 mm and the window has the transmission gap of 2 GHz around the desired frequencies. The transmission coefficient of the output beam passing through the common RF window at both the operating frequencies is around 99.97%.

In Chapter 5, design studies have been carried out to explore the 2 MW, CW operation at the third operating frequency of 283 GHz in an already designed dual regime coaxial cavity gyrotron. The cavity mode chosen for 283 GHz operation was $TE_{62,38}$ so that the same components of the gyrotron designed for the dual regime design studies can also be used for this new operation. Cold cavity calculation, mode competition studies and self consistent single mode calculations were performed for this 283 GHz operation. Time dependent multi-mode calculations and startup behavior studies were carried out and the results of these calculations confirmed that 2 MW CW operation is feasible at 283 GHz with the interaction efficiency of $\approx$33% in the already designed dual regime gyrotron. Design studies of the electron gun and output coupling system have been performed to verify whether the same physical components of the dual regime coaxial gyrotron can support the new 283 GHz operation. By tuning the electrode potentials of the MIG and the current in the magnetic coils, the hollow electron beam required for 283 GHz operation can be generated with the beam radius of 10.824 mm, velocity ratio of 1.23 and velocity ratio spread of 1.7%. For 283 GHz operation, transmission coefficient of the desired mode $TE_{62,38}$ in the designed NLT is greater than 99%. The common launcher converts the cavity mode into free space mode at 283 GHz with the fundamental Gaussian mode content of around 95.33%. The single disk CVD diamond window of thickness 2.00 mm already designed for the dual regime operation also has the transmission gap of 2 GHz around the desired frequency of 283 GHz.

Design studies of a triple frequency coaxial cavity gyrotron with the output RF power targeted to 3 MW have been carried out in Chapter 6. By increasing the single power output of gyrotron to 3 MW, number of RF sources in the ECRH system can be reduced. 236 GHz was selected as the principle design frequency so that the designed gyrotron could be used for plasma heating application in the DEMO tokamak. Other two lower frequencies (170/204 GHz) were chosen such that the same gyrotron can be used for other applications like plasma startup, bulk heating, and also in the upgraded systems of the existing tokamaks like ITER. For the proposed gyrotron, a single disk CVD diamond window of thickness 1.86 mm was designed to support the output transmission of

the desired frequencies. As the cavity wall loading increases with frequency and output RF power, for this 3 MW operation at 236 GHz, the modes with eigenvalue higher than 200 were considered. By considering multifrequency operational criteria, cavity modes were chosen as $TE_{46,27}/TE_{55,32}/TE_{64,37}$ for the respective frequencies 170/204/236 GHz. The interaction cavity dimensions were optimized through cold cavity simulations and Q_d calculated were 1231/1649/2212 for the respective frequencies 170/204/236 GHz. In the mode competition studies, beam coupling coefficient were calculated for the operating main mode along with the competing modes around the desired frequencies. The beam parameters and magnetic field at the interaction cavity center were optimized for the 3 MW output RF power at the desired frequencies through the self-consistent single mode calculation. Time dependent multi mode calculations were carried out for all the three desired frequencies and simulation results confirmed that for the chosen nominal parameters RF output power in the desired cavity modes reach the power level of 3 MW. The common electron gun along with the magnetic guidance system was designed for the generation of the electron beam with the nominal beam parameters required to support the triple frequency operation. Startup calculations were carried out for the three frequencies with beam parameters obtained from MIG design studies. The results of these calculations confirmed that 3 MW CW operation is feasible at all the three desired frequencies (170/204/236 GHz).

Analysis of the triangular corrugated coaxial cavity with misaligned insert have been carried out in Chapter 7. Misalignment in the insert changes the field structure in the interaction region, and these effects should be properly considered. For the coaxial cavity with misaligned insert, field analysis has been carried out using the SIM approach, and later the analysis has been extended for the general case using full wave approach (SHM). Using both approaches, dispersion relation has been derived for the cavity modes in the misaligned system. Effect of insert misalignment on the eigenvalue of the $TE_{34,20}$ mode in a 170 GHz, 2 MW coaxial cavity gyrotron has been studied. From these studies, the effect of insert misalignment on the cavity modes of the triangular corrugated coaxial cavity gyrotron has been qualitatively understood.

In summary, this research work contributes towards the design studies of the major components of coaxial cavity gyrotron supporting dual/multifrequency operation. These gyrotrons can be used for the ECRH application in the future experimental tokamaks.

8.2 Future Scope

Coaxial cavity gyrotron offers several advantages over the conventional cavity gyrotrons and are highly preferable for the ECRH application in the next generation fusion toka-

maks. The following aspects can explored as the future scope of the present work.

1. Start-up scenario considered in the design studies of this thesis is of diode type, where the modulation anode voltage varies proportionally with the beam voltage. For increasing the output RF power, triode type of startup can be explored. As the mode competition is severe for the high power operation (>2 MW), these studies should also investigate on the improved mode stability.
2. In the long pulse operation of gyrotron, due to the presence of residual gases plasma is formed in the interaction cavity and this affects the RF interaction mechanism of the gyrotron. Therefore, self consistent calculations should be carried out for the plasma loaded coaxial interaction cavity of gyrotrons.
3. Fast step-tunability of coaxial cavity gyrotron in steps of 2-3 GHz can be explored at sub-THz wave range as this would be advantageous for stabilization of non-classical tearing modes (NTM) in the fusion tokamaks by using non-steerable, fixed launchers.
4. Misalignment in the hollow electron beam with the interaction cavity axis leads to spread in the electron beam energy and consequently reduces the interaction efficiency of the gyrotron. This effect should be qualitatively studied for the megawatt class sub-THz wave coaxial cavity gyrotron.

Appendix A

Basics considerations for interaction cavity studies in gyrotrons

In the RF behavior studies of the gyrotron, dimensions of the interaction cavity and the electron beam parameters are optimized for the required output RF power at the desired frequency. For the chosen operating mode at the desired frequency, interaction cavity is optimized through cold cavity approximation and the resonant frequency, Q factor are determined for the chosen cavity mode. Initial optimization of beam parameters are carried through the equation of motion for the particles with fixed cavity field profile (adiabatic approximation). Further optimizations are performed through solving the equation of motion for the particles with the RF field equations (self-consistent calculations). Effects of mode competition on the RF power growth of the desired mode in the interaction cavity are understood through multi-mode calculations. The field expressions used in the interaction cavity studies are presented in this appendix chapter.

A.1 Cold Cavity Approximation

The knowledge of the electromagnetic field structure, eigen-frequency (ω) and quality factor are essential for the design of the interaction region of the gyrotron. In the conventional cavity gyrotrons, interaction region consists of input down taper, straight mid-section and output up-taper. Interaction cavity of the gyrotron behaves as the resonant circuit due to the reflection of RF fields at the taper regions. Field expressions of the cavity are obtained by solving the maxwell's equation in the cavity geometry. ω and Q are determined through the radiation boundary condition at the output section of the interaction cavity. The interaction cavity can be considered as the open-ended resonator with azimuthal field variation given by $e^{jm\theta}$, temporal field variation as $e^{j\omega t}$, where ω is given by $\omega_o(1+j/2Q)$. Maxwell's equation is given by

$$\nabla \times \boldsymbol{E} = -j\omega \boldsymbol{B} \tag{A.1a}$$

$$\nabla \times \boldsymbol{H} = \boldsymbol{J_c} + j\omega \boldsymbol{D} \tag{A.1b}$$

$$\nabla . \boldsymbol{D} = \rho_v \tag{A.1c}$$

$$\nabla . \boldsymbol{B} = 0 \tag{A.1d}$$

For axisymmetrical systems like waveguides, wave equation is obtained from the Maxwell's equation

$$(\nabla_t^2 + k_z^2)h = 0 \tag{A.2}$$

where h is the axillary function which satisfies the field expression of the TE/TM modes in the waveguide. For cylindrical waveguide, ∇_t^2 is given by

$$\nabla_t^2 = \frac{\partial^2}{\partial r^2} + \frac{1}{r}\frac{\partial}{\partial r} + \frac{1}{r^2}\frac{\partial^2}{\partial \theta^2} \tag{A.3}$$

k_z is the propagation wavenumber and is given by

$$k_z^2 = k_o^2 - k_{mp}^2 \tag{A.4}$$

k_{mp} is the cut-off wavenumber and for cylindrical waveguide it is given by k_{mp}=χ_{mp}/R_o. χ_{mp} is the pth root of the function $J'_m(\chi_{mp})$ for TE modes ($J_m(\chi_{mp})$ for TM modes). $\hat{\boldsymbol{n}}$ is the normal vector to the cavity surface and is given by

$$n_\theta = 0$$

$$n_r = -cos\theta_\omega$$

$$n_z = sin\theta_\omega$$

$$tan\theta_\omega = \frac{dR(z)}{dz} \tag{A.5}$$

θ_ω is the taper angle. Boundary conditions at the cavity wall can be written as

$$\hat{\boldsymbol{n}} . \boldsymbol{B} = 0$$

$$\hat{\boldsymbol{n}} \times \boldsymbol{E} = 0 \tag{A.6}$$

Radiation boundary conditions at the cavity output are given by

$$\frac{\partial \boldsymbol{E}}{\partial z} = -jk_z \boldsymbol{E}$$

$$\frac{\partial \boldsymbol{H}}{\partial z} = -jk_z \boldsymbol{H} \tag{A.7}$$

For TE modes, transverse component of electric field can be written in terms of orthonormal basis function as

$$\boldsymbol{E_t} = \sum_{mp} V_{mp}(z) \boldsymbol{e_{mp}}(r,z,\theta) \tag{A.8}$$

where $\boldsymbol{e_{mp}}$ is given as

$$\int_0^{2\pi} d\theta \int_o^{R(z)} r dr \boldsymbol{e^*_{mp}}.\boldsymbol{e_{m'q}} = \delta_{pq}\delta_{mm'} \tag{A.9}$$

$\boldsymbol{e_{mp}}$ can be expressed in terms of scalar function (membrane function) as

$$\boldsymbol{e_{mp}} = \hat{z} \times \nabla \psi_{mp} \tag{A.10}$$

The membrane function is given by

$$\psi_{mp} = C_{mp} J_m(k_{mp} r) e^{-jm\theta}$$

The membrane function (ψ_{mp}) satisfies the following equation

$$(\nabla_t^2 + k_{mp}^2)\psi_{mp} = 0$$

k_{mp} is given by $\chi_{mp}/R(z)$. For the TE mode, C_{mp} is given as

$$C_{mp}^{-1} = \sqrt{\pi(\chi_{mp}^2 - m^2)} J_m(\chi_{mp})$$

From the equation (A.1b), we obtain

$$-j\omega\varepsilon E_r - J_r = \frac{\partial H_\theta}{\partial z} - \frac{jm}{r} H_z \tag{A.11}$$

$$-j\omega\varepsilon E_\theta - J_\theta = \frac{\partial H_z}{\partial r} - \frac{\partial H_r}{\partial z} \tag{A.12}$$

Multiplying (A.11) by $(e^*_{mq})_r$ and (A.12) by $(e^*_{mq})_\theta$, adding and integrating over the transverse surface of the interaction region the following second order differential equation is

obtained for V_{mp}

$$\begin{aligned}
&\frac{d^2V_{mq}}{dz^2}+\left(\frac{\omega^2}{c^2}-k_{mq}^2\right)V_{mq}+\sum_p\left(2T_{qp}^m\frac{dV_{mp}}{dz}+V_{mp}\frac{dT_{qp}^m}{dz}\right)\\
&-2\left(\frac{R'}{R}\right)\sum_p V_{mp}T_{pq}^m+\left(\frac{R'}{R}\right)^2V_{qm}\frac{\left[4m^2-\left(\chi_{mq}^2-m^2\right)^2\right]}{3\left(\chi_{mq}^2-m^2\right)^2}\\
&-2\left(\frac{R'}{R}\right)^2\sum_{p\neq q}\frac{\chi_{mp}^2V_{mp}}{\left[\left(\chi_{mp}^2-m^2\right)\left(\chi_{mq}^2-m^2\right)\right]^{1/2}}\\
&\times\left\{\frac{4\chi_{mp}^2\chi_{mq}^2-2m^2\left(\chi_{mp}^2+\chi_{mq}^2\right)}{\left(\chi_{mp}^2-\chi_{mq}^2\right)^2}\right.\\
&\left.+m\left[1-\frac{4\left(\chi_{mp}^2+\chi_{mq}^2\right)}{\left(\chi_{mq}^2-\chi_{mp}^2\right)^2}\right]\left[1-\frac{1+m(m+1)/\chi_{mp}\chi_{mq}}{\chi_{mq}-\chi_{mp}}\right]\right\}\\
&+2\frac{2jm}{\sqrt{\chi_{mq}^2-m^2}}\sum_p\left[2\left(\frac{R'}{R}\right)\frac{dU_{mp}}{dz}\left(\frac{R'}{R}\right)'U_{mp}\right]\\
&=j\omega\mu J_{mq}
\end{aligned}\tag{A.13}$$

The mode coupling coefficient is given by

$$T_{pq}^m=2\pi\int_0^R re_{\boldsymbol{mq}}^*.\frac{\partial e_{\boldsymbol{mp}}}{\partial z}dr,\tag{A.14}$$

and

$$J_{mq}=\int d\theta\int_0^R re_{\boldsymbol{mq}}^*.\boldsymbol{J}dr\tag{A.15}$$

V_{mq} must also satisfies radiation boundary condition at the cavity output and is given by

$$\frac{dV_{mq}}{dz}=-jk_zV_{mq}\tag{A.16}$$

When the taper angles are less than 10°, coupling of power to other modes are negligible and hence the equation (A.13) reduces to the single mode Vlasov's equation which is given by

$$\frac{d^2V_{mq}}{dz^2}+\left(\frac{\omega^2}{c^2}-k_{mq}^2\right)V_{mq}\simeq+j\omega J_{mq}\tag{A.17}$$

For integrating the above equation (A.17), initial values are determined through the boundary condition at the input of the interaction cavity. The radiation boundary condition at the cavity output is re-modeled as

$$|R| = \left| \frac{\frac{dV}{dz} + jk_z V}{\frac{dV}{dz} - jk_z V} \right| = \text{minimum} \tag{A.18}$$

In absence of external sources, the equation (A.17) reduces to homogeneous wave equation with $\omega = \omega_o(1 + j/2Q)$ being the complex quantity. Imaginary part of ω denotes the radiating fields coming out of the resonator. Homogeneous case of equation (A.17) can be solved through Numerov algorithm and ω_o, Q are calculated for the desired mode in the designed interaction cavity. Longitudinal electric field profile of the desired TE mode in the interaction cavity can be obtained by solving the homogeneous Vlasov's equation.

A.2 Adiabatic Approximation

The output RF power and efficiency are calculated through the equation of motion for the electrons traveling in the electric and magnetic fields and computing energy loss or gain by the electron particles. The efficiency is calculated by averaging over the energy of particles. The equation of motion for charge particles in the electric and magnetic fields is given by,

$$\frac{d\boldsymbol{p}}{dt} = -e\,(\boldsymbol{E} + \boldsymbol{v} \times \boldsymbol{B}) \tag{A.19a}$$

$$\frac{d\varepsilon}{dt} = -e\boldsymbol{E}.\boldsymbol{v} \tag{A.19b}$$

where $\boldsymbol{p} = \gamma m_e \boldsymbol{v}$, $\varepsilon = \gamma m_e c^2$, and $\gamma = 1/\sqrt{1 - v^2/c^2}$. By using dimensionless variables ($\boldsymbol{u} = \gamma \boldsymbol{v}/c$, γ), equations (A.19) become,

$$\frac{d\gamma}{dt} = -\frac{e}{m_e c}\left(\boldsymbol{E}.\frac{\boldsymbol{u}}{\gamma}\right) \tag{A.20a}$$

$$\frac{d\boldsymbol{u}}{dt} = -\frac{e}{m_e c}\left(\boldsymbol{E} + \boldsymbol{u} \times \frac{c\boldsymbol{B}}{\gamma}\right) \tag{A.20b}$$

In the uniform axial magnetic field (B_o), the particles gyrate around the guiding center with the cyclotron frequency (ω_c) and is given by

$$\omega_c = eB_o/m_e\gamma = \Omega_o/\gamma \tag{A.21}$$

The lamour radius or gyration radius is given by

$$r_L = \frac{cu_t}{\Omega_o}$$

Since, the RF power growth occurs only when the gyrating frequency of the electron is equal to the RF frequency, equation of electron motion can be reduced through slow-variable transformation. Introducing slow time variables as

$$\Psi = \int_{t_o}^{t} \frac{\Omega_o}{\gamma} dt + \phi - \phi_o \tag{A.22}$$

Transverse motion of the electrons can be expressed in complex phasor form by using the slow-time variables as

$$\begin{aligned} j\frac{du_t}{dt} - \left(\frac{d\Psi}{dt} - \frac{\Omega_o}{\gamma}\right) u_t \simeq -\tilde{\eta}\left(E_r + jE_\theta\right) e^{j(\theta-\Psi)} \\ + \frac{j\tilde{\eta} c u_z}{2\gamma} \frac{dB_o}{dz} \left(R_e e^{j(\theta_e-\Psi)} + r_L\right) \end{aligned} \tag{A.23}$$

where $\tilde{\eta} = e/m_e c$. Transverse electric field components in the above equation (A.23) can be represented in terms of orthonormal basis function as

$$\boldsymbol{E_t} = \sum_{mp} V_{mp}(z) \boldsymbol{e_{mp}}(r, z, \theta)$$

Slow varying part of gyrophase Λ is given by $\Lambda = \omega_a t - \Psi$, where ω_a is the averaging frequency. Substituting the expressions for $\boldsymbol{E_t}$, introducing Λ and by using Graff's addition theorem, equation (A.23) is transformed as

$$\begin{aligned} \frac{du_t}{dt} + j\left(\omega_a - \frac{d\Lambda}{dt} - \frac{\Omega_o}{\gamma}\right) u_t = + \left(\frac{\tilde{\eta} c u_z r_L}{2\gamma}\right) \frac{dB_o}{dz} \\ - \frac{\tilde{\eta}}{2} \sum_{mp} C_{mp} k_{mp} V_{max} \hat{f}_{mp}(z) J_{s-1}\left(k_{mp} r_L\right) \\ \times e^{j(\omega_{mp} - s\omega_a)t + js(\Lambda+\theta_e)} J_{m-s}\left(k_{mp} R_e\right) e^{-jm\theta_e} \end{aligned} \tag{A.24a}$$

$$\frac{du_z}{dt} = -\left(\frac{\tilde{\eta} c u_t}{2\gamma r_L}\right) \frac{dB_o}{dz} \tag{A.24b}$$

Assuming $P = j u_t e^{-j(\Lambda+\theta_e)}$ and changing the independent variable from t to z as $z = \int_{t_o}^{t} \frac{cu_z}{\gamma} dt$, the above equation (A.24) becomes

$$\begin{aligned} \frac{dP}{dz} + \frac{j\omega}{cu_z}\left(\gamma - \frac{\Omega_o}{\omega}\right) P = + \frac{j\tilde{\eta}}{2} \frac{dB_o}{dz} \frac{P}{\Omega_o} \\ + \frac{j\tilde{\eta}}{2} \frac{\gamma}{u_{zo}} C_{mp} k_{mp} V_{max} \left(\frac{\hat{f}_{mp}(z)}{(s-1)!}\right) \\ \times J_{m-s}\left(k_{mp} R_e\right) \left(\frac{c k_{mp} P^*}{2\Omega_o}\right)^{s-1} \end{aligned} \tag{A.25a}$$

$$\frac{du_z}{dz} = -\left(\frac{\tilde{\eta} c u_t r_L}{u_z}\right)\frac{dB_o}{dz} \tag{A.25b}$$

By neglecting magnetic field tapering in the above equation (A.25), the equation of motion for electrons becomes a single differential equation which is given by

$$\begin{aligned}\frac{dP}{dz} + \frac{j\omega}{c\beta_{zo}}\left(\frac{\gamma}{\gamma_o} - \frac{\Omega_o}{\omega\gamma_o}\right)P = \frac{j\tilde{\eta}}{2}\frac{\gamma}{u_{zo}} C_{mp} k_{mp} V_{max}\left(\frac{\hat{f}_{mp}(z)}{(s-1)!}\right) \\ \times J_{m-s}\left(k_{mp}R_e\right)\left(\frac{c k_{mp} P^*}{2\Omega_o}\right)^{s-1}\end{aligned} \tag{A.26a}$$

$$u_z \simeq \text{constant} \tag{A.26b}$$

The factor $J_{m-s}\left(k_{mp}R_e\right)$ is usually denoted as G_{mp} and is related to the RF electron beam coupling coefficient. The above equation (A.26) is the adiabatic approximation of equation of motion for electron particles in the electric and magnetic fields. This equation is derived by neglecting the RF magnetic field as the gyrotron operates in the TE mode close to cutoff frequency and by neglecting the guiding center drift of the electron beam as the axial magnetic field is uniform through out the interaction region. The effect of space charge fields are neglected in the above approximation as these effect would not greatly affect the RF interaction efficiency. By including the space charge effect in the equation of motion, equation (A.26) becomes

$$\begin{aligned}\frac{dP}{dz} + \left(\frac{j\omega}{c\beta_{zo}}\right)\left(\frac{\gamma}{\gamma_o} - \frac{\Omega_o}{\omega\gamma_o}\right)P \\ = \left(\frac{\eta}{2}.\frac{\gamma}{u_{zo}}\right) C_{mp} J_{m-s}\left(k_{mp}R_e\right) k_{mp}\hat{f}_{mp}(z) V_{max} \\ + \left(\frac{j\omega_p^2}{2\Omega_o}\right)\left(\frac{\gamma}{c u_{zo}}\right)\left[\langle P\rangle - P\right]\end{aligned} \tag{A.27a}$$

where ω_p is the plasma frequency and is given by:

$$\omega_p^2 \simeq \frac{2\pi I_o}{8500}.\frac{\Omega_o c}{4\pi R_e \beta_\perp \beta_z}$$

The electronic efficiency η_{el} is given by

$$\eta_{el} = \left(\frac{\gamma_o - \langle\gamma(z_{out})\rangle}{\gamma_o - 1}\right) \tag{A.28}$$

The electronic efficiency can also be calculated by integrating the equation of electron motion and is given by

$$\eta_{el} = \left(\frac{e}{2m_e c^2}\right) C_{mp} G_{mp} k_{mp} V_{max(mp)} \left(\frac{Im\left\langle \int_{z_{in}}^{z_{out}} P(z)\hat{f}^*_{mp}(z)dz \right\rangle}{u_{zo}(\gamma_o - 1)}\right) \tag{A.29}$$

A.3 Self-Consistent Calculations

In the adiabatic approximation, the equation of electron motion are solved using the fixed field approximation and the output RF power and efficiency are calculated for the given beam parameters. However, effect of the electron beam on the RF field profile is not included in the adiabatic approximation. To include these effects, the single mode Vlasov's equation should be solved simultaneously with the equation of motion of electron beam. The current density term in the right hand side of the Vlasov's equation is modeled to include the influence of electron beam on the field profile and the equation (A.17) becomes

$$\frac{d^2V_{mq}}{dz^2} + \left(\frac{\omega^2}{c^2} - k_{mq}^2\right) V_{mq} = -Z_o I_o \left[\frac{C_{mq} k_{mq} G_{mq}}{(s-1)!}\right] \left(\frac{\omega_{mq}}{c u_{zo}}\right) \left(\frac{-jck_{mq}}{2\Omega_o}\right)^{s-1} \langle P^s \rangle \tag{A.30}$$

The equation of motion for electrons is re-written as

$$\frac{dP}{dz} + \frac{j\omega}{c\beta_{zo}} \left(\frac{\gamma}{\gamma_o} - \frac{\Omega_o}{\omega\gamma_o}\right) P = \frac{j\tilde{\eta}}{2} \frac{\gamma}{u_{zo}} C_{mp} k_{mp} G_{mp} \frac{V_{mp}(z)}{1022} \cdot \left(\frac{ck_{mp}P^*}{2\Omega_o}\right)^{s-1} \tag{A.31}$$

The output RF power is given by

$$P_{out} = \mathrm{Re}\left(\frac{1}{2\mu\omega}\right) k^*_{mp} \left|V_{mp}(z_{out})\right|^2 \tag{A.32}$$

To cross verify the self-consistent calculations, determined output power must be equal to

$$P_{out} = \eta_{el} U_o I_o$$

Coupled equations are solved numerically by leap frog algorithm for integrating the equation (A.30) and using predictor-corrector method for (A.31).

A.4 Multi-Mode Calculations

When the gyrotrons are operated in higher volume modes, mode competition would be severe as the mode spectrum is dense and the beam current is also higher than the start-

ing current of the most of the competing modes. To understand the mode competition, equation of motion for the particles in the RF fields, which are represented as the superposition of several modes, is derived. Later, energy transfer from the electron beam to the individual modes are calculated and the equilibrium state is determined.

The equation of motion in presence of superposition of several modes is given by

$$\frac{dP}{dz}+\frac{j\omega_a}{c\beta_{zo}}\left(\frac{\gamma}{\gamma_o}-\frac{\Omega_o}{\omega_a\gamma_o}\right)P=-j\frac{\gamma\omega_a}{cu_{zo}}\sum_{mp}F_{mp}\hat{f}_{mp}(z)e^{[j\psi_{mp}]}\left(\frac{jck_{mp}P^*}{2\Omega_o}\right)^{s_{mp}-1} \tag{A.33}$$

where F_{mp} and ψ_{mp} are given by

$$F_{mp}=\frac{eV_{max_{mp}}}{2m_ec^2}\frac{C_{mp}G_{mp}}{u_{\perp o}}\frac{ck_{mp}}{\omega_a}\frac{1}{(s_{mp}-1)!}\qquad\text{and}$$

$$\psi_{mp}=(\omega_{mp}-s_{mp}\omega_a)\,t+(s_{mp}\pm m_{mp})\,\theta_e$$

The field equation is given by

$$\frac{d^2F_{mp}\hat{f}_{mp}}{dz^2}+\left(\frac{\omega_{mp}^2}{c^2}-k_{mp}^2\right)F_{mp}\hat{f}_{mp}=-Z_oI_o\left[\frac{C_{mp}k_{mp}G_{mp}}{(s_{mp}-1)!}\right]\left(\frac{\omega_{mp}}{cu_{zo}}\right)\left(\frac{-jck_{mp}}{2\Omega_o}\right)^{s_{mp}-1}\left\langle P^s exp[-j(\psi_{mp}-\psi_1)]\right\rangle \tag{A.34}$$

where

$$\psi_{mp}-\psi_1=(\omega_{mp}-\omega_1)\,t+(m_1-m_{mp})\,\theta_e$$

Generally, when the system is in steady state, time dependence variation of the field amplitude is not considered. However, during startup or beam space charge neutralization, when the nominal beam parameters are varying it is better to consider the time dependence of the field amplitude and the field equation is given by

$$\frac{d^2F_{mp}\hat{f}_{mp}}{dz^2}+\left(\frac{\omega_{mp}^2}{c^2}-k_{mp}^2\right)F_{mp}\hat{f}_{mp}-\frac{j2\omega_{mp}^2}{c^2}\frac{\partial}{\partial t}\left(F_{mp}\hat{f}_{mp}\right)=-Z_oI_o\left[\frac{C_{mp}k_{mp}G_{mp}}{(s_{mp}-1)!}\right]\left(\frac{\omega_{mp}}{cu_{zo}}\right)\left(\frac{-jck_{mp}}{2\Omega_o}\right)^{s_{mp}-1}\left\langle P^s exp[-j(\psi_{mp}-\psi_1)]\right\rangle \tag{A.35}$$

The equations (A.33) and (A.35) are solved simultaneously and the power transfer from electron beam to the RF fields of different modes are calculated. The rate of energy

transfer to the jth mode is given by

$$\frac{d\gamma_j}{dt} = -\frac{e}{m_e c^2} \boldsymbol{E_j} . \frac{\boldsymbol{u}c}{\gamma} \tag{A.36}$$

Appendix B

Gyrotron Design Suite 2018 (GDS 2018)

To perform the design studies of major sub-assemblies of the gyrotron, MATLAB code package have been developed by our research group, named as "GDS 2018 (Gyrotron Design Suite 2018)". GDS 2018 is the updated version of the GDS 2016, which incorporates the features to perform the design studies of the components coaxial cavity gyrotron along with conventional cavity gyrotron. The main window of GDS 2018 is shown in Figure B.1.

B.1 Conventional Cavity Gyrotron

GDS 2018 includes design modules like mode selection procedure, starting current calculations, RF interaction studies (including cold cavity computations, Single mode calculations, time dependent multi mode calculations) to perform design studies of the conventional cavity gyrotron. In addition, initial design studies of the electron gun and magnetic coil design can be carried out through this package. This package also includes the codes to perform output system design of the gyrotron. Initial design studies of launcher, design studies of non-linear taper through particle swarm optimization technique, Single disk and double disk RF window design can be carried out through this package. The package also features modules to calculate the phase of the output RF beam and to synthesis the surface profiles of metallic mirrors to transform off-axis beam into desired Gaussian beam. The design tools available for the conventional gyrotron case are shown in Figure B.2. Figure B.3 shows the generated mirror profiles and Gaussian output beam obtained from the 'Mirror Synthesis'module of GDS 2018.

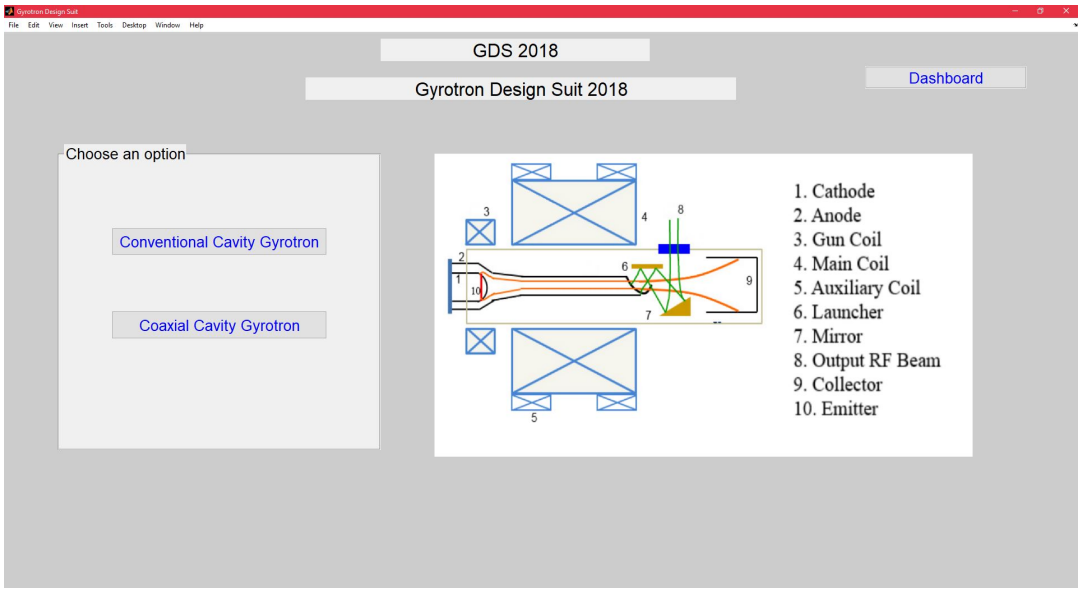

Figure B.1: Basic layout of main window of GDS 2018 with option of choosing conventional or coaxial cavity gyrotron design studies.

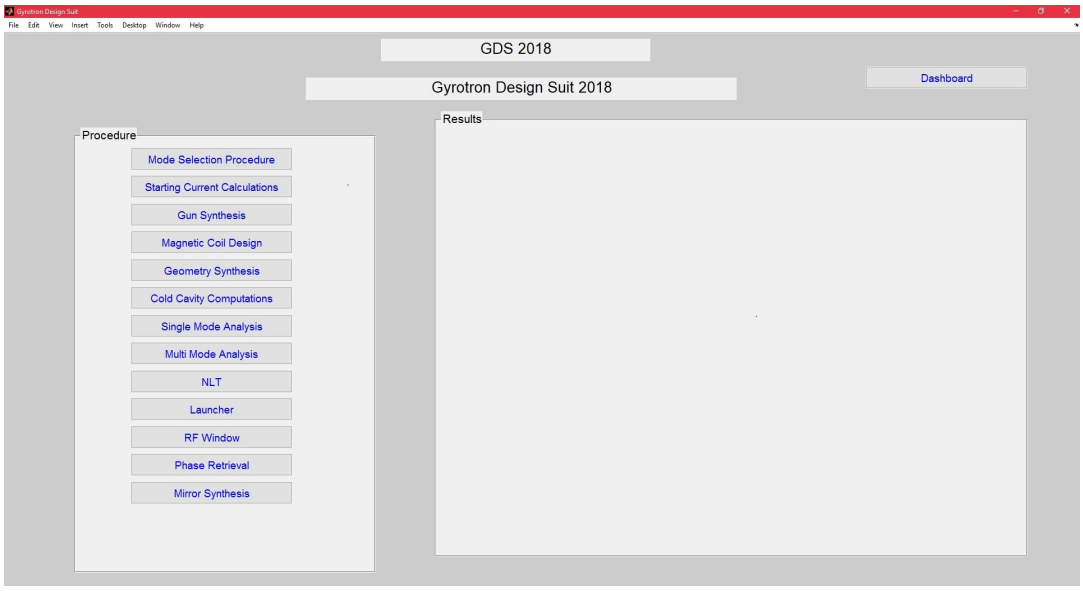

Figure B.2: Complete design options available in GDS 2018 for conventional cavity gyrotron case.

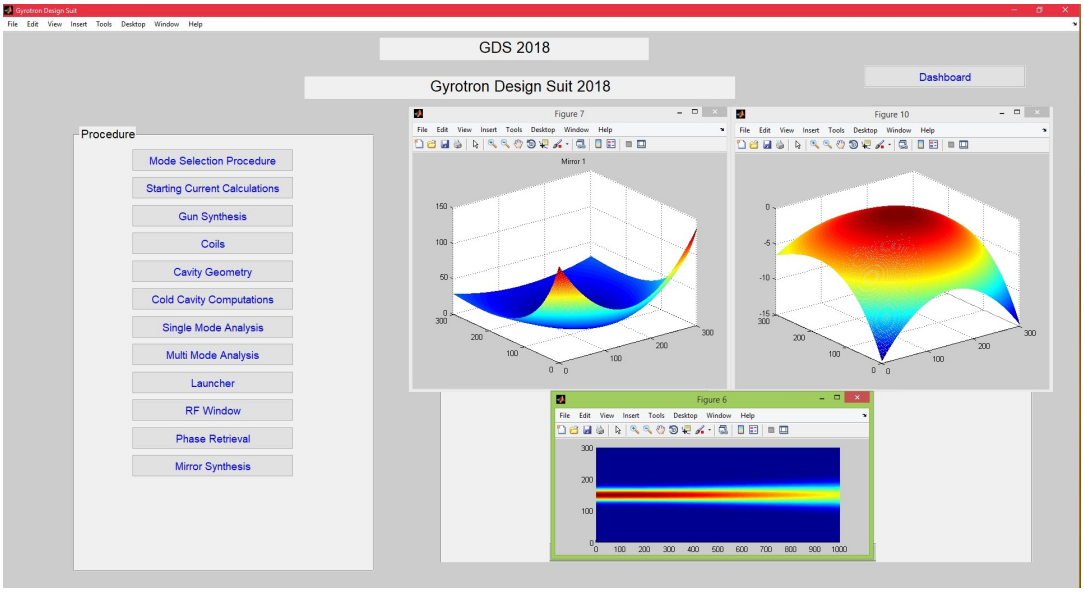

Figure B.3: Generated mirror profiles and output Gaussian beam in 'Mirror Synthesis'tool of GDS 2018.

B.2 Design expressions used in different modules of GDS 2018 (Conventional Cavity Gyrotron)

B.2.1 Mode Selection Procedure

In this module, operating cavity mode for gyrotron is selected by considering the following conditions:

- For the chosen mode ($TE_{m,p}$), the peak ohmic wall loading of the cavity should be less than $2\,kW/cm^2$ at the desired output power levels. The peak ohmic wall loading is given by

$$\frac{dP_{loss}}{dA} \simeq \left(\frac{\delta}{4\pi\mu_o\omega}\right)\left[\frac{1}{(\chi_{mp}^2 - m^2)}\right]\left(k_{mp}^4|V_{mp}|^2 + \frac{m^2}{R_o^2}\left|\frac{dV_{mp}}{dz}\right|^2\right)$$

  where δ is the skin depth of the conducting wall, R_o is the radius of the cavity, χ_{mp} is the eigenvalue of the cavity mode, V_{mp} is the the electric field amplitude of the chosen mode.
- Voltage depression of the beam for the chosen mode should be less than 10% of the applied accelerating voltage. Voltage depression of the beam is given by

$$\Delta V \simeq -60\frac{I_b}{\beta_z}\ln\left(\frac{R_o}{R_e}\right)$$

where I_b is the beam current, R_e is the electron beam radius and β_z is the normalized axial velocity of the electron beam.

- For the stable operation of the gyrotron, operational beam current should be less than half of the limiting current. Limiting current is the maximum value of current beyond which mirroring of electron beam occurs (i.e. $\beta_z \simeq 0$) and is given by

$$I_L = \frac{\left(\frac{511}{60}\right)\gamma_o\left[1-\left(1-\beta_{zo}^2\right)^{1/3}\right]^{3/2}}{\ln\left(\frac{R_o}{R_e}\right)}$$

where γ_o is the relativistic factor of the electron beam. For the chosen operating mode, limiting current should be as high as possible so that gyrotron can be operated with higher beam current.

Multifrequency Operation

This module also features mode selection procedure for the multifrequency operation of the gyrotron. In addition to the previously mentioned conditions, mode selection for the multifrequency operation of gyrotron is carried out by considering the following criteria:

1. For the given cavity radius, the resonant frequency of the chosen modes should be around the transparent frequencies of the designed RF window.
2. The beam radius of the modes selected must be close to the each other so that the designed electron gun can support the stable oscillation conditions at all operating frequencies.
3. The relative caustic radius of the modes selected must approximately be same so that a common output coupling system can be used for converting cavity modes into Gaussian like mode.

B.2.2 Start Current Calculations

Starting current (I_{start}) for the desired mode along with the competing modes are determined through this module for the chosen magnetic field range. Starting current is the minimum value of beam current required for the operating mode to start oscillating. The mathematical expression for the starting current is given by

$$\frac{-1}{I_{start}} = \left(\frac{QZ_o e}{8\gamma_o m_e c^2}\right)\left(\frac{\pi}{\lambda}\int_0^L |\hat{f}(z)|^2 dz\right)^{-1} \cdot \left(\frac{k_{mp}C_{mp}G_{mp}}{\beta_{zo}(s-1)!}\right)^2 \left(\frac{ck_{mp}\gamma_o\beta_{\perp o}}{2\Omega_o}\right)^{2(s-1)} \cdot \left(s+\frac{1}{2}\frac{\omega\beta_{\perp o}^2}{v_{z0}}\frac{\partial}{\partial\Delta_s}\right) \cdot \left|\int_0^L \hat{f}(z)e^{j\Delta_s z}dz\right|^2$$

In the above expression Δ_s is given by

$$\Delta_s(z) = \frac{\omega}{v_{zo}}\left(1 - \frac{s\Omega_o(z)}{\omega\gamma_o}\right)$$

$\hat{f}(z)$ is the normalized field amplitude and for the Gaussian field profile,

$$\left|\int_0^L \hat{f}(z)e^{i\Delta_s z}dz\right|^2 \simeq \frac{L^2\pi}{4}\exp\left[-\frac{(\Delta_s L)^2}{8}\right]$$

where L is length of the mid-section.

B.2.3 Gun Synthesis

Initial design studies of the electron gun are carried out through the Gun Synthesis module to determine the electron gun parameters like cathode radius, cathode-anode spacing, emitter current density, electric field at cathode, and cathode slant angle. These studies are performed through the Baird expressions which are derived under adiabatic approximation. Baird expressions are given by

$\Longrightarrow$ Emitter radius (R_c)

$$R_c = \sqrt{b}R_e$$

where b is the magnetic compression ratio which is given by B_o/B_g and the emitter radius thickness can be calculated from

$$\Delta R_c = \sqrt{b}\Delta R_e$$

$\Longrightarrow$ Emitter Length (l_e) can be determined through the total beam current and is given by

$$I_b = (2\pi R_c l_s) J_c$$

$\Longrightarrow$ Cathode electric field (E_c) is given by

$$E_c cos\phi_c = \frac{B_o\gamma_o v_{\perp o}}{b^{3/2}}$$

where ϕ_c is the cathode slant angle.

$\Longrightarrow$ The cathode-anode spacing (d) is calculated through

$$d = R_c\frac{r_{Lo}D_F\mu}{cos\phi_c}$$

where r_{Lo} is the Larmor radius, D_F is the cathode-anode spacing factor (D_F should be greater than 2), μ is given by $\mu = 1/\sqrt{(r_{go}/r_{Lo})^2 - 1}$ and r_{go} is the guiding center radius

at the interaction cavity.

B.2.4 Magnetic Coil Design

In this module, axial magnetic field profile can be optimized through the magnetic coil data. The axial magnetic field for a solenoid containing N number of turns, carrying current I is given by

$$B(z) = \frac{1}{2}\frac{\mu_o IN}{t*w}.[t_{21}+t_{22}]$$

where t_{21}, t_{22} are given by

$$t_{21} = (z_{max}-z)*\log\left(\frac{r_{max}+\sqrt{r_{max}^2+(z_{max}-z)^2}}{r_{min}+\sqrt{r_{min}^2+(z_{max}-z)^2}}\right)$$

$$t_{22} = (z-z_{min})*\log\left(\frac{r_{max}+\sqrt{r_{max}^2+(z-z_{min})^2}}{r_{min}+\sqrt{r_{min}^2+(z-z_{min})^2}}\right)$$

where z_{max}, z_{min}, r_{max}, r_{min} are the maximum and minimum positions of the coil in axial and radial directions. t is the thickness of the coil in radial direction and w is the width of the coil in axial direction.

B.2.5 Cold Cavity Computations

Geometry of the interaction cavity is optimized by solving the homogeneous Vlasov's equation and is given by

$$\frac{d^2V_{mq}}{dz^2}+\left(\frac{\omega^2}{c^2}-k_{mq}^2\right)V_{mq}=0$$

The resonant frequency and diffractive Q factor are calculated for the desired mode in the designed interaction cavity through this design module.

B.2.6 Single Mode Analysis

The electron beam parameters and the magnetic field at the interaction region are optimized by simultaneously solving equation of electron motion and single mode Vlasov's equation in this design module. The expressions for equation of motion for electron beam is given by

$$\frac{dP}{dz}+\frac{j\omega}{c\beta_{zo}}\left(\frac{\gamma}{\gamma_o}-\frac{\Omega_o}{\omega\gamma_o}\right)P=\frac{j\tilde{\eta}}{2}\frac{\gamma}{u_{zo}}C_{mp}k_{mp}G_{mp}\frac{V_{mp}(z)}{1022}.\left(\frac{ck_{mp}P^*}{2\Omega_o}\right)^{s-1}$$

The single mode field equation is given by

$$\frac{d^2V_{mq}}{dz^2}+\left(\frac{\omega^2}{c^2}-k_{mq}^2\right)V_{mq}=-Z_oI_o\left[\frac{C_{mq}k_{mq}G_{mq}}{(s-1)!}\right]\left(\frac{\omega_{mq}}{cu_{zo}}\right)\left(\frac{-jck_{mq}}{2\Omega_o}\right)^{s-1}\langle P^s\rangle$$

The output RF power and efficiency are determined by self-consistently solving the above equations.

B.2.7 Multi-Mode Analysis

In the time dependent multi-mode analysis, the beam parameters are varied over the time and RF power growth in the desired mode along with the competing modes are calculated. The equation of electron motion in presence of superposition of several modes is given by

$$\frac{dP}{dz}+\frac{j\omega_a}{c\beta_{zo}}\left(\frac{\gamma}{\gamma_o}-\frac{\Omega_o}{\omega_a\gamma_o}\right)P=-j\frac{\gamma\omega_a}{cu_{zo}}\sum_{mp}F_{mp}\hat{f}_{mp}(z)e^{[j\psi_{mp}]}\left(\frac{jck_{mp}P^*}{2\Omega_o}\right)^{s-1}$$

The above equation is solved self-consistently with the field equation which is given by

$$\begin{aligned}\frac{d^2F_{mp}\hat{f}_{mp}}{dz^2}+\left(\frac{\omega_{mp}^2}{c^2}-k_{mp}^2\right)F_{mp}\hat{f}_{mp}-\frac{j2\omega_{mp}^2}{c^2}\frac{\partial}{\partial t}\left(F_{mp}\hat{f}_{mp}\right)\\=-Z_oI_o\left[\frac{C_{mp}k_{mp}G_{mp}}{(s_{mp}-1)!}\right]\left(\frac{\omega_{mp}}{cu_{zo}}\right)\left(\frac{-jck_{mp}}{2\Omega_o}\right)^{s_{mp}-1}\\\left\langle P^s exp[-j(\psi_{mp}-\psi_1)]\right\rangle\end{aligned}\tag{B.1}$$

These equations are solved simultaneously and the power transfer from electron beam to the RF fields of different modes are calculated.

B.2.8 NLT

In this module, the raised cosine nonlinear taper (NLT) is synthesized using particle swarm optimization techniques and the transmission coefficients of the different modes in the NLT are calculated using scattering matrix analysis. The expressions for the synthesis of the NLT are given by:

$$\alpha=-1.0+2.0\left(\frac{i}{l}\right)^{\gamma}$$

$$r(z) = \frac{r_2 - r_1}{2} \cdot \left(\alpha + \frac{1}{\pi} sin(\pi\alpha) \right) + \frac{r_2 - r_1}{2}$$

$$r = r_1 + r(z)$$

where r_1, r_2 are the input and output radius of the nonlinear taper. γ is the parameter affecting the transmission characteristics of the nonlinear taper.

B.2.9 Launcher

The initial design studies of the quasi optical launcher are carried out using this module of GDS 2018. The minimum launcher cut length (L_c) is given by

$$L_c = 2\pi R_o^2 \left(\frac{\beta}{\chi_{mp}} \right) \left(\frac{\sqrt{1 - (m/\chi_{mp})^2}}{cos^{-1}(m/\chi_{mp})} \right)$$

where β is the propagation constant of the mode.

B.2.10 RF window

Transmission and reflection coefficients of RF output beam along the frequency are determined for single disk and double disk RF window through this module. The transparent frequency (f_t) of RF window of thickness 'd'is given by

$$f_t = \frac{c}{2d\sqrt{\varepsilon_r}} N$$

where ε_r is the dielectric constant of the RF window and N is an integer.

B.2.11 Phase Retrieval

In this module, the phase of the output RF beam is calculated using iterative phase retrieval algorithm (IPRA) [209], [210]. The design flow of the algorithm is shown in Figure B.4.

1. Initially, amplitude of output RF beam are measured at two planes (A_1,A_2) separated by some distance. The phase of beam at plane 1 is assumed as ϕ_1.
2. The field at the plane 1 is determined by

   $$f_1(x,y) = A_1(x,y) exp[j\phi_1(x,y)]$$

   The field at the plane 2 is calculated through propagation algorithm and is given by

   $$f_2(x,y) = F^{-1}\{exp[j(z_2 - z_1)k_z] \times F[f_1(x,y)]\}$$

   where F and F^{-1} are the Fourier and inverse Fourier transform.
3. At plane 2, amplitude and phase of the beam are determined as $\tilde{A_2}$, $\tilde{\phi_2}$. Now

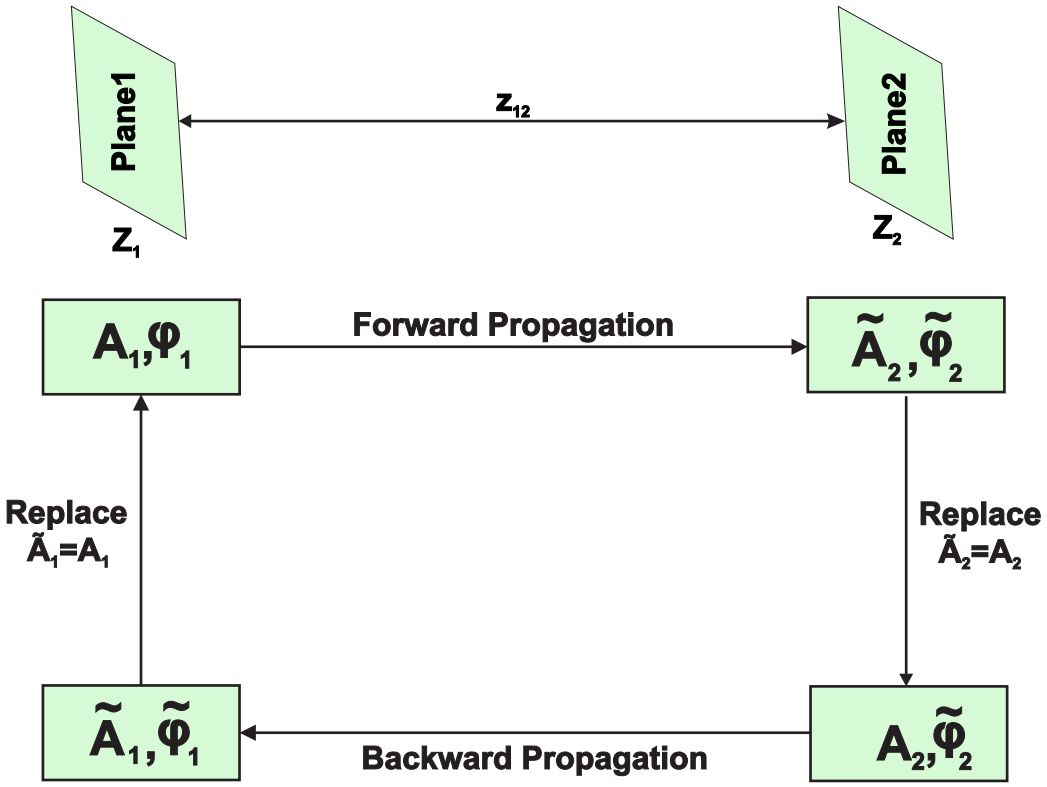

Figure B.4: Phase retrieval algorithm used in GDS 2018 [209], [210].

amplitude of beam is replaced by A_2 from $\tilde{A_2}$ and the beam is back propagated using same propagation algorithm.

4. Now, at plane 1 amplitude and phase of back propagated beam are calculated. $\tilde{A_1}$ is compared with original measured A_1 through the error function which is given by

$$E = \int_S \left|A_1 - \tilde{A_1}\right|^2 ds$$

5. If the error function is minimum then $\tilde{\phi_1}$ is the phase of the RF beam at the plane 1. Otherwise, the calculations are repeated with the new phase value $\tilde{\phi_1}$, with the amplitude of the beam as A_1.
6. The propagator algorithm used in this module is Huygens-Fresnel which is given by

$$h_{i\to j}(x,y) = \frac{1}{j\lambda\Delta z} exp\left\{j2\pi\frac{\Delta z}{\lambda}\right\}.exp\left\{j\pi\frac{x^2+y^2}{\lambda\Delta z}\right\}$$

where $\Delta z = (z_j - z_i)$.

B.2.12 Mirror Synthesis

In this module, matching optics system consisting of beam-shaping mirrors can be designed which can transform the off-axis Gaussian like beam into desired Gaussian beam to support the output coupling system of gyrotron. The fundamental Gaussian beam propagating along z direction is given by

$$u_{oo} = \sqrt{\frac{2}{\pi w_x w_y}} exp\left(-\frac{(x-x_o)^2}{w_x^2} - \frac{(y-y_o)^2}{w_y^2} - j\phi\right)$$

where w_x and w_y are the beam waist in x and y direction, x_o and y_o are the centroid positions of the beam. The phase distribution of incident beam and reflected desired Gaussian beam on the mirror surface are given by

$$\phi_{in} = \phi_{cin} + \Delta\phi_{in} = \left(\frac{\phi_{oxin} + \phi_{oyin}}{2}\right) - kz - \frac{k}{2}\left(\frac{(x-x_o)^2}{R_{xin}} + \frac{(y-y_o)^2}{R_{yin}}\right)$$

$$\phi_{cin} = -kz_c + \frac{1}{2}\left(\tan^{-1}\left[\frac{\lambda(z_c - z_{oxin})}{\pi w_{oxin}^2}\right]\tan^{-1}\left[\frac{\lambda(z_c - z_{oyin})}{\pi w_{oyin}^2}\right]\right)$$

$$\phi_{out} = \phi_{cout} + \Delta\phi_{out} = \left(\frac{\phi_{oxout} + \phi_{oyout}}{2}\right) - kz - \frac{k}{2}\left(\frac{(x-x_o)^2}{R_{xout}} + \frac{(y-y_o)^2}{R_{yout}}\right)$$

$$\phi_{cout} = -kz_c + \frac{1}{2}\left(\tan^{-1}\left[\frac{\lambda(z_c - z_{oxout})}{\pi w_{oxout}^2}\right]\tan^{-1}\left[\frac{\lambda(z_c - z_{oyout})}{\pi w_{oyout}^2}\right]\right)$$

where R_x and R_y are the beam radius in x and y direction. z_c is the z-coordinate at the centroid point (x_o, y_o). The mirror surface deformation to achieve the desired Gaussian beam is given by

$$S(x,y,z) = \frac{(\phi_{out} - \phi_{cout}) - (\phi_{in} - \phi_{cin})}{2k\cos\beta}$$

where k is the free space wave number and β is the propagation constant of the wave.

B.3 Coaxial Cavity Gyrotron

GDS 2018 features the modules to perform the design studies of the coaxial cavity gyrotrons. Figure B.5 shows the options available in GDS to perform design studies using coaxial interaction cavity with rectangular corrugated insert and triangular corrugated insert. Modules available in GDS 2018 to perform coaxial cavity gyrotron design studies

are shown in Figure B.6.

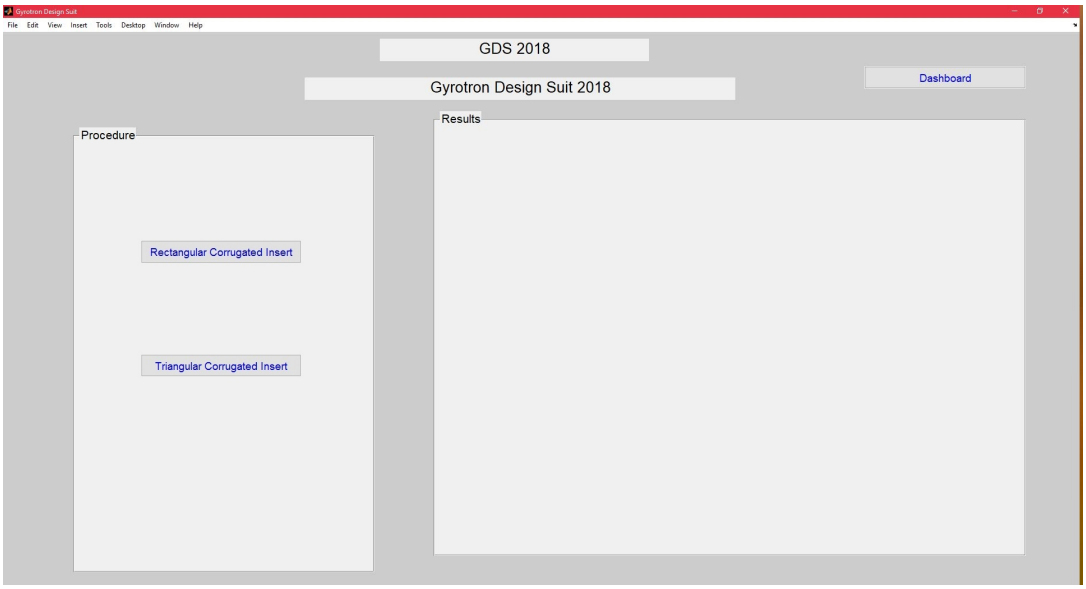

Figure B.5: Option of choosing rectangular or triangular corrugated insert of the coaxial cavity gyrotron.

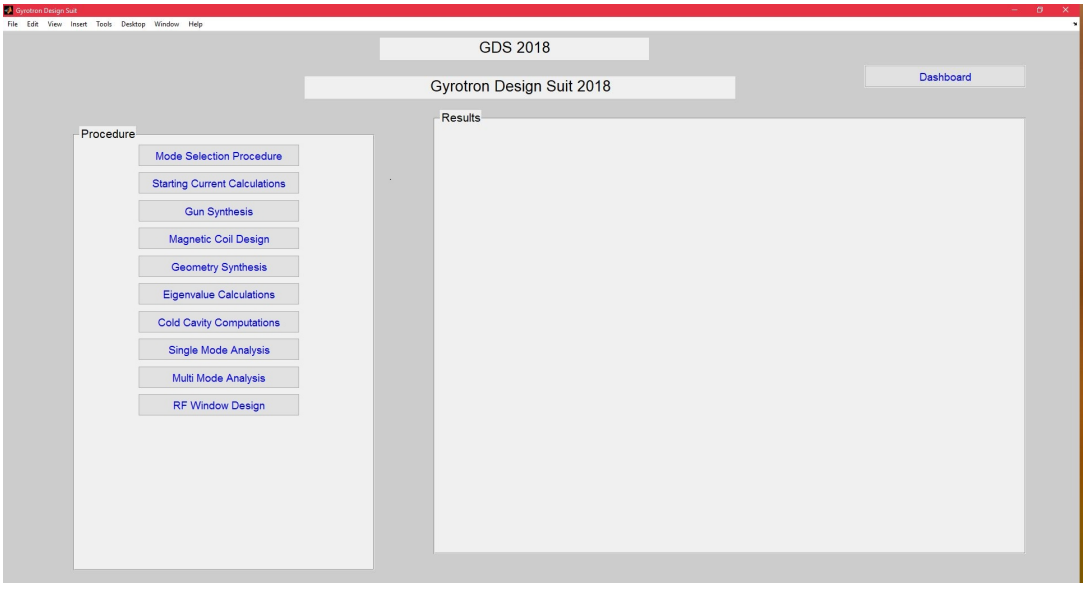

Figure B.6: Complete design options available in GDS 2018 for the coaxial cavity gyrotron case.

B.4 Design expressions used in different modules of GDS 2018 (Coaxial Cavity Gyrotron)

To perform the design studies of coaxial cavity gyrotrons in GDS 2018, major changes are incorporated in the design modules such as Mode Selection Procedure, Eigenvalue Calculations and Cold Cavity Computations. Design expressions used in the other modules are similar to that of conventional cavity gyrotron case.

B.4.1 Mode Selection Procedure

In coaxial cavity gyrotrons, operating cavity modes are selected with relative caustic radius of 0.3, so that mode competition can better controlled by the coaxial insert. Apart from the condition on relative caustic radius, other conditions related to mode selection procedure for coaxial cavity gyrotron case is similar to that of conventional gyrotron case. The voltage depression of the electron beam in the coaxial cavity gyrotron is given by

$$\Delta V \simeq -60\frac{I_b}{\beta_z}\ln\left(\frac{R_o}{R_e}\right)\frac{\ln\left(\frac{R_e}{R_i}\right)}{\ln\left(\frac{R_o}{R_i}\right)}$$

where R_i is the coaxial insert radius. Limiting current I_L is given by

$$I_L = \frac{\left(\frac{511}{60}\right)\gamma_o\left[1-\left(1-\beta_{zo}^2\right)^{1/3}\right]^{3/2}}{\ln\left(\frac{R_o}{R_e}\right)\frac{\ln\left(\frac{R_e}{R_i}\right)}{\ln\left(\frac{R_o}{R_i}\right)}}$$

It is to be noted from the above expressions that voltage depression of the electron beam is reduced due to the presence of insert and hence, the value of limiting current is high. Thus, the coaxial cavity gyrotrons can be operated at higher power levels.

B.4.2 Eigenvalue Calculations

The eigenvalue of cavity mode (χ) in coaxial cavity is dependent on the radii ratio $C = R_o/R_i$. Using this module, eigenvalue of the main mode and other competing modes in the coaxial cavity are determined. The dispersion relation for the coaxial cavity with rectangular corrugated insert is given by

$$J_m^{'}(\chi)\left(Y_m^{'}(\chi/C)+WY_m(\chi/C)\right)-Y_m^{'}(\chi)\left(J_m^{'}(\chi/C)+WJ_m(\chi/C)\right)=0$$

where W is the normalized surface impedance and is given by

$$W = \frac{l}{S}\tan\left(\chi\frac{d}{R_o}\right)$$

l is the spacing between the slot, d is the depth of the slot and S is the period of the slots given by $S = 2\pi R_i/N$. The dispersion relation for the coaxial cavity with triangular corrugated insert is given by

$$J_m^{'}(\chi)\left(Y_m^{'}(\chi/C)+WY_m(\chi/C)\right)-Y_m^{'}(\chi)\left(J_m^{'}(\chi/C)+WJ_m(\chi/C)\right)=0$$

While the normalized surface impedance W is given by

$$W = \frac{l}{S}\frac{J_1(\chi d/R_o)}{J_0(\chi d/R_o)}$$

where J_0 and J_1 are the Bessel function of the order 0 and 1, respectively.

B.4.3 Cold Cavity Computations

In this module, the resonant frequency and diffractive Q factor are calculated for the desired mode in the coaxial cavity by solving the Vlasov's equation given by

$$\frac{d^2V_{mq}}{dz^2}+\left(\frac{\omega^2}{c^2}-k_{mq}^2\right)V_{mq}=0$$

where cutoff wave number (k_{mp}) is given by

$$k_{mp}^2 = (\chi/R_o)^2 - 2(\chi/R_o)^2$$
$$\times\left[\frac{\Delta R_o}{R_o}\left(1-\frac{C}{\chi}\frac{d\chi}{dC}\right)+\frac{\Delta R_i}{R_i}\left(1-\frac{C}{\chi}\frac{d\chi}{dC}\right)\right]$$

$\frac{d\chi}{dC}$ is the slope of the eigenvalue curve along the cavity.

Bibliography

[1] "World Population Prospects: The 2017 Revision, Methodology of the United Nations Population Estimates and Projections," United Nations, Department of Economic and Social Affairs, Population Division, New York: United Nations., Tech. Rep. ESA/P/WP.250., 2017.

[2] "Energy access outlook 2017: From poverty to prosperity," International Energy Agency, World Energy Outlook: Special Report, Tech. Rep., 2017.

[3] F. Romanelli, "Fusion Electricity, A roadmap to the realisation of fusion energy," European Fusion Development Agreement (EFDA), Tech. Rep., 2012.

[4] A. Einstein, "Elementary derivation of the equivalence of mass and energy," *Bulletin of the American Mathematical Society*, vol. 41, no. 4, pp. 223–230, 1935.

[5] J. D. Lawson, "Some criteria for a power producing thermonuclear reactor," in *Proceedings of the Physical Society, Section B*, vol. 70, no. 1, 1957, pp. 6–10.

[6] F. F. Chen, *An Indispensable Truth*. Springer, New York, 2011.

[7] R. Hemsworth, H. Decamps, J. Graceffa, B. Schunke, M. Tanaka, M. Dremel, A. Tanga, H. D. Esch, F. Geli, J. Milnes, T. Inoue, D. Marcuzzi, P. Sonato, and P. Zaccaria, "Status of the ITER heating neutral beam system," *Nuclear Fusion*, vol. 49, no. 4, p. 045006, 2009.

[8] D. F. H. Start, J. Jacquinot, V. Bergeaud, V. P. Bhatnagar, G. A. Cottrell, S. Clement, L.-G. Eriksson, A. Fasoli, A. Gondhalekar, C. Gormezano, G. Grosshoeg, K. Guenther, P. Harbour, L. D. Horton, A. Howman, H. Jackel, O. N. Jarvis, K. D. Lawson, C. Lowry, M. Mantsinen, F. B. Marcus, R. Monk, E. Righi, F. G. Rimini, G. J. Sadler, G. R. Saibene, R. Sartori, B. Schunke, S. Sharapov, A. C. C. Sips, M. Stamp, and P. van Belle, "D-T Fusion with Ion Cyclotron Resonance Heating in the JET Tokamak," *Physics Review Letters*, vol. 80, pp. 4681–4684, May 1998.

[9] V. A. Flyagin and G. S. Nusinovich, "Gyrotron oscillators," *Proceedings of the IEEE*, vol. 76, no. 6, pp. 644–656, June 1988.

[10] Erckmann, V., Kasparek, W., Plaum, B., Lechte, C., Petelin, M.I., Braune, H., Gantenbein, G., Laqua, H. P., Lubiako, L., Marushchenko, N. B., Michel, G., Turkin, Y., Weissgerber, M., the W7-X ECRH- teams at IPP Greifswald, IPF Stuttgart, and KIT, "Large Scale CW ECRH Systems: Some considerations," *EPJ Web of Conferences*, vol. 32, p. 04006, 2012.

[11] G. Giruzzi, M. Lennholm, A. Parkin, G. Aiello, M. Bellinger, J. Bird, F. Bouquey, H. Braune, A. Bruschi, P. Butcher, R. Clay, E. de la Luna, G. Denisov, T. Edlington, J. Fanthome, D. Farina, J. Farthing, L. Figini, S. Garavaglia, J. Garcia, M. Gardener, T. Gerbaud, G. Granucci, J. Hay, M. Henderson, S. Hotchin, V. Ilyin, M. Jennison, W. Kasparek, P. Khilar, N. Kirneva, D. Kislov, S. Knipe, A. Kuyanov, X. Litaudon, A. Litvak, A. Moro, S. Nowak, V. Parail, B. Plaum, G. Saibene, C. Sozzi, P. Späh, D. Strauss, E. Trukhina, A. Vaccaro, A. Vagdama, V. Vdovin, and J. E. Contributors, "Objectives, physics requirements and conceptual design of an ECRH system for JET," *Nuclear Fusion*, vol. 51, no. 6, p. 063033, 2011.

[12] E. Poli, G. Tardini, H. Zohm, E. Fable, D. Farina, L. Figini, N. Marushchenko, and L. Porte, "Electron-cyclotron-current-drive efficiency in DEMO plasmas," *Nuclear Fusion*, vol. 53, no. 1, p. 013011, 2013.

[13] K. Rawat, B. Gowrish, G. Ajmera, R. Kalyan, A. Basu, S. Koul, and F. M. Ghannouchi, "Design strategy for tri-band Doherty power amplifier," in *WAMICON 2014*, June 2014, pp. 1–3.

[14] K. Rawat, B. Gowrish, G. Ajmera, A. Basu, and S. K. Koul, "Design scheme for broadband Doherty power amplifier using broadband load combiner," *International Journal of RF and Microwave Computer-Aided Engineering*, vol. 25, no. 8, pp. 655–674, 2015.

[15] A. Basu, S. K. Koul, S. Basak, and A. Chakrabarti, "Development of an analog phase shifter for particle accelerator control circuits," in *2011 IEEE Applied Electromagnetics Conference (AEMC)*, Dec 2011, pp. 1–4.

[16] A. Gilmour, *Microwave Tubes*. Artech House, 1986.

[17] M. V. Kartikeyan, E. Borie, and M. Thumm, *Gyrotrons: High-Power Microwave and Millimeter Wave Technology*. Berlin, Germany: Springer-Verlag, 2004.

[18] K. L. Felch, B. G. Danly, H. R. Jory, K. E. Kreischer, W. Lawson, B. Levush, and R. J. Temkin, "Characteristics and applications of fast-wave gyrodevices," *Proceedings of the IEEE*, vol. 87, no. 5, pp. 752–781, May 1999.

[19] R. S. Symons and H. R. Jory, "Cyclotron resonance devices," *Advances in Electronics and Electron Physics*, vol. 55, pp. 1–75, 1981.

[20] J. L. Hirshfield and V. L. Granatstein, "The Electron Cyclotron Maser - An Historical Survey," *IEEE Transactions on Microwave Theory and Techniques*, vol. 25, no. 6, pp. 522–527, Jun 1977.

[21] G. Nusinovich, V. Granatstein, and R. Temkin, *Introduction to the Physics of Gyrotrons*. Johns Hopkins University Press, 2004.

[22] V. A. Flyagin, A. V. Gaponov, I. Petelin, and V. K. Yulpatov, "The Gyrotron," *IEEE Transactions on Microwave Theory and Techniques*, vol. 25, no. 6, pp. 514–521, Jun 1977.

[23] K. E. Kreischer, B. G. Danly, J. B. Schutkeker, and R. J. Temkin, "The Design of Megawatt Gyrotrons," *IEEE Transactions on Plasma Science*, vol. 13, no. 6, pp. 364–373, Dec 1985.

[24] R. Angalakurthi and K. C. J. Raju, "Dielectric, ferroelectric and mechanical Properties of Microwave Sintered Bi based High temperature Piezoelectric Ceramics," *IOP Conference Series: Materials Science and Engineering*, vol. 18, no. 9, p. 092028, 2011.

[25] E. S. Reddy, S. Sukumaran, and K. J. Raju, "Microwave assisted synthesis, sintering of lead-free ferroelectric CaBi4Ti4O15 ceramics," *Materials Today: Proceedings*, vol. 3, no. 6, pp. 2213 – 2219, 2016.

[26] M. Y. Glyavin, T. Idehara, and S. P. Sabchevski, "Development of THz Gyrotrons at IAP RAS and FIR UF and Their Applications in Physical Research and High-Power THz Technologies," *IEEE Transactions on Terahertz Science and Technology*, vol. 5, no. 5, pp. 788–797, Sept 2015.

[27] Y. Tatematsu, Y. Yamaguchi, R. Ichioka, I. Ogawa, T. Idehara, and T. Saito, "Development of a multiple-frequency gyrotron, gyrotron FU CW GV," in *2014 39th International Conference on Infrared, Millimeter, and Terahertz waves (IRMMW-THz)*, Sept 2014, pp. 1–2.

[28] A. Sawant, M. S. Choe, M. Thumm, and E. Choi, "Orbital Angular Momentum (OAM) of Rotating Modes Driven by Electrons in Electron Cyclotron Masers," *Scientific Reports*, vol. 7, no. 3372, 2017.

[29] A. Sawant, M. S. Choe, M. Thumm, and E. Choi, "Orbital angular momentum of gyrotron modes," in *2017 42nd International Conference on Infrared, Millimeter, and Terahertz Waves (IRMMW-THz)*, Aug 2017, pp. 1–2.

[30] T. M. Tran, B. G. Danly, K. E. Kreischer, J. B. Schutkeker, and R. J. Temkin, "Optimization of gyroklystron efficiency," *The Physics of Fluids*, vol. 29, no. 4, pp. 1274–1281, 1986.

[31] G. S. Park, V. L. Granatstein, S. Y. Park, C. M. Armstrong, and A. K. Ganguly, "Experimental study of efficiency optimization in a three-cavity gyroklystron amplifier," *IEEE Transactions on Plasma Science*, vol. 20, no. 3, pp. 224–231, June 1992.

[32] G. Gulotta, S. Alberti, B. G. Danly, T. Kimura, W. L. Menninger, J. L. Rullier, and R. J. Temkin, "Cyclotron autoresonance maser (CARM) oscillator experiment at 28 GHz," in *1992 9th International Conference on High-Power Particle Beams*, vol. 3, May 1992, pp. 1532–1537.

[33] K. D. Pendergast, B. G. Danly, and R. J. Temkin, "Operation of a long-pulse CARM oscillator," *Nuclear Instruments and Methods in Physics Research Section A: Accelerators, Spectrometers, Detectors and Associated Equipment*, vol. 304, no. 1, pp. 121–126, 2002.

[34] G. S. Park, S. Y. Park, R. H. Kyser, C. M. Armstrong, A. K. Ganguly, and R. K. Parker, "Broadband operation of a Ka-band tapered gyro-traveling wave amplifier," *IEEE Transactions on Plasma Science*, vol. 22, no. 5, pp. 536–543, Oct 1994.

[35] G. S. Park, J. J. Choi, S. Y. Park, C. M. Armstrong, A. K. Ganguly, K. T. Nguyen, R. H. Kyser, and R. K. Parker, "Operational two-stage tapered gyro-TWT amplifier," in *Proceedings of 1994 IEEE International Electron Devices Meeting*, Dec 1994, pp. 255–258.

[36] M. Garven, J. P. Calame, B. G. Danly, K. T. Nguyen, B. Levush, F. N. Wood, and D. E. Pershing, "A gyrotron-traveling-wave tube amplifier experiment with a ceramic loaded interaction region," *IEEE Transactions on Plasma Science*, vol. 30, no. 3, pp. 885–893, June 2002.

[37] M. Blank, P. Borchard, S. Cauffman, and K. Felch, "Development and demonstration of a broadband W-band gyro-TWT amplifier," in *2005 Joint 30th International Conference on Infrared and Millimeter Waves and 13th International Conference on Terahertz Electronics*, vol. 2, Sept 2005, pp. 652–653 vol. 2.

[38] V. Kesari, P. K. Jain, and B. N. Basu, "Analysis of a tapered disc-loaded waveguide for a wideband gyro-TWT," *IEEE Transactions on Plasma Science*, vol. 34, no. 3, pp. 541–546, June 2006.

[39] M. Mineo and C. Paoloni, " Improved rod shapes for helix slow wave structures," in *2010 IEEE International Vacuum Electronics Conference (IVEC)*, May 2010, pp. 229–230.

[40] C. Paoloni, M. Mineo, M. Henry, and P. G. Huggard, "Double Corrugated Waveguide for Ka-Band Traveling Wave Tube," *IEEE Transactions on Electron Devices*, vol. 62, no. 11, pp. 3851–3856, Nov 2015.

[41] P. E. Latham, W. Lawson, V. Irwin, B. Hogan, G. S. Nusinovich, H. W. Matthews, and M. K. E. Flaherty, "High power operation of an X-band gyrotwistron," *Phys. Rev. Lett.*, vol. 72, pp. 3730–3733, Jun 1994.

[42] G. S. Nusinovich, P. M. Malouf, and V. L. Granatstein, "Theory of gyrotwystrons with mixed transverse geometries of the various stages," *IEEE Transactions on Plasma Science*, vol. 22, no. 5, pp. 518–525, Oct 1994.

[43] C. R. Donaldson, W. He, A. W. Cross, F. Li, A. D. R. Phelps, L. Zhang, K. Ronald, C. W. Robertson, C. G. Whyte, and P. McElhinney, "Experimental demonstration of a W-band gyro-BWO using a helically corrugated waveguide," in *2010 IEEE International Vacuum Electronics Conference (IVEC)*, May 2010, pp. 195–196.

[44] J. Feng, Y. Tang, D. Gamzina, X. Li, B. Popovic, M. Gonzalez, L. Himes, R. Barchfeld, H. Li, P. Pan, R. Letizia, C. Paoloni, and N. C. Luhmann, "Fabrication of a 0.346-THz BWO for Plasma Diagnostics," *IEEE Transactions on Electron Devices*, vol. 65, no. 6, pp. 2156–2163, June 2018.

[45] W. He, C. R. Donaldson, L. Zhang, P. McElhinney, A. D. R. Phelps, K. Ronald, and A. W. Cross, "Latest experiments of W-band gyro-BWO using helically corrugated waveguides," in *2013 38th International Conference on Infrared, Millimeter, and Terahertz Waves (IRMMW-THz)*, Sept 2013, pp. 1–2.

[46] A. V. G. A. L. G. M. I. P. V. G. U. A. A. Andronov, V. A. Flyagin and V. K. Yulpatov, "The gyrotron: High-power source of millimeter and submillimeter waves," *Infrared Physics*, vol. 18, no. 5-6, p. 385–393, 1978.

[47] M. Thumm, S. Alberti, A. Arnold, P. Brand, H. Braune, G. Dammertz, V. Erckmann, G. Gantenbein, E. Giguet, R. Heidinger, J. Hogge, S. Illy, W. Kasparek, H. P. Laqua, F. Legrand, W. Leonhardt, C. Lievin, G. Michel, G. Neffe, B. Piosczyk,

M. Schmid, K. Schworer, and M. Q. Tran, "EU megawatt-class 140-GHz CW gyrotron," *IEEE Transactions on Plasma Science*, vol. 35, no. 2, pp. 143–153, 2007.

[48] T. Rzesnicki, I. G. Pagonakis, A. Samartsev, K. Avramidis, G. Gantenbein, S. Illy, J. Jelonnek, J. Jin, C. Lechte, M. Losert, B. Piosczyk, and M. Thumm, "Recent experimental results of the European 1 MW, 170 GHz short-pulse gyrotron prototype for ITER," in *2015 40th International Conference on Infrared, Millimeter, and Terahertz waves (IRMMW-THz)*, Aug 2015, pp. 1–2.

[49] I. Gr, F. Albajar, S. Alberti, K. Avramidis, T. Bonicelli, F. Braunmueller, A. Bruschi, I. Chelis, F. Cismondi, G. Gantenbein, V. Hermann, K. Hesch, J.-p. Hogge, J. Jelonnek, J. Jin, S. Illy, Z. C. Ioannidis, T. Kobarg, G. P. Latsas, F. Legrand, M. Lontano, B. Piosczyk, Y. Rozier, T. Rzesnicki, A. Samartsev, C. Schlatter, M. Thumm, I. G. Tigelis, M.-q. Tran, T.-m. Tran, and J. Weggen, "Status of the development of the EU 170 GHz / 1 MW / CW gyrotron," *Fusion Engineering and Design*, vol. 96-97, pp. 149–154, 2015.

[50] K. Sakamoto, R. Ikeda, Y. Oda, T. Kobayashi, K. Kajiwara, H. Shidara, K. Takahashi, and S. Moriyama, "Status of high power gyrotron development in JAEA," in *2015 IEEE International Vacuum Electronics Conference (IVEC)*, April 2015, pp. 1–2.

[51] G. G. Denisov, A. G. Litvak, A. V. Chirkov, A. G. Eremeev, V. I. Malygin, E. M. Tai, V. E. Myasnikov, L. G. Popov, E. A. Soluyanova, Y. N. Belov, I. V. Kazansky, A. V. Kruglov, V. O. Nichiporenko, E. V. Sokolov, S. V. Usachev, and I. N. Roy, "Development status of gyrotron setup for ITER ECW system," in *2015 40th International Conference on Infrared, Millimeter, and Terahertz waves (IRMMW-THz)*, Aug 2015, pp. 1–2.

[52] K. Sakamoto, A. Kasugai, K. Takahashi, R. Minami, N. Kobayashi, and K. Kajiwara, "Achievement of robust high-efficiency 1 MW oscillation in the hard-self-excitation region by a 170 GHz continuous-wave gyrotron," *Nature Physics*, pp. 411–414, 2007.

[53] G. Nusinovich, M. Read, O. Dumbrajs, and K. Kreischer, "Theory of gyrotrons with coaxial resonators," *IEEE Transactions on Electron Devices*, vol. 41, no. 3, pp. 433–438, 1994.

[54] C. T. Iatrou, S. Kern, and A. B. Pavelyev, "Coaxial cavities with corrugated inner conductor for gyrotrons," *IEEE Transactions on Microwave Theory and Techniques*, vol. 44, no. 1, pp. 56–64, 1996.

[55] T. Rzesnicki, G. Gantenbein, J. Jelonnek, J. Jin, B. Piosczyk, A. Samartsev, A. Schlaich, and M. Thumm, "2 MW, 170 GHz Coaxial-Cavity Short-Pulse Gyrotron - single stage depressed collector operation," in *39th International Conference on Infrared, Millimeter and Terahertz Waves, IRMMW-THz*, 2014, pp. 1–2.

[56] A. W. Morris, "MHD instability control, disruptions, and error fields in tokamaks," *Plasma Physics and Controlled Fusion*, vol. 34, no. 13, p. 1871, 1992.

[57] M. Thumm, J. Franck, P. Kalaria, K. Avramidis, G. Gantenbein, S. Illy, I. Pagonakis, M. Schmid, C. Wu, J. Zhang, and J. Jelonnek, "Towards a 0.24-THz 1-to-2-MW-class gyrotron for DEMO," *Terahertz Science and Technology*, vol. 8, no. 3, pp. 85–100, September 2015.

[58] S. Garavaglia, W. Bin, A. Bruschi, G. Granucci, G. Grossetti, J. Jelonnek, A. Moro, N. Rispoli, D. Strauss, Q. M. Tran, and T. Franke, "Preliminary conceptual design of demo ec system," *AIP Conference Proceedings*, vol. 1689, no. 1, p. 090009, 2015.

[59] R. Wenninger, F. Arbeiter, J. Aubert, L. Aho-Mantila, R. Albanese, R. Ambrosino, C. Angioni, J.-F. Artaud, M. Bernert, E. Fable, A. Fasoli, G. Federici, J. Garcia, G. Giruzzi, F. Jenko, P. Maget, M. Mattei, F. Maviglia, E. Poli, G. Ramogida, C. Reux, M. Schneider, B. Sieglin, F. Villone, M. Wischmeier, and H. Zohm, "Advances in the physics basis for the European DEMO design," *Nuclear Fusion*, vol. 55, no. 6, p. 063003, 2015.

[60] G. Gantenbein, A. Samartsev, G. Aiello, G. Dammertz, J. Jelonnek, M. Losert, A. Schlaich, T. A. Scherer, D. Strauss, M. Thumm, and D. Wagner, "First Operation of a Step-Frequency Tunable 1-MW Gyrotron With a Diamond Brewster Angle Output Window," *IEEE Transactions on Electron Devices*, vol. 61, no. 6, pp. 1806–1811, 2014.

[61] R. Ikeda, Y. Oda, T. Kobayashi, M. Terakado, K. Kajiwara, K. Takahashi, S. Moriyama, and K. Sakamoto, "Development of multi-frequency gyrotron for ITER and DEMO at QST," in *2016 41st International Conference on Infrared, Millimeter, and Terahertz waves (IRMMW-THz)*, Sept 2016, pp. 1–2.

[62] D. H. Wagner, J. K. Stober, F. Leuterer, G. Sips, G. Grünwald, F. Monaco, M. J. Munich, E. Poli, H. Schütz, F. Volpe, W. Treutterer, H. Zohm, T. Franke, M. Thumm, R. Heidinger, G. Gantenbein, A. Meier, W. Kasparek, C. Lechte, A. G.

Litvak, G. G. Denisov, A. Chirkov, E. Tai, L. Popov, V. Nichiporenko, V. Myasnikov, E. Solyanova, and S. Malygin, "Progress and first results with the new multifrequency ECRH system for ASDEX upgrade," *IEEE Transactions on Plasma Science*, vol. 37, no. 3, pp. 395–402, 2009.

[63] T. Kobayashia, S. Moriyama, A. Isayama, M. Sawahata, M. Terakado, S. Hiranai, K. Wada, Y. Sato, J. Hinata, K. Yokokura, K. Hoshino, and K. Sakamoto, "Development of a dual frequency (110/138 GHz) gyrotron for JT-60SA and its extension to an oscillation at 82 GHz," *EPJ Web of Conferences*, vol. 87, p. 04008(5 pp.), mar 2015.

[64] S. Alberti, F. Braunmueller, J. Genoud, J. P. Hogge, T. M. Tran, M. Q. Tran, K. Avramidis, I. G. Pagonakis, J. Jin, S. Illy, G. Gantenbein, J. Jelonnek, and F. Cismondi, "Dual-frequency, 126/84 ghz, 1 mw gyrotron for the upgrade of the tcv ec-system," in *2015 40th International Conference on Infrared, Millimeter, and Terahertz waves (IRMMW-THz)*, Aug 2015, pp. 1–2.

[65] L. Waganer, F. Najmabadi, and M. Tillack, "What must DEMO do?" in *16th International Symposium on Fusion Engineering*, 1995.

[66] R. Hiwatari, K. Okano, Y. Asaoka, K. Shinya, and Y. Ogawa, "Demonstration tokamak fusion power plant for early realization of net electric power generation," *Nuclear Fusion*, vol. 45, no. 2, p. 96, 2005.

[67] G. Federici, G. Giruzzi, C. Lowry, R. Kemp, D. Ward, R. Wenninger, , and H. Zohm, "EU DEMO design and R&D studies," in *25th Symposium on Fusion Engineering (SOFE)*, 2013.

[68] G. Federici, R. Kemp, D. Ward, C. Bachmann, T. Franke, S. Gonzalez, C. Lowry, M. Gadomska, J. Harman, B. Meszaros, C. Morlock, F. Romanelli, and R. Wenninger, "Overview of EU DEMO design and R&D activities," *Fusion Engineering and Design*, vol. 89, no. 7, pp. 882 – 889, 2014, proceedings of the 11th International Symposium on Fusion Nuclear Technology-11 (ISFNT-11) Barcelona, Spain, 15-20 September, 2013.

[69] T. Imai, N. Kobayashi, R. Temkin, M. Thumm, and M. Q. Tran, "ITER R&D: Auxiliary Systems: Electron Cyclotron Heating and Current Drive System," *Fusion Engineering and Design*, vol. 55, no. 2-3, pp. 281–289, 2001.

[70] K. Sakamoto, K. Takahashi, A. Kasugai, R. Minami, N. Kobayashi, S. Nishio, M. Sato, and K. Tobita, "Conceptual study of ECH/ECCD system for fusion

DEMO plant," *Fusion Engineering and Design*, vol. 81, no. 8, pp. 1263 – 1270, 2006, proceedings of the Seventh International Symposium on Fusion Nuclear Technology.

[71] G. Federici, C. Bachmann, W. Biel, L. Boccaccini, F. Cismondi, S. Ciattaglia, M. Coleman, C. Day, E. Diegele, T. Franke, M. Grattarola, H. Hurzlmeier, A. Ibarra, A. Loving, F. Maviglia, B. Meszaros, C. Morlock, M. Rieth, M. Shannon, N. Taylor, M. Tran, J. You, R. Wenninger, and L. Zani, "Overview of the design approach and prioritization of R&D activities towards an EU DEMO," *Fusion Engineering and Design*, vol. 109-111, pp. 1464 – 1474, 2016, proceedings of the 12th International Symposium on Fusion Nuclear Technology-12 (ISFNT-12).

[72] J. J. Barroso and R. A. Correa, "Design of a TE42 7 Coaxial Cavity for a 1 MW, 280 GHz Gyrotron," *International Journal of Infrared and Millimeter Waves*, vol. 13, no. 4, pp. 443–455, 1992.

[73] B. Piosczyk, G. Dammertz, O. Dumbrajs, M. V. Kartikeyan, M. K. Thumm, and X. Yang, "165-GHz coaxial cavity gyrotron," *IEEE Transactions on Plasma Science*, vol. 32, no. 3, pp. 853–860, 2004.

[74] S. Singh and M. V. Kartikeyan, "Analysis of a Triangular Corrugated Coaxial Cavity for Megawatt-Class Gyrotron," *IEEE Transactions on Electron Devices*, vol. 62, no. 7, pp. 2333–2338, July 2015.

[75] C. J. Edgcombe, "The dispersion equation for the gyrotron amplifier," *International Journal of Electronics*, vol. 48, no. 6, pp. 471–486, 1980.

[76] G. S. Nusinovich, "Mode interaction in gyrotrons," *International Journal of Electronics*, vol. 51, no. 4, pp. 457–474, 1981.

[77] D. Pozar, *Microwave Engineering 3rd Edition*. Wiley, 2004.

[78] C. Edgcombe, *Gyrotron Oscillators - Their Principles and Practice.* Taylor and Francis Ltd., Cambridge, MA, USA, 1993.

[79] J. Y. Choe and S. Ahn, "General mode analysis of a gyrotron dispersion equation," *IEEE Transactions on Electron Devices*, vol. 28, no. 1, pp. 94–102, Jan 1981.

[80] S. C. Zhang, "On the gyrotron dispersion equation for a general mode," *International Journal of Electronics*, vol. 60, no. 2, pp. 297–299, 1986.

[81] V. B. Naidu, S. K. Datta, and S. Kamath, "3D Analysis of fabrication misalignments in electron gun," in *2011 IEEE International Vacuum Electronics Conference (IVEC)*, Feb 2011, pp. 503–504.

[82] P. Janardhan, S. Kamath, V. L. Christie, and L. Kumar, "3-dimensional particle-in-cell modeling of a shadow-gridded electron gun," in *2000 International Vacuum Electronics Conference*, May 2000, pp. 2 pp.–.

[83] B. Piosczyk, "A novel 4.5-MW electron gun for a coaxial cavity gyrotron," *IEEE Transactions on Electron Devices*, vol. 48, no. 12, pp. 2938–2944, 2001.

[84] M. H. Beringer, S. Illy, J. Jin, S. Kern, J. C. Rode, and M. Thumm, "Further design steps towards a 4 MW 170 GHz coaxial-cavity gyrotron," in *2009 34th International Conference on Infrared, Millimeter, and Terahertz Waves*, Sept 2009, pp. 1–2.

[85] Y. Yamaguchi, Y. Tatematsu, T. Saito, R. Ikeda, J. C. Mudiganti, I. Ogawa, and T. Idehara, "Formation of a laminar electron flow for 300 GHz high power pulsed gyrotron," *Physics of Plasmas*, vol. 19, no. 11, p. 113113, 2012.

[86] F. Chen, *Introduction to plasma physics*. Plenum Press, 1974.

[87] S. Tsimring, "Gyrotron electron beams: Velocity and energy spread and beam instabilities," *International Journal of Infrared and Millimeter Waves*, vol. 22, no. 10, pp. 1433–1468, Oct 2001.

[88] G. Gantenbein, G. Dammertz, J. Flamm, S. Illy, S. Kern, G. Latsas, B. Piosczyk, T. Rzesnicki, A. Samartsev, A. Schlaich, M. Thumm, and I. Tigelis, "Experimental Investigations and Analysis of Parasitic RF Oscillations in High-Power Gyrotrons," *IEEE Transactions on Plasma Science*, vol. 38, no. 6, pp. 1168–1177, June 2010.

[89] S. N. Vlasov, G. M. Zhislin, I. M. Orlova, M. I. Petelin, and G. G. Rogacheva., "IrregularWaveguides as Open Resonators," *Radiophysics and Quantum Electronics*, vol. 12, pp. 972–978, 1969.

[90] B. G. Danly and R. J. Temkin, "Generalized nonlinear harmonic gyrotron theory," *The Physics of Fluids*, vol. 29, no. 2, pp. 561–567, 1986.

[91] L.A.Weinstein, *Open resonators and open waveguides*, ser. Golem series in electromagnetics. Golem Press, Boulder, CO, USA, 1969.

[92] S. N. Vlasov, L. I. Zagryadskaya, and I. M. Orlova., "OpenCoaxial Resonators for Gyrotrons," *Radio Engineering and Electronic Physics*, vol. 21, pp. 96–102, 1976.

[93] S. Kern, "Numerische Simulation der Gyrotron-Wechselwirkung in koaxialen Resonatoren," *Wissenschaftliche Berichte FZKA 5837, Forschungszentrum Karlsruhe, Germany*, November 1996.

[94] O. Dumbrajs and G. S. Nusinovich, "Coaxial gyrotrons: Past, present, and future (review)," *IEEE Transactions on Plasma Science*, vol. 32, no. 3, pp. 934–946, 2004.

[95] V. R. K. Murthy, K. C. J. Raju, and B. Viswanathan, "Characteristics of materials for microwave devices," *Bulletin of Materials Science*, vol. 15, no. 3, pp. 213–217, Jun 1992.

[96] K. Singh, P. K. Jain, and B. N. Basu, "Analysis of a coaxial waveguide corrugated with wedge-shaped radial vanes or ridges considering azimuthal harmonic effects," *Progress in Electromagnetic Research*, vol. 47, no. 4, pp. 297–312, 2004.

[97] J. R. Sirigiri, K. E. Kreischer, J. Machuzak, I. Mastovsky, M. A. Shapiro, and R. J. Temkin, "Photonic Band Gap Resonator Gyrotron," *Physics Review Letters*, vol. 86, pp. 5628–5631, Jun 2001.

[98] M. A. G. Laso, M. J. Erro, D. Benito, M. J. Garde, T. Lopetegi, F. Falcone, and M. Sorolla, "Analysis and design of 1-D photonic bandgap microstrip structures using a fiber grating model," *Microwave and Optical Technology Letters*, vol. 22, no. 4, pp. 223–226, Jul. 1999.

[99] F. Martin, F. Falcone, J. Bonache, T. Lopetegi, M. A. G. Laso, and M. Sorolla, "New periodic loaded electromagnetic bandgap coplanar waveguide with complete spurious passband suppression," *IEEE Microwave and Wireless Components Letters*, vol. 12, no. 11, pp. 435–437, Nov 2002.

[100] F. Falcone, T. Lopetegi, and M. Sorolla, "1-D and 2-D photonic bandgap microstrip structures," *Microwave and Optical Technology Letters*, vol. 22, no. 6, pp. 411–412, Aug. 1999.

[101] J. N. Tripathi, J. Mukherjee, P. R. Apte, R. K. Nagpal, N. K. Chhabra, and R. Malik, "A novel EBG power plane structure for suppressing SSN in high speed systems," in *2013 IEEE Electrical Design of Advanced Packaging Systems Symposium (EDAPS)*, Dec 2013, pp. 237–240.

[102] A. Mobius and M. Thumm, *Gyrotron output launchers and output tapers. In Gyrotron Oscillators - Their Principles and Practice Ed. C. J. Edgcombe, Ch. 7.* Taylor and Francis, London, 1993.

[103] A. Chittora, J. Mukherjee, S. Singh, and A. Sharma, "Dielectric loaded TM_{01}toTE_{11} mode converter for S-band applications," *IEEE Transactions on Dielectrics and Electrical Insulation*, vol. 22, no. 4, pp. 2057–2063, August 2015.

[104] A. Chittora, S. Singh, A. Sharma, and J. Mukherjee, "A Novel TM_{01}toTE_{11} Mode Converter Designed With Radially Loaded Dielectric Slabs," *IEEE Transactions on Microwave Theory and Techniques*, vol. 64, no. 4, pp. 1170–1175, April 2016.

[105] A. Patri, A. Chittora, and J. Mukherjee, "Compact TM01to TE11mode converter designed with matching sections," in *2017 IEEE International Symposium on Antennas and Propagation USNC/URSI National Radio Science Meeting*, July 2017, pp. 2217–2218.

[106] W. G. Lawson, "Theoretical evaluation of nonlinear tapers for a high-power gyrotron," *IEEE Transactions on Microwave Theory and Techniques*, vol. 38, no. 11, pp. 1617–1622, Nov 1990.

[107] J. N. Tripathi, R. K. Nagpal, N. K. Chhabra, R. Malik, and J. Mukherjee, "Maintaining Power Integrity by damping the cavity-mode anti-resonances' peaks on a power plane by Particle Swarm Optimization," in *Thirteenth International Symposium on Quality Electronic Design (ISQED)*, March 2012, pp. 525–528.

[108] S. Kamisetty, J. Garg, J. N. Tripathi, and J. Mukherjee, "Optimization of Analog RF Circuit parameters using randomness in particle swarm optimization," in *2011 World Congress on Information and Communication Technologies*, Dec 2011, pp. 274–278.

[109] S. N. Vlasov, L. I. Zagriadskaia, and M. I. Petelin, "Transformation of a whispering gallery mode, propagating in a circular waveguide, into a beam of waves." *IRadiotekhnika i Elektronika*, vol. 20, pp. 2026–2030, 1975.

[110] Y. Tatematsu, Y. Yamaguchi, T. Idehara, T. Kawase, H. Kato, R. Ikeda, T. Kanemaki, I. Ogawa, and T. Saito, "Development of gyrotron fu cw giii with a gaussian beam output," in *2012 37th International Conference on Infrared, Millimeter, and Terahertz Waves*, Sept 2012, pp. 1–2.

[111] A. V. Chirkov, G. G. Denisov, M. L. Kulygin, V. I. Malygin, S. A. Malygin, A. B. Pavel'ev, and E. A. Soluyanova, "Use of huygens' principle for analysis and synthesis of the fields in oversized waveguides," *Radiophysics and Quantum Electronics*, vol. 49, no. 5, pp. 344–353, May 2006.

[112] G. G. Denisov, A. N. Kuftin, V. I. Malygin, N. P. Venediktov, D. V. Vinogradov, and V. E. Zapevalov, "110 GHz gyrotron with a built-in high-efficiency converter," *International Journal of Electronics*, vol. 72, no. 5-6, pp. 1079–1091, 1992.

[113] D. Gamzina, L. G. Himes, R. Barchfeld, Y. Zheng, B. K. Popovic, C. Paoloni, E. Choi, and N. C. Luhmann, "Nano-CNC Machining of Sub-THz Vacuum Electron Devices," *IEEE Transactions on Electron Devices*, vol. 63, no. 10, pp. 4067–4073, Oct 2016.

[114] O. Prinz, A. Arnold, G. Gantenbein, Y.-h. Liu, M. Thumm, and D. Wagner, "Highly Efficient Quasi-Optical Mode Converter for a Multifrequency High-Power Gyrotron," *IEEE Transactions on Electron Devices*, vol. 56, no. 5, pp. 828–834, 2009.

[115] J. Jin, J. Flamm, S. Kern, T. Rzesnicki, and M. Thumm, "Design of phase correcting mirror system for coaxial-cavity ITER gyrotron," in *2010 IEEE International Vacuum Electronics Conference (IVEC)*, May 2010, pp. 29–30.

[116] J. Jin, M. Thumm, B. Piosczyk, and T. Rzesnicki, "Theoretical investigation of an advanced launcher for a 2-MW 170-GHz TE34,19 coaxial cavity gyrotron," *IEEE Transactions on Microwave Theory and Techniques*, vol. 54, no. 3, pp. 1139–1145, March 2006.

[117] M. Thumm, "Development of output windows for high-power long-pulse gyrotrons and ec wave applications," *International Journal of Infrared and Millimeter Waves*, vol. 19, no. 1, pp. 3–14, Jan 1998.

[118] V. Kesari, A. K. Singh, R. Seshadri, and S. Kamath, "Boron Nitride and Sapphire Windows for 95-GHz Gaussian RF Beam," *IEEE Transactions on Electron Devices*, vol. 63, no. 8, pp. 3257–3261, Aug 2016.

[119] M. Thumm, "MPACVD-diamond windows for high power and long pulse millimeter wave transmission," *Diamond and Related Materials*, vol. 10, pp. 1692–1699, 2001.

[120] B. Sindam and K. C. James Raju, "Microwave dielectric properties of Ba(Zn1/3Ta2 / 3)O3 for application in high power waveguide window," *The European Physical Journal B*, vol. 89, no. 4, p. 92, Apr 2016.

[121] R. Heidinger, G. Dammertz, A. Meier, and M. K. Thumm, "CVD diamond windows studied with low- and high-power millimeter waves," *IEEE Transactions on Plasma Science*, vol. 30, no. 3, pp. 800–807, June 2002.

[122] M. Thumm, A. Arnold, R. Heidinger, M. Rohde, R. Schwab, and R. Spoerl, "Status report on CVD-diamond window development for high power ECRH," *Fusion Engineering and Design*, vol. 53, no. 1, pp. 517 – 524, 2001.

[123] A. Singh, D. S. Weile, S. Rajapatirana, and V. L. Granatstein, "Integrated design of depressed collectors for gyrotrons," *IEEE Transactions on Plasma Science*, vol. 25, no. 3, pp. 480–491, June 1997.

[124] S. Illy, I. Danilov, S. Raff, and B. Piosczyk, "Design studies of the collector sweeping system for the 2 MW 170 GHz coaxial gyrotron for ITER," in *Infrared and Millimeter Waves, Conference Digest of the 2004 Joint 29th International Conference on 2004 and 12th International Conference on Terahertz Electronics, 2004.*, Sept 2004, pp. 231–232.

[125] B. Piosczyk, C. T. Iatrou, G. Dammertz, and M. Thumm, "Single-Stage Depressed Collectors for Gyrotrons," *IEEE Transactions on Plasma Science*, vol. 24, no. 3, pp. 579–585, 1996.

[126] A. Singh, V. L. Granatstein, G. Hazel, G. Saraph, J. M. Cooperstein, and T. Hargreaves, "A depressed collector system for a quasi-optical gyrotron with precisely controlled magnetic flux lines," *International Journal of Infrared and Millimeter Waves*, vol. 12, no. 4, pp. 323–334, Apr 1991.

[127] C. Wu, I. Pagonakis, S. Illy, M. Thumm, G. Gantenbein, and J. Jelonnek, "Preliminary studies on Multistage Depressed Collectors for fusion gyrotrons," in *2016 German Microwave Conference (GeMiC)*, March 2016, pp. 365–368.

[128] C. Wu, I. G. Pagonakis, G. Gantenbein, S. Illy, M. Thumm, and J. Jelonnek, "Conceptual designs of E X B multistage depressed collectors for gyrotrons," *Physics of Plasmas*, vol. 24, no. 4, p. 043102, 2017.

[129] M. K. Thumm, "State-of-the-Art of High Power Gyro-Devices and Free Electron Masers Update 2017," *KIT Scientific Report, Germany*, no. 7750, 2018.

[130] O. Braz, G. Dammertz, M. Kuntze, and M. Thumm, "D-Band Frequency Step-tuning of a 1 MW gyrotron using a Brewster Output Window," *International Journal of Infrared and Millimeter Waves*, vol. 18, no. 8, pp. 1465–1477, 1997.

[131] K. Koppenburg, G. Dammertz, M. Kuntze, B. Piosczyk, and M. Thumm, "Fast frequency-step-tunable high-power gyrotron with hybrid-magnet-system," *IEEE Transactions on Electron Devices*, vol. 48, no. 1, pp. 101–107, 2001.

[132] E. Borie, O. Drumm, S. Illy, M. Kartikeyan, B. Piosczyk, D. Wagner, G. Dammertz, and M. Thumm, "Possibilities for multifrequency operation of a gyrotron at fzk," *IEEE Transactions on Plasma Science*, vol. 30, no. 3, pp. 828–834, jun 2002.

[133] A. Samartsev, K. A. Avramidis, G. Gantenbein, G. Dammertz, M. Thumm, and J. Jelonnek, "Efficient frequency step-tunable megawatt-class D-band gyrotron," *IEEE Transactions on Electron Devices*, vol. 62, no. 7, pp. 2327–2332, 2015.

[134] G. G. Denisov, A. G. Litvak, V. E. Myasnikov, E. M. Tai, and V. E. Zapevalov, "Development in Russia of high-power gyrotrons for fusion," *Nuclear Fusion*, vol. 48, no. 054007(5pp), 2008.

[135] A. G. Litvak, G. G. Denisov, V. E. Myasnikov, E. M. Tai, E. V. Sokolov, and V. I. Ilin, "New results of megawatt power gyrotrons development," in *2013 38th International Conference on Infrared, Millimeter, and Terahertz Waves (IRMMW-THz)*, Sept 2013, pp. 1–2.

[136] M. Blank, K. Felch, P. Borchard, P. Cahalan, S. R. Cauffman, T. S. Chu, and H. Jory, "Demonstration of a high-power long-pulse 140-GHz gyrotron oscillator," *IEEE Transactions on Plasma Science*, vol. 32, no. 3, pp. 867–876, 2004.

[137] K. Felch, M. Blank, P. Borchard, and S. Cauffman, "Status of testing activities on gyrotrons for magnetic fusion applications," in *2017 42nd International Conference on Infrared, Millimeter, and Terahertz Waves (IRMMW-THz)*, Aug 2017, pp. 1–2.

[138] S. Cauffman, M. Blank, P. Borchard, and K. Felch, "Design and testing of a 900 kW, 140 GHz gyrotron," in *2015 40th International Conference on Infrared, Millimeter, and Terahertz waves (IRMMW-THz)*, Aug 2015, pp. 1–2.

[139] K. Felch, M. Blank, P. Borchard, and S. Cauffman, "Recent tests on 117.5 GHz and 170 GHz gyrotrons," in *2015 EPJ Web of Conferences*, vol. 87, no. 04006, Aug 2015, pp. 1–4.

[140] A. Kasugai, K. Kajiwara, K. Takahashi, N. Kobayashi, T. Kariya, Y. Mitsunaka, and K. Sakamoto, "Steady State Operation of High Power Gyrotron for ITER," in *2007 IEEE International Vacuum Electronics Conference*, May 2007, pp. 1–4.

[141] Z. C. Ioannidis, T. Rzesnicki, F. Albajar, S. Alberti, K. A. Avramidis, W. Bin, T. Bonicelli, A. Bruschi, I. Chelis, P. Frigot, G. Gantenbein, V. Hermann, J. Hogge, S. Illy, J. Jin, J. Jelonnek, S. Member, W. Kasparek, G. Latsas, C. Lechte, F. Legrand, T. Kobarg, I. G. Pagonakis, Y. Rozier, C. Schlatter, M. Schmid, I. G.

Tigelis, M. Thumm, M. Q. Tran, A. Zein, and A. Zisis, "CW Experiments With the EU 1-MW , 170-GHz Industrial Prototype Gyrotron for ITER at KIT," *IEEE Transactions on Electron Devices*, vol. 64, no. 9, pp. 3885–3892, 2017.

[142] J. P. Hogge, F. Albajar, S. Alberti, K. Avramidis, W. Bin, T. Bonicelli, F. Braunmueller, A. Bruschi, J. Chelis, P. E. Frigot, G. Gantenbein, V. Hermann, S. Illy, Z. C. Ioannidis, J. Jelonnek, J. Jin, W. Kasparek, T. Kobarg, G. P. Latsas, C. Lechte, M. Lontano, M. Losert, I. G. Pagonakis, Y. Rozier, T. Rzesnicki, C. Schlatter, M. Schmid, M. Thumm, I. G. Tigelis, M. Q. Tran, J. L. Vomvoridis, and A. I. Zisis, "Status and experimental results of the European 1 MW, 170 GHz industrial CW prototype Gyrotron for ITER," in *2016 41st International Conference on Infrared, Millimeter, and Terahertz waves (IRMMW-THz)*, Sept 2016, pp. 1–3.

[143] V. E. Myasnikov, M. V. Agapova, A. N. Kuftin, V. E. Zapevalov, G. G. Denisov, L. M. Belnova, A. V. Chirkov, A. P. Gnedenkov, A. G. Litvak, V. I. Malygin, V. N. Manuilov, V. O. Nichiporenko, V. N. Novikov, L. G. Popov, I. N. Roy, V. G. Rukavishnikova, E. V. Sokolov, E. A. Soluyanova, E. M. Tai, S. V. Usachev, and Y. M. Yashnov, "New results of extra-powerful 1.5MW/170GHz gyrotron development," in *2014 39th International Conference on Infrared, Millimeter, and Terahertz waves (IRMMW-THz)*, Sept 2014, pp. 1–2.

[144] K. Sakamoto, Y. Oda, R. Ikeda, T. Kobayashi, K. Kajiwara, K. Hayashi, K. Takahashi, and S. Moriyama, "Progress on high power long pulse gyrotron development in JAEA," in *2014 39th International Conference on Infrared, Millimeter, and Terahertz waves (IRMMW-THz)*, Sept 2014, pp. 1–2.

[145] R. Ikeda, K. Kajiwara, Y. Oda, K. Takahashi, and K. Sakamoto, " High-power and long-pulse operation of TE31,11 mode gyrotron." *Fusion Eng. and Design*, pp. 482–487, 2015.

[146] E. Choi, A. J. Cerfon, I. Mastovsky, W. Mulligan, M. A. Shapiro, J. R. Sirigiri, and R. J. Temkin, "Experimental study of a 1.5 MW, 110 GHz gyrotron with a single-stage depressed collector," in *2007 Joint 32nd International Conference on Infrared and Millimeter Waves and the 15th International Conference on Terahertz Electronics*, Sept 2007, pp. 98–99.

[147] D. S. Tax, B. Y. Rock, B. J. Fox, S. K. Jawla, S. C. Schaub, M. A. Shapiro, R. J. Temkin, and R. J. Vernon, "Experimental Results for a Pulsed 110/124.5-GHz Megawatt Gyrotron," *IEEE Transactions on Plasma Science*, vol. 42, no. 5, pp. 1128–1134, May 2014.

[148] J. P. Anderson, M. A. Shapiro, R. J. Temkin, I. Mastovsky, and S. R. Cauffman, "Studies of the 1.5-MW 110-GHz gyrotron experiment," *IEEE Transactions on Plasma Science*, vol. 32, no. 3, pp. 877–883, June 2004.

[149] E. M. Choi, C. Marchewka, J. R. Sirigiri, M. A. Shapiro, and R. J. Temkin, "Experimental results for a 1.5 MW, 110 GHz gyrotron with an improved cavity," in *2005 Joint 30th International Conference on Infrared and Millimeter Waves and 13th International Conference on Terahertz Electronics*, Sept 2005, pp. 241–242.

[150] Y. Hidaka, E. Choi, I. Mastovsky, M. A. Shapiro, C. D. Joye, Jagadishwar, R. Sirigiri, and R. J. Temkin, "Experimental Investigation of Filamentary Arrays in a Breakdown Plasma Generated by a 1.5 MW, 110 GHz Gyrotron," in *2007 IEEE 34th International Conference on Plasma Science (ICOPS)*, June 2007, pp. 903–903.

[151] A. V. Gaponov, V. A. Flyagin, A. L. Goldenberg, G. S. Nusinovich, S. E. Tsimring, V. G. Usov, , and S. N. Vlasov, "Powerful millimeter-wave gyrotrons," *International Journal of Electronics*, vol. 51, no. 4, pp. 277–302, 1981.

[152] J. J. Barroso and R. A. Correa, "Coaxial resonator for a megawatt 280 GHz gyrotron," *International Journal of Infrared and Millimeter Waves*, vol. 12, no. 7, pp. 717–728, 1991.

[153] M. E. Read, G. S. Nusinovich, S. Member, G. Bird, J. P. Hogge, K. Kreischer, and M. Blank, "Design of a 3 MW 140-GHz Gyrotron with a coaxial Cavity," *IEEE Transactions on Plasma Science*, vol. 24, no. 3, pp. 586–595, 1996.

[154] R. Advani, J. P. Hogge, K. E. Kreischer, M. Pedrozzi, M. E. Read, J. R. Sirigiri, and R. J. Temkin, "Experimental investigation of a 140-GHz coaxial gyrotron oscillator," *IEEE Transactions on Plasma Science*, vol. 29, no. 6, pp. 943–950, 2001.

[155] C. T. Iatrou, "Mode selective properties of coaxial gyrotron resonators," *IEEE Transactions on Plasma Science*, vol. 24, no. 3, pp. 596–605, 1996.

[156] B. Piosczyk, O. Braz, C. T. Iatrou, S. Kern, M. Kuntze, V. I. Malygin, A. B. Pavelyev, and V. E. Zapevalov, "A 1.5MW 140 GHz TE28,16 Coaxial Cavity Gyrotron," *IEEE Transactions on Plasma Science*, vol. 25, no. 3, pp. 460–469, 1997.

[157] B. Piosczyk, O. Braz, G. Dammertz, C. Iatrou, S. Illy, M. Kuntze, G. Michel, a. Mobius, M. Thumm, V. Flyagin, V. Khishnyak, a.B. Pavelyev, and V. Zapevalov, "Coaxial cavity gyrotron with dual RF beam output," *IEEE Transactions on Plasma Science*, vol. 26, no. 3, pp. 393–401, 1998.

[158] B. Piosczyk, O. Braz, G. Dammertz, C. T. Iatrou, S. Illy, M. Kuntze, G. Michel, and M. Thumm, "165 GHz 1.5 MW Coaxial Cavity Gyrotron with Depressed Collector," *IEEE Transactions on Plasma Science*, vol. 27, no. 2, pp. 484–489, 1999.

[159] V. A. Flyagin, V. I. Khizhnyak, V. N. Manuilov, M. A. Moiseev, A. B. Pavelyev, V. E. Zapevalov, and N. A. Zavolsky, "Investigations of advanced coaxial gyrotrons at IAP RAS," *International Journal of Infrared and Millimeter Waves*, vol. 24, no. 1, pp. 1–17, 2003.

[160] O. Dumbrajs and G. I. Zaginaylov, "Ohmic losses in coaxial gyrotron cavities widh corrugated insert," *IEEE Transactions on Plasma Science*, vol. 32, no. 3 I, pp. 861–866, 2004.

[161] Z. C. Ioannidis, O. Dumbrajs, and I. G. Tigelis, "Eigenvalues and ohmic losses in coaxial gyrotron cavity," *IEEE Transactions on Plasma Science*, vol. 34, no. 4, pp. 1516–1522, 2006.

[162] J. Jin, M. Thumm, B. Piosczyk, S. Kern, J. Flamm, and T. Rzesnicki, "Novel numerical method for the analysis and synthesis of the fields in highly oversized waveguide mode converters," *IEEE Transactions on Microwave Theory and Techniques*, vol. 57, no. 7, pp. 1661–1668, 2009.

[163] S. Singh and M. V. Kartikeyan, "Full Wave Analysis of Coaxial Gyrotron Cavity With Triangular Corrugations on the Insert," *IEEE Transactions on Electron Devices*, vol. 64, no. 4, pp. 1756–1762, April 2017.

[164] R. A. Correa, J. J. Barroso, and P. J. Castro, "Eigenmodes in gyrotron coaxial cylindrical resonators with corrugated inner conductor," in *Microwave and Optoelectronics Conference, 1997. Linking to the Next Century. Proceedings., 1997 SBMO/IEEE MTT-S International*, vol. 2, Aug 1997, pp. 611–616.

[165] B. Piosczyk, a. Arnold, G. Dammertz, M. Kuntze, G. Michel, O. S. Lamba, and M. K. Thumm, "Step-frequency operation of a coaxial cavity from 134 to 169.5 GHz," *IEEE Transactions on Plasma Science*, vol. 28, no. 3, pp. 918–923, 2000.

[166] O. Dumbrajs, "A novel method of improving performance of coaxial gyrotron resonators," *IEEE Transactions on Plasma Science*, vol. 30, no. 3, pp. 836–839, 2002.

[167] M. V. Kartikeyan, A. Pavelyev, B. Piosczyk, and M. Thumm, "A step towards a 170 GHz, 5 MW coaxial super gyrotron," in *4th IEEE International Conference on Vacuum Electronics*, 2003, pp. 36–37.

[168] M. V. Kartikeyan, B. Piosczyk, and M. Thumm, "Feasibility of a 140 GHz, 3.0-3.5 MW, CW coaxial gyrotron with dual beam output," in *Joint 29th International Conference on Infrared and Millimeter Waves and 12th International Conference on Terahertz Electronics*, 2004, pp. 36–37.

[169] M. H. Beringer, S. Kern, and M. Thumm, "Mode Selection and Coaxial Cavity Design for a 4-MW 170-GHz Gyrotron, Including Thermal Aspects," *IEEE Transactions on Plasma Science*, vol. 41, no. 4, pp. 853–861, April 2013.

[170] B. Piosczyk, G. Dammertz, O. Dumbrajs, O. Drumm, S. Illy, J. Jin, and M. Thumm, "A 2-MW, 170-GHz coaxial cavity gyrotron," *IEEE Transactions on Plasma Science*, vol. 32, no. 2, pp. 413–417, April 2004.

[171] M. Thumm, "Recent Advances in the Worldwide Fusion Gyrotron Development," *IEEE Transactions on Plasma Science*, vol. 42, no. 3, pp. 590–599, March 2014.

[172] D. Wagner, G. Grünwald, F. Leuterer, A. Manini, F. Monaco, M. Münich, H. Schütz, J. Stober, H. Zohm, T. Franke, M. Thumm, G. Gantenbein, R. Heidinger, A. Meier, W. Kasparek, C. Lechte, A. Litvak, G. Denisov, A. Chirkov, E. Tai, L. Popov, V. Nichiporenko, V. Myasnikov, E. Solyanova, S. Malygin, F. Meo, and P. Woskov, "Status of the new multi-frequency ECRH system for ASDEX Upgrade," *Nuclear Fusion*, vol. 48, no. 5, p. 054006, 2008.

[173] N. Komerath, B. Dessanti, and S. Shah, "Millimeter wave Space Power Grid architecture development 2012," in *IEEE Aerospace Conference*, March 2013, pp. 1–10.

[174] G. S. Baghel, M. V. Kartikeyan, and M. K. Thumm, "A 220/247.5/275-GHz, 1.0-MW, Triple Frequency Regime Gyrotron," *IEEE Transactions on Electron Devices*, vol. 64, no. 4, pp. 1774–1780, April 2017.

[175] J. Franck, K. Avramidis, G. Gantenbein, S. Illy, J. Jin, M. Thumm, and J. Jelonnek, "A generic mode selection strategy for high-order mode gyrotrons operating at multiple frequencies," *Nuclear Fusion*, vol. 55, no. 1, pp. 1–6, 2015.

[176] S. Yuvaraj, G. S. Baghel, S. Singh, and M. V. Kartikeyan, "Gyrotron Design Suite 2018 (GDS 2018)," *Private Communication*, 2018.

[177] S. Illy, J. Zhang, and J. Jelonnek, "Gyrotron electron gun and collector simulation with the ESRAY beam optics code," in *2015 IEEE International Vacuum Electronics Conference (IVEC)*, April 2015, pp. 1–2.

[178] G. S. Nusinovich, O. V. Sinitsyn, L. Velikovich, M. Yeddulla, T. M. Antonsen, A. N. Vlasov, S. R. Cauffman, and K. Felch, "Startup scenarios in high-power gyrotrons," *IEEE Transactions on Plasma Science*, vol. 32, no. 3, pp. 841–852, June 2004.

[179] G. S. Nusinovich, M. Yeddulla, T. M. Antonsen, and A. N. Vlasov, "Start-Up Scenario in Gyrotrons with a Nonstationary Microwave-Field Structure," *Physics Review Letters*, vol. 96, p. 125101, Mar 2006.

[180] O. V. Sinitsyn, G. S. Nusinovich, T. M. Antonsen, and A. N. Vlasov, "Startup scenarios in MW-class gyrotrons with diode and triode-type electron guns," in *2008 33rd International Conference on Infrared, Millimeter and Terahertz Waves*, Sept 2008, pp. 1–2.

[181] T. Numakura, T. Imai, T. Kariya, R. Minami, K. Tsumura, Y. Ebashi, and S. Kajino., "Code development for the calculations of time-dependent multimode oscillations in the cavity of the future high-power gyrotrons," in *AIP Conference Proceedings*, vol. 1771, no. 1. AIP Publishing, 2016, p. 030023.

[182] M. V. Kartikeyan, A. Kumar, S. Kamakshi, P. K. Jain, S. Illy, E. Borie, B. Piosczyk, and M. K. Thumm, "RF Behavior of a 200-kW CW Gyrotron," *IEEE Transactions on Plasma Science*, vol. 36, no. 3, pp. 631–636, June 2008.

[183] O. Dumbrajs, T. Saito, and Y. Tatematsu, "Start-up scenario of a high-power pulsed gyrotron for 300 GHz band collective Thomson scattering diagnostics in the large helical device," *Physics of Plasmas*, vol. 23, no. 2, p. 023106, 2016.

[184] G. S. Nusinovich, O. V. Sinitsyn, T. M. Antonsen, A. N. Vlasov, S. R. Cauffman, and K. L. Felch, "Slow processes in startup scenarios of long-pulse gyrotrons," *Physics of Plasmas*, vol. 13, no. 8, p. 083106, 2006.

[185] A. Schlaich, C. Wu, I. Pagonakis, K. Avramidis, S. Illy, G. Gantenbein, J. Jelonnek, and M. Thumm, "Frequency-Based Investigation of Charge Neutralization Processes and Thermal Cavity Expansion in Gyrotrons," *Journal of Infrared, Millimeter, and Terahertz Waves*, vol. 36, no. 9, pp. 797–818, 2015.

[186] G. Dammertz, O. Brat, C. T. Iatrou, M. Kuntze, A. Mobius, B. Piosczyk, and M. Thumm, "Long-pulse operation of a 0.5 MW TE10,4 gyrotron at 140 GHz," *IEEE Transactions on Plasma Science*, vol. 24, no. 3, pp. 570–578, Jun 1996.

[187] G. S. Nusinovich, A. N. Vlasov, T. M. Antonsen Jr., J. Lohr, B. G. Danly, and J.-P. Hogge, "Excitation of parasitic modes in gyrotrons with fast voltage rise," *Physics of Plasmas*, vol. 15, no. 10, p. 103101, 2008.

[188] G. S. Baghel and M. V. Kartikeyan, "Extended RF Behavior of a 77/154 GHz, 0.5 MW Continuous Wave Gyrotron," *IEEE Transactions on Electron Devices*, vol. 63, no. 6, pp. 2538–2543, jun 2016.

[189] J. Neilson, "Surf3d and LOT : computer codes for design and analysis of high-performance QO launchers in gyrotrons," in *Infrared and Millimeter Waves, Conference Digest of the 2004 Joint 29th International Conference on 2004 and 12th International Conference on Terahertz Electronics, 2004.*, Sept 2004, pp. 667–668.

[190] S. Yuvaraj, M. V. Kartikeyan, and M. K. Thumm, "RF Behavior of a 220/251.5-GHz, 2-MW, Triangular Corrugated Coaxial Cavity Gyrotron," *IEEE Transactions on Electron Devices*, vol. 64, no. 10, pp. 4287–4294, Oct 2017.

[191] J. M. Baird and W. Lawson, "Magnetron injection gun (MIG) design for gyrotron applications," *Internation Journal of Electronics*, vol. 61, no. 6, p. 969–984, June 1986.

[192] R. L. Ives, L. R. Falce, S. Schwartzkopf, and R. Witherspoon, "Controlled porosity cathodes from sintered tungsten wires," *IEEE Transactions on Electron Devices*, vol. 52, no. 12, pp. 2800–2805, Dec 2005.

[193] B. Piosczyk, "A Coaxial Magnetron Injection Gun (CMIG) for a 2 MW, 170 GHz Coaxial Cavity Gyrotron," *International Journal of Infrared and Millimeter Waves*, vol. 27, no. 8, pp. 1041–1061, August 2006.

[194] J. Neilson, "Analysis and Optimal Synthesis of Quasi-Optical Launchers for High Power Gyrotrons," in *2006 Joint 31st International Conference on Infrared Millimeter Waves and 14th International Conference on Teraherz Electronics*, Sept 2006, pp. 337–337.

[195] A. R. Choudhury, D. D'Andrea, and M. Thumm, "Study of Dynamic After Cavity Interaction in Gyrotrons — Part II: Influence of a Nonuniform Magnetic Field," *IEEE Transactions on Electron Devices*, vol. 62, no. 1, pp. 192–199, Jan 2015.

[196] O. Dumbrajs, H. Kalis, and A. Reinfelds, "Are Coaxial Super Power Gyrotrons Feasible?" vol. 26, no. 6, pp. 787–805, Jun 2005.

[197] O. Dumbrajs and G. S. Nusinovich, "Azimuthal instability of radiation in gyrotrons with overmoded resonators," *Physics of Plasmas*, vol. 12, no. 5, p. 053106, 2005.

[198] E. Abaka, "TE and TM modes in transmission lines with circular outer conductor and eccentric circular inner conductor," *Electronics Letters*, vol. 5, no. 11, pp. 251–252, May 1969.

[199] G. I. Veselov and S. G. Semenov, "Theory of circular waveguide with eccentrically placed metallic conductor," *Radio Engineering and Electron Physics*, vol. 15, pp. 687–690, 1970.

[200] H. Y. Yee and N. F. Audeh, "Cutoff Frequencies of Eccentric Waveguides," *IEEE Transactions on Microwave Theory and Techniques*, vol. 14, no. 10, pp. 487–493, October 1966.

[201] M. J. Hine, "Eigenvalues for a uniform fluid waveguide with an eccentric-annulus cross-section," *Journal of Sound Vibration*, vol. 15, pp. 295–305, 1971.

[202] J. R. Kuttler, "A New Method for Calculating TE and TM Cutoff Frequencies of Uniform Waveguides with Lunar or Eccentric Annular Cross Section," *IEEE Transactions on Microwave Theory and Techniques*, vol. 32, no. 4, pp. 348–354, Apr 1984.

[203] B. N. Das and O. J. Vargheese, "Analysis of dominant and higher order modes for transmission lines using parallel cylinders," *IEEE Transactions on Microwave Theory and Techniques*, vol. 42, no. 4, pp. 681–683, April 1994.

[204] O. Dumbrajs and A. B. Pavelyev, "Insert misalignment in coaxial cavities and its influence on gyrotron operation," *International Journal of Electronics*, vol. 82, no. 3, pp. 261–268, 1997.

[205] S.-C. Zhang and M. Thumm, "Eigenvalue equations and numerical analysis of a coaxial cavity with misaligned inner rod," *IEEE Transactions on Microwave Theory and Techniques*, vol. 48, no. 1, pp. 8–14, Jan 2000.

[206] G. N. Watson, *Theory of Bessel Functions*. London, U.K.: Cambridge Univ. Press, 1952.

[207] I. G. Tigelis, M. Pedrozzi, P. G. Cottis, and J. L. Vomvoridis, "Calculation of eigenmodes in a nonperiodic corrugated waveguide," *IEEE Transactions on Microwave Theory and Techniques*, vol. 45, no. 2, pp. 236–244, Feb 1997.

[208] I. G. Tigelis, J. L. Vomvoridis, and S. Tzima, "High-frequency electromagnetic modes in a dielectric-ring loaded beam tunnel," *IEEE Transactions on Plasma Science*, vol. 26, no. 3, pp. 922–930, June 1998.

[209] R. W. Gerchberg and W. O. Saxton, “A Practical Algorithm for the Determination of Phase from Image and Diraction Plane Pictures,” *Optik*, vol. 35, pp. 237–246, 1971.

[210] J. R. Fienup, “Phase retrieval algorithms: a comparison,” *Appl. Optics*, vol. 21, no. 15, pp. 2758–2769, Aug 1982.

List of Publications

Journal publications

1. **S. Yuvaraj**, M. V. Kartikeyan and M. K. Thumm, "Design Studies of a 3MW, Multifrequency (170/204/236 GHz) DEMO Class Triangular Corrugated Coaxial Cavity Gyrotron," *IEEE Trans. Electron Devices*, vol. 66, no. 1, pp. 702-708, Jan. 2019.
2. **S. Yuvaraj**, S. Illy and M. V. Kartikeyan, "Electron Gun and Output Coupling System for a 220-/251.5-GHz, 2-MW Triangular Corrugated Coaxial Cavity Gyrotron," *IEEE Trans. Electron Devices*, vol. 64, no. 12, pp. 5134-5140, Dec. 2017.
3. **S. Yuvaraj**, M. V. Kartikeyan and M. K. Thumm, "RF Behavior of a 220/251.5-GHz, 2-MW, Triangular Corrugated Coaxial Cavity Gyrotron," *IEEE Trans. Electron Devices*, vol. 64, no. 10, pp. 4287-4294, Oct. 2017.
4. **S. Yuvaraj**, D. A. Jose, S. Singh and M. V. Kartikeyan, "Effect of Insert Misalignment on a Triangular Corrugated Coaxial Cavity Gyrotron, " *IEEE Trans. Electron Devices*, (Under Review) 2019.

Conference publications

1. **S. Yuvaraj**, D. A. Jose, M. S. Chauhan, Stefan Illy, M.V. Kartikeyan, Manfred Thumm, "Design studies of a Magnetron Injection Gun for a 2 MW, Multi-frequency (220/251.5/283 GHz) Triangular Corrugated Coaxial Cavity Gyrotron," in *2018 19th International Vacuum Electronics Conference (IVEC 2018)*, Monterey, USA, April 24-26, 2018.
2. **S. Yuvaraj**, D. A. Jose, M. S. Chauhan, M. V. Kartikeyan and M. K. Thumm, "RF behavior of a 220/251.5 GHz, 2MW, triangular corrugated coaxial cavity gyrotron extended to the third operating frequency 283 GHz," in *2018 11th German Microwave Conference (GeMiC)*, Freiburg, Germany, 2018, pp. 295-298.
3. **S. Yuvaraj**, D. A. Jose, S. Singh, M. S. Chauhan and M. V. Kartikeyan, "Eigenvalue analysis of a triangular corrugated coaxial cavity with misaligned inner rod," in *2018 11th German Microwave Conference (GeMiC)*, Freiburg, Germany, 2018, pp. 195-198.
4. **S. Yuvaraj**, Delphine Alphonsa Jose, Madan Singh Chauhan and M. V. Kartikeyan, "Mode Selection Studies for a 2 MW, DEMO class Multi-frequency Coaxial Cavity Gyrotron,"*National Symposium on Vacuum Electronic Devices & Applications (VEDA-2017)*, Roorkee, India, November 17-19, 2017.
5. **Yuvaraj S**, Sukwinder Singh, G. S. Baghel and M. V. Kartikeyan, "Mode selection and interaction structure design of a megawatt class, sub-THz wave coaxial cavity

gyrotron," in *2015 International Conference on Microwave, Optical and Communication Engineering (ICMOCE)*, Bhubaneswar, 2015, pp. 307-309.

Publication in Pipeline

1. **S. Yuvaraj**, D. A. Jose, S. Singh and M. V. Kartikeyan, "Fullwave analysis of a triangular corrugated coaxial cavity with misaligned inner rod, " Manuscript prepared to submit to *IEEE Trans. Electron Devices*, 2019.

Other Publications

1. Sukwinder Singh, **S. Yuvaraj**, Gaurav Singh Baghel, M. V. Kartikeyan, "Design Studies of a RF Interaction Cavity for a 4 MW, 170 GHz Triangular Corrugated Coaxial Cavity Gyrotron," in *2018 19th International Vacuum Electronics Conference (IVEC 2018)*, Monterey, USA, April 24-26, 2018.
2. Madan S. Chauhan, **S. Yuvaraj**, P. K. Jain, M. V. Kartikeyan, "Design of a W-Band, 100 kW, Frequency Doubling Gyroklystron Amplifier," in *2018 19th International Vacuum Electronics Conference (IVEC 2018)*, Monterey, USA, April 24-26, 2018.
3. **S. Yuvaraj**, M. S. Chauhan, D. A. Jose, M.V. Kartikeyan, "Design study of a Quasi-Optical Launcher for 2 MW,170 GHz Coaxial Cavity Gyrotron," in *2018 3rd International Conference on Microwave and Photonics (ICMAP 2018)*, Dhanbad, India, Feb. 9-11, 2018.
4. Delphine Alphonsa Jose, **S. Yuvaraj**, Madan Singh Chauhan, and M.V. Kartikeyan, "Design of a Magnetron Injection Gun for a 4 MW, 170 GHz, Coaxial Cavity Gyrotron," in *2017 14th IEEE India Council International conference (INDICON-2017)*, Roorkee, India, December 15-17, 2017.
5. Delphine Alphonsa Jose, **S. Yuvaraj**, Madan Singh Chauhan, and M. V. Kartikeyan, "Design Studies of a Triode type Magnetron Injection Gun for a Megawatt class, sub-THz wave Coaxial Cavity Gyrotron,"*National Symposium on Vacuum Electronic Devices & Applications (VEDA-2017)*, Roorkee, India, November 17-19, 2017.
6. Madan Singh Chauhan, **S. Yuvaraj**, and M. V. Kartikeyan, "Preliminary Design of a Frequency Doubling Gyroklystron,"*National Symposium on Vacuum Electronic Devices & Applications (VEDA-2017)*, Roorkee, India, November 17-19, 2017.
7. Sukwinder Singh, **Yuvaraj S**, G. S. Baghel and M. V. Kartikeyan, "Study of Plasma loaded Gyrotron Coaxial cavity with Triangular corrugations on the insert," *National Conference on Emerging Trends in Vacuum Electronic Devices & Applications VEDA*, 2016.
8. **Yuvaraj S**, Sukwinder Singh, Gaurav Singh Baghel and M. V. Kartikeyan, "RF behavior of a 165 GHz, 1.5 MW, Triangular Corrugated Coaxial Cavity Gyrotron,"

National Conference on Emerging Trends in Vacuum Electronic Devices & Applications VEDA, 2016.